POLITECNICO
MILANO 1863

SCUOLA DI INGEGNERIA CIVILE,
AMBIENTALE E TERRITORIALE

Numerical investigation of a base reinforced piled embankment solution on inclined bearing layer

TESI DI LAUREA MAGISTRALE IN
INGEGNERIA CIVILE - GEOTECNICA

Vladislav Troitskii

Student ID: 960893
Advisor: Prof. Dr. Cristina Jommi
Co-advisor: Ing. Dr. Andrea Masella
Academic Year: 2021-22

Abstract

The work addresses a viable solution for a railway track located on a very soft deposit made of mine tailing. For such soft soil deposits base reinforced piled embankments are common solution, since are able to transfer the load of the structure to stiff bearing layers. However, in the case analysed, the geological investigation showed a dipping bearing layer whose inclination could not be fully identified. Yet, for these conditions, the corresponding soil-structure interaction might not be completely defined, leading to potential uncertainties in terms of structure performance. Given this uncertainty, the design of the structure on end-bearing and floating piles was analysed in detail including a sensitivity analysis on variable, though reasonable, inclinations of the bearing layer. Only drained conditions were considered, as the site investigation had not detected a water table over the depth of interest. Based on the results of 3D numerical simulations, the postulated behaviour of the system is that first piles close to the bearing layer tend to provide the resistance to applied loads while the piles over a higher thickness of soft soil require settlement development to provide resistance, As a consequence, rotation of the embankment is observed. Ultimate limit state (failure) was never reached, and serviceability limit states is more likely to govern the design specifications. As the result of the complex soil-structure interaction investigation, design recommendations are provided.

Keywords: Numerical analysis, pile-supported embankment, geosynthetic reinforcement, inclined bearing layer

Sommario

Il lavoro affronta lo studio di una soluzione progettuale per una linea ferroviaria da costruire su un deposito estrememanete soffice costituito da residui di attività mineraria. In queste condizioni, una scelta comune è la costruzione di rilevati su pali, che trasferiscano i carichi a un substrato portante in profondità. Tuttavia, nel caso analizzato, l'indagine geologica aveva evidenziato un substrato portante inclinato, ma senza chiarire quale ne fosse l'inclinazione effettiva. Per una simile situazione, la complessa interazione terreno-struttura potrebbe non essere completamente definita, portando a potenziali incertezze in termini di prestazioni della struttura. Date le incertezze rimaste a seguito dell'indagine, la progettazione della struttura è stata affrontata ipotizzando sia pali portanti di punta sia pali sospesi. Una analisi di sensitività è stata condotta per valutare l'influenza sul comportamento della struttura dell'inclinazione dello strato portante, scegliendo inclinazioni variabili ancorché realistiche. Nell'analisi, si è fatto riferimento solo a condizioni drenate, perché l'indagine non aveva individuato un piano di falda. I risultati delle analisi numeriche 3D evidenziano che i pali più vicini al substrato portante si caricano per primi, mentre quelli immersi in strati soffici di maggiore spessore necessitano lo sviluppo di cedimenti per contribuire alla portata, generando così rotazione del rilevato. Lo stato limite ultimo (fallimento) non viene mai raggiunto e sono pertanto gli stati limite di servizio a governare la progettazione e l'esecuzione di questo tipo di opera. Come risultato finale della complessa analisi di interazione terreno-struttura, vengono fornite indicazioni e raccomandazioni progettuali.

Parole chiave: Analisi numerica, rilevati su pali, rinforzo di base in geosintetici, strato portante inclinato

Contents

Introduction

The process of ore extraction requires the production of large volume of waste material, similar to mud, which is typically stored in dedicated tailing ponds These materials are usually represented by mix of clays and silts with low values of mechanical parameters. Construction carried out under these conditions can lead to large surface settlements due to applied loads which reveals unfeasible for several types of standards. Therefore, before construction, such soils must be improved in order to carry the loads from buildings, roads and other infrastructures.

Another point is that usually the tailings are stored without any control on the thickness and distribution of deposits throughout the area. This makes an investigation planning difficult as it is hard to predict if the planned activities are enough to give full characterisation of the system. Therefore, sometimes the uncertainties can arise during the process of interpretation.

As in the case described in this work. During the interpretation of data received from a geological survey it reveals that there is enormous thickness of anthropogenic material (tailings) and that performed investigations at some places do not reveal the bearing layer up to the maximum investigated depth. Accordingly, to perform the design of a freight railway, needed to transfer the treated ore material, in such conditions a solution of the base reinforced piled embankment was proposed. However there is still uncertainty on the piles length and how the system would deform in case of piles not reaching the bearing layer.

The purpose of this study is to perform a comparative analysis in prediction of piled embankment response constructed over a mine tailings using numerical methods including the fact that there exist an uncertainty on the inclination of a bearing layer. Given this fact the following questions are addressed:

- What are the conditions in which piles are working?

- What is the main pattern of a system's deformation?

- What are the possible design solutions given the uncertainty?

The numerical analyses were performed using the Finite element method through PLAXIS 3D commercial software. Decision to use 3D numerical analysis was made due to the complex three-dimensional processes which take place within the embankment body. It is difficult to account for such effects with 2D analysis with similar quality of results. A comparison of results is made to analyse the system's behaviour and to provide design recommendations.

The results of the study are reported in the following sequence. In first chapter a general revision of the project geometry and literature review are provided. Second chapter provides the site conditions including geology, climatology, hydrology, seismic and geotechnical description of a construction site and as a result the geotechnical model is reported. The third chapter aims at description of numerical procedures and the model parameters calibration, whereas the fourth chapter gives an insight in the numerical model used for investigation.

Chapter five contains the most representative results of the investigation, their discussion and conclusions in terms of design recommendations. The sixth chapter is dedicated to the summary of the work done including conclusions and proposals for further studies.

1 | Project description

1.1. General project information

The project provides for the construction of a railway embankment along the axis indicated on the plan (see appendix D, sheet **1-1**). This section of the railway line is expected to increase the transport of treated ore to a second factory for further processing. The line serves for the heavy freight trains. The general plan of the site is represented in the appendix D on sheet **1-1**.

The projected section includes a single-track railway which is designed in accordance with SP 119.13330.2017 "Railway with 1520 mm track". The section is a typical standard cross-section of a railway track on an embankment, and it is shown in fig. 1.1.

The project provides for the removal of the upper layer of soil to a final ground elevation of 565 meters relative to sea level. In this case, the construction site can be assumed to be a horizontal plane and already prepared for further construction of the railway embankment.

The embankment is located on soils with low mechanical parameters and in this case it is expected to improve the mechanical characteristics of the soils using rigid inclusions with basal reinforcement including geogrid. Therefore, the preparation of the site for the construction of the embankment involves the removal of 1 meter of soil followed by the installation of piles inside the pit and further construction of a mat from the granular backfill material (see table 1.1), with a compaction with rollers layer by layer. After the construction of the piles and mat, the subsequent construction of the embankment is carried out in layers with the compaction of each layer. The material of the embankment is the same as the material of the mat also compacted with the rollers. Proposed in the project basal reinforcement is represented in the fig. 1.2.
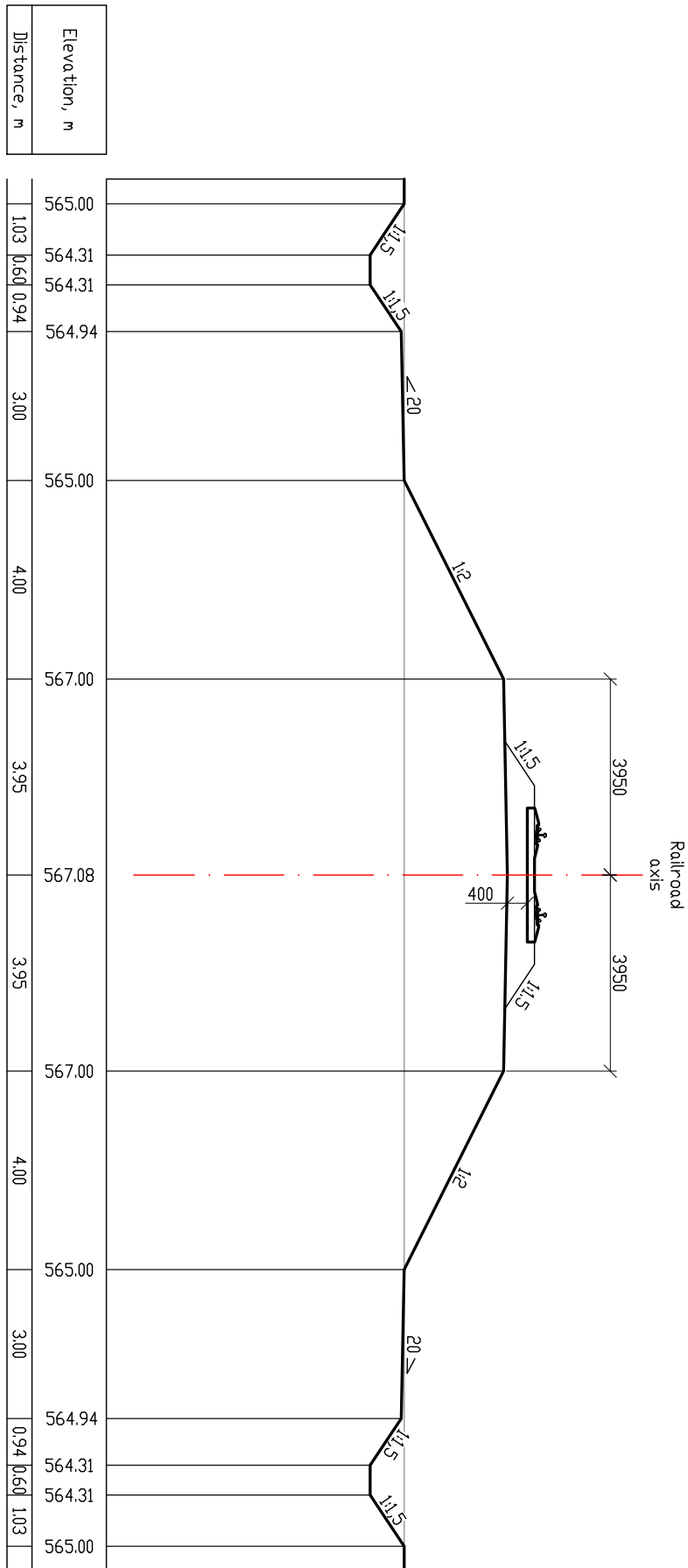
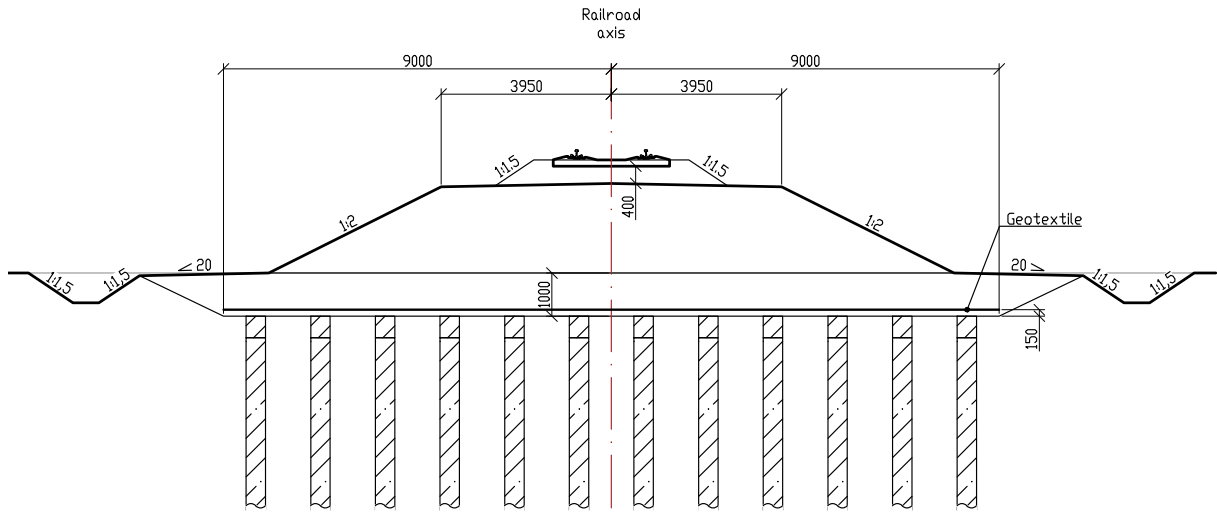Figure 1.1: Cross-section of the designed embankment

Figure 1.2: Proposed basal reinforcement of the embankment

Table 1.1: Estimated physical and mechanical characteristics of the construction material

Characteristics	Units	Value
Natural unit weight, γ_n	kN/m^3	18.0
Friction angle, φ'	°	34
Cohesion, c'	kPa	0
Operational Young's modulus, E_{op}	MPa	30.0
Poisson's ratio, ν	-	0.25

Rigid inclusions are casted in place using the concrete C25/30 and it has a diameter of 450 mm (material properties are given in the table 1.2). The location of inclusions in the plan is provided in a rectangular pattern with the same distance in two directions, an example of the piles pattern is shown in fig. 1.3.
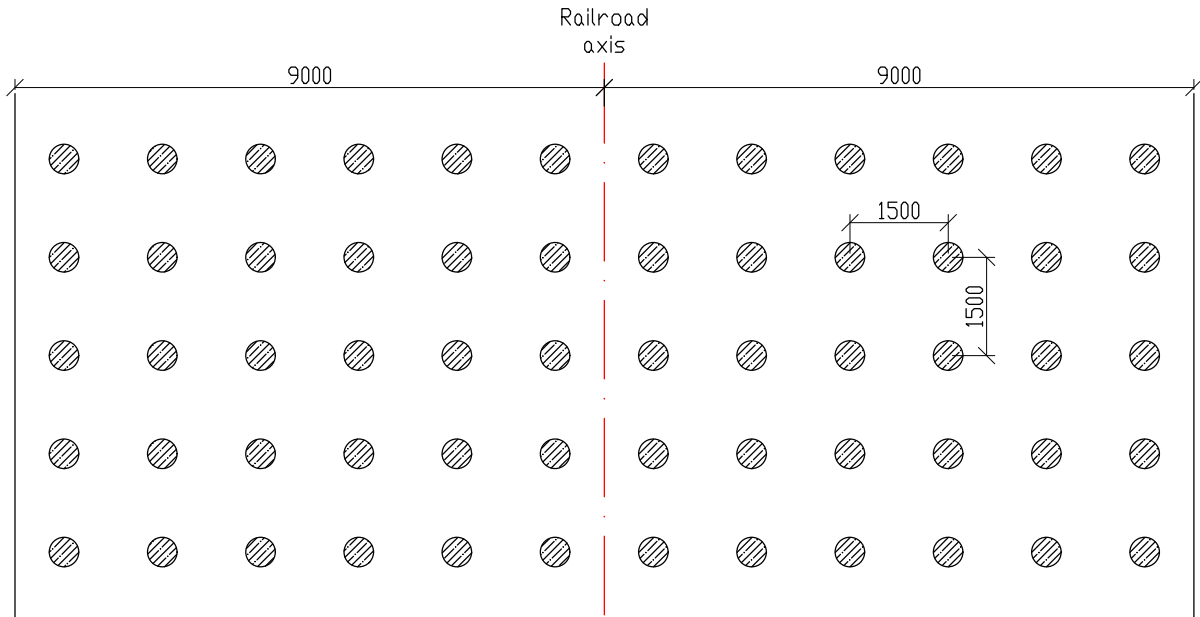
Figure 1.3: Rectangular pile layout

Table 1.2: Physical and mechanical parameters of the concrete C25/30

Characteristics	Units	Value
Unit weight, γ	kN/m³	24.0
Compressive strength, f_{ck}	MPa	30.0
Mean compressive strength, f_{cm}	MPa	38
Mean tensile strength, f_{ctm}	MPa	2.9
Mean Young's modulus, E_{cm}	GPa	33.0
Poisson's ratio, ν	-	0.15

Deformations

According to the rules of technical exploitation of the railway roads (according to PTE of the Russian Railways - Rules for the technical operation of the railways of the Russian Federation) the maximum acceptable settlement is equal to 50 mm and the maximum difference in rail elevations is 50 mm (induced rotation). After reaching these values the further operation of the rail road is unacceptable and it should be closed. For simplicity the limiting values are collected in the table 1.3.

Table 1.3: Admissible railway deformations

Type of deformation	Units	Value
Maximum settlement	mm	50.0
Maximum difference in rail elevation	mm	50.0
Maximum rail bed rotation	°	1.9

Loads

The normative temporary vertical load from the rolling stock of railways should be taken (taking into account the prospects for the development of railway vehicles) in the form of total maximum equivalent loads n, kN/m of the track obtained from individual groups of concentrated loads weighing up to $24.5 \cdot K$ kN, and uniformly distributed load of $9.81 \cdot K$ kN/m, where K is a class of the load, equal to 14 for freight railways.

1.2. Literature review

It is a well-known fact that during the construction of an embankment over highly deformable soils, which are previously reinforced with more rigid inclusions, a redistribution of pressure occurs within the embankment body and most of the load is then transferred on the rigid inclusions. This phenomenon is known as soil arching. Terzaghi (Terzaghi, 1943) was the first to describe this phenomenon as a redistribution of pressure from yielding soil mass to more stable stationary parts. In simple words, this mechanism arises from the relative movement of the soil which is resting on the different in stiffness parts (soft soil and stiff rigid inclusion). Due to the relative movement in the soil mass, shear stresses occur which results in the sort of arch within the embankment body.

1.2.1. Arching models

Over time, various authors have investigated this phenomenon and put forward hypotheses about how the arch is formed and how the load is distributed inside the embankment body. All models agree that part of the total load falls on the piles (direct load) and a portion that is coming to the subsoil (residual load).

The following models were proposed up to now:

- Rigid arching model;

- Limit equilibrium model;

- Concentric arches model.

Rigid arching model

This model implies the formation of an arch of a certain shape, above which all loads, namely backfill and external loads, are transferred to the piles, and inside the arch, the weight of the soil is perceived by the soil between the piles and geogrid.

The best known of these is the model described by Carlsson (Carlsson, 1987) in which the arch forms in the inter-pile space, is linear, and extends 30 degrees from the extreme point of the pilecap. This model takes into account 2D conditions and does not account for the arch development in the diagonal space between piles, which results in less load on geogrid and piles.

Rogbeck (Rogbeck et al., 1998) further developed Carlsson's model to 3D conditions, still considering the fixed triangular arch shape, but increasing the 2D load according to the following equation:

$$F_{3D} = \frac{1 + \frac{c}{a}}{2} \cdot F_{2D} \tag{1.1}$$

Where a is a pile cap width and c is the pile spacing.

Proposed SINTEF method by Eiksund (Eiksund et al., 2000) that also assumed a development of the 3D wedge within the embankment body with the wedge borders slope inclined of $1 : \beta$ with β belonging to the range between 2.5 and 3.5. The value of β should be calibrated as a function of the ratio c/a and embankment height H (as represented in the fig. 1.4). For low value of c/a ratio and small height H the inclination β increases in order to account for a weak development of the arch effect and vice versa.
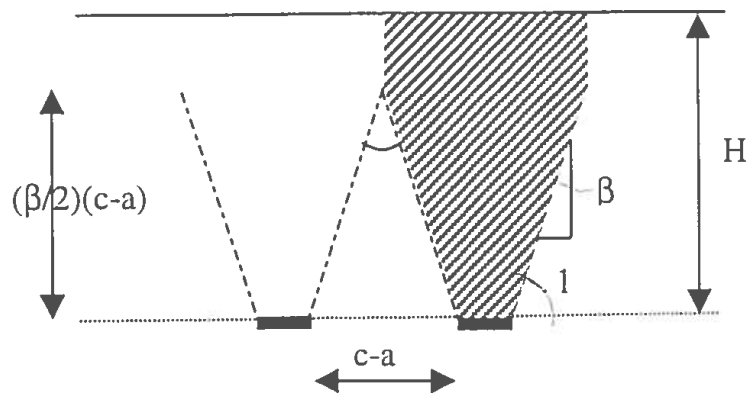

Figure 1.4: Arching by SINTEF's method (Eiksund et al., 2000)

The rigid arch model proposed by Collin (Collin, 2004) also known as the Enhanced

Arching Model, which assumes a formation of 3D soil wedge with the borders inclination of 45°. In this case for a triangular pattern of piles a tetrahedron will be formed, while for rectangular pattern of piles a pyramid will be formed (as represented in the fig. 1.5).
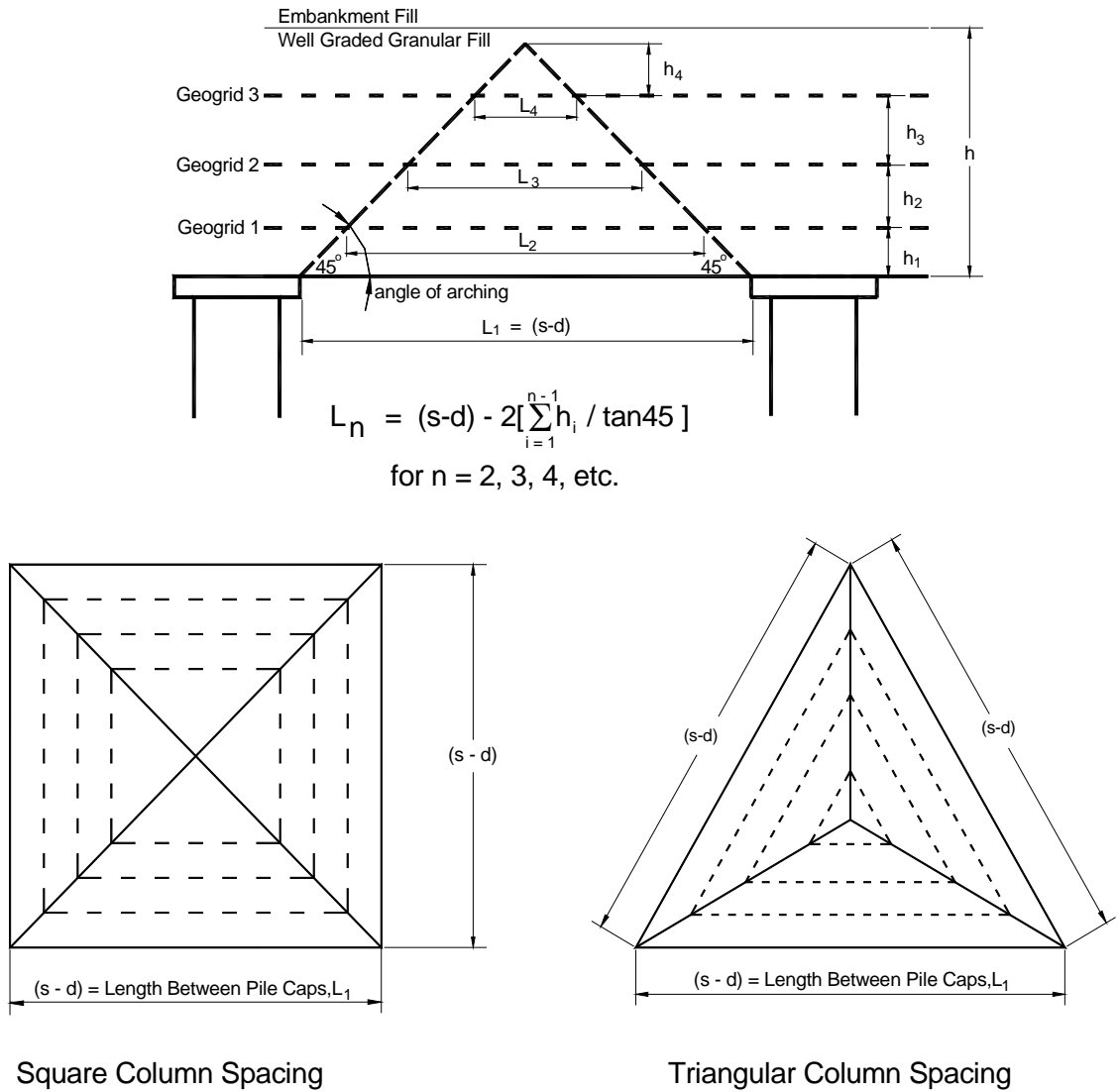

Figure 1.5: Enhanced Arching Model proposed by Collin (Collin, 2004)

According to this model the load distributed on a layer (n) of reinforcement (W_{T_n}) for an angle of arching of 45° may be determined from the following equation:

$$W_{T_n} = \frac{[A_n + A_{n+1}] \cdot h_n \cdot \gamma}{2 \cdot A_n} \tag{1.2}$$

Where A - Area at reinforcement layer n or $n + 1$.

The Collin's model accounts for 3 and more layers of reinforcement and it is the only

model among the rigid arch models that considers multi-layered systems.

Limit Equilibrium arching models

The following arching models are based on the equations of limit equilibrium for which a certain failure mode is determined and arching efficiency equations are derived accordingly.

First model based on the limit equilibrium was proposed by the Helwett and Randolph (Helwett and Randolph, 1988). This model assumes a formation of semi-circular (2D conditions) and semi-spherical (3D conditions) arches. The model is based on the set of experiments that were carried out on the small scale model and experimental evidence is that hemispherical arch is developing between the piles. Taking into consideration a cross section of this hemisphere it could be shown that failure of arch is more likely to occur in the crown or above the pile cap, thus it is possible to consider an equilibrium of infinitesimal volume to define the stability and efficiency of the arch (as shown in the fig. 1.6).
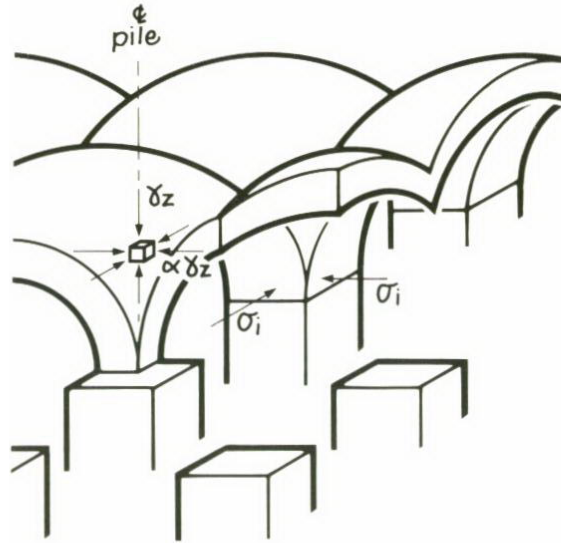
Figure 1.6: Isometric view of the general arrangement (Helwett and Randolph, 1988)

The efficiency of the piles system is expressed as a function of the cap size b, pile spacing s, embankment height H and material friction angle φ (included in passive earth pressure coefficient K_p) as following:

$$E = \frac{\beta}{1 + \beta} \tag{1.3}$$

$$where \quad \beta = \frac{2 \cdot K_p}{K_p + 1} \cdot \frac{1}{1 + b/s} \cdot \left[(1 - b/s)^{-K_p} - (1 + K_p \cdot b/s) \right] \tag{1.4}$$

Proposed model was adopted in the BS8006 (2010) British design guideline, ASIRI (2012) French design guideline and as a possible option of the arch in the EBGEO (2010) German design guideline.

There are two major drawbacks of the Helwett and Randolph model: 1) it does not account for the basal geosynthetics reinforcement, thus it does not account for the load transfer to the piles due to geogrid presence. 2) It does not account for development of partial arch in small embankments and may underestimate the load transfer in this case.

The second model among Limit Equilibrium models family is the model proposed by Za-eske. This model is also based on the 3D small scale experiments the idea of which was to investigate the arching effect as well as the distribution of the subgrade reaction (element that was not accounted for in the previous studies). During the test a control of the stresses was carried out with the pressure cells at various heights within the embankment body and above the pile cap.

Another new aspect with respect to the Helwett and Randolph's model is the fact that this study investigated the formation of the partial arching. Hence, in case when the arch height is larger than the mattress height.

Therefore, considering the equilibrium of the infinitesimal element at the crown of the arch it is possible to write a differential equation governing its equilibrium as following:

$$-\sigma_z \cdot dA_u + (\sigma_z + d\sigma_z) \cdot dA_0 - 4 \cdot \sigma_\Phi \cdot dA_s \cdot sin\left(\frac{\delta\Phi_m}{2}\right) + \gamma \cdot dV = 0 \qquad (1.5)$$

Where σ_z is the vertical stress, dA_u, dA_0, dA_s are the area of the bottom, top and lateral sides of the infinitesimal element, σ_Φ is the lateral earth pressure, dV is the volume of the infinitesimal element and γ is the soil unit weight (refer to the fig. 1.7).
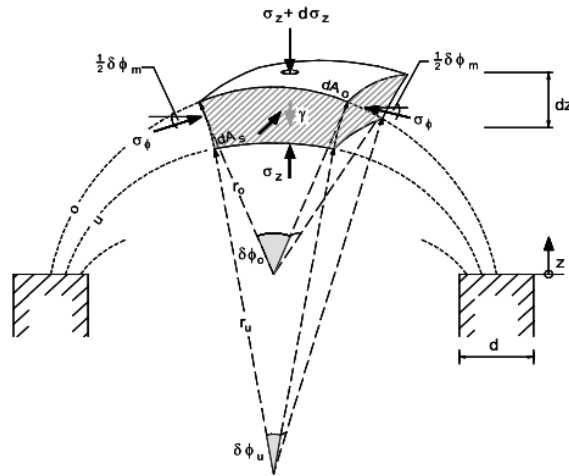
Figure 1.7: Infinitesimal soil element equilibrium according to Zaeske (Zaeske and Kempfert, 2002)

As the solution of the differential equation the distribution of the vertical stress on the subsoil as a function of the embankment height to pile spacing and material friction angle was obtained (as represented in the fig. 1.8).
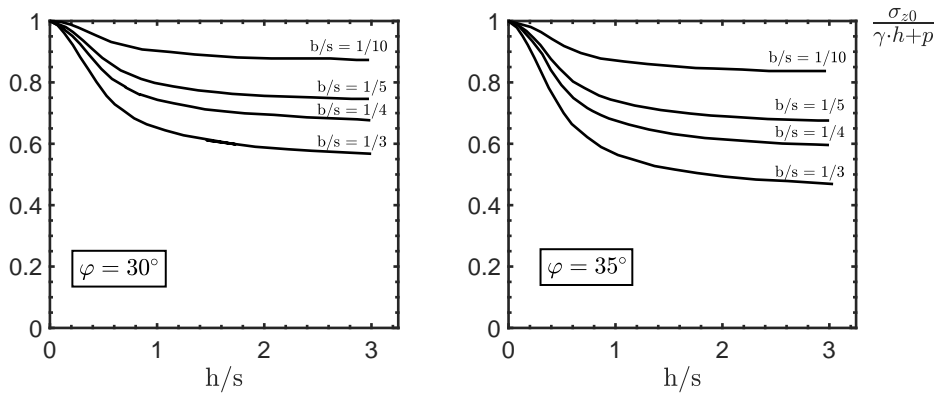

Figure 1.8: Vertical stress on the soft soil or the geosynthetic-reinforcement, line elements (Zaeske and Kempfert, 2002)

Zaeske's model was implemented in the EBGEO (2010) and in the CUR226 (2010).

Concentric arches model

The model consisting of concentric hemispheres was introduced by Van Eekelen in 2013 (van Eekelen et al., 2013). The model implements both 3D hemispheres and 2D arches (see fig. 1.9). The formation of the hemispheres takes place above the area between four

piles and the arches are formed in the area above the two neighbour piles. The formed system distributes load over the geo-synthetics and piles.
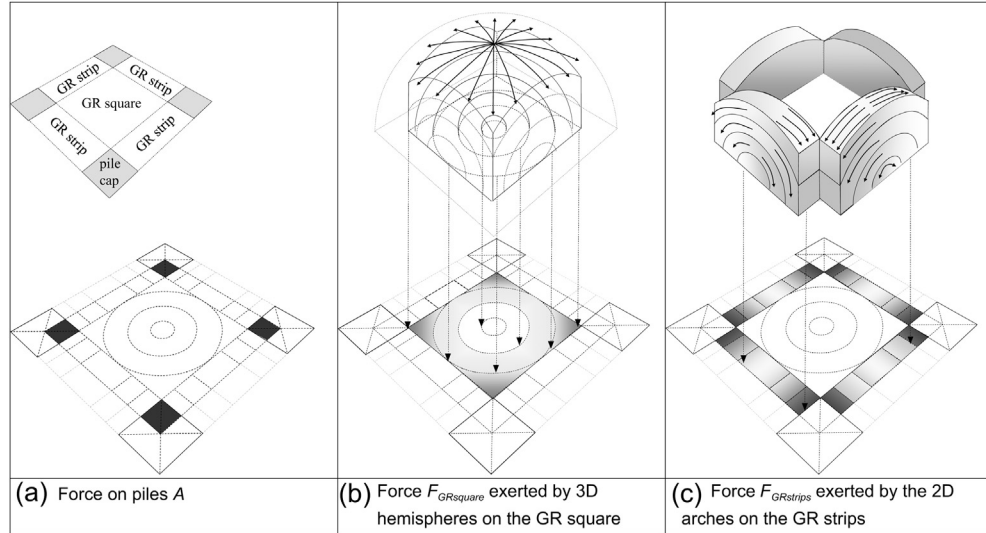
Figure 1.9: Distribution of the load on the geo-reinforcement area between the piles and the determination of arching part going to the pile (van Eekelen et al., 2013)

The distribution of the load over the space in between two adjacent piles could be represented as an inverse triangular load distribution with increase at the pile caps (schematised in the fig. 1.10).
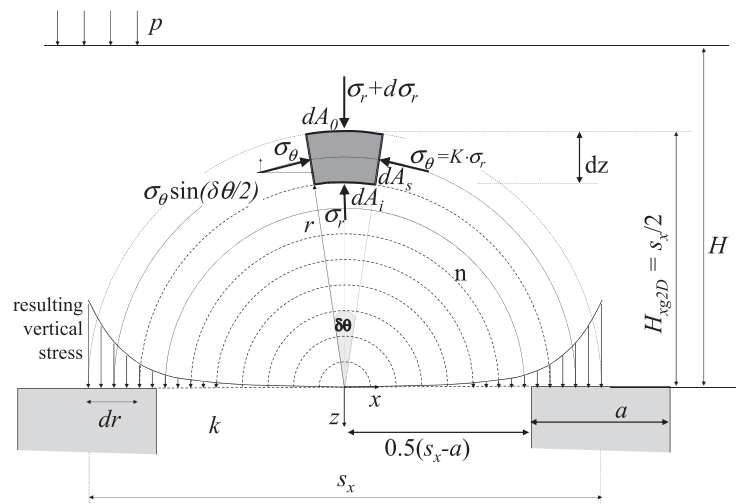
Figure 1.10: 2D concentric arches, the tangential stress in the arches result in a vertical stress exerted on the subsurface that resembles the simplified inverse triangle (van Eekelen et al., 2013)

1.2.2.   Conclusions

This review provides the summary of the most recent arching models described by different authors and considering different conditions. These models were implemented in the design codes of different countries. Based on the information provided, the assessment of the accuracy in predicting the system behaviour the following points could be highlighted:

- The estimation of the arching effect could be underestimated or overestimated depending on the embankment material, geometry and reinforcement parameters. For example in Zaeske's model the arching load is overestimated for low fill friction angle φ values and more reliable results at higher friction angle φ values. Such sensitivity to friction angle φ is also highlighted by the Helwett and Randolph's model.

- Regarding the distribution of load over the subsoil, it is highlighted that this choice is highly dependent on the subsoil type: a uniformly distributed load is more suitable for the higher subsoil stiffness, while an inverse triangular load distribution is more suitable for lower subsoil stiffness.

- All the models consider the initial time of the arch formation, while in case when clays/silts are present with time due to consolidation process and accumulation of the displacement an arching effect can become more stable and stronger.

- All the models disregard bearing layer compressibility and assume that a sufficient support could be provided, however depending on the bearing layer compressibility a more complex behaviour could be observed.

In this work an investigation on the basal reinforced embankment behaviour will be carried out for the case of the different inclination of the competent bearing layer. As in the case of the rotational deformation of embankment a complex arch development is expected as it will lose its symmetry. This phenomenon will be discussed more in detail based on the evidence of numerical simulations.

2 | Geotechnical model

2.1. General site information

The area under consideration is located in the area close to an industrial city of the Republic of Uzbekistan. The territory is characterized by mountainous terrain with valleys and plains. Its genesis is very complex, associated with ancient dislocations of continental plates. The formation of the relief is associated with the abrasive and accumulative activity of water mountain streams. Human industrial activity has played an important role in the formation of modern micro-relief. In particular, over the last 50 years of operation of the open pit mine, a deposition of waste rock by man levelled most of the irregularities.

The climate of the work area is sharply continental, characterized by large annual and daily amplitudes of air temperature fluctuations. The average annual air temperature is +14.8°C. The average monthly air temperature in July is from +28°C and above, the average maximum temperature in July is +35.2°C, the absolute maximum reaches +43.3°C. The average monthly air temperature in January is from -10°C to +4°C, the average minimum temperature in January is -2.4°C, the absolute minimum is -20.5°C. Stable snow cover is observed in less than 50% of winters.

In area under consideration, precipitation per year averages 532 mm, with fluctuations in some years from 333 to 955 mm. About 96% of precipitation occurs in autumn, winter and spring periods, the largest amount is in March-April (40% of the annual amount). The prevailing winds are east, north-east in January (average speed 3.0-3.7 m/s), in July - east, north-east, west (average speed 3.1-3.3 m/s).). The depth of soil freezing on the watersheds reaches 0.6 m, in the lowlands 0.2 m.

Measurements of seismicity were carried out to assess the seismic hazard of the site and the value of the design seismic score, to determine the design seismic score and expected accelerations. The value $I = 7.0$ should be taken as the initial intensity for micro-zoning of the site since the return period of earthquake with intensity $I = 8.0$ exceeds 5000 years and the probability of earthquake with such intensity for 50 years in the construction area

does not exceed $P = 0.005$. The expected values of peak accelerations on medium soils should not exceed $a_{max} = 200 \ cm/s^2$. The intensity of seismic impacts on the soils of the sedimentary layer depends on their thickness.

The plan of the investigations is presented in the appendix D on the sheet **1-1**.

2.2.   Geological conditions

The relief of the work site in geomorphological terms is confined to the alluvial-proluvial piedmont plain with a dissected relief. Average absolute elevation is equal to 569.0 m with variation of ±1.5 m. Part of the foothill plain is occupied by a former tailing dump, so there are anthropogenic soils underlain by alluvial-proluvial Middle Quaternary loams and bedrock.

Anthropogenic soils are represented by silty alluvial sands of gray and bluish-gray colors, with layers of silt and, in the lower part of the section, grayish-blue silty clays. Sands are dry (up to 10 m) and low-moisture, silts are soft-plastic. The thickness of the deposits varies from 15.0 to 29.5 m.

Field measurements of soil density and moisture in natural occurrence showed that the density varies from 16.4 to 20.1 kN/m^3, averaging 18.4 kN/m^3; the density of dry soil varies from 13.8 to 17.0 kN/m^3, the average value is 15.7 kN/m^3; natural water content varies from 0.06 (6.0%) to 0.305 (30%), averaging 0.169 (17%).

The sands are mainly loose with practically no cohesion.

They are underlain by loams of alluvial-proluvial origin. Loams are silty, yellowish and light brown, semi-solid, in contact with bedrock with inclusions of gravel and crushed rock.

Bedrocks are represented by dolomite, brownish-gray, fissured.

2.3.   Characterisation of the soils

Since all the structures are located on the same site and the same soils take part in the lithological structure of the sites for the structures, they were combined in engineering geological elements (EGE) by type, based on the genesis, physical and mechanical properties, to determine the normative and design characteristics. From the foregoing, several types of soils are observed at the construction site: 1. Anthropogenic soils (industrial tailing waste and bulk soils); 2. Middle Quaternary sedimentary soils (loams); 3. Terrigenous

deposits (crushed stone and gravel); 4. Igneous (dolomites).

Derivation of the physical and mechanical parameters was done based on the correlations reported in the appendix B. Here the summary of the parameters to be used in the geotechnical model is reported.

2.3.1. Anthropogenic soils (EGE-1)

Anthropogenic alluvial soils, which are represented by production wastes, are uncovered throughout the whole construction site on the alluvial-proluvial plain, the territory of the former tailing dump. They have thicknesses from 0.5 m (marginal parts of the tailings) to 29.5 m. They are represented in the upper part by fine and silty sands with silt interlayers from 1 to 10 cm, rarely the thickness of the interlayers reaches 30 cm. From the surface, the sands are often dry and loose, with a depth (more than 10 m) they become low-moisture and, in some places, wet. In the lower part they are represented by clays with layers of silty sand 1-3 cm thick. Clays have a soft-plastic consistency.

Anthropogenic soils will be allocated to one engineering-geological element (EGE-1). Inside this element sands and clays will be identified in their own engineering-geological sub elements (EGE-1.1 and EGE-1.2) due to different physical, mechanical and strength properties.

2.3.2. Middle Quaternary cohesive soils (EGE-2)

Middle Quaternary cohesive soils are exposed almost everywhere under anthropogenic soils. They have thickness from 1 m to 30 m. They are constituted by clays.

Clays are the most widespread. The age of clays is the same, but due to the nuances of origin, they have different dry densities. It is impossible to correlate them by area and depth. Soft layers can occur both from the surface and at depth, or they can be an interlayer in stiff clays. Under anthropogenic soils, where the impact of water and a large thickness of artificial soils has had its effect over time, the clays have become compacted. Where the thickness of the anthropogenic soil is small (0.5-2.5 m) and the action of water was short, clays retained soft consistency.

Colours are light brown, yellowish brown, greyish brown and brownish; hard and semi-solid, rarely hard-plastic, often with inclusions of carbonate salts and crystalline gypsum. In the thickness of the clays, interlayers with inclusions of crushed stone are sometimes found, but often inclusions of crushed stone and gravel are found at the bottom of the layer, at contact with bedrock.

Middle Quaternary cohesive soils are singled out into one engineering-geological element: EGE-2 - clays. Clays are subdivided into three engineering-geological sub-elements according to their shear strength parameters coming from CPT and N_{SPT} value (EGE-2.1 - soft and very soft soils, EGE-2.2 - moderate soils, EGE-2.3 - hard soils).

2.3.3. Terrigenous deposits (EGE-3)

These deposits are represented by crushed stone and gravel with sandy-clay aggregate. They consist of the material of the parent rock on which they lie. Throughout the site, coarse-grained soils are found fragmentarily and have small thicknesses, up to 1-4 meters.

Coarse soils are allocated to a single engineering-geological element EGE-3.

2.3.4. Igneous (dolomites) (EGE-4)

Bedrock is overlain by Quaternary deposits. On the contact with more modern soils, they are fissured, weathered.

Igneous rock is allocated to the engineering-geological element EGE-4.

2.4. Physical and mechanical properties of soils

The characteristics of physical and mechanical properties were determined in the laboratory on undisturbed samples and interpreting the results of in-situ tests. The in-situ investigations were performed by means of standard penetration testing (SPT), cone penetration testing (CPT) and micro-seismic down-hole (DH) tests. The testing methodology is described in Appendix A.

The processing of the obtained data on the physical and mechanical properties of soils with the determination of normative and design characteristics was carried out in accordance with the instructions and requirements of GOST 25100-2011 "Soils. Classification", KMK 2.02.02-98 and RSTU 20522-96 "Soils. Method of statistical processing of the results of determinations of characteristics".

Below is a description of the composition, physical-mechanical and strength properties of the selected engineering-geological elements (EGE) within the explored depth.

2.4.1.   EGE-1 - Anthropogenic soils (tQ)

Anthropogenic soils are formed by industrial production waste. According to their physics-mechanical properties, they are divided into silty sands and clays, differ in granular composition, and the latter have plastic properties. According to the water saturation, anthropogenic soils show a variety of average degree of water saturation (humid).

Anthropogenic soils cannot serve as a base for structures due to low strength properties and the susceptibility to liquefaction. Where feasible, the soil must be removed from under the foundation of structures.

EGE-1.1 - Silty sands. The soil is anthropogenic, alluvial, loose from the surface, low-moisture, compacted with depth, moist. It has layers of silt with a thickness of 1-7 cm to 15-30 cm. The granulometric composition of silty sand is given in fig. 2.1. The physical and mechanical parameters are summarised in the table 2.1.
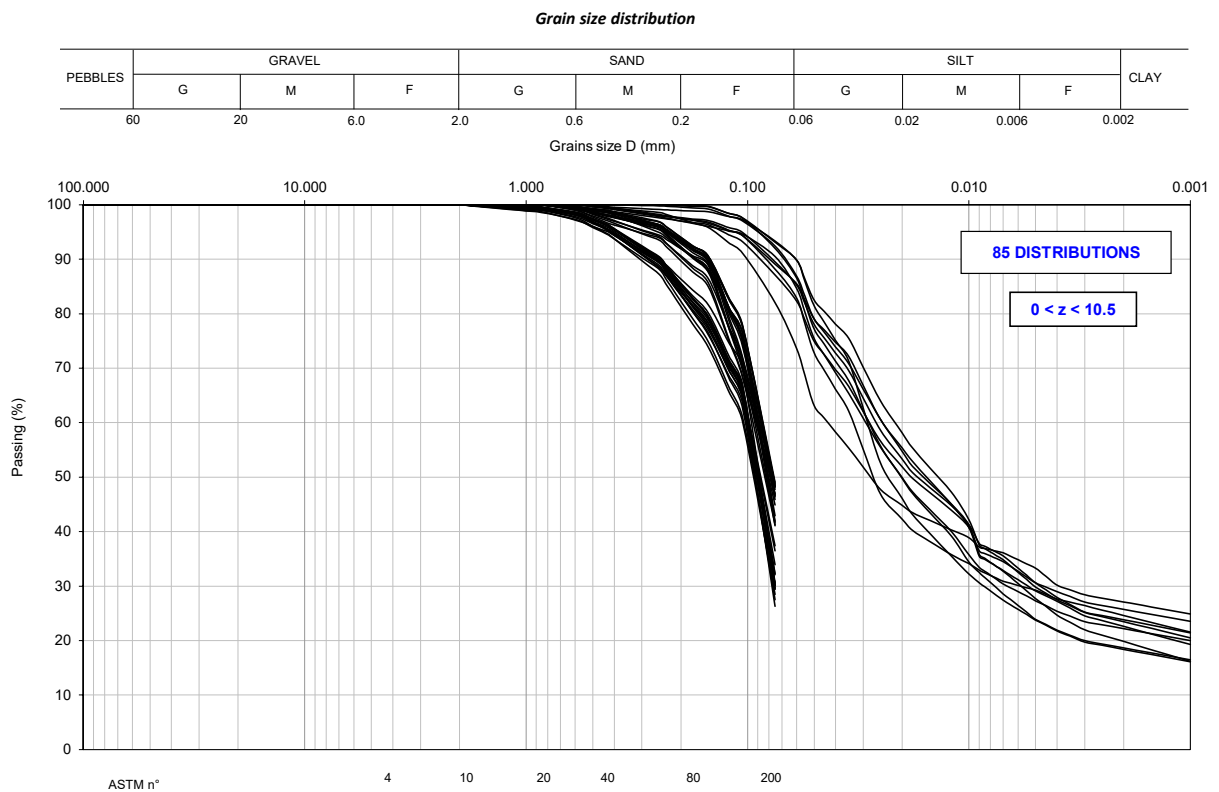
Figure 2.1: Grain size distribution curves for EGE-1.1

Table 2.1: Estimated physical and mechanical characteristics EGE-1.1

Characteristics	Units	Value
Natural water content, w_n	%	22-24
Soil grain density, ρ_s	Mg/m^3	2.70
Natural unit weight, γ_n	kN/m^3	19.0
Dry unit weight, γ_d	kN/m^3	15.0
Void ratio, e_0	-	0.65
Friction angle, φ'	°	28-31
Cohesion, c'	kPa	0-7
Operational Young's modulus (at 656 m a.s.l.), E_{op}	MPa	3.0
Operational Young's modulus increment, ΔE_{op}	MPa/m	0.80
Poisson's ratio, ν	-	0.25

Silty sands cannot serve as a base for structures due to their low strength properties and susceptibility to liquefy. Where feasible, the soil must be removed under the foundation of structures.

EGE-1.2 - clay. The soil is cohesive, sedimentary, polymineral, clayey. With respect to GOST 25100-2011, according to the averaged values of the granulometric composition and plasticity number, they belong to light silty clays. The granulometric composition of clay is given in the fig. 2.2. The physical and mechanical parameters are summarised in the table 2.2.
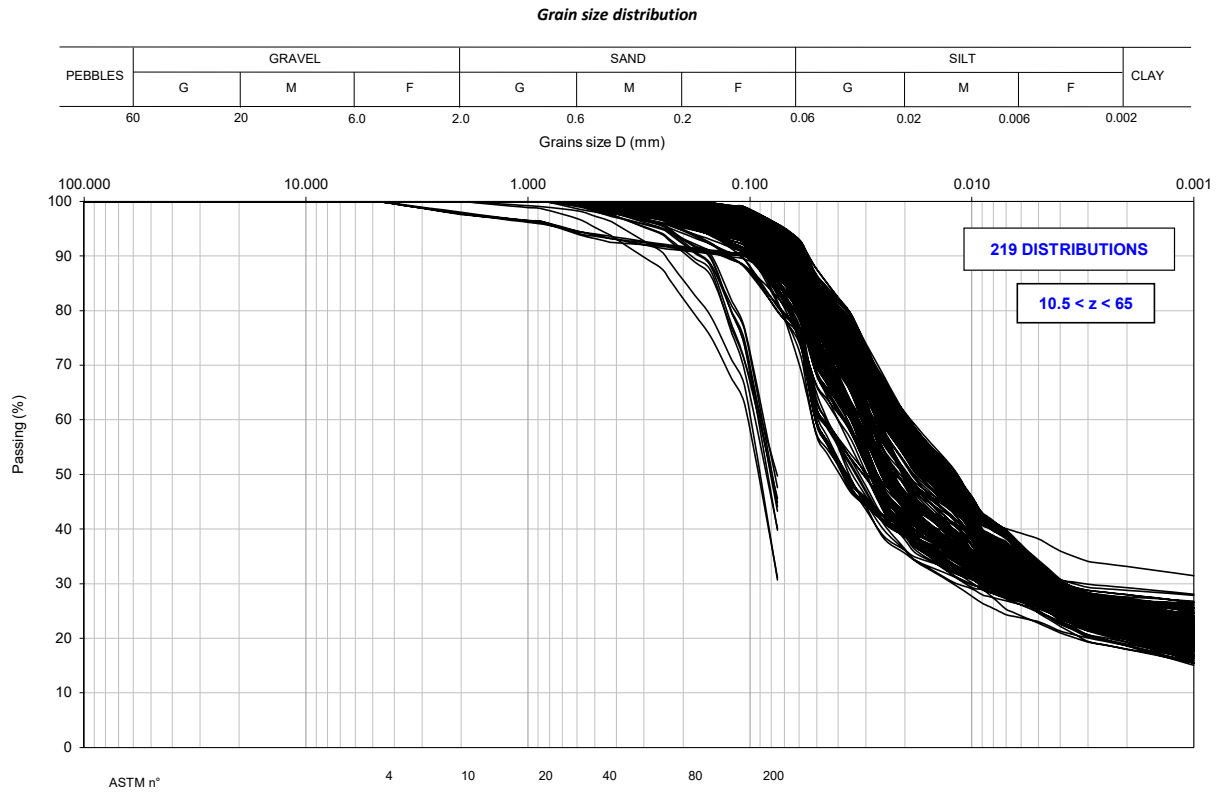
Figure 2.2: Grain size distribution curves for EGE-1.2

Table 2.2: Estimated physical and mechanical characteristics EGE-1.2

Characteristics	Units	Value
Natural water content, w_n	%	25-30
Liquid limit, w_l	%	29-33
Plastic limit, w_p	%	20-23
Plasticity index, I_p	%	9-10
Soil grain density, ρ_s	Mg/m^3	2.70
Natural unit weight, γ_n	kN/m^3	19.5
Dry unit weight, γ_d	kN/m^3	16.0
Void ratio, e_0	-	0.78
Friction angle, φ'	°	13-18
Cohesion, c'	kPa	0-12
Operational Young's modulus (at 565 m a.s.l.), E_{op}	MPa	2.0
Operational Young's modulus increment, ΔE_{op}	MPa/m	0.62
Poisson's ratio, ν	-	0.25

According to the degree of saturation (Sr = 0.95), clayey soils belong to varieties of medium degree of water saturation (wet).

According to KMK 2.03.11-96, clays in terms of the total content of chloride ions and sulfate ion (2310 mg / kg) given in terms of sulfate ion is highly aggressive to concrete and reinforced concrete structures based on Portland cement according to GOST 10178-94 and non-aggressive to concrete on sulfate-resistant grades of cement according to GOST 22286-94.

Anthropogenic clays cannot serve as a foundation due to low strength properties.

2.4.2. EGE-2 - Clays (dpQ_{II})

Dispersed, cohesive, sedimentary, polymineral, clay soil of deluvial-proluvial origin, Middle Quaternary age (GOST 25100-2011).

EGE-2.1 - Soft and very soft clays. The physical and mechanical parameters are summarised in the table 2.3.

Table 2.3: Estimated physical and mechanical characteristics EGE-2.1

Characteristics	Units	Value
Natural water content, w_n	%	22-26
Liquid limit, w_l	%	30-34
Plastic limit, w_p	%	20-22
Plasticity index, I_p	%	10-12
Soil unit density, ρ_s	Mg/m^3	2.70
Natural unit weight, γ_n	kN/m^3	19.3
Dry unit weight, γ_d	kN/m^3	15.8
Void ratio, e_0	-	0.72
Friction angle, φ'	°	16-20
Cohesion, c'	kPa	10-20
Operational Young's modulus (at 565 m a.s.l.), E_{op}	MPa	5.0
Operational Young's modulus increment, ΔE_{op}	MPa/m	0.70
Poisson's ratio, ν	-	0.25

EGE-2.2 - Soft and very soft clays. The physical and mechanical parameters are summarised in the table 2.4.

Table 2.4: Estimated physical and mechanical characteristics EGE-2.2

Characteristics	Units	Value
Natural water content, w_n	%	22-26
Liquid limit, w_l	%	30-34
Plastic limit, w_p	%	20-22
Plasticity index, I_p	%	10-12
Soil grain density, ρ_s	Mg/m^3	2.70
Natural unit weight, γ_n	kN/m^3	19.5
Dry unit weight, γ_d	kN/m^3	16.0
Void ratio, e_0	-	0.70
Friction angle, φ'	°	18-22
Cohesion, c'	kPa	12-20
Operational Young's modulus (at 565 m a.s.l.), E_{op}	MPa	8.0
Operational Young's modulus increment, ΔE_{op}	MPa/m	0.68
Poisson's ratio, ν	-	0.25

EGE-2.3 - Soft and very soft clays. The physical and mechanical parameters are summarised in the table 2.5.

Table 2.5: Estimated physical and mechanical characteristics EGE-2.3

Characteristics	Units	Value
Natural water content, w_n	%	22-26
Liquid limit, w_l	%	30-36
Plastic limit, w_p	%	20-23
Plasticity index, I_p	%	10-13
Soil grain density, ρ_s	Mg/m^3	2.71
Natural unit weight, γ_n	kN/m^3	19.5
Dry unit weight, γ_d	kN/m^3	16.0
Void ratio, e_0	-	0.68
Friction angle, φ'	°	18-20
Cohesion, c'	kPa	10-20
Operational Young's modulus (at 565 m a.s.l.), E_{op}	MPa	17.0
Operational Young's modulus increment, ΔE_{op}	MPa/m	0.69
Poisson's ratio, ν	-	0.25

Easily soluble salts in the water extract contain from 0.194 to 1.862%, on average it is 0.820%; they contain gypsum from 0.040 to 0.525%, on average 0.221%. According to the total content of easily soluble salts and gypsum (1.041%), they belong to non-saline soils (GOST 25100-2011).

The content of chlorine ions in the water extract varies from 40 to 320 mg/kg, on average it contains 90 mg/kg. The content of sulfate ion varies from 520 to 14190 mg/kg, averaging 2820 mg/kg. According to KMK 2.03.11-96, clays in terms of the total content of chlorine and sulfate ions (2910 mg / kg) in terms of sulfate ion are highly aggressive to concrete and reinforced concrete structures based on Portland cement according to GOST 10178-94 and non-aggressive to concrete on sulfate-resistant grades cement according to GOST 22286-94.

Clays can serve as a base for foundations for light structures or those which can bear settlements.

2.4.3. EGE-3 - Crushed rock $(dpQ_{II}t)$

The soil is poorly sorted, from metamorphic and igneous rocks, dense. Natural unit weight of material is assumed to be $\gamma_n = 23$ kN/m^3.

2.4.4. EGE-4 - Dolomite (D_1)

Dolomite is even-grained rock of gray, greenish-gray and pinkish-gray color with a transition to a dark brown, medium and coarse-grained porphyritic structure. The main minerals that make up the rock varieties are: plagioclase, K-feldspar, biotite, hornblende. According to GOST 25100-2011, the EGE-4 soil is rocky, intrusive, silicate of medium composition.

The physical and mechanical properties of Dolomite is given according to laboratory data performed during the survey, after their analysis and processing in accordance with KMK and GOSTs. The physical and mechanical parameters are summarised in the table 2.6.

Table 2.6: Estimated physical and mechanical characteristics EGE-4

Characteristics	Units	Value
Unit density, ρ	g/cm^3	2.76
Natural unit weight, γ_n	kN/m^3	25.5
Uniaxial compressive strength, σ_c	MPa	72
Young's modulus, E_{rm}	GPa	13.0
Poisson's ratio, ν	-	0.15
Geological Strength Index, GSI	-	50

2.5. Hydro-geological conditions

On the site location, groundwater flow is developed, confined to the rocks of the Paleozoic and Mesozoic age. As a rule, they are confined to faults and tectonic cracks. The waters are free-flowing, the depth of occurrence is 37.0 m or more.

Groundwater is fed by filtering through the cracks of the underground subchannel flow of groundwater of the closest river, where rocks come to the surface in the riverbed, before it enters the plain.

Most of the time of the year, the river bed is dry, but in the under-channel pebble deposits there is a constantly acting flow of groundwater, fed by springs and having a direction of movement that coincides with the direction of the river bed.

The results of the drilled wells showed the following: the depth of the groundwater level in the territory of the site under construction reaches 37.0 meters or more, i.e. outside the zone of influence of the designed structures; the distribution of groundwater is discrete: their presence in fractured rocks and their absence in monolithic fused rocks.

The waters are hydrocarbonate-sulphate, fresh, with a mineralization of about 1.0 g/l, with a weak alkaline reaction, pH is 7.41. The composition of water throughout the year is stable, changes are within the margin of measurement error.

The hydraulic conductivity of clays under anthropogenic soils from 0.1 m/day or less; anthropogenic soils, depending on the particle size distribution from 0.036 to 1.66 m/day. While, the hydraulic conductivity of fractured rocks varies from 0.001 m/day to hundreds of meters per day and depends on the nature of fracture, the number and size of fractures.

2.6.   Conclusions and recommendations

The geotechnical cross-sections of the site are represented in the appendix D on sheets from 2-1 to 2-8 (here reported in the fig. 2.3 a small scale copy for brevity).

Based on the work done, the following conclusions could be made:

1. In the geological structure of the work site, several types of soils are distinguished: 1. Anthropogenic soils (industrial tailing waste and bulk soils); 2. Middle Quaternary sedimentary soils (clays); 3. Terrigenous deposits (rock fragments); 4. Igneous rocks (Dolomites). In accordance with the nomenclature type of soils and composition, 5 engineering geological elements (EGE) were identified: EGE-1 - anthropogenic soils, EGE-2 - clays, EGE-3 - coarse clastic soils, EGE-4 - igneous rocks (dolomites);

2. The engineering-geological element EGE-1 cannot be the basis for foundations due to low physical and mechanical parameters and high deformability;

3. Analysis of CPT data showed that at a depth of 10-12 meters there is a layer of deformable soil with qc = 1MPa. The thickness of the layer is up to 4 meters;

4. The EGE-4 can be selected as bearing layer. However, the bearing layer was found only in the northern part of the considered construction site, and subsequently was not found in deeper wells in the southern part of the site. This aspect imposes uncertainty on subsequent engineering solutions and design of the foundation;

5. The results of the drilled boreholes showed the following: the depth of the groundwater level in the construction area reaches 37.0 meters or more, i.e. outside the zone of influence of the designed structures; the distribution of groundwater is discrete: their presence in fractured rocks and their absence in monolithic fused rocks. The waters are hydrocarbonate-sulfate, fresh, with a mineralization of about 1.0 g/l, with a weak alkaline reaction;

Moreover, the important aspects affecting the decisions taken during the data interpretation are as following:

- During the investigation data analysis the insufficiency of performed tests and investigations was identified. This does not allow a full assessment of the current geological conditions, thereby introducing uncertainty into the design and increasing the correction factors;

- A detailed analysis of the results of oedometer tests showed that most of the samples are underconsolidated (feature related to the EGE-1.2 and EGE-2). This review

casts doubt on the reliability of these results, since underconsolidation could be considered possible in the upper tailing material (EGE-1.2), but not in the natural soils (EGE-2). The oedometer tests results are treated carefully and they were considered mostly as for information only;

- Sometimes the provided investigation data was not in a good correlation with each other (e.g. CPT versus SPT/Borehole log). When this happen the data was treated carefully and with lower reliability.

Based on the aforementioned information the design of the deep foundation is recommended. The foundation should be able to transfer the vertical load to the competent strata and to sustain lateral loads. The following options are considered to be reasonable: piles or soil-improved columns.
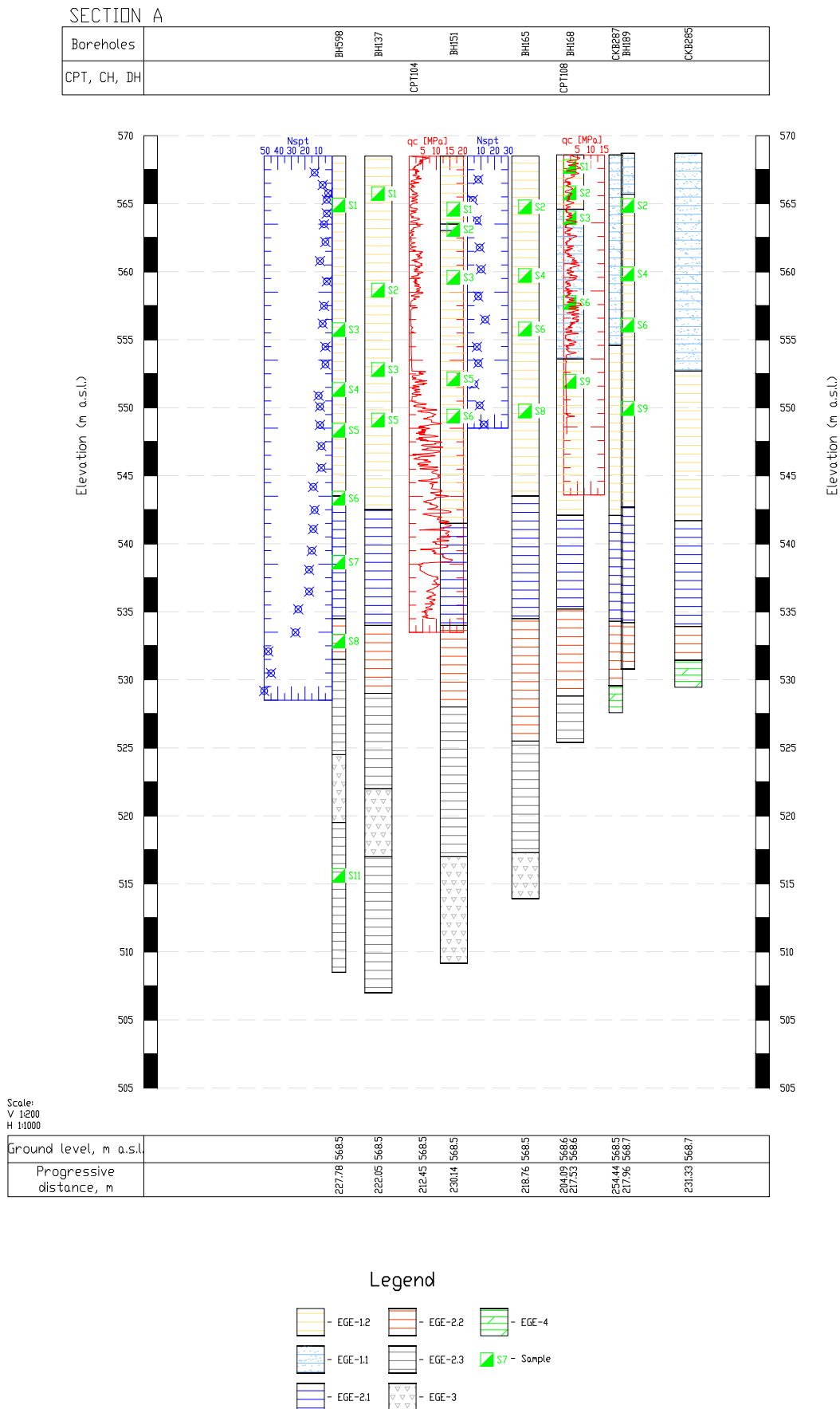
Figure 2.3: Geotechnical cross-section A

3 | Numerical modelling

3.1. Numerical model

PLAXIS 3D was chosen among the different commercial software due to its availability in Studio Geotecnico Italiano srl.

PLAXIS 3D is a full three-dimensional finite element program developed for the analysis of deformations and stability in geotechnical engineering and design. It is used for analysis of stresses, deformations and structural forces in geotechnical structures such as embankments, excavations, foundations and tunnels.

This chapter reports the most relevant features of PLAXIS 3D that were used in construction of numerical model. It was purposefully written in a detailed manner, presenting the theory behind these features, to justify their use in the following.

3.1.1. Material models

Material models define the stress-strain behaviour of the modelled soil, according to the type of material. The more complex models are capable to catch specific peculiarities of the behaviour, but usually require more input parameters that should be calibrated according to the tests performed on soils.

Mohr-Coulomb (MC) model – linear elastic perfectly plastic model generally used for a first approximation of the soil behaviour. The input parameters are basic and include the soil unit weight γ, a constant Young's modulus E, Poisson's ratio ν, effective cohesion c', effective friction angle φ', dilatancy angle ψ and tension cut-off and tensile strength σ_t. The MC model is usually used for modelling frictional behaviour of the embankments fill.

Hoek-Brown (HB) model – elastic perfectly plastic model which is used to simulate the isotropic behaviour of rock. Stiffness of rock can be assumed constant due to low dependency on the stress level, while shear failure and tension failure are described by a non-linear strength envelop.

The input parameters are including unit weight γ, rock mass Young's modulus $E_r m$, Poisson's ratio ν, uni-axial compressive strength of the intact rock $|\sigma_{ci}|$, intact rock parameter m_i, geological strength index GSI, disturbance factor D and dilatancy angle ψ_{max}.

Hardening soil (HS) model – advanced elastoplastic hyperbolic model that accounts for shear hardening plasticity. This means that the yield surface is not fixed with respect to the principal stress space but evolve during the accumulation of the plastic strains.

To account for a stiffness stress dependency the HS model requires three stiffness values E_{oed}^{ref}, E_{50}^{ref}, E_{ur}^{ref} and a power m:

  - The oedometer stiffness E_{oed}^{ref} also called as tangent stiffness for primary oedometer loading. This parameter is derived at a reference vertical pressure of $\sigma_1' = p^{ref}$ – usually assumed to be 100 kPa – from an oedometer test as shown in fig. 3.1 below. If the oedometer tests data is unavailable, PLAXIS suggests to use the approximation $E_{oed}^{ref} \approx E_{50}^{ref}$.
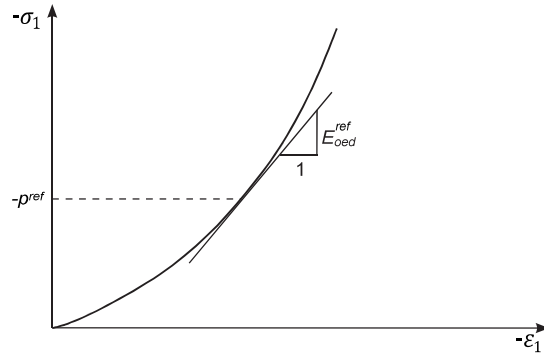
Figure 3.1: Definition of the E_{oed}^{ref} in oedometer test (Bentley, 2021a)

  - The secant stiffness in standard drained triaxial test E_{50}^{ref}. This parameter is defined for a reference minor principal effective stress of $\sigma_3' = p^{ref}$ (cell pressure) as the secant stiffness at 50% of the maximum deviatoric stress (see the fig. 3.2). If the drained triaxial tests data is unavailable, PLAXIS suggests to use the approximation $E_{50}^{ref} \approx E_{oed}^{ref}$.

deviatoric stress
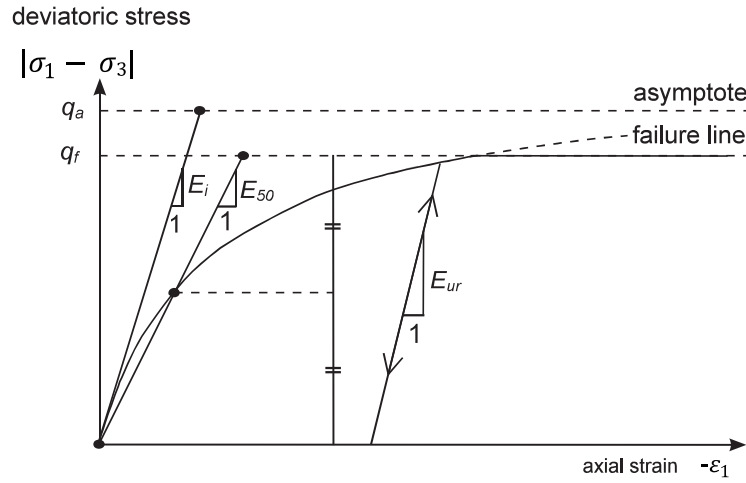
Figure 3.2: Hyperbolic stress-strain relation in primary loading for a standard drained triaxial test (Bentley, 2021a)

- Unloading-reloading stiffness E_{ur}^{ref}. This parameter is also defined from the triaxial test at a reference pressure $\sigma_3' = p^{ref}$ (see the fig. 3.2). If the triaxial tests data is unavailable, PLAXIS uses a default value of $E_{ur}^{ref} = 3 \cdot E_{50}^{ref}$.

- The power m defines the amount of stress dependency of stiffness. As it is observed from the literature Janbu (Janbu, 1963) reports values of m around 0.5 for Norwegian sands and silts, on the contrary von Soos (von Soos, 2001) reports values in the range of $0.5 < m < 1.0$. The procedure for the derivation of the m parameter is summarized in the fig. 3.3.

$$E_{50} = E_{50}^{ref} \cdot \left(\frac{c' \cdot cos(\varphi') - \sigma_3' \cdot sin(\varphi')}{c' \cdot cos(\varphi') + p^{ref} \cdot sin(\varphi')} \right)^m \tag{3.1}$$

$$E_{oed} = E_{oed}^{ref} \cdot \left(\frac{c' \cdot cos(\varphi') - \sigma_1' \cdot sin(\varphi')}{c' \cdot cos(\varphi') + p^{ref} \cdot sin(\varphi')} \right)^m \tag{3.2}$$

$$E_{ur} = E_{ur}^{ref} \cdot \left(\frac{c' \cdot cos(\varphi') - \sigma_3' \cdot sin(\varphi')}{c' \cdot cos(\varphi') + p^{ref} \cdot sin(\varphi')} \right)^m \tag{3.3}$$
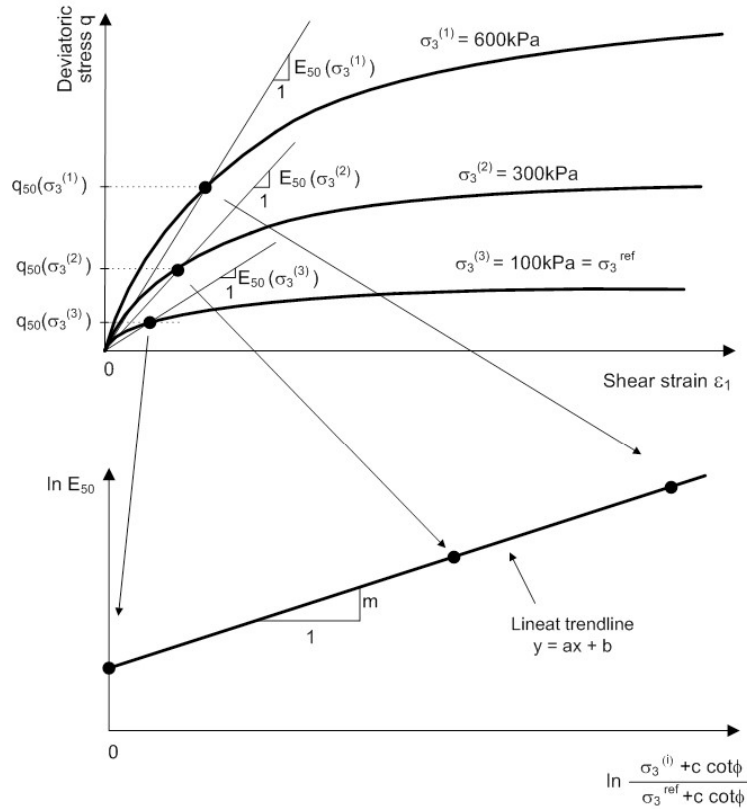
Figure 3.3: Determination of the stiffness stress dependency parameter m from three curves derived from the triaxial drained compression tests (Obrzud and Truty, 2018)

If none of the abovementioned parameters can be defined, PLAXIS allows for using the following alternative input parameters, which could be derived from a one-dimensional compression test (e.g. oedometer test):

- Compression index C_c, which defines the slope of the primary (virgin) compression line in the void ratio - $log(\sigma'_v)$ plane: $C_c = \frac{\Delta e}{log(\sigma'_v)}$.

- Swelling index C_r or C_s, which defines the slope of unloading-reloading line in the void ratio - $log(\sigma'_v)$ plane: $C_r = \frac{\Delta e}{\sigma'_v}$.

- Initial void ratio e_0, or the in-situ void ratio of the soil.

3.1.2.   Embedded beam row (EBR) element

The embedded beam element was introduced in PLAXIS for more accurate modelling of piles, rock bolts or grouted bodies. It can be placed in any arbitrary direction in the subsoil and that interacts with the surrounding soil by means of special interface elements. The interaction is composed of a skin resistance as well as a base resistance, which are

derived from the relative displacement between the soil and the pile.

The advantage of embedded beam element with respect to model of pile as volume elements is that it does not occupy volume, but a particular volume around the pile is assumed in which the plastic soil behaviour is excluded. This volume is based on the pile diameter. This fact allows to use less elements without strong deviation of the results, which results in reduction of computational time.

The embedded beams are suitable for pile types that cause negligible or limited disturbance of the surrounding soil during installation. This category includes some types of bored piles (e.g. displacement screw piles). This aspect is important as the installation has a significant influence on the soil stress ratio (K_0) and the pile skin friction (T_{skin}).

The Embedded beam row element could be chosen to behave as a pile, rock bolt or grout body. In the following element will be considered to have the properties of a pile. To characterize the pile behaviour of the EBR, the following input parameters are required:

- *Connection point* – the choice is set to be top or bottom node of the element. The type of connection behaviour of such a point could be free, hinged, or rigid. In case of free connection behaviour, the connection point is free to move and rotate relative to the surrounding soil and the interaction occurs only by the interface. A rigid connection implies that both displacement and rotation are coupled with the soil element, while hinged connection implies coupled displacement and independent relative rotation of the element.

- *Material type* – the choice consists of Elastic or Elastoplastic constitutive behaviour. In the case of a concrete pile, an Elastoplastic material type is recommended.

- *Material properties* - includes the Young's modulus, unit weight and yield stress of the material.

- *Beam type* – define the geometrical parameters of the beam, can be set to predefined (massive circular beam, circular tube, massive square beam) or user defined cross-section. For predefined massive circular beam a diameter should be given as an input, a width for a massive square beam and diameter and thickness for circular tube beam. This input data serve to determination of the geometrical characteristics of the cross-section as will be discussed later.

The interaction of the element with the surrounding soil is determined by PLAXIS 3D by means of a special interface along the beam length. This interface is described by linear elastic behaviour with a finite strength and is defined by the following parameters:

- Skin resistance F_{skin} – is entered in units of force per unit length and can be described in one of the following rules: linear, multi-linear or layer dependent. In case of linear skin resistance, two limiting values on top and bottom of the beam should be inputted by user ($T_{(skin,start,max)}$ and $T_{(skin,end,max)}$). In case of multilinear skin resistance, the user shall define a table which describes the behaviour of skin resistance with depth. In case of layer dependent resistance PLAXIS uses the surrounding soil's parameters of cohesion c', friction angle φ' and interface strength reduction factor R_inter to calculate a depth dependent skin resistance. Summarizing, one of the following values of skin resistance apply:

$$Linear: \ F_{skin} = \frac{1}{2} \cdot (T_{skin,start,max} + T_{skin,end,max}) \cdot L \tag{3.4}$$

$$Multi-linear: \ F_{skin} = \Sigma(L_{i+1} - L_i) \cdot \frac{T_{i+1} + T_i}{2} \tag{3.5}$$

$$Layer \ dependent: \ F_{skin} = \int_0^L 2 \cdot \pi \cdot R_{eq} \cdot \tau_i \tag{3.6}$$
$$where \ \tau_i = R_{inter} \cdot (c' + \sigma'_n \cdot tan(\varphi'))$$

- Base resistance F_{max} – maximum force allowed at the base of the embedded beam. In order to ensure a realistic load transfer at the bottom of the pile, a certain zone in the soil volume elements surrounding the beam is identified and in this zone any kind of soil plasticity is excluded (elastic zone, see fig. 3.4). The size of this zone is characterized by the beam's equivalent radius as $R_{eq} = max(\sqrt{(A/\pi)}, \sqrt{2 \cdot I_{avg}/A})$ with $I_{avg} = \frac{(I_2 + I_3)}{2}$. The elastic zone makes the embedded beam to behave almost like a pile of volume elements. However, the installation effects are not taken into account and the pile-soil interaction is modelled at the centreline rather than at the circumference.
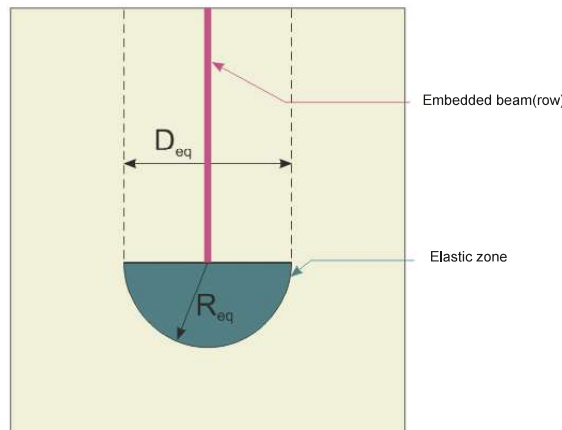
Figure 3.4: Elastic zone surrounding the bottom of the pile (Bentley, 2021b)

3.1.3. Geogrids

Geogrid is represented by a membrane structure characterized by axial stiffness but without any bending stiffness. Moreover, it can sustain only tensile forces without development of compression force. These structural objects are generally used to introduce a soil reinforcement.

To characterize an elastic material behaviour only an axial stiffness EA has to be introduced. For the case of biaxial geogrid isotropic option should be selected, in case of anisotropic behaviour the stiffness in two principal directions should be specified:

  - EA_1 [force per unit length] – Elastic stiffness in the 1-direction;

  - EA_2 [force per unit length – elastic stiffness in the 2-direction.

The above values are usually provided by the manufacturer of the product under the name "Axial stiffness J" or can be obtained from a diagram of tensile force versus tensile strain.

To characterize the elastoplastic behaviour of the geogrid the following parameters should be added:

  - $N_{p,1}$ - Maximum tensile force in 1-direction;

  - $N_{p,2}$ – maximum tensile force in 2-direction.

Another possible way to introduce the elastoplastic behaviour is to input the $N-\varepsilon$ diagram to specify a strain-dependence of strength. The following diagrams shall be introduced:

  - $N_1 - eps_1$ – The $N - \varepsilon$ diagram in 1-direction;

  - $N_2 - eps_2$ – The $N - \varepsilon$ diagram in 2-direction.

PLAXIS calculates the axial force at the stress points of the geogrid and if N_p is exceeded, stresses are redistributed with respect to the theory of plasticity, so that the maximum forces are compatible with. As a consequence, the irreversible deformations will take place.

To characterise the viscous time dependent behaviour of the geogrid The following parameters should be introduced:

  - $EA_{1,short}$ - Elastic stiffness during initial (instantaneous) strain increment in 1-direction;

  - $EA_{2,short}$ - Elastic stiffness during initial (instantaneous) strain increment in 2-direction;

- $EA_{1,long}$ - Elastic stiffness during (infinitely) long strain increment in 1-direction;

- $EA_{2,long}$ - Elastic stiffness during (infinitely) long strain increment in 2-direction;

- $N_{p,1}$ - Maximum force in 1-direction;

- $N_{p,2}$ - Maximum force in 2-direction;

- t_R -Retardation time - The time where a linear extrapolation of the initial creep rate intersects the long-term displacement line fig. 3.5.
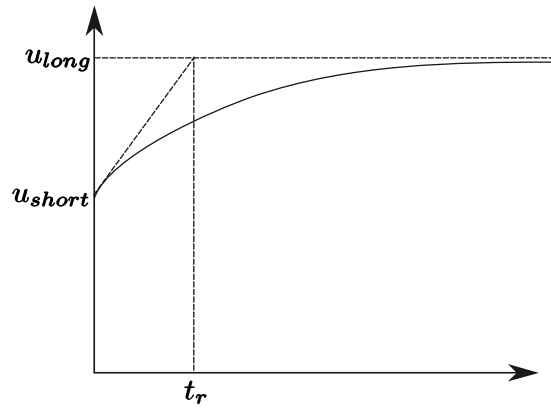
Figure 3.5: Displacement versus time in a Creep test (Bentley, 2021b)

Note, that in order to account for a membranal behaviour of the geogrid element the use of updated mesh is required. In order to correctly model th biaxial material behaviour, the stiffness is set to anisotropic and the stiffness in shear, GA, is set to zero.

3.2.   Parameters calibration

The parameter calibration is performed based on the data of available tests performed during the investigation stage.

3.2.1.   Mohr-Coulomb model

This model is used for modelling of the embankment frictional behaviour. The material of the embankment is specified in the project thus the parameters are already known and are reported in the table 3.1.

Table 3.1: Estimated physical and mechanical characteristics of the embankment fill material

Characteristics	Units	Value
Natural unit weight, γ_n	kN/m^3	18.0
Dry unit weight, γ_d	kN/m^3	15.0
Friction angle, φ'	°	34
Cohesion, c'	kPa	0
Design Young's modulus , E_{op}	MPa	30.0
Poisson's ratio, ν	-	0.25

3.2.2.   Hardening soil model

This model is decided to be used for the modelling of all the subsoils including both cohesive and sandy materials. The following parameters should be calibrated:

- The secant stiffness in standard drained triaxial test E_{50}^{ref};

- The power m.

First the power parameter will be calibrated on the basis of drained triaxial tests performed on the materials. As was outlined in the fig. 3.3 the reference stiffness at 50% of maximum deviator stress should be chosen (see fig. 3.6 and fig. 3.7) and plotted versus minor principal stress normalized with respect to the reference minor principal stress (equal 100 kPa) (see fig. 3.8 and fig. 3.9). The following steps were followed:

- Find three values of E_{50} corresponding to σ_3 respectively;

- Find a trend line $y = a \cdot x + b$ by assigning variables

   y as $ln(E_{50})$ and

   x as $ln\left(\frac{\sigma + c' \cdot cot(\varphi')}{\sigma_{ref} + c' \cdot cot(\varphi')}\right)$

- Then the determined slope of the trend line α is the parameter m.
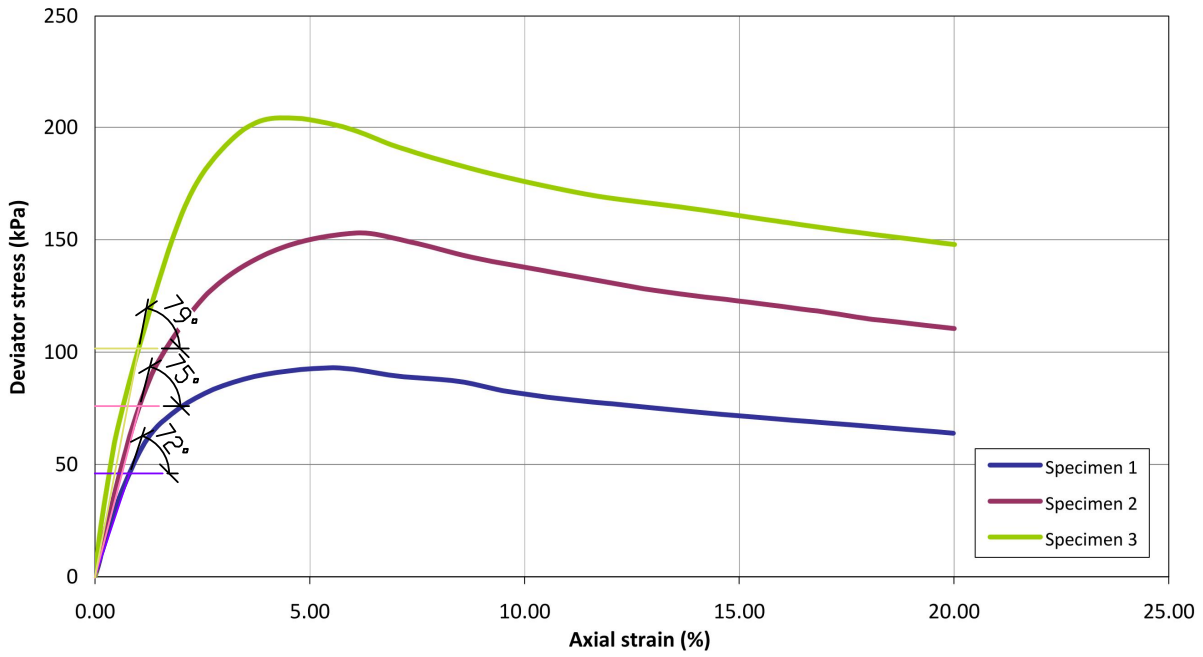
Figure 3.6: Estimation of E_{50} for EGE-1.1
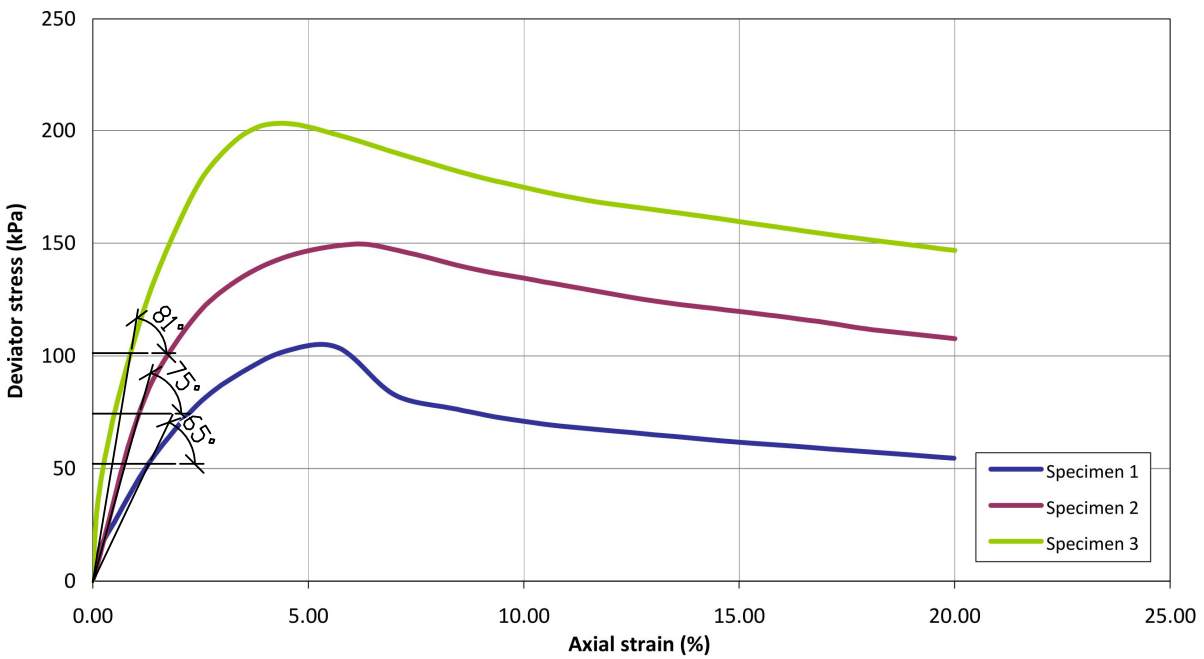
Figure 3.7: Estimation of E_{50} for EGE-1.2
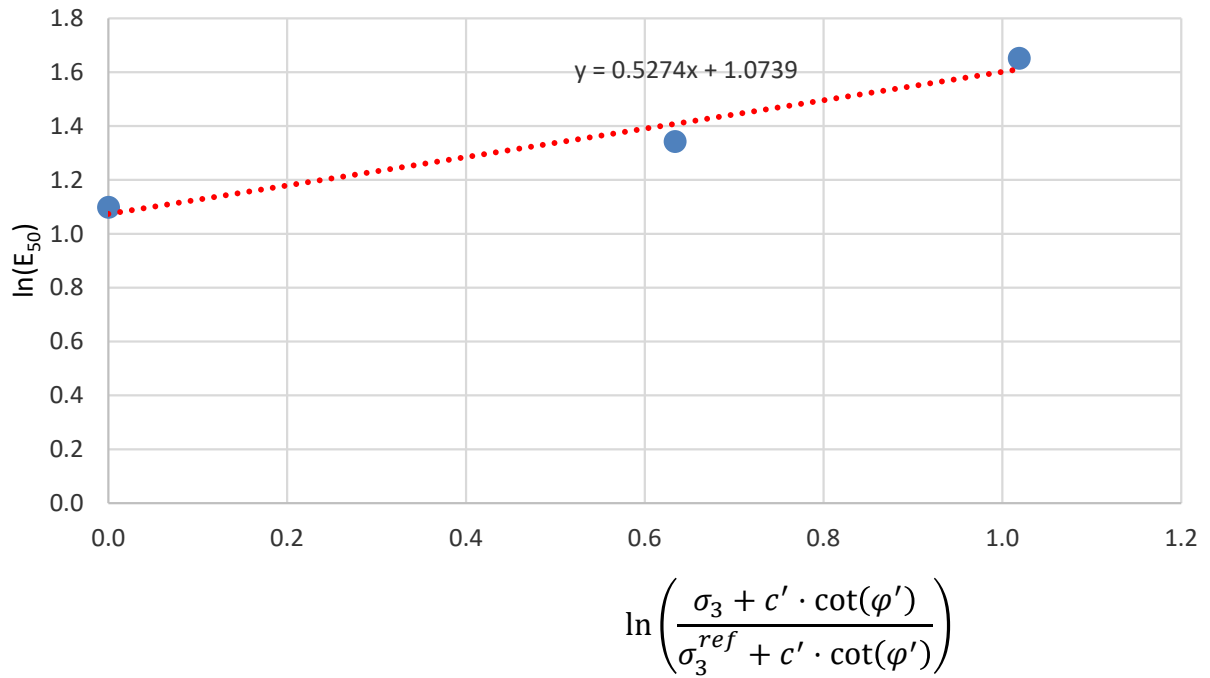
Figure 3.8: Definition of the power m for EGE-1.1
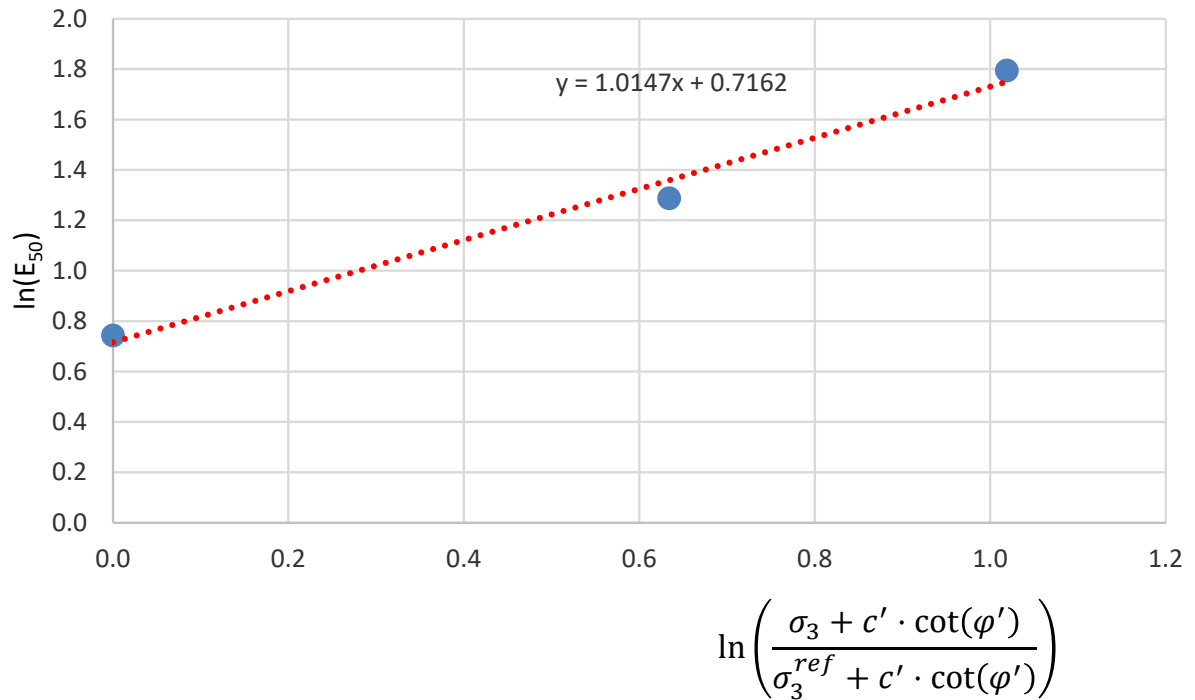
Figure 3.9: Definition of the power m for EGE-1.2

Note that the most representative values were chosen and reported here, for all results refer to the appendix B.

As it could be seen from the figures the value of the parameters m for two geological units are as following:

EGE-1.1 – m = 0.5;

EGE-1.2 – m = 1.0.

For the Rest of geological units, the calibration is performed based on the least-squares method minimizing the error and optimizing parameters. Whereas, to calibrate the secant stiffness the least-squares method is applied minimizing the error function and varying the stiffness parameter. The final results of the calibration are represented in the fig. 3.10.
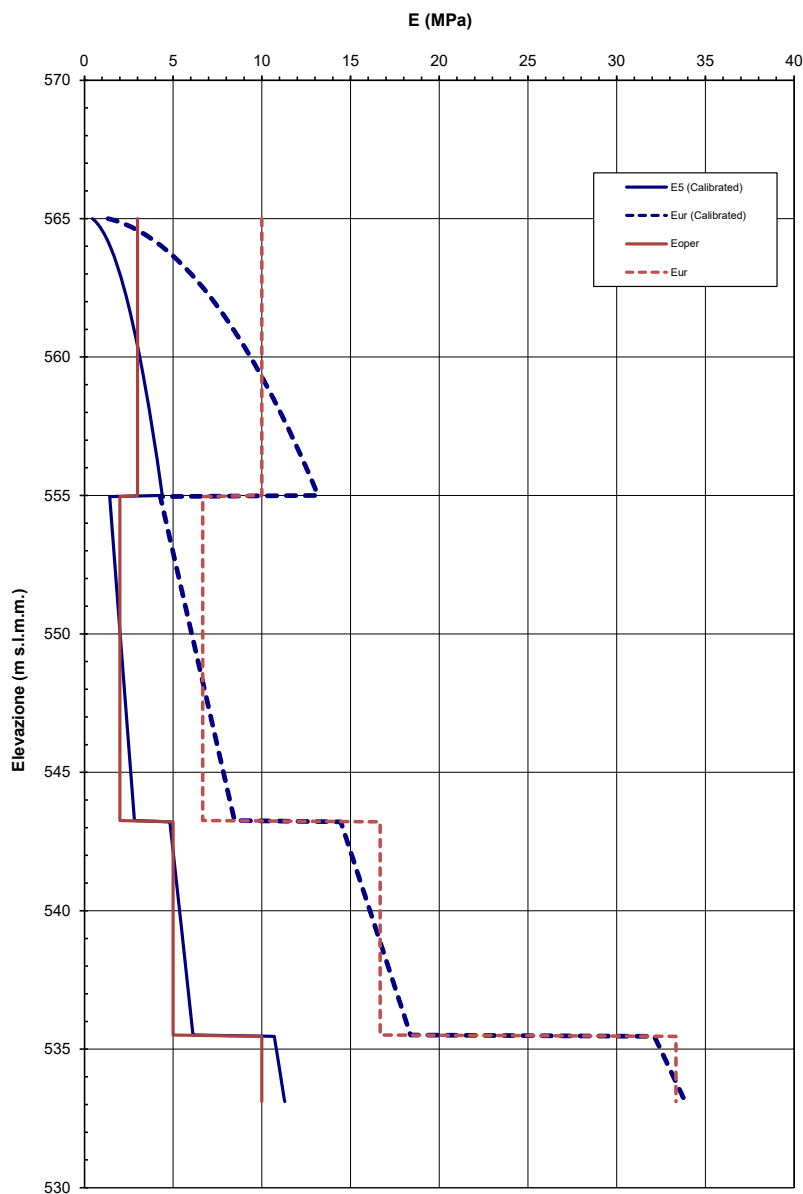
Figure 3.10: Calibrated profile of the Young's modulus with depth

3.2.3. Embedded beam element

To provide a confirmation that the modelling of piles as a beam elements could be considered acceptable an investigation of the performance was done. The comparison of the performance between pile made of volume elements and beam element was performed assuming bored piles - to comply with the assumption of limited disturbance to the surrounding soil.

A model considers a single pile under the centreline of the embankment and loaded with the uniform load (considering a static loading). Then the comparison of the stresses within the soil, loads on the pile and settlements was done and here reported.

As it could be seen from the fig. 3.11 developed settlements are close to each other in two modelling approaches. Additionally the plane of equal settlements is developed in both systems at the same height (approximately 1.5 meters above the pile head).
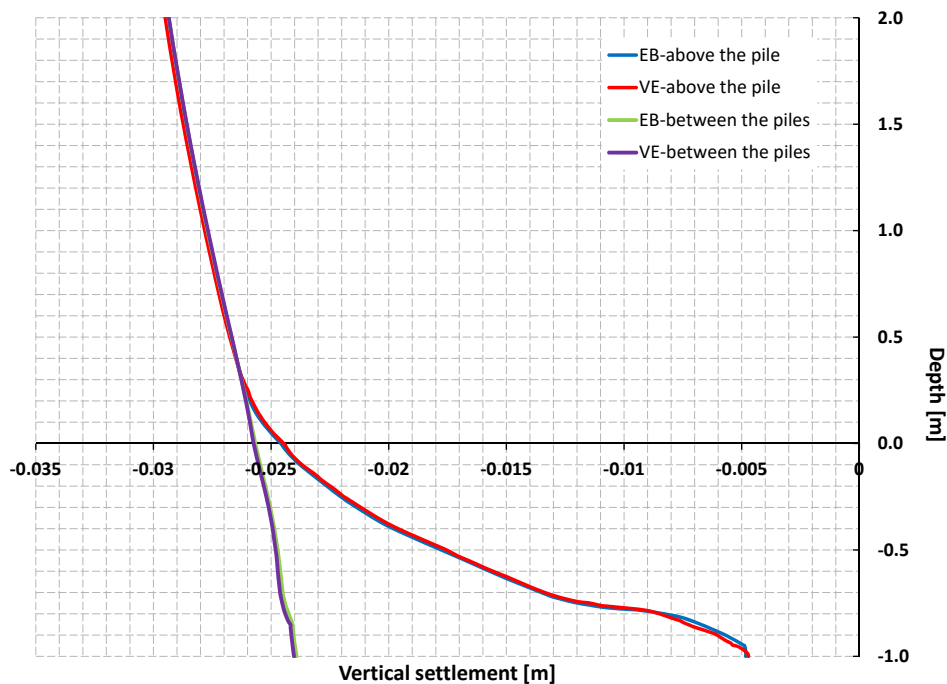
Figure 3.11: Settlements within the embankment body along the pile centrelines and between the piles

In terms of the pile behaviour the developed compression of piles is close in both cases (4.8 mm for embedded beam element and 4.7 mm for volume elements). Comparing the axial force developed in both cases (reference to the fig. 3.12) it could be noted that in the case of pile comprised from the volume elements the values developed are different

from the case of beam element, but the general trend coincides. The non correspondence of the values could be justified by the errors in integration of stresses to the axial forces.
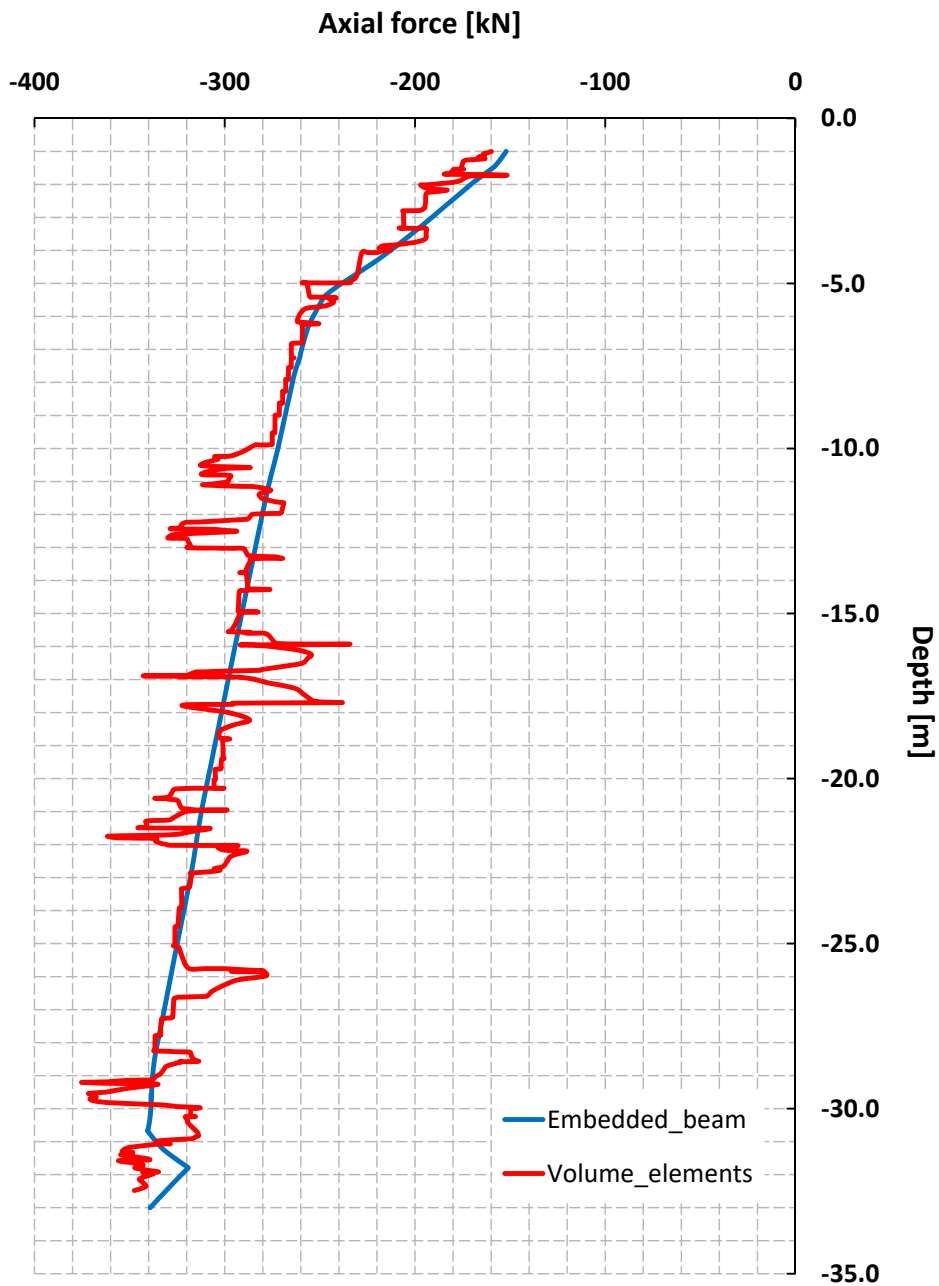
Figure 3.12: Axial load in the piles for both cases

Model parameters for the base and shaft bearing capacity of the pile were derived according to the CPT tests performed as reported in the appendix B.1.2.

3.3. Summary

This chapter includes the main features of PLAXIS that will be used in model as follows:

- *Model geometry:* A 3D analysis is the most appropriate to capture the three-dimensional effects of the soil-structure interaction problem, as 2D plain strain cannot be a fair representation of the three-dimensional arching effect that takes please within the embankment.

- *Embedded beam row elements:* These are linear elements superimposed on the soil mesh of the model with a specific spacing between the piles according to the project geometry. Interaction with the surrounding soil takes place through a set of interface elements, whose behaviour is automatically calculated by PLAXIS according to the user-defined limiting values.

- *Geogrid:* Specific element of the basal reinforcement which is aimed to resist active thrust mobilized over the embankment. The most important properties are the axial stiffness and strain-dependent strength.

- *Soil model:* The most important aspect of the analysis as a proper choice of the soil model allows to catch the peculiarities of the system response. The hardening soil model is chosen as this model allows to properly track both loading and unloading-reloading phases as well as soil "hardening". While for the frictional behaviour of the embankment a standard Mohr-Coulomb soil model is chosen and for the bedrock Hoek and Brown soil model is adopted. Parameters calibration will be performed in the following.

4 | Methodology

4.1. General model description

Based on the previously provided information a numerical model was built up. The embankment extends over 16 m (in-plane), has a height of 2 meters and its slopes are inclined of 1:2 as represented in the fig. 1.1. The piles are placed according to the rectangular pattern with 1.5 m spacing as represented in the fig. 1.3.

As it could be seen from the transversal cross-section represented in fig. 2.3, the soil profile is composed of the 7 layers described in the chapter 2. However within the dimensions of modelled domain only 5 of them are present. All layers were modelled under dry conditions as no constant water table was found at site. To model the soil domain the Hardening soil (HS) model was used. The input parameters are reported in the table 4.1.

Table 4.1: Input parameters for the HS model with respect to the geological units

	EGE-1.1	EGE-1.2	EGE-2.1	EGE-2.2
γ, $[kN/m^3]$	19.0	19.0	19.0	19.0
e_0, $[-]$	0.65	0.78	0.72	0.7
c', $[kPa]$	0	3	10	15
φ', $[°]$	28	13	18	18
ν, $[-]$	0.25	0.25	0.25	0.25
m, $[-]$	0.50	1.00	0.95	0.85
E_{50}^{ref}, $[MPa]$	4.72	1.41	3.34	6.51
E_{oed}^{ref}, $[MPa]$	4.72	1.41	3.34	6.51
E_{ur}^{ref}, $[MPa]$	16.53	4.97	10.69	20.60

For the bedrock a Hoek and Brown model was chosen, with the following parameters: rock unit weight $\gamma = 25\ kN/m^3$, rock mass stiffness $E'_{rm} = 13\ GPa$, Poisson's ratio $\nu = 0.15$, uniaxial compression resistance $|\sigma_{ci}| = 72\ MPa$, rock parameter $m_i = 9$, Geological Strength Index $GSI = 50$ and disturbance factor $D = 0$.

For the embankment and load transfer mat the input parameters are reported in the table 3.1.

Within the dimensions of modelled domain the EGE-2.2 is in contact with the bedrock, therefore it is assumed that it will substitute bedrock in case of its various inclinations. And the EGE-3 is included within the EGE-4 for modelling simplicity.

The model dimensions were choosen to be as 90 meters in horizontal (in-plane) direction to avoid boundary condition effects and of 6 meters (out of plane) to include multiple rows of piles under the train loads. In the vertical direction the height of 75 meters was chosen to include all the possible bedrock inclinations (see fig. 4.1).

10-node tetrahedra elements were used for discretization of the domain with partial mesh refinement. Total number of elements used is equal to 44623. For all cases, except the one with implemented solution, the same mesh was used for calculation.

As was discussed in section 3.2.3 the piles were modelled with embedded beam elements, provided the fact that bored piles are used which introduce low disturbance to surrounding soil. The material properties that were used for modelling are reported in the table 4.2.

Table 4.2: Input parameters for the Embedded beam

Material type	Elastoplastic
E, $[GPa]$	27.4
γ, $[kN/m^3]$	23
Beam type	Predefined
Predefined beam type	Massive circular beam
Diameter, [m]	0.45
Yield stress σ_y, $[MPa]$	2
Axial skin resistance	Layer dependent
T_{max}, $[kN/m]$	35
Base resistance F_{max}, $[kN]$	310

In case where the pile was an end-bearing element strength of the concrete was used to calculate the maximum base force, equal to $F_{max} = 4100[kN]$ (for the concrete class C25/30 and a pile diameter 450 mm).

The geogrid is modelled as built-in geogrid element with the parameters reported in the table 4.3.

Figure 4.1: Model cross-section

Table 4.3: Input parameters for the Geogrid

	Geogrid
Material type	Elastoplastic $N - \varepsilon$
Isotropic	No
EA_1, $[kN/m]$	550
EA_2, $[kN/m]$	1100
$N_1(0\%)$, $[kN/m]$	0
$N_1(10\%)$, $[kN/m]$	55
$N_2(0\%)$, $[kN/m]$	0
$N_2(10\%)$, $[kN/m]$	110

4.1.1. Staged construction

The calculation was subdivided in the major steps according to the embankment construction procedure. The following steps could be outlined:

1. **Initial phase** at this phase an initial geostatic stress is calculated. The procedure is set to be gravity loading due to presence of non horizontal layers.

2. **Geostep** At this step nothing was changed with respect to the previous one. This step is to remove all the possible residual errors of geostatic stress calculation.

3. **Excavation** At this step a removal of in-situ material is performed to allow for pile construction and further load transfer mat construction.

4. **Piles** At this step all the piles (embedded beam elements) and pile caps (plates) are activated.

5. **Geogrid** At this step an initial 150 mm of soil is placed over the pile caps, geogrid is put on top and another 150 mm of fill material is put over to cover the geogrid.

6. **Mat** At this stage a mat is constructed in one step (as there is no need to account for the undrained response the construction could be done in one single step).

7. **Embankment** At this step the embankment is constructed.

8. **Sleepers and rails** At this step the railroad track is placed over the embankment for further load application.

9. **Train load** At this step the static load is applied to the railroad track to model passing train. The load from wheel pair is assumed to be placed in the middle of out of plane length of the model.

4.2.   Plan of analyses

After the model set up the following cases were planned:

1. Case where the bedrock was assumed to be horizontal and piles were assumed to be clamped in bedrock.

2. Case where the bedrock was assumed to be absent from the system and clay layer was assumed to be infinitely long (substitution of the bedrock with the clay layer found at the same depth). In this case the piles are floating.

3. Case where the bedrock inclined of 5°. Piles could be partially clamped and partially floating.

4. Case where the bedrock inclined of 10°. Piles could be partially clamped and partially floating.

5. Case where the bedrock inclined of 15°. Piles could be partially clamped and partially floating.

6. Case where the bedrock inclined of 20°. Piles could be partially clamped and partially floating.

7. Case where the bedrock inclined of 25°. Piles could be partially clamped and partially floating.

8. Case where the bedrock inclined of 30°. Piles could be partially clamped and partially floating.

The first two cases were planned to analyse in details the behaviour of a system under two limiting conditions - for clamped (end-bearing) and floating (shaft-bearing) piles. The idea is that for fixed pile length and varying bedrock inclination part of the piles can be in the clamped situation and part could be in the floating conditions.

The following aspects were checked with utmost care:

• Overall maximum settlement of the system;

• Lateral spreading of the embankment's toes;

• Relative rotation of the top embankment's platform;

• Geogrid strains;

• Piles lateral displacement;

• Development of the arching effect.

5 | Results and Discussion

5.1. Comparison of limiting cases

For the following cases an attention was put to the elements represented in the fig. 5.1 which are highlighted in red colour.
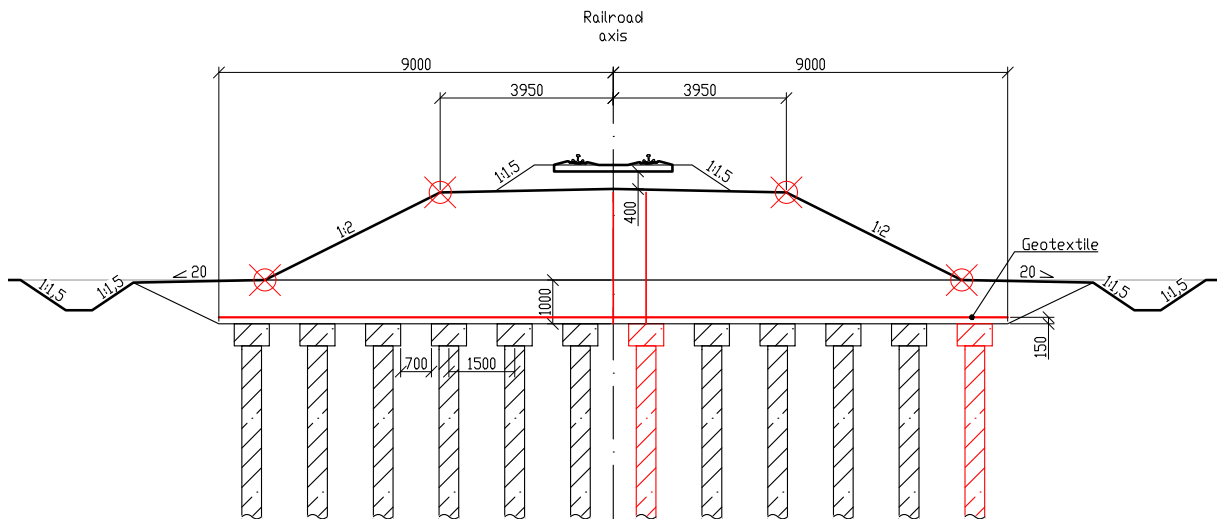
Figure 5.1: Embankment cross-section with the elements of interest (highlighted in red)

5.1.1. End-bearing piles

Based on the model developed in the previous sections the analysis for the first base case here is reported. The system is shown in the fig. 5.2.
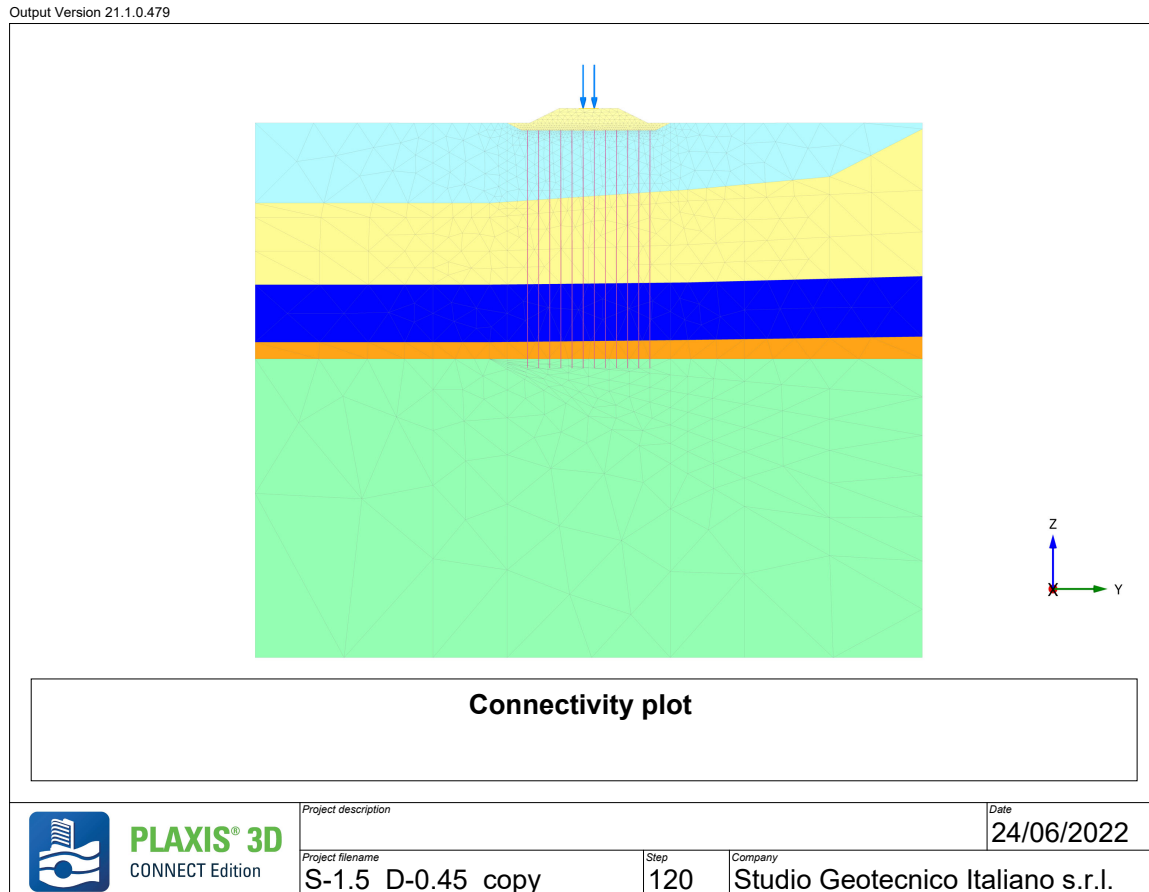
Figure 5.2: Model view for the case of the clamped piles

Displacement analysis

The total maximum settlement in this case is equal to 0.060 m and the point corresponding to this value is on the centreline of the embankment under applied loads. In the fig. 5.3 is represented distribution of the vertical settlement within the embankment body at the centreline. As it could be seen the plane of equal settlements could be identified at 1.5 m above the pile cap, ratio between this height and pile spacing is equal to $h/s = 1$. Therefore a conclusion could be made on the minimum height of the embankment, given the position of equal plane settlements, this height is equal to 0.5 m from the ground level.
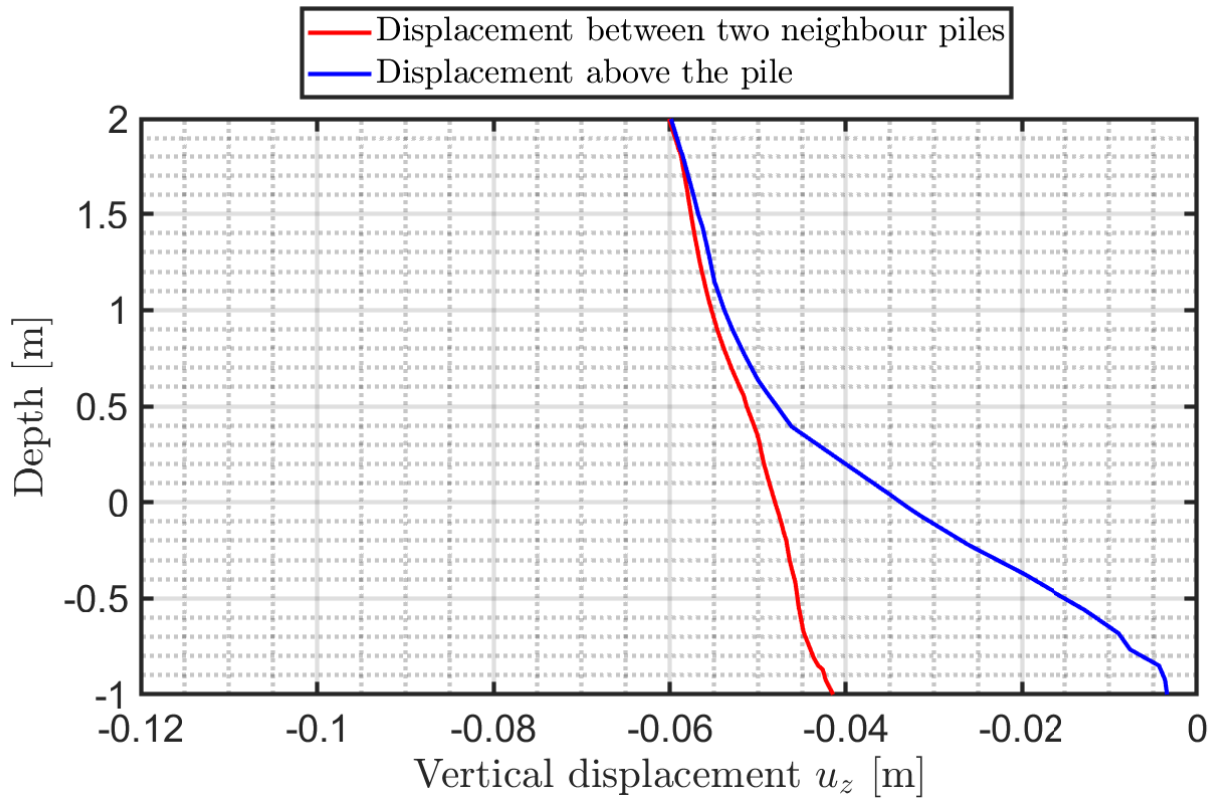
Figure 5.3: Vertical settlement of the embankment body

As the layers are approximately horizontal then the developed relative rotation measured between two embankment's crests is 0 and could be neglected. The lateral toe displacement is equal to $u_y = 0.017$ m.

For brevity in this case the displacement of only two piles (closest to centreline and the extreme ones) was analysed. In fig. 5.4 the displacement of piles is represented. Due to restricted end the pile could move mostly in horizontal direction, compression of the pile under embankment centreline is equal to 0.001 m, which is negligible.

Pile structural analysis

The response of the piles within this case is represented in fig. 5.4. <u>**Note:**</u> Self weight of the pile material is subtracted from the axial force. Initially, the pile experiences an increase in force with depth due to developed negative skin friction with subsequent decrease, correspondent to the part where the displacements of the pile are concentrated. It is worth to note that within the unit EGE-1.2 (from -10 to -29 m depth) the skin friction is almost 0, due to absent relative pile-soil displacement and due to low mechanical parameters of the soil itself. Maximum bending moment is developed at the top part of the pile within EGE-1.1 where the soft soil is located.
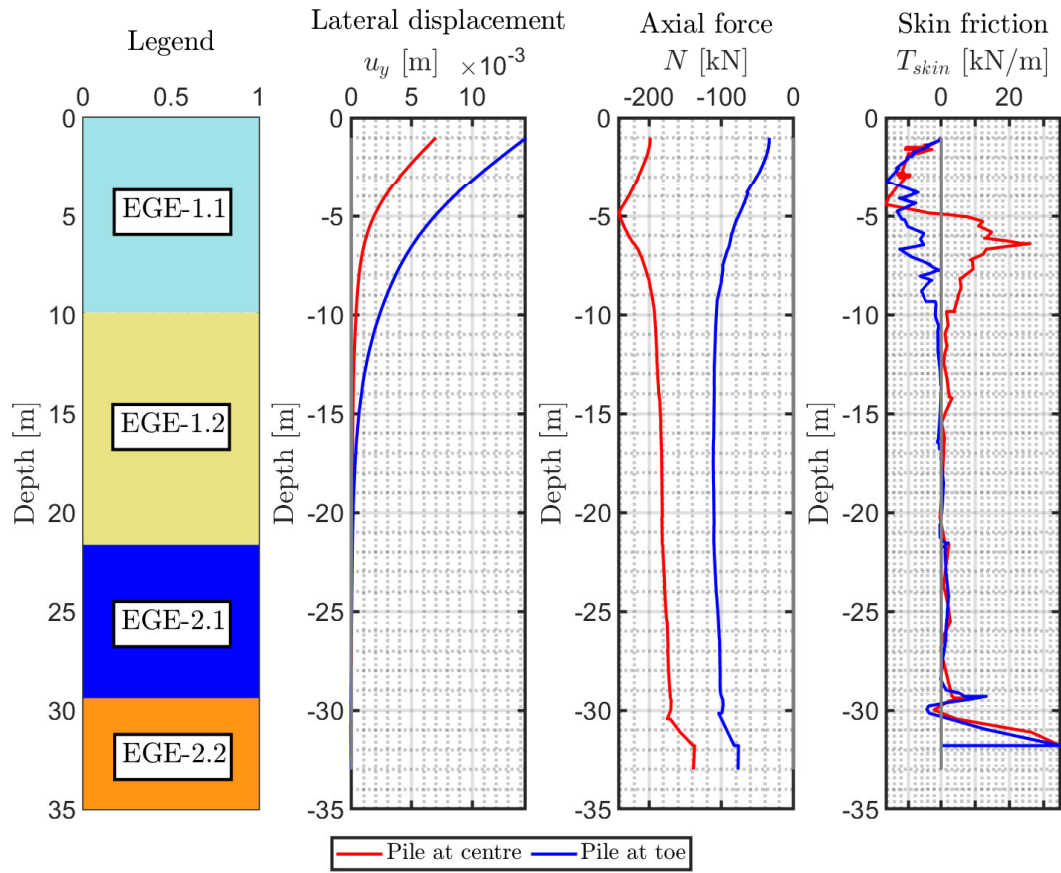
(a) Lateral displacement, axial force and skin friction
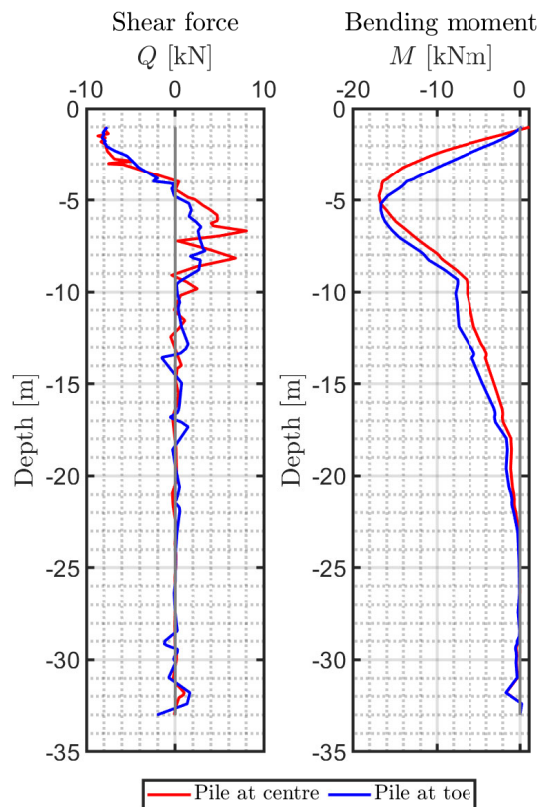
(b) Shear force and bending moment

Figure 5.4: Pile response in the case of end-bearing piles

Geogrid analysis

Maximum displacement of the geogrid developed is equal to the 0.045 m at the centreline
of embankment. Displacement distribution is represented in fig. 5.5.
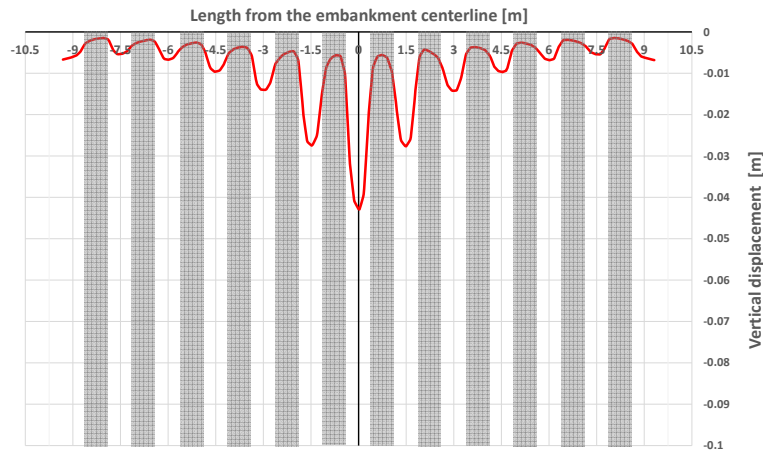
Figure 5.5: Vertical displacement within the geogrid along the cross-section including
piles

Tensile force developed within the geogrid is reported in fig. 5.6. As it is could be seen the
force concentration is developed at the brink of pile caps (shown on fig. 5.6 in the light
grey colour). This behaviour is expected as the geogrid is strained more due to sharp
change of conditions below it (passage from high stiffness concrete to low stiffness soil),
thus it develops larger tension force, as described in details by van Eekelen (van Eekelen
et al., 2015).
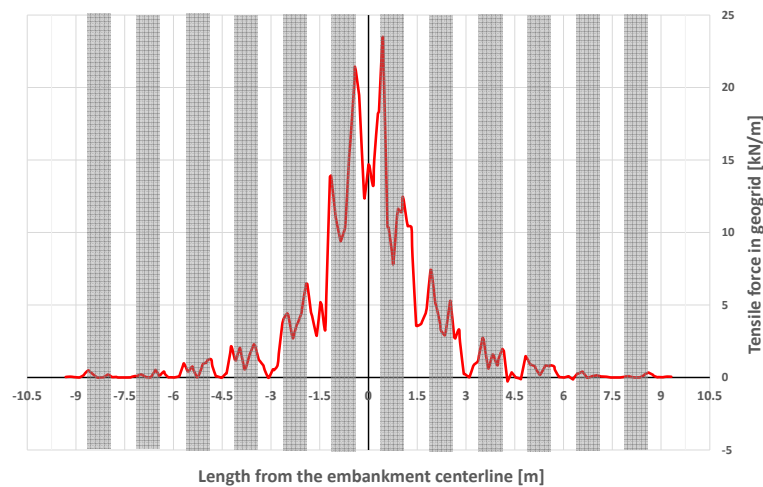
Figure 5.6: Tensile force distribution within geogrid along the cross-section including piles

5.1.2. Floating piles

On the contrary, here the second limiting case is reported. The system is shown in fig. 5.7. In this case the pile length was kept the same as before, it was done to better understand the system's behaviour in terms of soil-structure interaction within the first soft layers independently of the pile tip conditions.
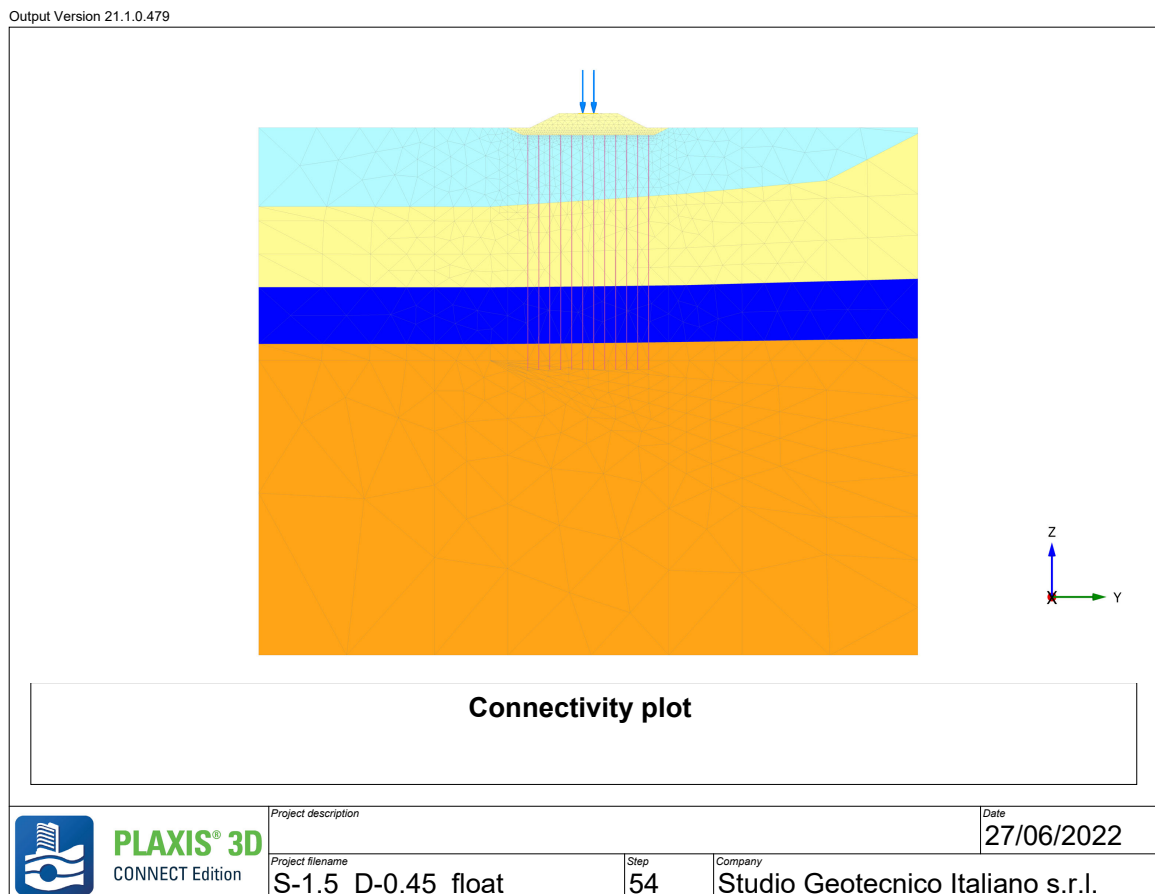
Figure 5.7: Model view for the case of floating piles

Displacement analysis

The total maximum settlement in this case is equal to $0.102\,\text{m}$ and the point corresponding to this value is on the centreline of embankment under applied loads. In fig. 5.8 is represented the distribution of vertical settlement within the embankment body at the centreline. As it could be seen the plane of equal settlements could be identified at the same height as in previous case at $1.5\,\text{m}$ above the pile cap, ratio between this height and pile spacing is equal to $h/s = 1$.
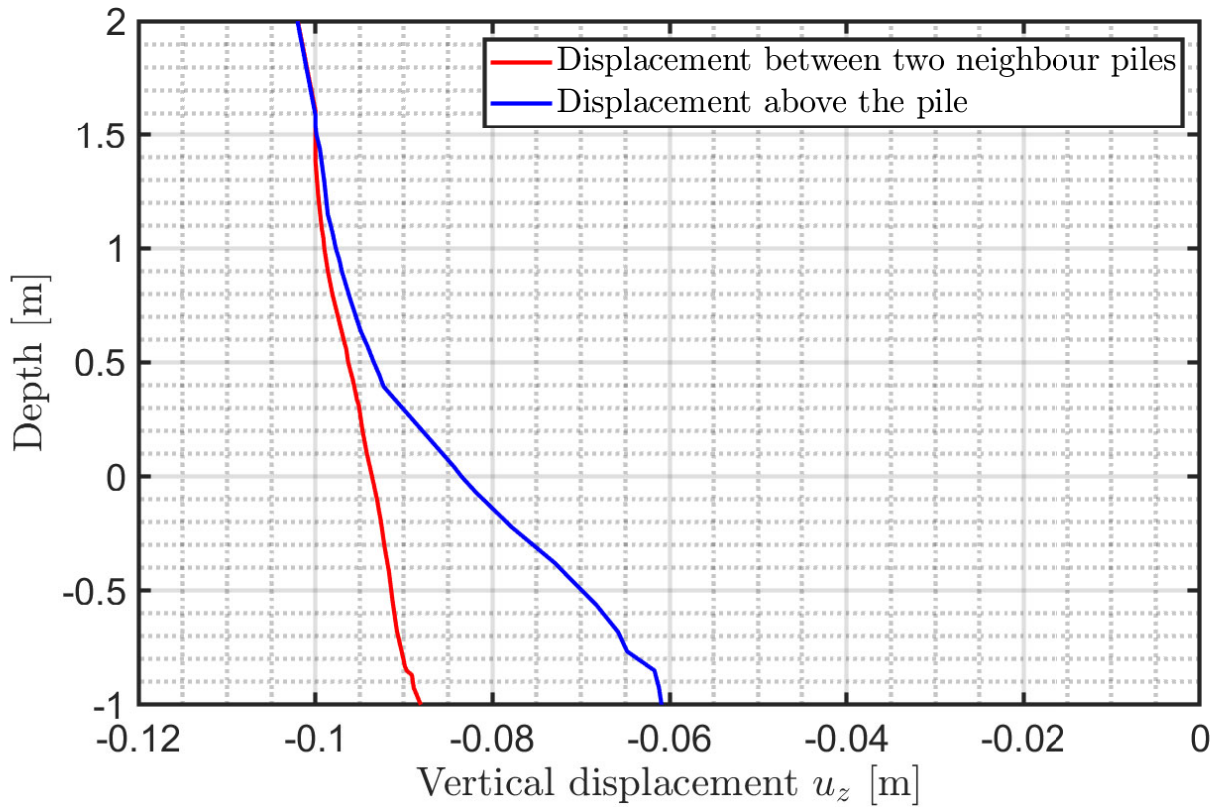
Figure 5.8: Vertical settlement of the embankment body

Also in this case the developed relative rotation measured between two embankment's crests is 0 and could be neglected. The lateral toe displacement is equal to $u_y = 0.002$ m. In this case the system mostly settles, with little lateral spreading.

For brevity in this case the displacement of only two piles (closest to centreline and the extreme ones) was analysed. In fig. 5.9 the displacement of piles is represented. In this case the pile is free to move in every direction, hence a more complex behaviour is observed, compression of the pile under embankment centreline is equal to 0.001 m, which is negligible.

Pile structural analysis

The pile response is represented in fig. 5.9. **Note:** Self weight of the pile material is subtracted from the axial force. Initially, the pile experiences an increase in force with depth due to developed negative skin friction with subsequent decrease, correspondent to the part where displacements of the pile are concentrated. It is worth to note that within the unit EGE-1.2 (from -10 to -29 m depth) the skin friction is almost 0 due to low mechanical parameters of the soil itself. Bending moment distribution in this case is more complex as piles bend differently depending on section position.
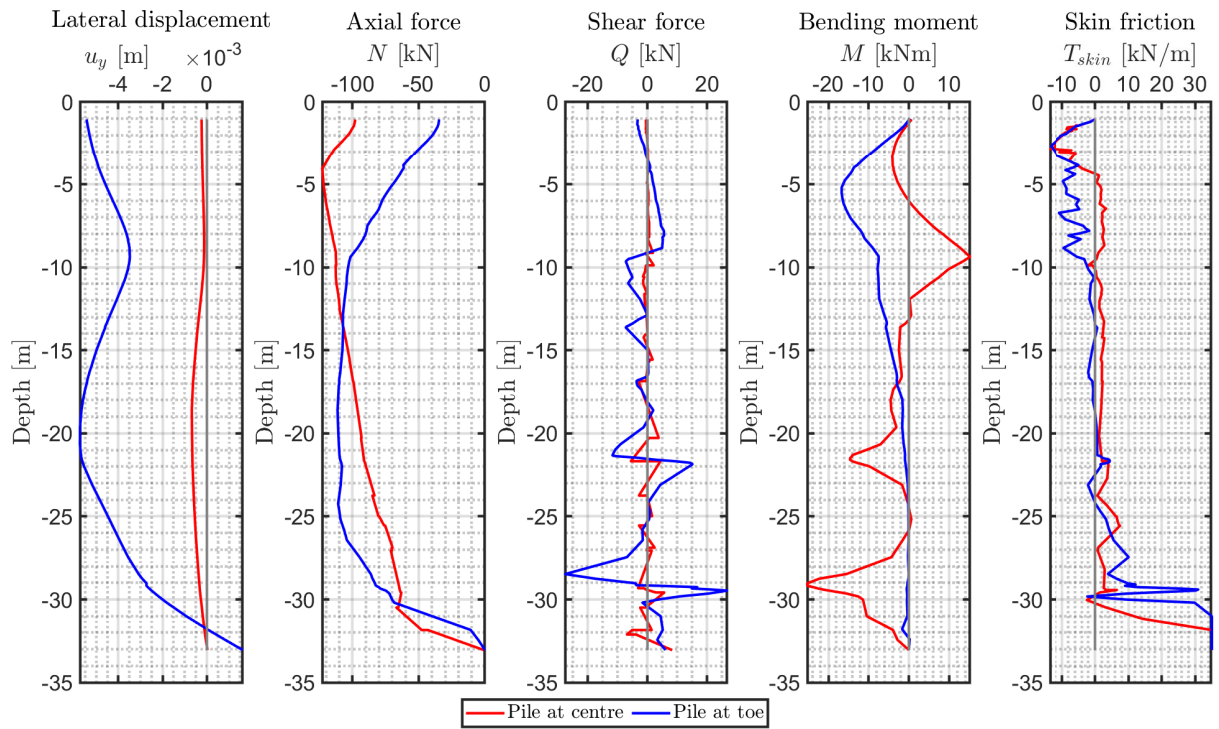
Figure 5.9: Pile response in the case of floating piles

Geogrid analysis

The maximum displacement of the geogrid developed is equal to 0.089 m at the centreline of embankment. Displacement distribution is represented in the fig. 5.10.
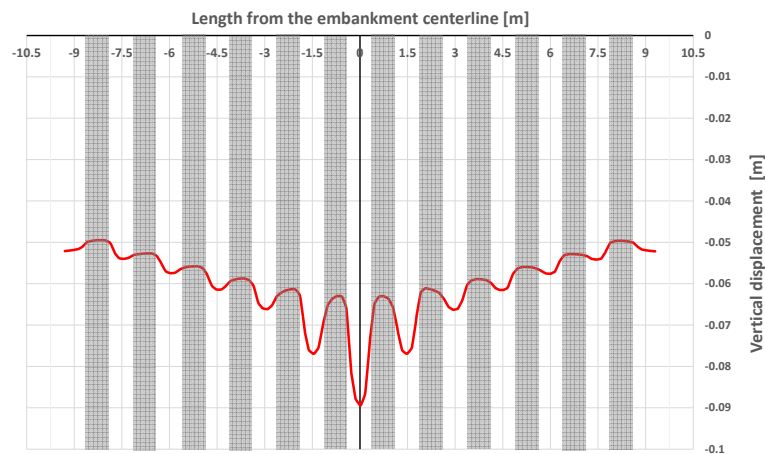
Figure 5.10: Vertical displacement within the geogrid along the cross-section including piles

Tensile force developed within the geogrid is reported in fig. 5.11. As it is could be seen the force concentration is developed at the brink of pile caps (shown on fig. 5.11 in light

grey). In this case a force in the geogrid is lower due to a better interaction of the elements within the system as part of load is transferred to the subsoil between piles and not concentrated on the piles (see axial force in figs. 5.4 and 5.9).
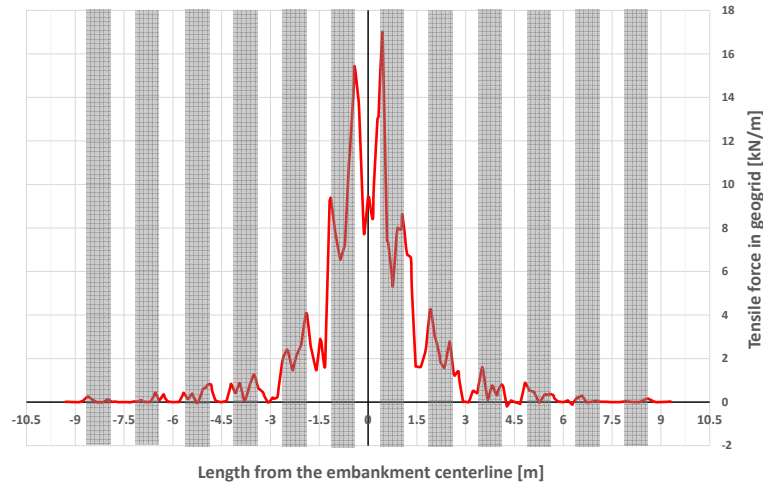
Figure 5.11: Tensile force distribution within the geogrid along the cross-section including piles

5.1.3.   Comparison of the two limiting cases

Here is the comparison of the two previously reported results is made. As it could be seen depending on the pile conditions a different pattern of deformation is observed also a pile response is different.

Settlements analysis

As it is expected in case of floating piles a larger settlement is developed due to the need of displacement to activate bearing capacity of the piles. Disregarding the fact of excessive displacement and comparing the overall response of the system it could be outlined that in both cases the plane of equal settlement is developed at the same height from the pile caps, hence it is independent of the pile bottom conditions.

Comparison of displacement in both cases for the pile at centre of the embankment and at the toe is represented in fig. 5.12 and fig. 5.13.

Structural pile response

Pile response is represented in fig. 5.12 and fig. 5.13. As it could be seen the response in terms of pile behaviour is similar in both cases.
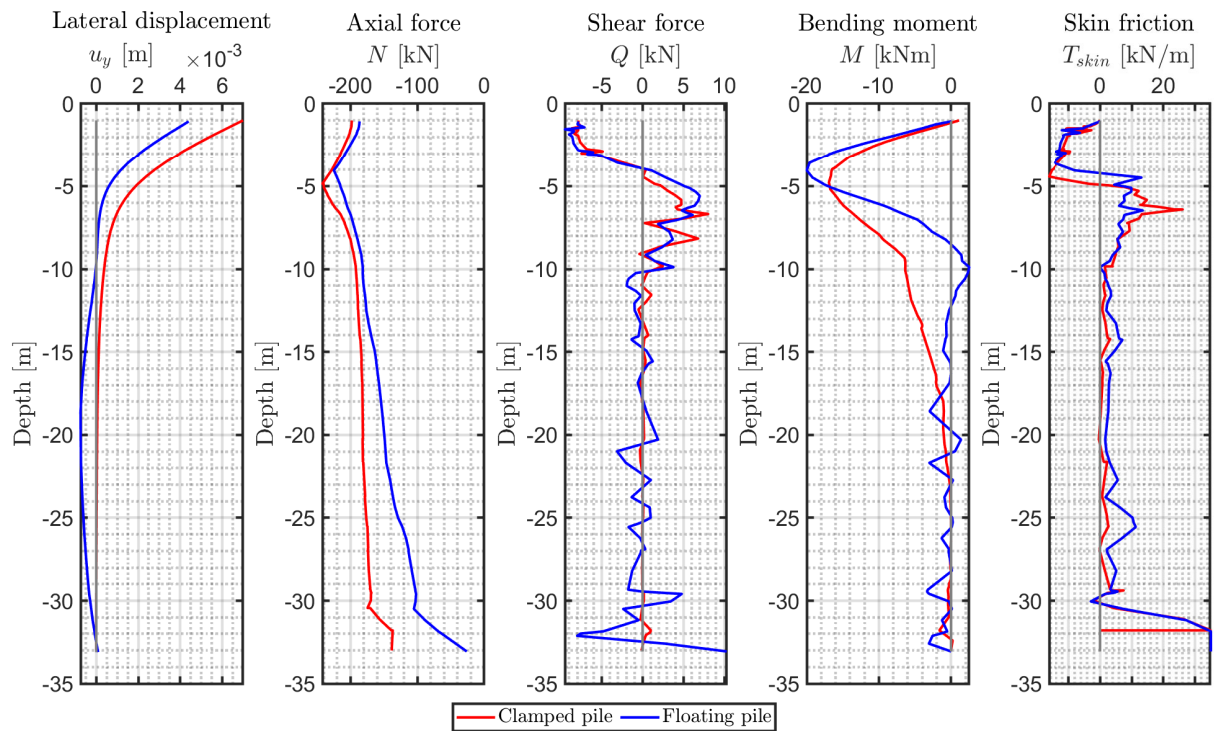
Figure 5.12: Comparison of pile behaviour close to the centreline of embankment for the base cases
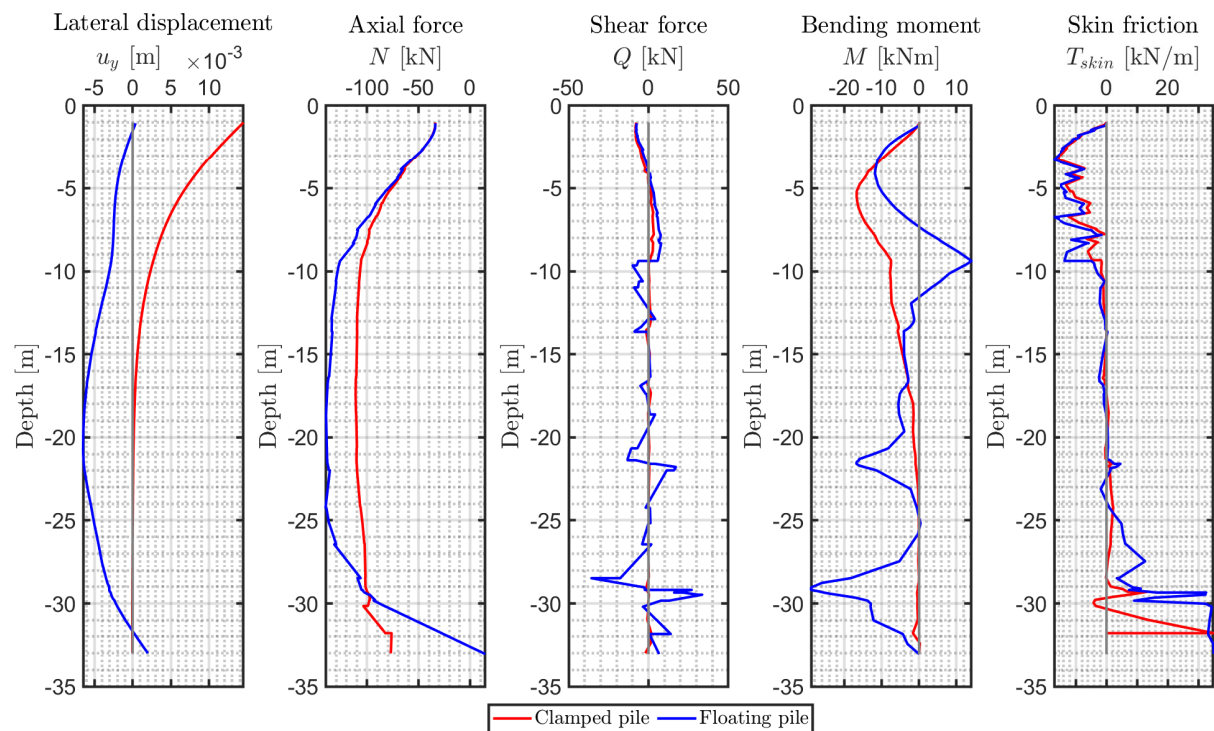
Figure 5.13: Comparison of pile behaviour at the toe of embankment for the base cases

Geogrid analysis
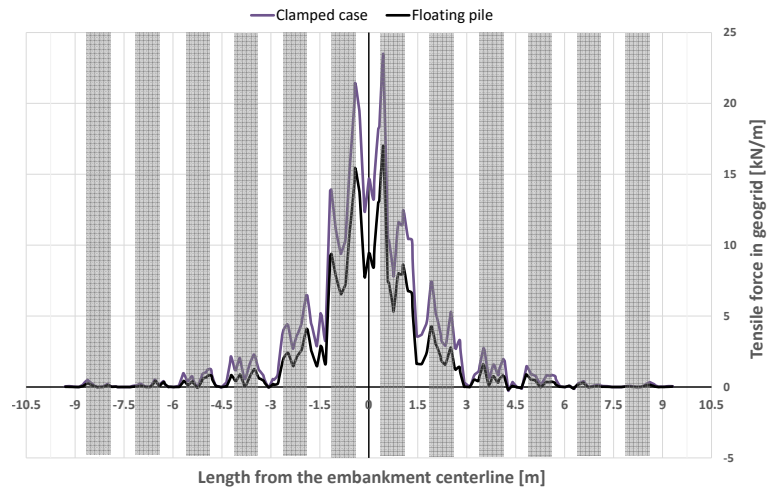
Figure 5.14: Comparison of the tensile force within the geogrid
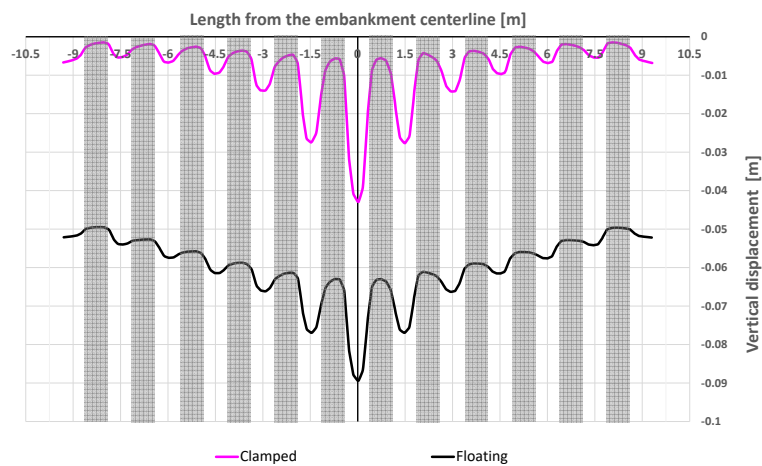
Figure 5.15: Comparison of the settlement of geogrid

Here the comparison of two cases is reported. It is expected that varying the bedrock inclination, for fixed pile length, the piles will pass from the end-bearing to floating conditions. Thus the embankment is expected to settle on one side more than on the other, where piles are close to the bedrock. The piles that will be in floating conditions will resist mainly due to skin friction.

5.2. Various bedrock inclination

To investigate the influence of a bedrock inclination on the behaviour of a system the following values of inclination were assumed: 5°, 10°, 15°, 20°, 25° and 30°. Value of 5° was derived from the investigations provided as a minimum possible value, however there is no indication on the maximum value. Provided the two boreholes of a certain depth separated by a certain distance from each other.

In fig. 5.16 are represented the points of interest to characterise the behaviour of a system. The structural elements of interest are lateral piles, piles at the embankment shoulders, pile at the centreline and geogrid. Within the embankment body settlement is checked along the several lines: four lines at the embankment's shoulders and at the centreline. This system is chosen to capture the behaviour of an embankment and to track the changes over a system due to rotation.

Note: In the following all references in directions are made with respect to the centreline of an embankment represented in fig. 5.16 (bedrock is sloping towards right). In all the axial force plots a self weight of the pile is subtracted. In all the lateral displacement plots the opposite sign appears due to the position with respect to an axis of embankment (axis has 0 coordinate).
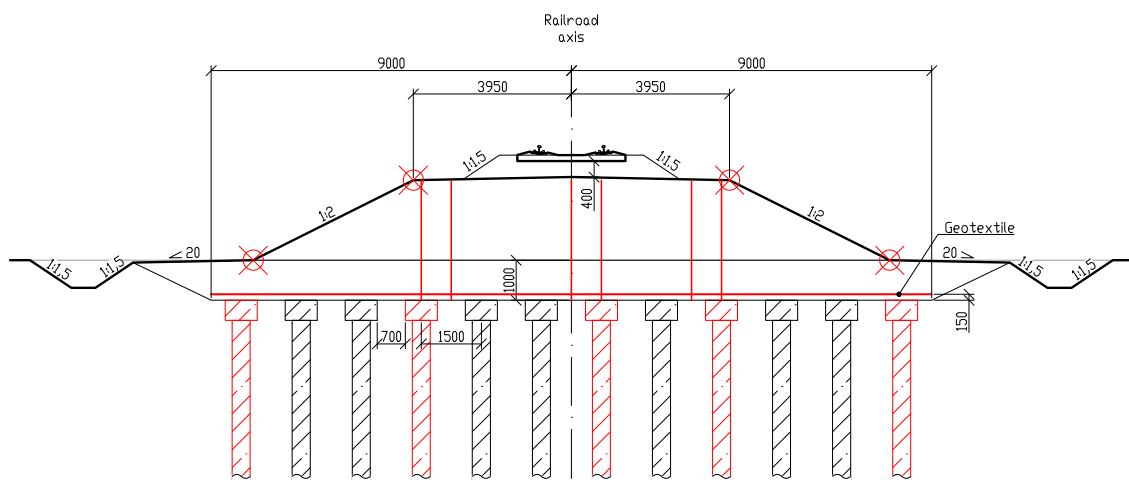
Figure 5.16: Elements of interest (highlighted in red)

In the following most relevant results are reported, thus 5°, 15° and 30°. Results for all cases are reported in appendix C.

5.2.1.   Inclination of $5°$

The model is shown in fig. 5.17. In this case piles at left toe are clamped within the bedrock , while piles at the right toe are floating over the bedrock.
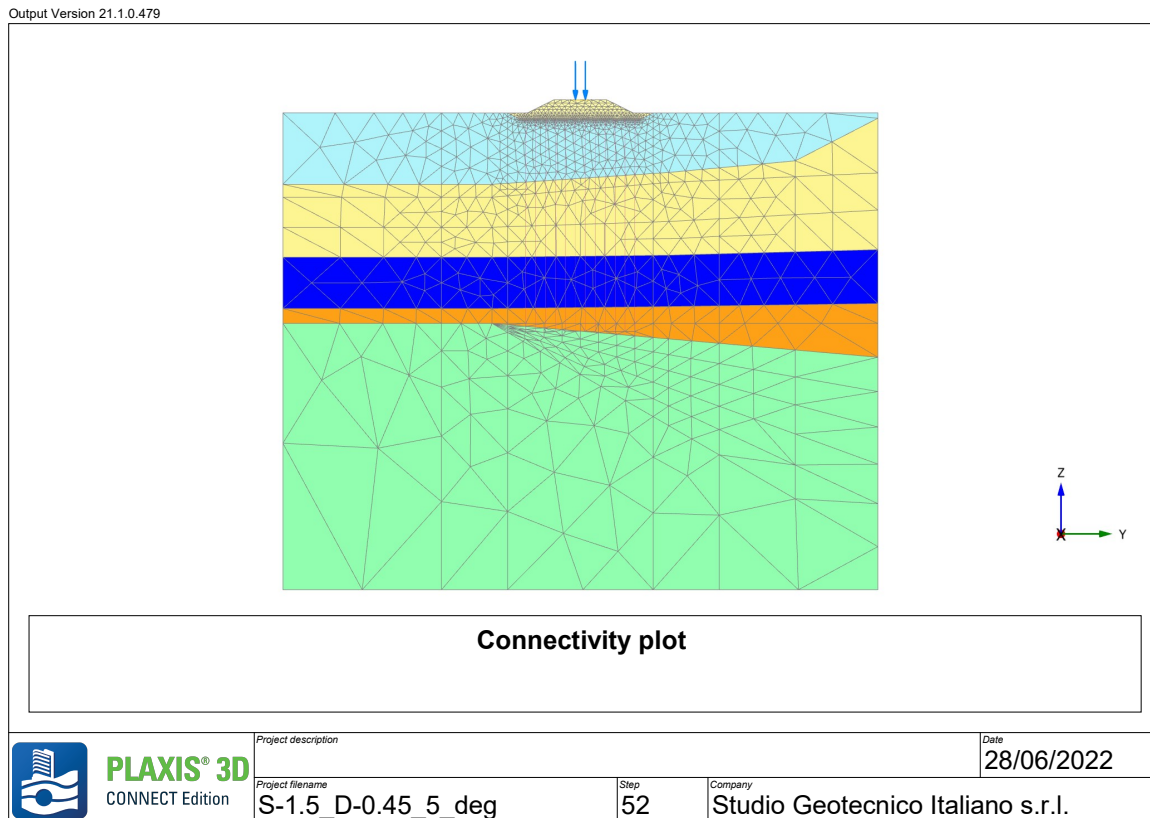
Figure 5.17: Model view for the case of 5° bearing layer inclination

Therefore the displacement developed within the embankment body are reported in fig. 5.18. As it could be seen the values at two embankment shoulders are approximately the same, which is the consequence of low difference between the piles condition. Relative rotation of the embankment top platform in this case is equal to 0.007°, thus negligible, and the maximum settlement along the centreline in this case is equal to 0.062 m.
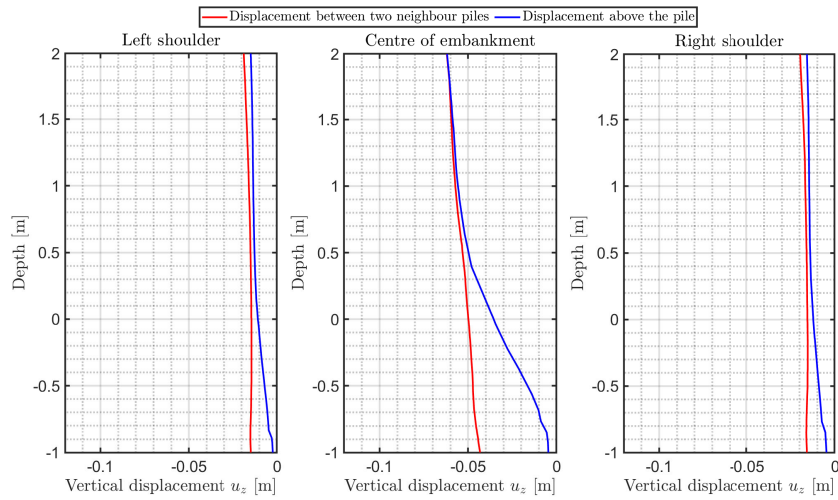
Figure 5.18: Vertical displacement developed in the embankment in case of 5° bearing layer inclination
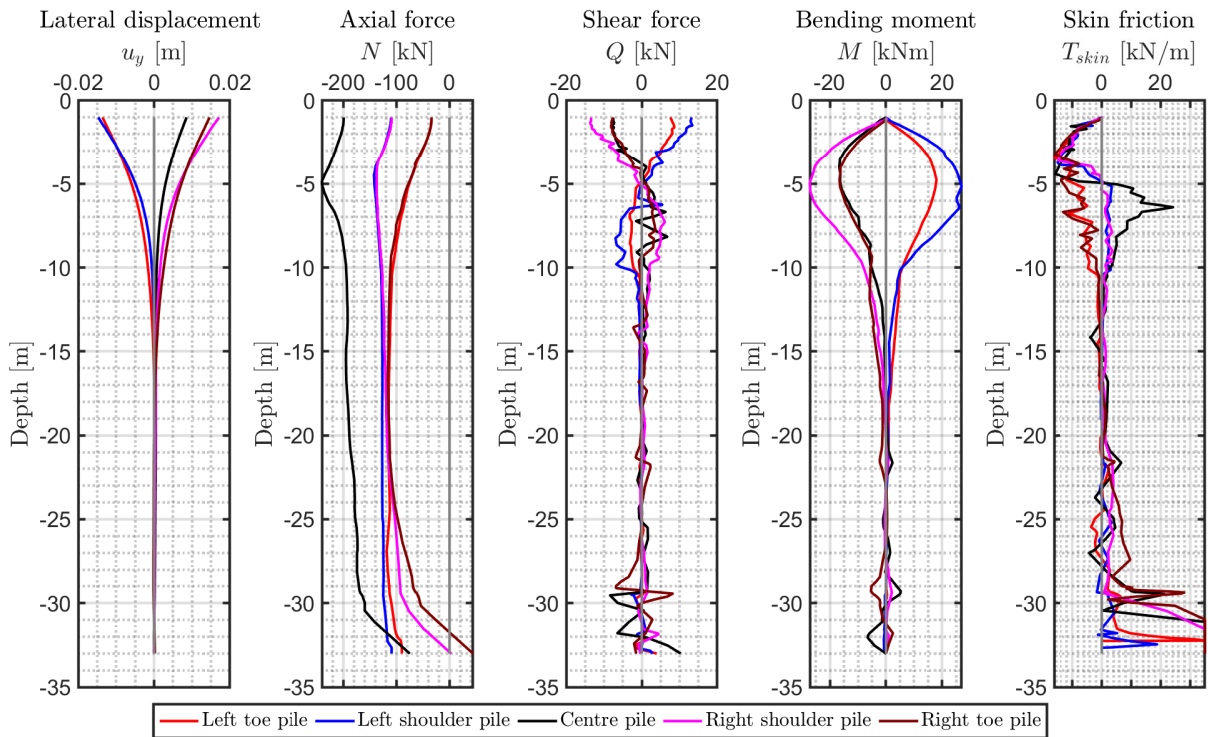
Figure 5.19: Pile behaviour in case of 5° bearing layer inclination

In fig. 5.19 the behaviour of piles along a cross section is reported. As it could be seen, the piles react in a similar way independently of their bottom condition. This is characterised by the fact that pile which are in floating conditions arrive close to the bedrock (pile at right toe has 680 mm of clay under its end) and thus it transmits load to the rock layer which is close to the tip.

In terms of the forces within geogrid, represented in fig. 5.20, the response is similar to the one of end-bearing piles. While in terms of the geogrid displacement, represented in fig. 5.21, an asymmetry is observed as the right end settles more.
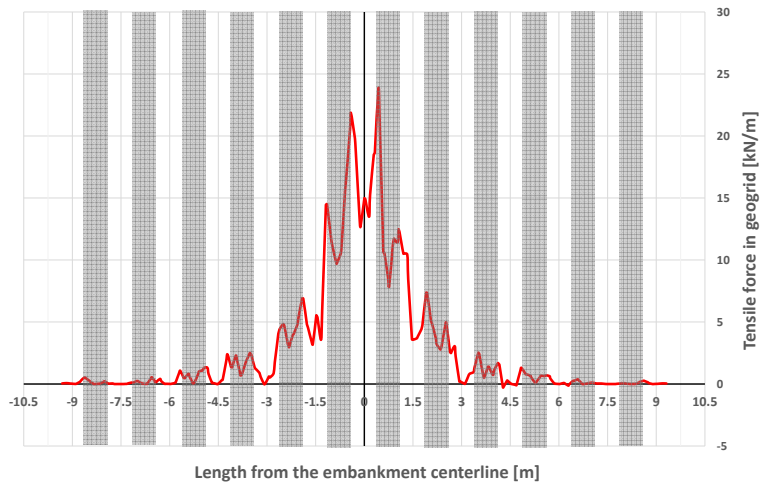
Figure 5.20: Forces developed within the geogrid in case of 5° bearing layer inclination
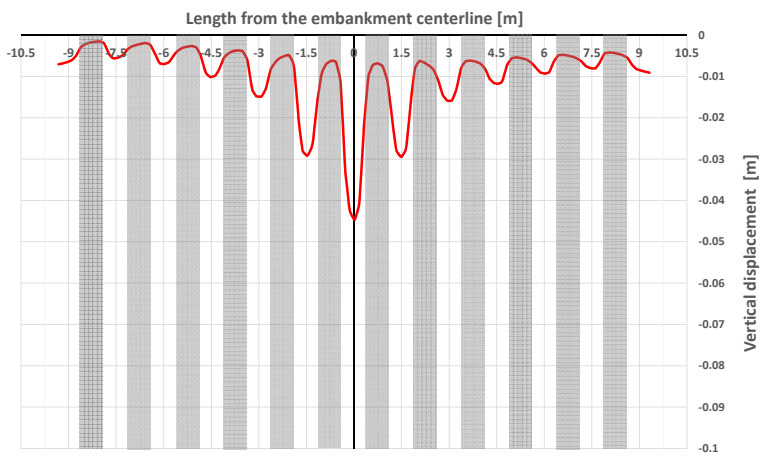
Figure 5.21: Vertical displacement of the geogrid in case of 5° bearing layer inclination

5.2.2.   Inclination of 15°

The model is shown infig. 5.22. In this case piles at left toe is 0.16 m far from the bedrock, while piles at the right toe are floating over the bedrock at 4.6 m.
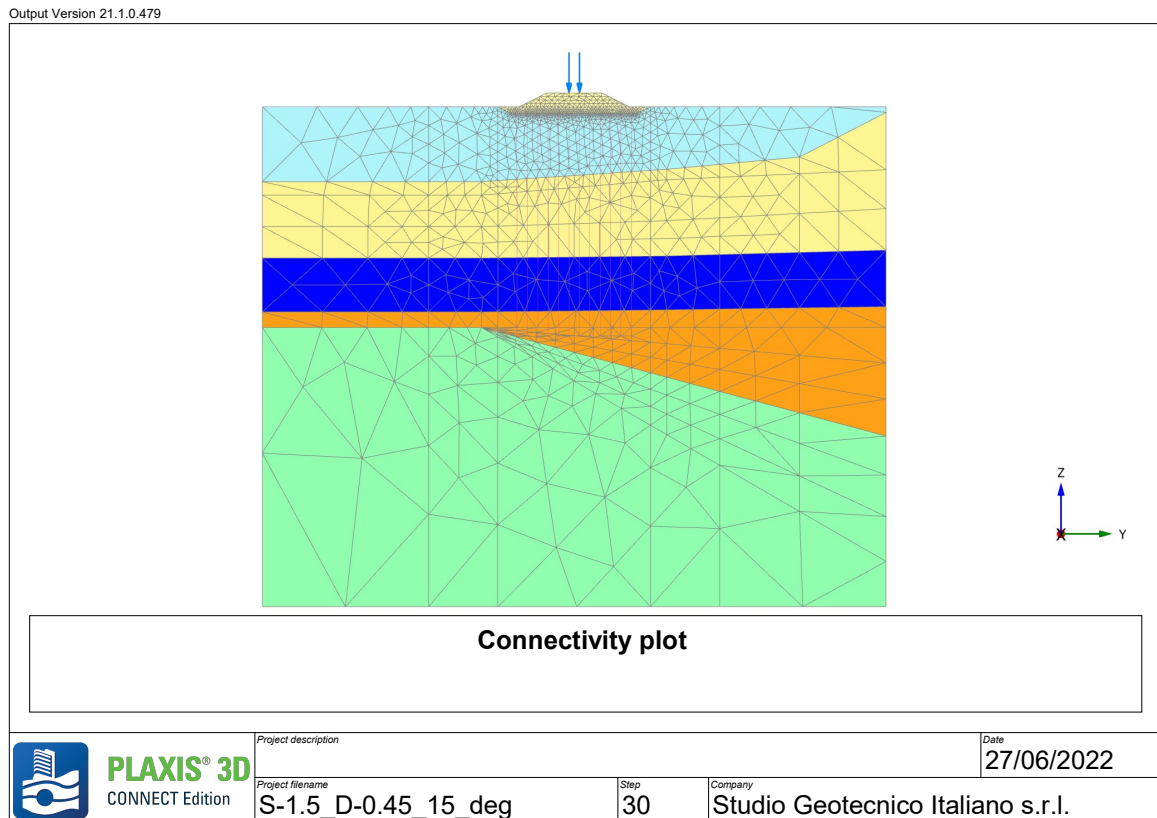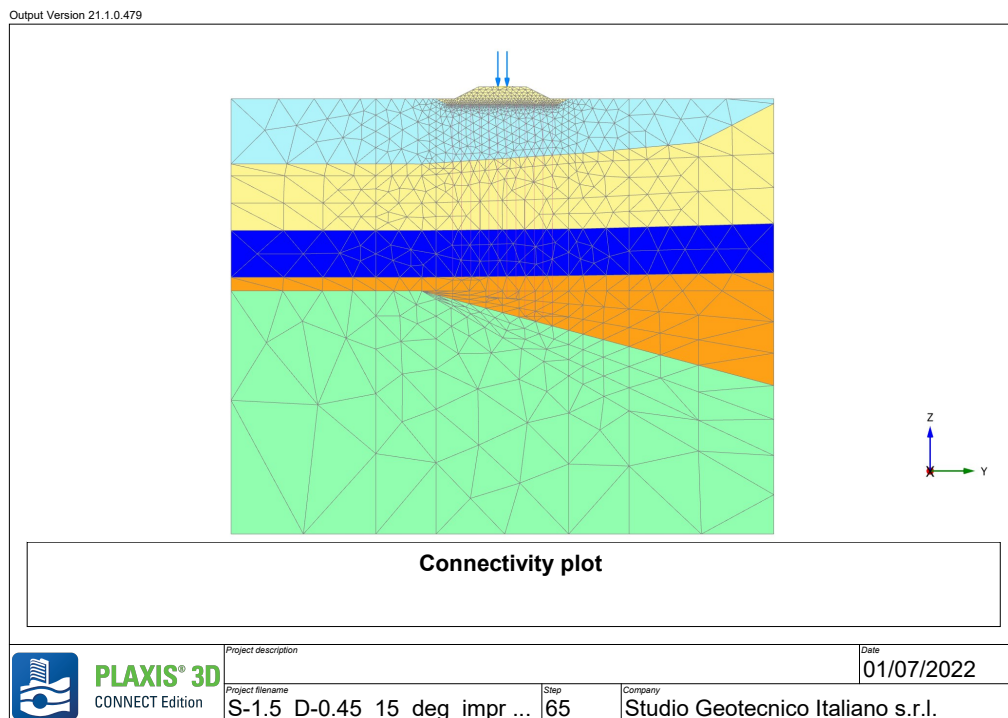

Figure 5.22: Model view for the case of 15° bearing layer inclination

Displacement developed within the embankment body are reported in fig. 5.23. Relative rotation of the embankment top platform in this case is equal to 0.01° which is negligible and the maximum settlement along the centreline in this case is equal to 0.068 m.
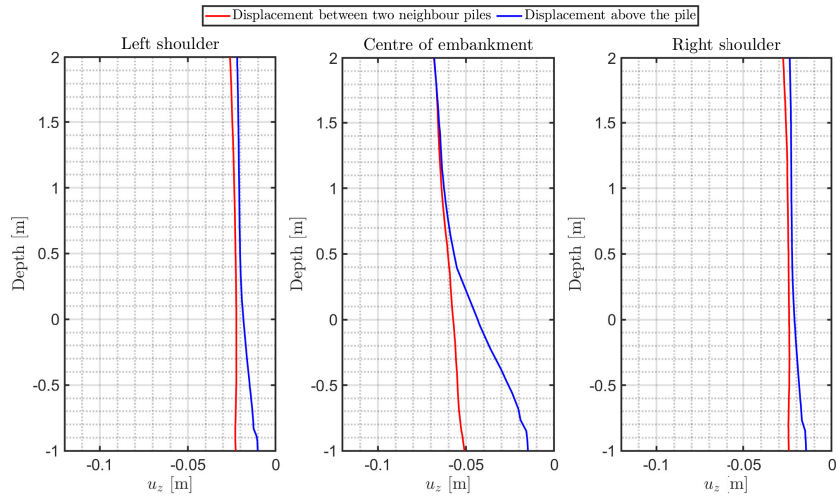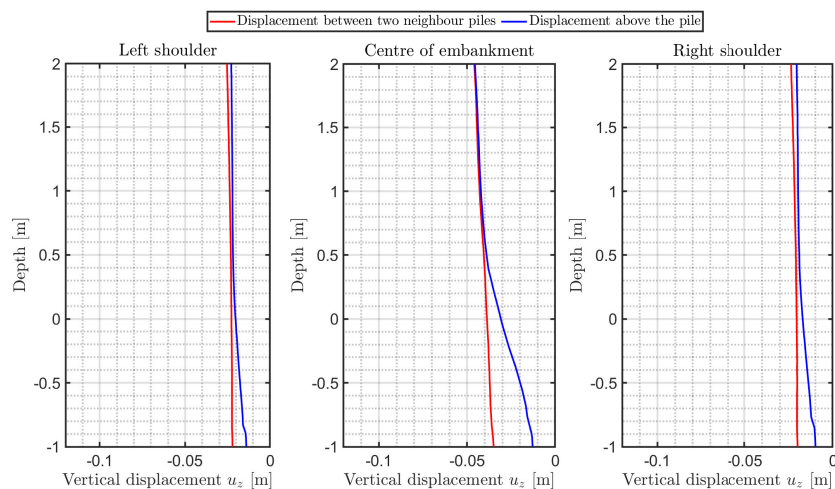
Figure 5.23: Vertical displacement developed within the embankment in case of 15° bearing layer inclination
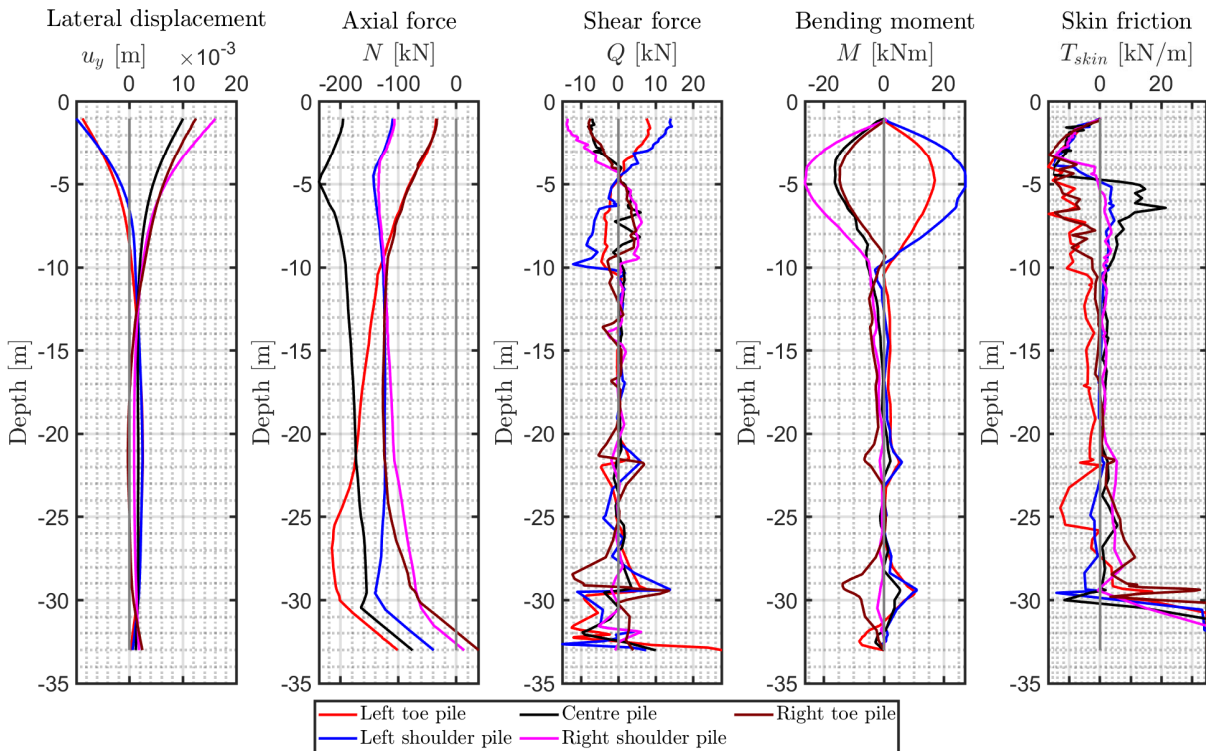
Figure 5.24: Pile behaviour in case of 15° bearing layer inclination

In fig. 5.24 the pile behaviour along a cross section is reported. As it could be seen the response has changed due to inclination of the bearing strata. In particular a mean value of the pile lateral displacement has moved towards the dip of bedrock (to the right with reference to fig. 5.22), therefore a sort of sliding (lateral translation) is observed.

In terms of internal pile forces a sharp increase in the axial force of a pile at left lateral extent of embankment is observed. This is characterised by the overall behaviour of the system: piles which has a thicker deformable layer under its tip are tend to displace more, than the pile which is since the beginning close to the bedrock. Given this larger potential to displace and a constraint on the contrary it results in negative skin friction over the extreme pile (which is 160 mm far from the bedrock at the beginning). For better understanding of the system's behaviour an iso-lines of settlement is plotted in fig. 5.27.

In terms of the forces within geogrid, represented in fig. 5.25, the response is similar to the previous case, however a small decrease in the developed force is observed. While in terms of the geogrid displacement, represented in fig. 5.26, an asymmetry observed is more pronounced.
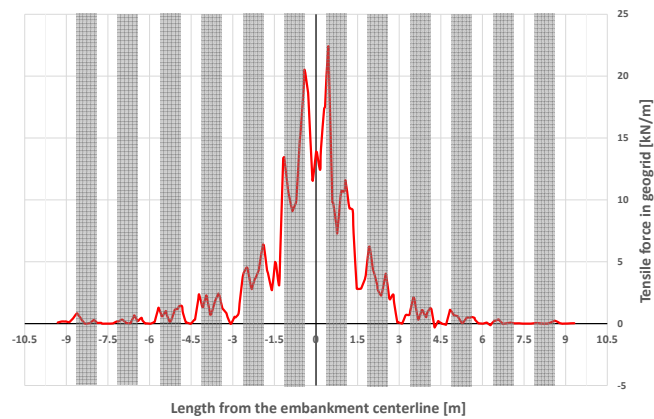
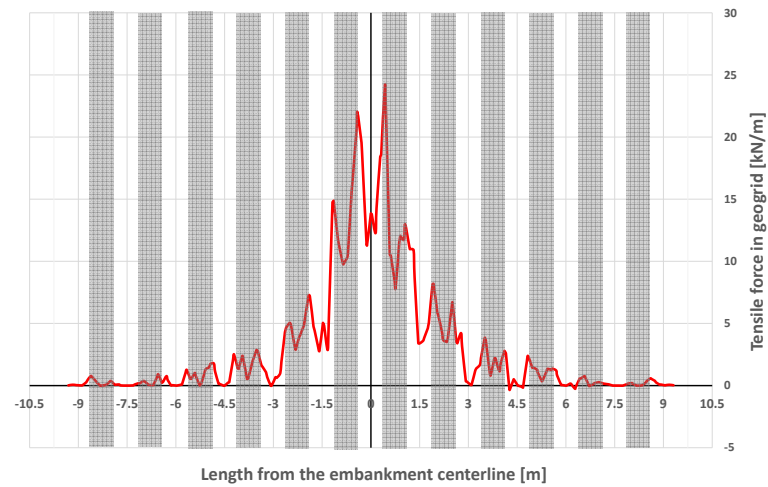Figure 5.25: Forces developed within the geogrid in case of 15° bearing layer inclination
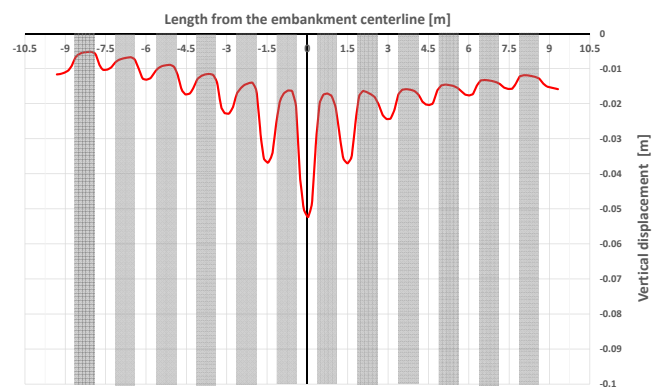
Figure 5.26: Vertical displacement of the geogrid in case of 15° bearing layer inclination
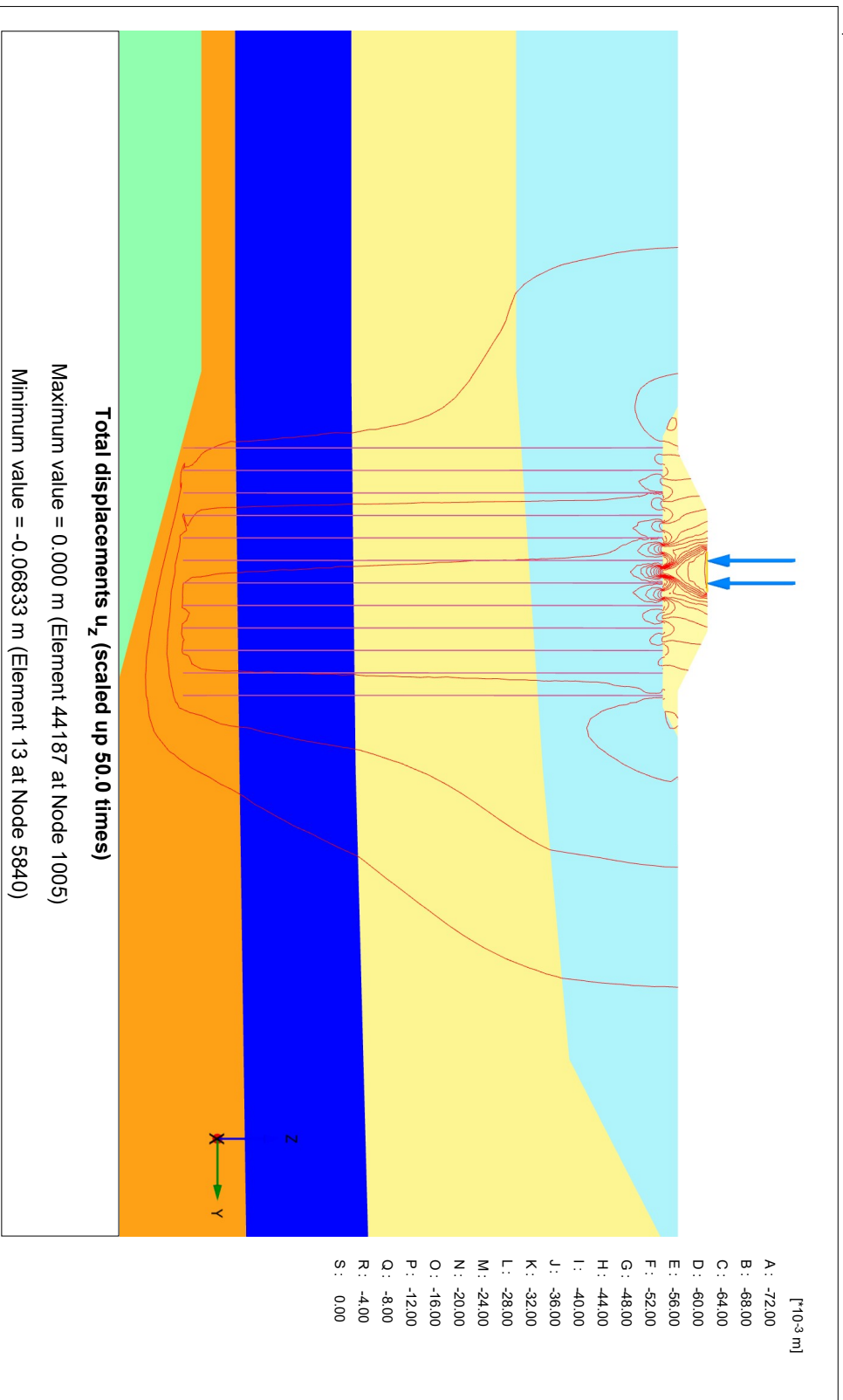
Figure 5.27: Iso-lines of developed displacement within the system

5.2.3. Inclination of 30°

The model is shown in fig. 5.28 and 3D view of the model is shown in fig. 5.29. In this case piles at left toe is 1.7 m far from the bedrock, while piles at the right toe are floating over the bedrock at 11.3 m.
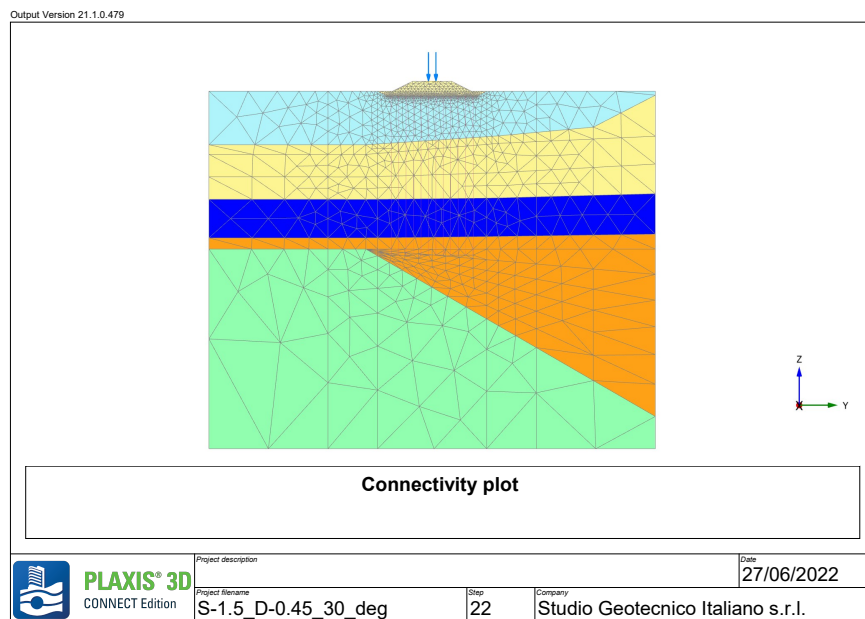
Figure 5.28: Model view for the case of 30° bearing layer inclination
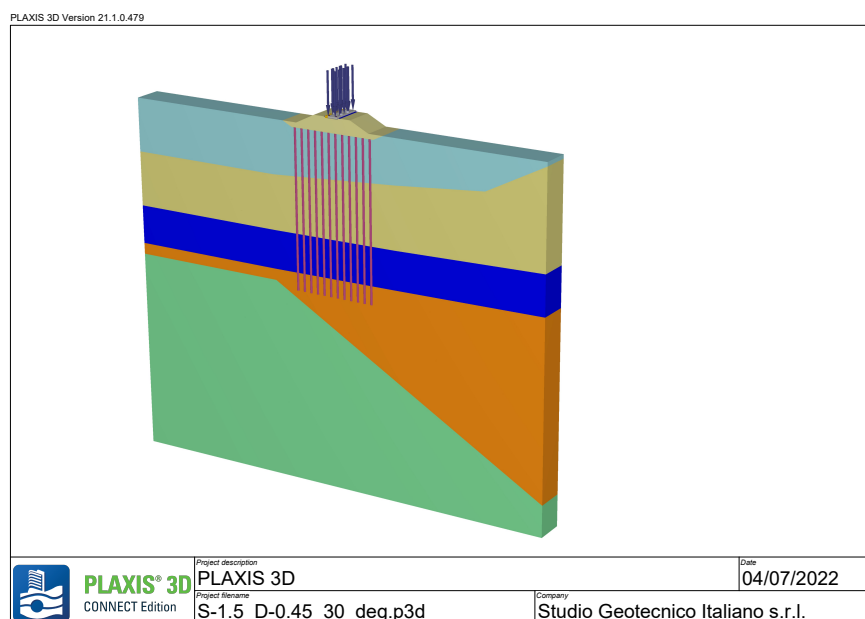
Figure 5.29: 3D model view for the case of 30° bearing layer inclination

Displacement developed within the embankment body are reported in fig. 5.30 and 3D view of the system's settlement is shown in fig. 5.31. As it could be seen the values at two embankment shoulders are approximately the same, however at the right side a more uniform settlement is observed, which gives an idea that pile and embankment settle uniformly and that arching effect is not much pronounced. Relative rotation of the embankment top platform in this case is equal to 0.02° which is negligible and the maximum settlement along the centreline in this case is equal to 0.075 m.
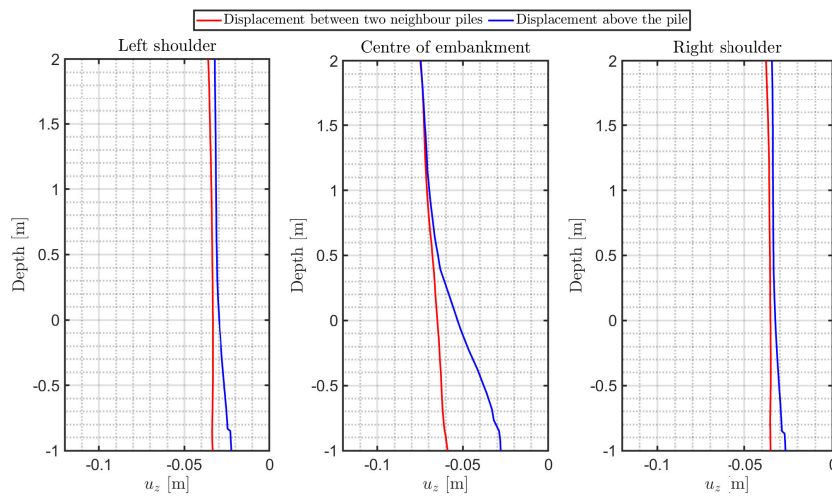
Figure 5.30: Vertical displacement developed in the embankment in case of 30° bearing layer inclination
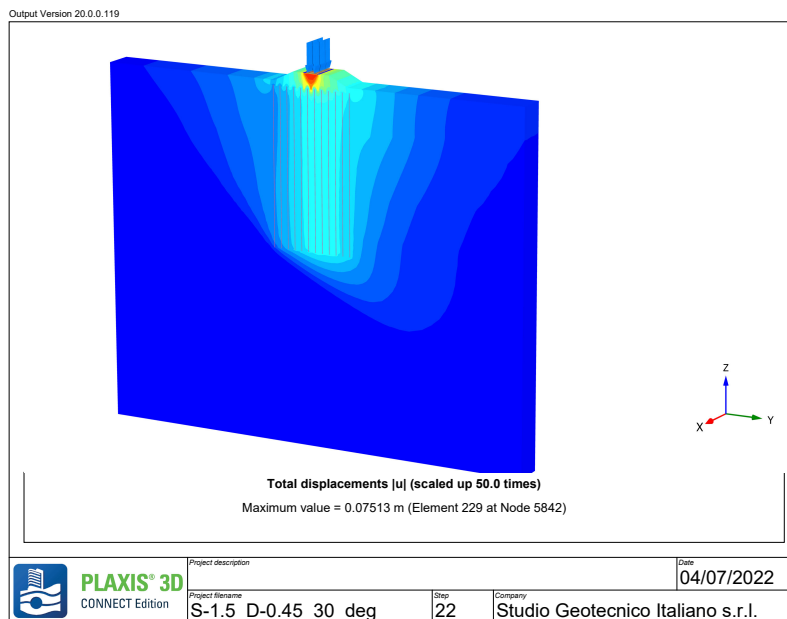
Figure 5.31: 3D model view of system's settlement for the case of 30° bearing layer inclination
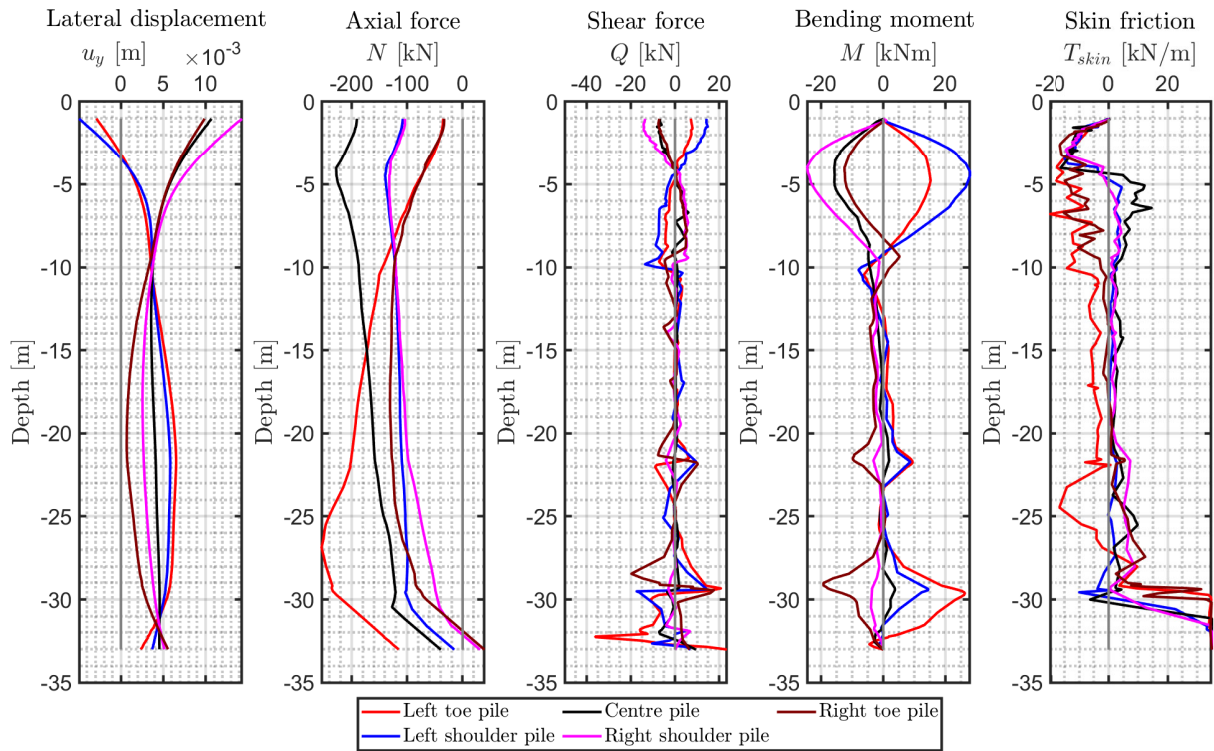
Figure 5.32: Pile behaviour in case of 30° bearing layer inclination

In fig. 5.32 the pile behaviour along a cross section is reported. The overall response of a system reported for 15° case became more pronounced. In particular a mean value of lateral displacement has changed more indicating the lateral translation of the system (see lateral displacement in fig. 5.32).

In terms of internal pile forces the behaviour did not change significantly with respect to the 15° case.

In terms of the forces within geogrid, represented in fig. 5.33, the response is similar to the previous cases, however a small decrease in the developed force is observed. While in terms of the geogrid displacement, represented in fig. 5.34, an asymmetry observed is even more pronounced. In addition, both the displacement and force tend to be more uniform in all the spans between piles.
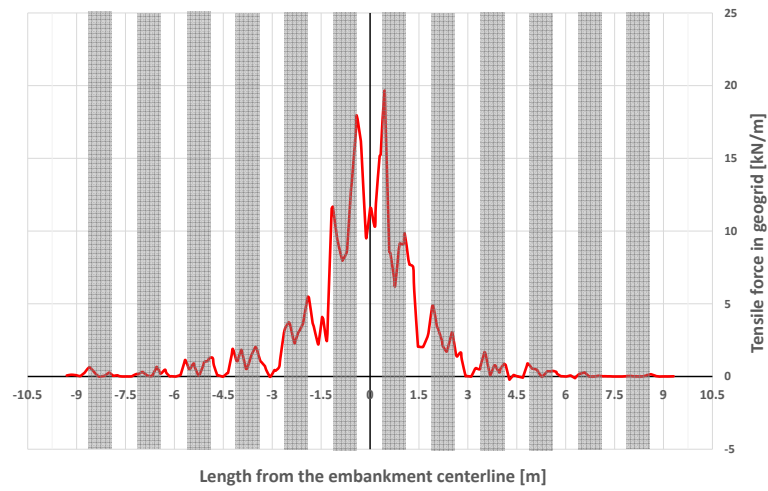
Figure 5.33: Forces developed within the geogrid in case of 30° bearing layer inclination
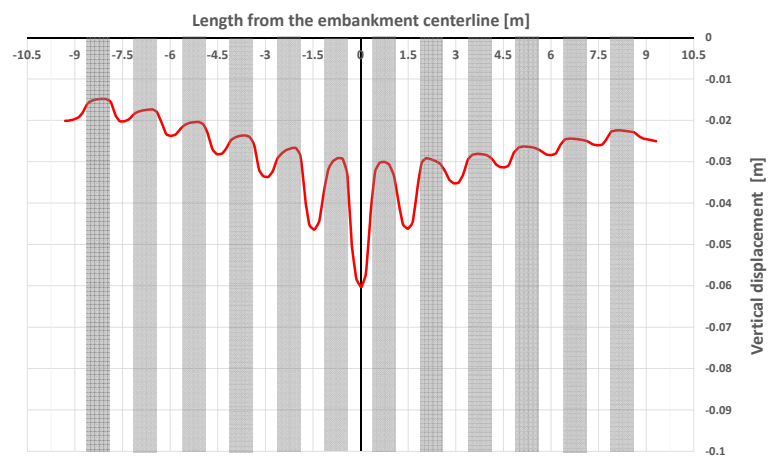
Figure 5.34: Vertical displacement of the geogrid in case of 30° bearing layer inclination

5.3. Results discussion

Based on the previously reported results the following general aspects of a system deformation mechanism could be stated. First of all, with increasing bearing layer inclination the maximum developed settlement in the system is increasing, due to necessity of piles to settle to provide the resistance. The maximum developed settlement for each case is reported in fig. 5.35.
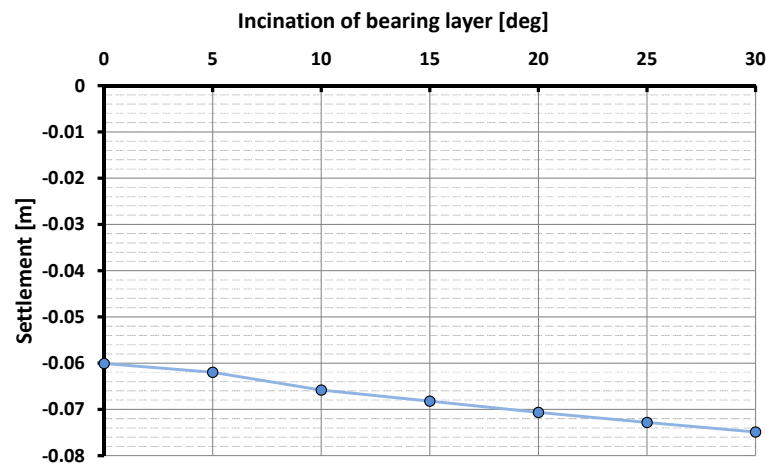
Figure 5.35: Forces developed within the geogrid in case of various bearing layer inclinations

Then, with increasing inclination piles consequently passed from an end-bearing condition to the floating conditions. This aspect is clearly seen comparing the pile response in terms of the internal forces developed (with reference to figs. 5.4, 5.9, 5.19, 5.24 and 5.32). As well as in terms of the geogrid behaviour (represented in figs. 5.5, 5.6, 5.10, 5.11, 5.36 and 5.37). Force within geogrid becomes lower and more uniformly distributed between the piles with development of settlement.
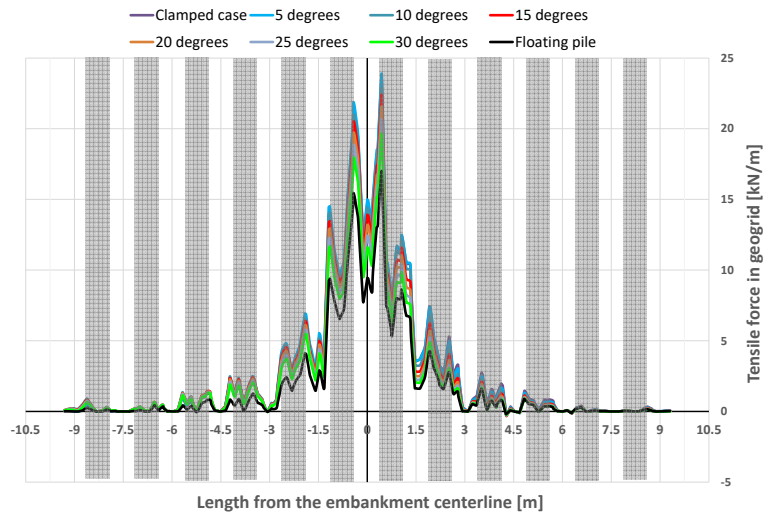
Figure 5.36: Forces developed within the geogrid in case of various bearing layer inclinations
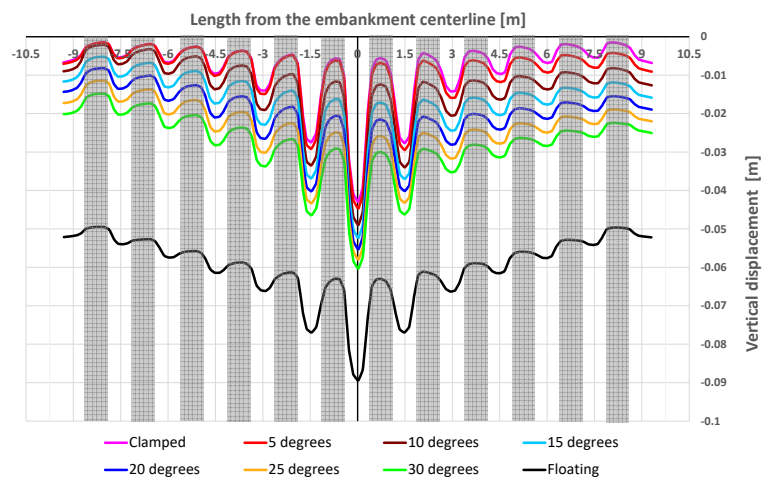
Figure 5.37: Vertical displacement of the geogrid in case of various bearing layer inclinations

The dependency of the maximum geogrid tensile force is reported in fig. 5.38. As it could be seen with the increasing inclination a maximum reached force is decreasing. Which shows that with more settlement within the system an arching effect develops stronger and thus the geogrid is becoming less effective structural element.
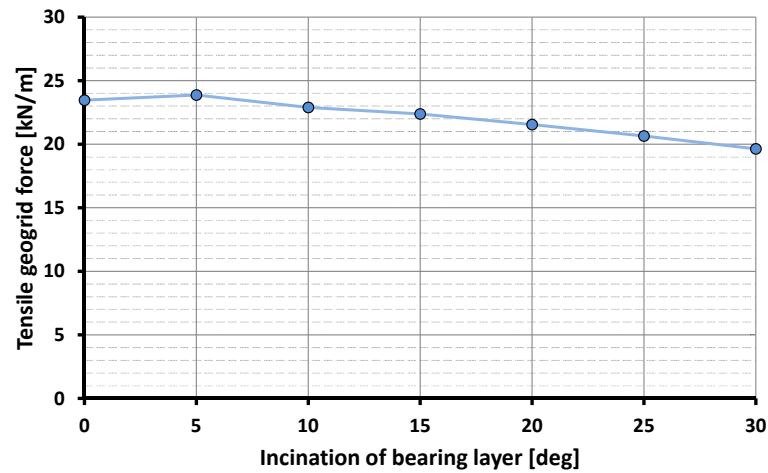
Figure 5.38: Change of geogrid tensile force with bearing layer inclination

The change in pile end conditions leads to an increase in load in the pile whose end is closest to the bearing layer, as it is the first to yield the maximum resistance to applied loads. While the other piles still need to displace in order to reach equilibrium, this movement results in an increase in load on the outermost pile in the form of negative skin friction (with reference to figs. 5.4, 5.9, 5.19, 5.24, 5.27 and 5.32). In fig. 5.39 a comparison of axial force within the pile is reported. As it could be seen an increase in the axial force is almost 115% comparing cases of end-bearing piles and 30 degrees inclination. Another aspect is that axial force for the case of 10° degrees inclination does not follow the general pattern as the cases of 15°, 20°, 25° and 30° degrees do. This is justified by the fact that lateral pile is still within the bedrock, therefore stressed more, and indeed it could be seen that in its top part it follows the general trend, whereas at the bottom reaches a significant increase in axial force due to its end condition.
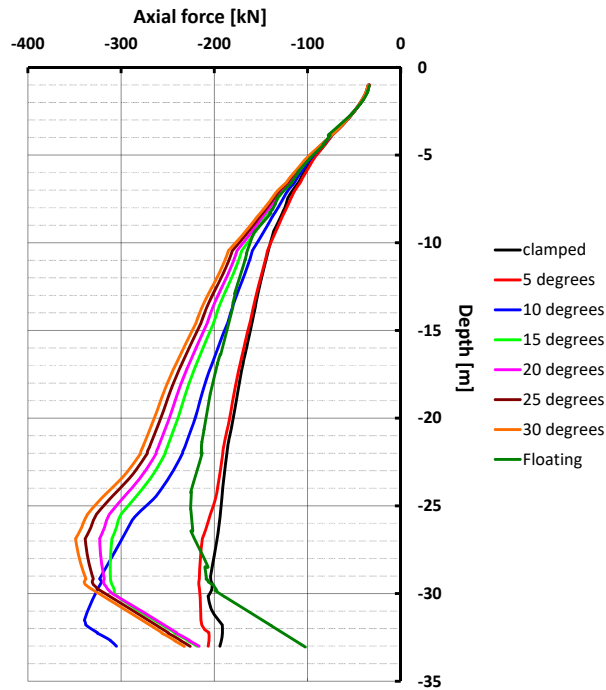
Figure 5.39: Comparison of the axial force developed in the pile placed at left toe of the embankment

The maximum axial force developed in the piles for three different piles throughout the cross-section of embankment is reported in the fig. 5.40. As it could be seen with increasing inclination the pile closest to the bedrock (left toe pile) experiences an increase in axial force. Whereas the pile close to the centreline experiences a decrease in axial force and tends to the same asymptote as the right toe pile does, their final value will be one developed in floating piles case.
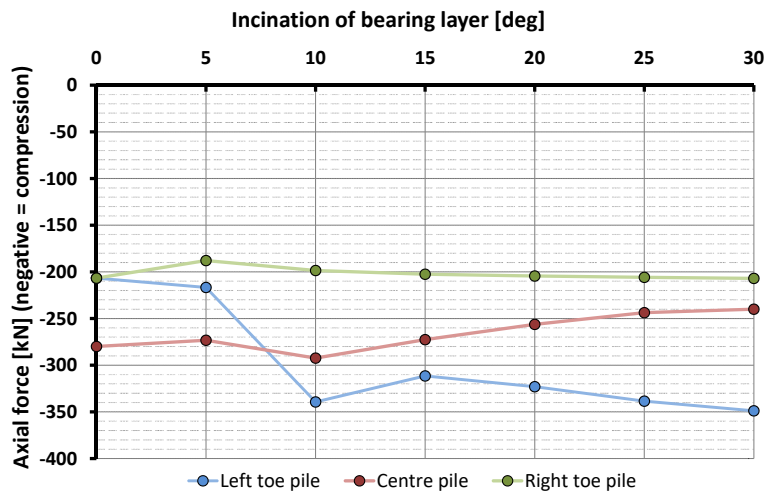
Figure 5.40: Comparison of the axial force developed in the piles within the embankment's cross-section

The lateral displacement of the pile head is reported in fig. 5.41. It is seen that with increasing inclination the lateral pile head displacement decreases for the piles at the toes due to less lateral load which is transferred to them, whereas pile at the centre experiences an increase in lateral displacement.
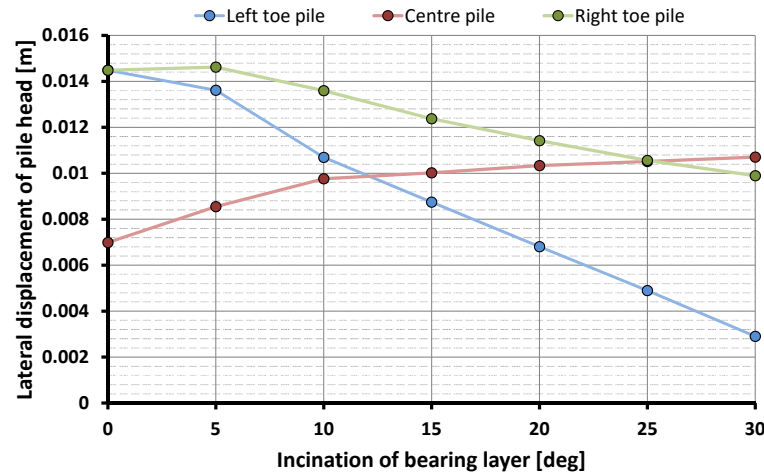
Figure 5.41: Pile head lateral displacement with respect to the bearing layer inclination

Finally, as the angle of inclination of the bearing layer (bedrock) increases, there is almost a rigid translation of the system rather than rotation, as originally envisaged (with reference to figs. 5.4, 5.9, 5.19, 5.24, 5.27 and 5.32).

5.3.1. Design recommendations

Given described behaviour of the system under varying inclination of a bearing layer it is thus now possible to provide a solution for an efficient design within such conditions.

1. The first solution is to drive all piles into the bedrock. Thus it will provide a sufficient resistance and stiffness to the system, however, given an uncertainty on the inclination of the bearing layer the length of piles can result in high values and, consequently, the solution may become extremely expensive.

2. A second possible option is to add inclined, with respect to the vertical plane, piles. This will result in increase of resistance to the lateral displacement, however, the construction of inclined piles is quite complicated.

3. A third solution is to implement piles or group of piles of different length (increasing length in known direction of the sloping bedrock). This solution will result in a more uniform distribution of the forces between piles, without unnecessary overloading

of certain piles. Additionally the cost of solution will not change significantly with respect to the proposed one as the average length of piles could be kept the same.

Moreover, what concerns the aspect of geological investigation, an additional boreholes or more deep CPT tests could be suggested. This will allow a reduction of an uncertainty on the geological profile.

5.3.2. Implementation of the solution

In this section an implementation of the design solution is reported. That it is assumed a stepwise length of the piles and in total 3 group of piles of 4 piles in total as shown in fig. 5.42. As there is still uncertainty on the bedrock inclination it is assumed the case of 15 degrees inclination as intermediate average case. For this case the model view is represented in fig. 5.43.
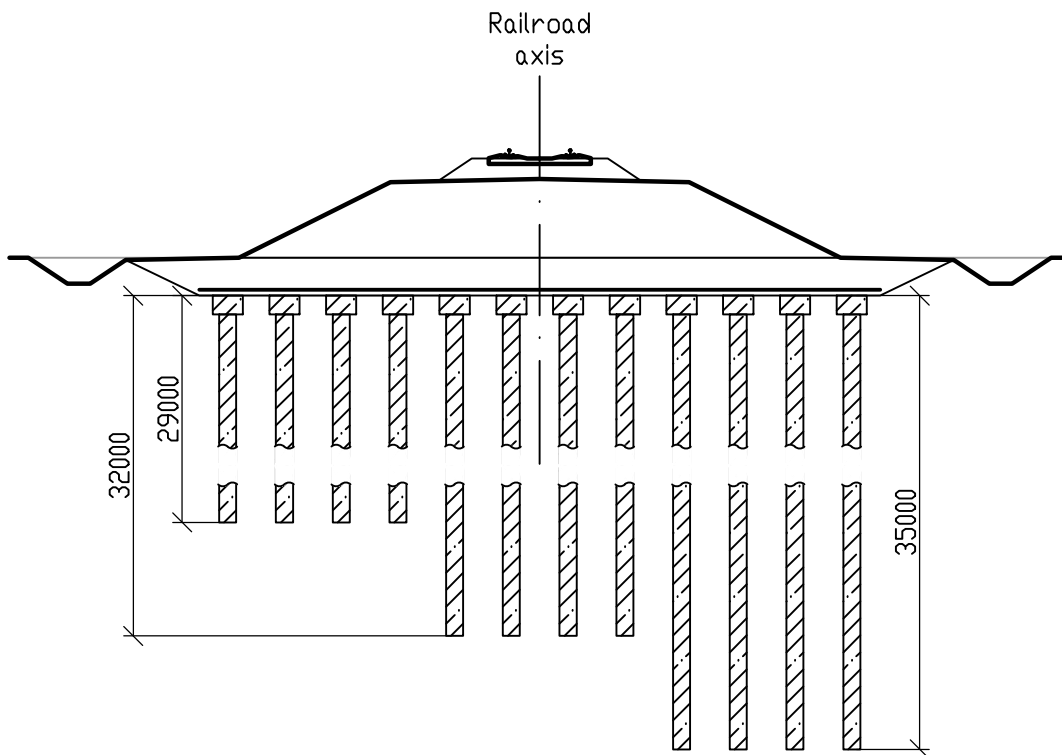
Figure 5.42: Cross-section of the implemented solution

Figure 5.43: Model view for the case of 15° bearing layer inclination with stepwise pile groups

Displacement developed within the embankment body are reported in fig. 5.44. As it could be seen the values at two embankment shoulders are approximately the same. Relative rotation of the embankment top platform in this case is equal to 0.02° which is negligible and the maximum settlement along the centreline in this case is equal to 0.046 m.

Figure 5.44: Vertical displacement developed in the embankment in case of 15° bearing layer inclination with stepwise pile groups
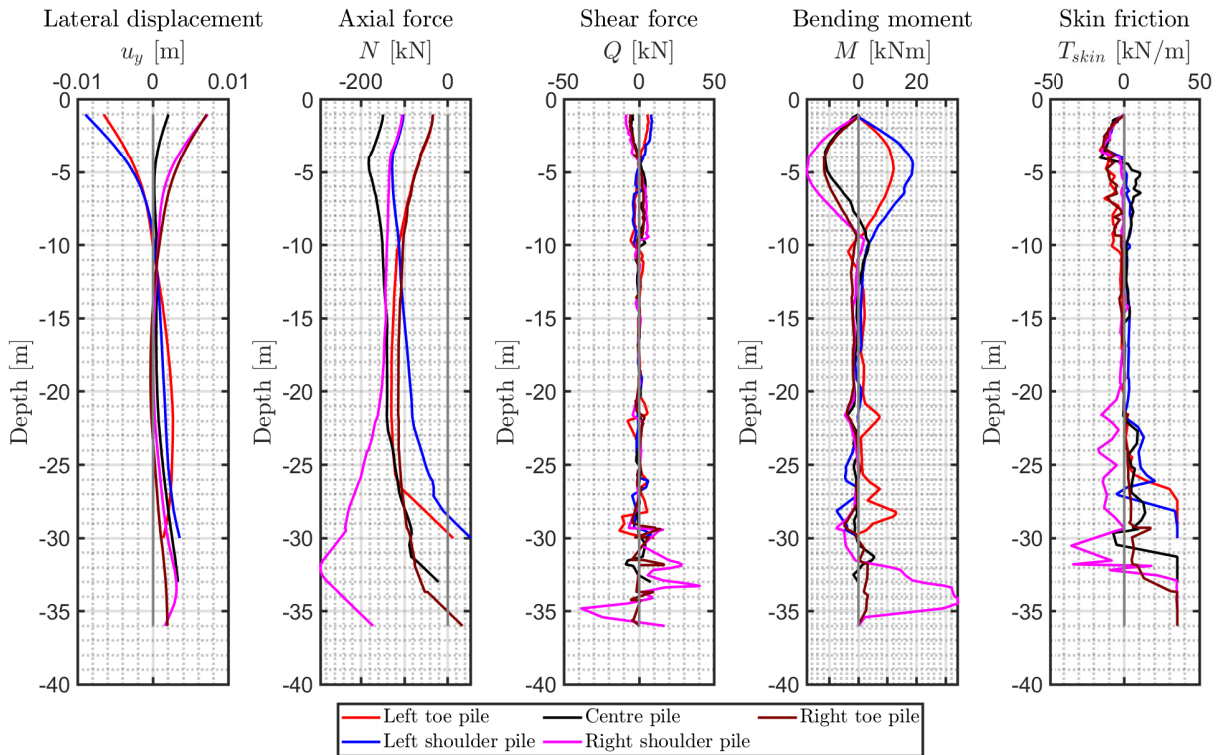
Figure 5.45: Pile behaviour in case of 15° bearing layer inclination with stepwise pile groups

In fig. 5.45 the pile behaviour along a cross section is reported. The behaviour of a system became more complex due to presence of different groups, as each group tends to behave in its own way. In general, between 2 piles, which change the length, an increase of axial force is observed within longer pile.

In terms of the forces within geogrid, represented in fig. 5.46, the response is similar to the previous cases. While in terms of the geogrid displacement, represented in fig. 5.47, an asymmetry is observed, in particular a little rotation of the system towards the side where piles are allowed to displace more.

Figure 5.46: Forces developed within the geogrid in case of 15° bearing layer inclination with stepwise pile groups
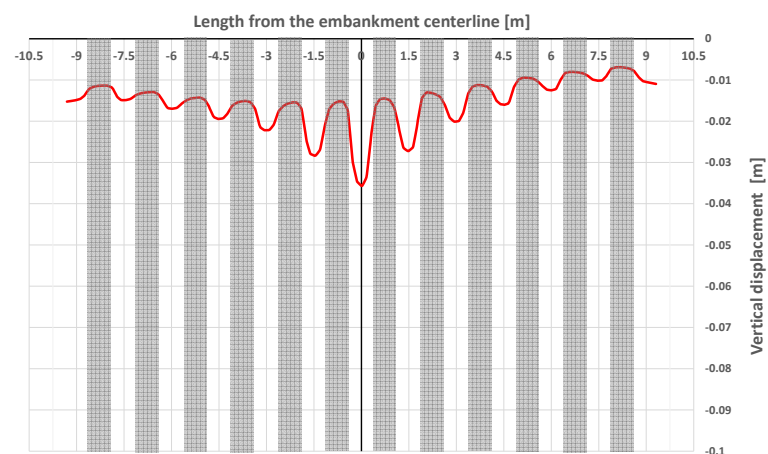
Figure 5.47: Vertical displacement of the geogrid in case of 15° bearing layer inclination with stepwise pile groups

As for this case the inclination of the bedrock is different from inclination of the pile groups - the pile at right shoulder arrives close to the bedrock and it could be seen a behaviour similar to the one observed before. In general, rotation of system is observed (see lateral displacement in fig. 5.45), however, disregarding the right shoulder pile, the distribution of forces throughout the piles became more uniform. Consequently, the maximum settlement of the embankment decreased below the limiting value of 0.050 m. To further decrease the settlement a use of a stiffer geogrid or multiple geogrid layers is suggested. However, this study was not conducted in the present work.

6 | Conclusions and recommendations

6.1. Conclusions

The aim of this work is to numerically investigate a behaviour of base reinforced piled embankment in the case of inclined bearing layer.

First of all, based on the provided in-situ and laboratory investigations a geotechnical model of the area of construction was built up. The stratigraphic profile revealed a presence of mine tailings of the thickness up to 30 meters depth overlaying the natural clay deposit with the bedrock at the bottom of a system. The analysis of the data showed some deficiency of information, in particular:

1. Unreliable results of oedometer tests as the most of samples appeared to be under-consolidated which could be considered true for remoulded tailing material, but is totally untrue for more older clay deposits.

2. Provided in-situ tests data was not in a good correlation with each other. The tests reveal different parameters at the same spatial position.

3. Insufficient depth of the boreholes. Hence an insufficient information on the strata that could be considered competent to be a bearing layer. This results in an uncertainty on the whole design as the presence of bearing layer is not confirmed in some parts of the construction area.

Secondly, a numerical model was set up according to the outcomes of the geotechnical model and an investigation plan was proposed. To represent the mechanical behaviour of the soils a Hardening soil model was chosen and its parameters were calibrated.

Then a numerical investigation was performed to analyse the response of a system. Investigation included the following cases: end-bearing (horizontal bedrock) and floating (absence of bedrock) piles which were considered as a limiting base cases and then cases for $5 - 30°$ of bedrock inclination with a step of $5°$. Considering the first two cases a hypothesis on the system's behaviour under the case of inclined bedrock was made.

In the following a system's behaviour was analysed under the cases of inclined bedrock. The following main aspects were observed:

1. Under increasing inclination, given the fact that initially piles are clamped in the horizontal bedrock, piles passed from the end-bearing to floating conditions with a characteristic change of behaviour observed in the base cases.

2. Under applied load a pile, closest to the bedrock, experiences a significant increase in axial force due to developed negative skin friction, which is developing due to higher potential of other piles to displace.

3. With increasing bedrock inclination a larger settlement is observed, however the rotation of an embankment's platform does not develop - a translation of the system is observed.

Provided the characterization of a system's behaviour the design recommendations are proposed to improve the design under given uncertainty conditions.

6.2.   Recommendations

The investigation was performed for a given specific conditions of the area, they are as following:

- Drained conditions were considered, as according to the investigation reports no constant water table was found, despite the high water content.

- Seismic action was not considered, however the area is characterised by the seismic action.

- Below the investigated depth was assumed a strata that was found the latest in borehole log.

Therefore a suggestions for the further investigation could be derived. First of all, a seismic action may be introduced as, even with the absence of constant water table, given the high water content of sandy material which is characterised by a low relative density a volumetric collapse may cause full saturation and an increase of pore water pressure may trigger soil liquefaction under seismic action.

Secondly, a parametric study could be performed varying properties of geogrid (such as stiffness or number of layers) and rigid inclusions (such as spacing or diameter).

Bibliography

Bentley. *PLAXIS 3D - Material Models Manual CONNECT Edition V22.00.* 2021a.

Bentley. *PLAXIS 3D - Reference manual CONNECT Edition V22.00.* 2021b.

M. D. Bolton. The strength and dilatancy of sands. *Geotechnique,* 36:65–78, 6 1986. ISSN 17517656. doi: 10.1680/geot.1986.36.1.65.

M. Bustamante and L. Gianeselli. Pile bearing capacity prediction by means of static penetrometer cpt. *Proc. of the Second European Symposium of Penetration Testing, Amsterdam,* pages p493–500, 1982.

B. Carlsson. Reinforced soil, principles for calculation. *Terratema AB,* 1987.

J. G. Collin. Column supported embankment design considerations. 2004.

G. R. Eiksund, G. Svanø, and A. Watn. Alternative calculation principle for design of piled embankments with base reinforcement. 2000. URL https://www.researchgate.net/publication/327652189.

W. J. Helwett and M. F. Randolph. Analysis of piled embankments. *Ground Engineering,* Vol 21:12–18, 1988.

N. Janbu. Soil compressibility as determined by oedometer and triaxial tests. *Proc. Europ. Conf.,* Vol. I, 1963.

R. Lancellotta. Analisi di affidabilita in ingegneria geotecnica. *Atti dell'Istituto di Scienza delle Costruzioni,* 1983.

T. Lunne, P. K. Robertson, and J. J. M. Powell. *Cone Penetration Testing in Geotechnical Practice (1st ed.). CRC Press.* 1997. ISBN 9780429177804. doi: https://doi.org/10.1201/9781482295047.

P. W. Mayne, G. J. Rix, and H. J. Pincus. Gmax-qc relationship for clays. *ASTM Geotechnical Testing Journal,* 16:54–60, 1993.

R. F. Obrzud and A. Truty. *The hardening soil model - a practical guidebook.* 2018.

Y. Ohta and N. Goto. Empirical shear wave velocity equations in terms of characteristic soil indexes. *Earthquake Engineering Structural Dynamics*, 6:167–187, 6 1978. ISSN 00988847. doi: 10.1002/eqe.4290060205.

G. J. Rix and K. H. Stokoe. Correlation of initial tangent modulus and cone penetration resistance. *Proc, 1 st International Symposium on Calibration Chamber Testing/ ISOCCT1*, pages 351–362, 6 1991. URL https://www.researchgate.net/profile/ An-Bin-Huang/publication/235197318_Calibration_Chamber_Testing/links/ 5a839a890f7e9bda86a461bb/Calibration-Chamber-Testing.pdf#page=346.

P. K. Robertson. Soil behaviour type from the cpt: An update. *2nd International Symposium on Cone Penetration Testing*, 2:575–583, 2010.

Y. Rogbeck, S. Gustavsson, I. Södergren, and D. Lindquist. Reinforced piled embankments in sweden - design aspects. *Proceedings of the Sixth international Conference on Geosynthetics*, Vol II:755–762, 1998.

G. Sanglerat. *The Penetrometer and Soil Exploration.* 1st edition, 6 1982. ISBN 9780444599360.

A. W. Skempton. Standard penetration test procedures and the effect in sands of overburden pressure, relative density, particle size, ageing and overconsoidation. *Geotechnique*, Vol.36:425–447, 1986.

M. A. Stroud. The standard penetration test in insensitive clays and soft rocks. *Proceedings of the European Symposium on Penetration Testing*, 2:367–375, 6 1975. URL https://eurekamag.com/research/020/448/020448105.php.

K. Terzaghi. *Theoretical Soil Mechanics.* 1943.

S. J. M. van Eekelen, A. Bezuijen, and A. F. van Tol. An analytical model for arching in piled embankments. *Geotextiles and Geomembranes*, 39:78–102, 6 2013. ISSN 02661144. doi: 10.1016/j.geotexmem.2013.07.005.

S. J. M. van Eekelen, A. Bezuijen, and A. F. van Tol. Validation of analytical models for the design of basal reinforced piled embankments. *Geotextiles and Geomembranes*, 43: 56–81, 6 2015. ISSN 02661144. doi: 10.1016/j.geotexmem.2014.10.002.

P. von Soos. Properties of soil and rock (in german). *Grundbautaschenbuch*, vol. 1, 2001.

D. Zaeske and H. G. Kempfert. Berechnung und wirkungsweise von unbewehrten und bewehrten mineralischen tragschichten auf punkt-und linienförmigen traggliedern. *Bauingenieur Band 77*, 2002.

A | Tools and methods of investigation

A.1. In-situ tests

Borehole drilling

Drilling of engineering geological boreholes was performed using Soilmec "SM-8G" (schematically represented in the Figure A.1) drilling rig according to "Wireline" system. The drilling pipe (rod) with a diameter of 50 mm pushing a drilling bit with an external diameter of 114 mm and a sampler with a diameter of 108 mm were penetrated into the soil by rotation to a desired depth of investigation by 1.5 m steps.
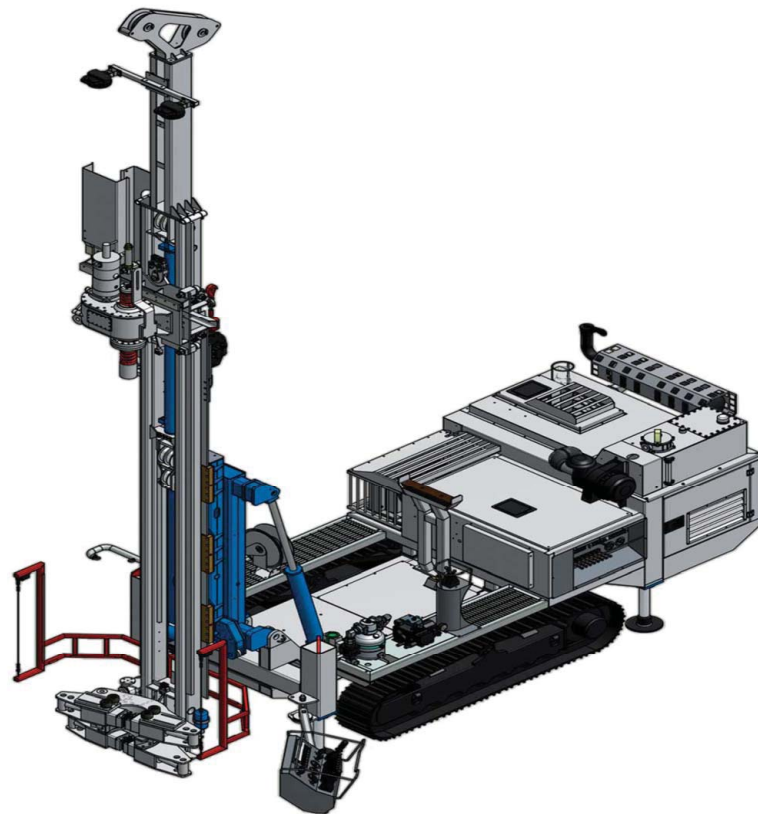
Figure A.1: Soilmec "SM-8G" drilling rig

Sampling

Soil sampling was performed simultaneously with the drilling procedure. After the drilling rig advanced into the soil for 1.5 m the sampler by means of a grip on the cable was lifted by a winch to the ground surface. In order to maintain the natural conditions of taken samples, field geologist immediately wrapped the samples in polyethylene, then aluminium foil and at last isolated from environmental influence by wrapping them in paraffin. Consequently after the test results were obtained disturbance factor was calculated for each sample.

Standard penetration test

The standard penetration tests (SPT) were performed in accordance with ASTM D1586, D3550, D6066 and EN ISO 22476-3 using a split-barrel sampler. The SPT sampler is driven with a 63.5 kg (140 lbs) hammer repeatedly dropped from a height of 760 mm (30 in) to achieve three successive increments of 150 mm (6 in) each. The first increment is recorded as a "seating", while the number of blows to advance second and third increments are summed to provide the N30-value ("blow count") or SPT-resistance (reported in no. blows/0.3 meters or blows per foot). Soil samples acquired with a split-barrel sampler are considered disturbed samples and are used for soil description and soil classification tests only. The SPT refusal criteria was pre set at 50 blows per 150 mm (6 in). Standard penetration test enables to study physical and mechanical properties of soil in-situ condition.

Cone penetration test

Cone penetration testing (CPT) is conducted with squeezing (driving) of special penetrometer to soil mass in in-situ condition in vertical direction by means of hydraulic cylinder. During the penetration the cone tip resistance, sleeve friction and induced pore water pressure are measured.

Prior starting to the penetration operations the calibration of the penetrometer was conducted and the results of calibration are recorded to data vase automatically (program memory). The driving of the penetrometer to the soil is continued along the penetration rod with the velocity of 20 mm/s up to project depth.

A.2.   Laboratory testing

On the basis of the borehole logs and in-situ tests performed, a laboratory testing program was developed to obtain relevant material properties of the soil strata at the project site for engineering purposes. All soil samples recovered from the boreholes were sealed in the sampling tubes and transported to the laboratory. Laboratory testing has been performed

in accordance with the procedures described in ASTM.

Water content

The water content is determined by placing selected moist/wet soil material for at least 18 hours to a 110° C drying oven until a constant mass reached. The difference in mass before and after drying is used as mass of the water in tested material. The mass of material remaining after drying is used as the mass of solid particles. The ratio of the mass of water to the measured mass of solid particles is the water content of the material. This ratio is usually shown in %.
Test reference: ASTM D 2216.

Unit weight

The unit weights are determined from measurements of mass and volume of the soil. For cohesive soils, a specimen is generally obtained from a standard steel cylinder with cutting edge, which is pushed manually into the extruded soil sample. Preference is given to a 100 mm cylinder (area ratio of 12 %). The cylindrical soil sample is trimmed on the end surfaces and the height and diameter are measured.
The unit weight γ (kN/m^3) refers to the unit weight of the soil at the sampled water content. The dry unit weight γ_d is determined from the mass of oven dried soil and initial volume.

Particle size analysis

Particle size analysis can be performed by means of sieving and/or hydrometer readings. Sieving is carried out for particles that would be retained on a 0.075 mm sieve, while additional hydrometer readings may be carried out when a significant fraction of the material passes 0.075 mm sieve.
In a sieve analysis, the mass of the soil retained on each sieve is determined and expressed as a percentage of the total mass of the sample. Prior to sieving, samples are treated with a dispersing agent (sodium hexametaphosphate).
Particle size is presented on a logarithmic scale so that two soils having the same degree of uniformity are represented by curves of the same shape regardless of their position in the particle size distribution plot. The general slope of the distribution curve may be described by the coefficient of uniformity C_u, where $C_u = D_{60}/D_{10}$, and the coefficient of curvature C_c, where $C_c = (D_{30})^2/(D_{10} \cdot D_{60})$. D_{60}, D_{30} and D_{10} are effective particle sizes indicating that 60%, 30% and 10% of particles (by weight) are smaller than the given effective size.
Test reference: ASTM D 422.

Atterberg limits

Atterberg limits are determined on soil specimens with a particle size of less than 0.425 mm. If necessary, coarser material is removed by dry sieving. The Atterberg limits refer to arbitrary defined boundaries between the liquid and plastic states (Liquid limit, LL) and between the plastic and brittle states (Plastic limit, PL) of fine grained soils. They are expressed as water content, in percent. The liquid limit is defined as the water content at which a part of soil is placed in a standard cup will flow together at the base of the groove, when the cup is subjected to 25 standard shocks. The one-point liquid limit test is usually carried out. Distilled water may be added during soil mixing to achieve the required consistency. The plastic limit is defined as the water content at which a soil can no longer be deformed by rolling into 3 mm diameter threads without crumbling.

The range of water contents over which a soil behaves plastically is Plasticity index, PI. This is the difference between the liquid limit and the plastic limit (LL-PL).

Test reference: ASTM D 4318.

Oedometer - incremental loading test

The oedometer test covers determination of the rate and magnitude of consolidation of a laterally constrained soil specimen, which is axially loaded in increments of constant stress until the excess pore water pressures have dissipated for each increment. Normally, each load increment is maintained for 24 hours. The test is generally carried out on undisturbed cohesive specimens using a consolidometer (oedometer) apparatus, which is placed in a thermostatically controlled room (at $10° C$). Selection of mounting method depends on soil characteristics. Soils that show a tendency to swell, such as peat or over consolidated clays are mounted dry. Moist sponges are placed in the oedometer cell to retain sample moisture conditions. Other samples are usually mounted using the wet mounting method. Distilled water is added to the cell when loads are applied to the loading arm. When required the initial load is increased to prevent swell.

Key parameters that can be obtained from this test are pre-consolidation pressure σ'_p and the coefficient of consolidation c_v. The preconsolidation pressure is estimated using the graphical "Casagrande" method. The log-time method is used for determination of c_v.

Other parameters that may be derived from this test are compression index C_c, swelling index C_r, coefficient of volume compressibility m_v and vertical permeability k_v.

Test reference: ASTM D 2435.

Unconsolidated undrained triaxial test (TX-UU)

This type of test is usually performed on undisturbed samples of cohesive soils. Depending on the consistency of the cohesive material, the test specimen is prepared by trimming the sample or by pushing a mould into the sample. A latex membrane with thickness of approximately 0.3 mm is paced around the specimen. A lateral confining pressure

is maintained constant during axial compression of the specimen. Consolidation and drainage of pore water during the testing is not allowed. Application of the axial load to produce axial strain at a rate of approximately 1 %/min for plastic materials and 0.3 %/min for brittle materials that achieve maximum deviator stress at approximately 3 to 6 % strain. At these rates, the elapsed time to reach maximum deviator stress will be approximately 15 to 20 minutes. Continue the loading to 15 % axial strain, except loading may be stopped when the deviator stress has peaked the dropped 20 % or the axial strain has reached 5 % beyond the strain at which the peak is deviator stress occurred. The deviator stress is calculated from the measured load assuming that the specimen deforms as a rigid cylinder.

The presentation of test results includes a plot of deviator stress versus axial strain. The undrained strength (s_u) is taken as half of the maximum deviator stress.

Test reference: ASTM D 2850.

Consolidated undrained triaxial test (TX-CIU)

A cylinder of saturated soil is subjected to isotropic consolidation and then sheared in compression under constant confining pressure. The test is carried out in three stages: saturation, consolidation and shearing. The first two stages saturate the specimen and bring it to the desired state of effective stress for the compression test.

Drainage may take place at one or both ends of the specimen during consolidation. For soils of low permeability, it is often advantageous to fit filter paper drains to the specimen. This allows drainage to take place simultaneously from the radial boundary and from the ends.

By carrying out tests on a set (usually three) of similar specimens under different effective consolidation pressures the effective strength parameters c' and φ' can be derived. The specimens are usually consolidated over a range of effective stresses related to the vertical effective stress (σ'_v) of the sample in-situ. For a set of three specimens, effective consolidation pressures of $\sigma'_v/2$, σ'_v and $2 \cdot \sigma'_v$ are often suitable. Drainage during the shearing phase is not allowed.

Test reference: ASTM D 4767.

Point load strength index test of rock (PL)

The axial test is conducted on rock core sample of small length. Minimum of 10 test specimens required to find the average value of point load strength index. Test procedure includes the following:

- This test can be conducted on the core specimens which are completely dry or after soaking it for 7 days;

- Measure the total length (l) and diameter (d) of the core samples. Specimen of l/d in between 0.3 to 1.0 are considered to be suitable for this test;

- Place the specimen vertically in between two platens;

- Measure the distance between two platen contact points (D) with the help of the scale attached to the loading frame. Measure the specimen width (W) which is equal to the diameter of the core specimen;

- Apply the load to the sample such that failure occur within 10-60 seconds, record the failure load P.

Then the following calculations are performed: Uncorrected point load strength index $I_s = (P \cdot 1000)/D_e^2$ MPa. Where D_e - equivalent core diameter ($D_e^2 = 4 \cdot A/\pi$). And A is calculated as $A = W \cdot D$.

Corrected point load strength index for the standard core size of 50 mm(I_{s50}) diameter is given by the following equation: $I_{s50} = (P \cdot 1000)/(D_e \cdot \sqrt[1.5]{50}$ MPa.

Uniaxial compressive strength of rock may be predicted from the following equation: $q_c = 22 \cdot I_{s50}$ MPa.

The corrected mean value of the point load strength index I_{s50} is reported in MPa.

Test reference: ASTM D 573.

Uniaxial compression test (UCS)

The axial compression of the sample is performed under the action of a vertical load without taking into account the lateral expansion. In this test the ultimate (breaking) resistance to maximum admissible compression is the maximum load per unit area or 15 % of the axial deformation load applied to this area. These tests are performed with cylindrical monoliths with a diameter of 70 to 100 mm.

Test reference: ASTM D 2938.

B | Interpretation and calibration

In this appendix the information on the correlations used for interpretation of in-situ test results is reported.

B.1. Correlations used for test results interpretation

Grain size distribution curves

The following figures summarizes the results of sieve analyses. As can be depicted from the fig. B.1 fine content along depth is always higher than 60 %. First 10.5 meters contain 69 % of fine particles with increase up to 80 % in the following. fig. B.2 and fig. B.3 represent the grain size distribution along depth and curves of sieve and hydrometer analysis.
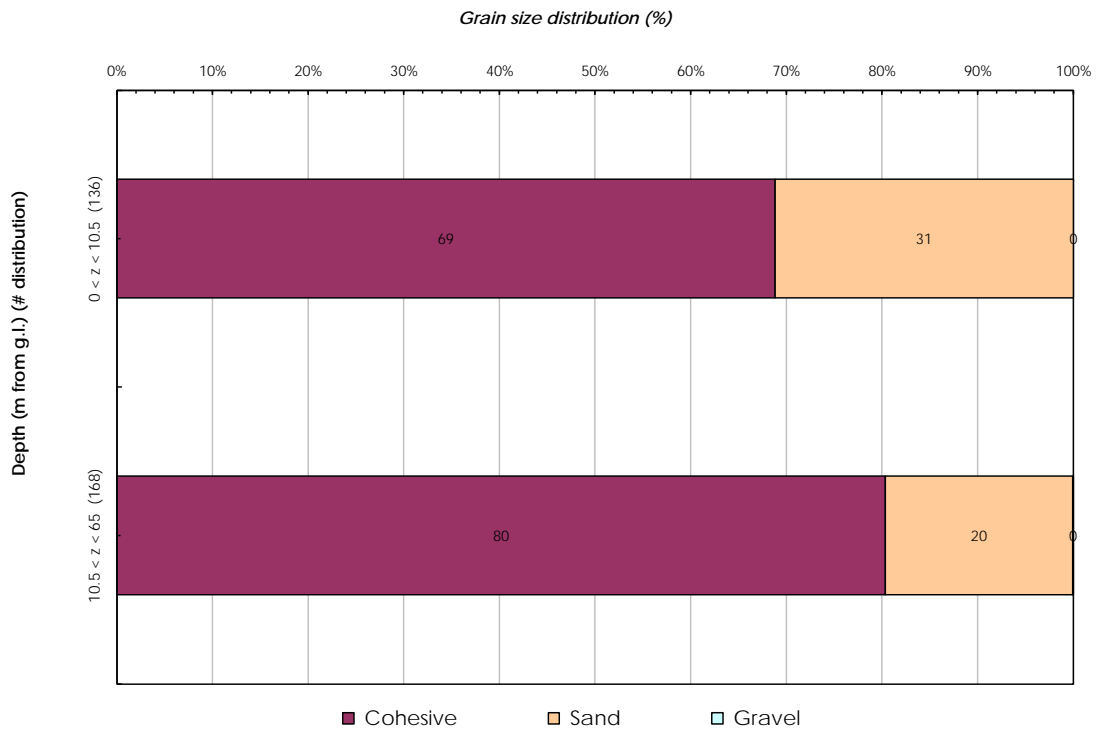
Figure B.1: Percentages
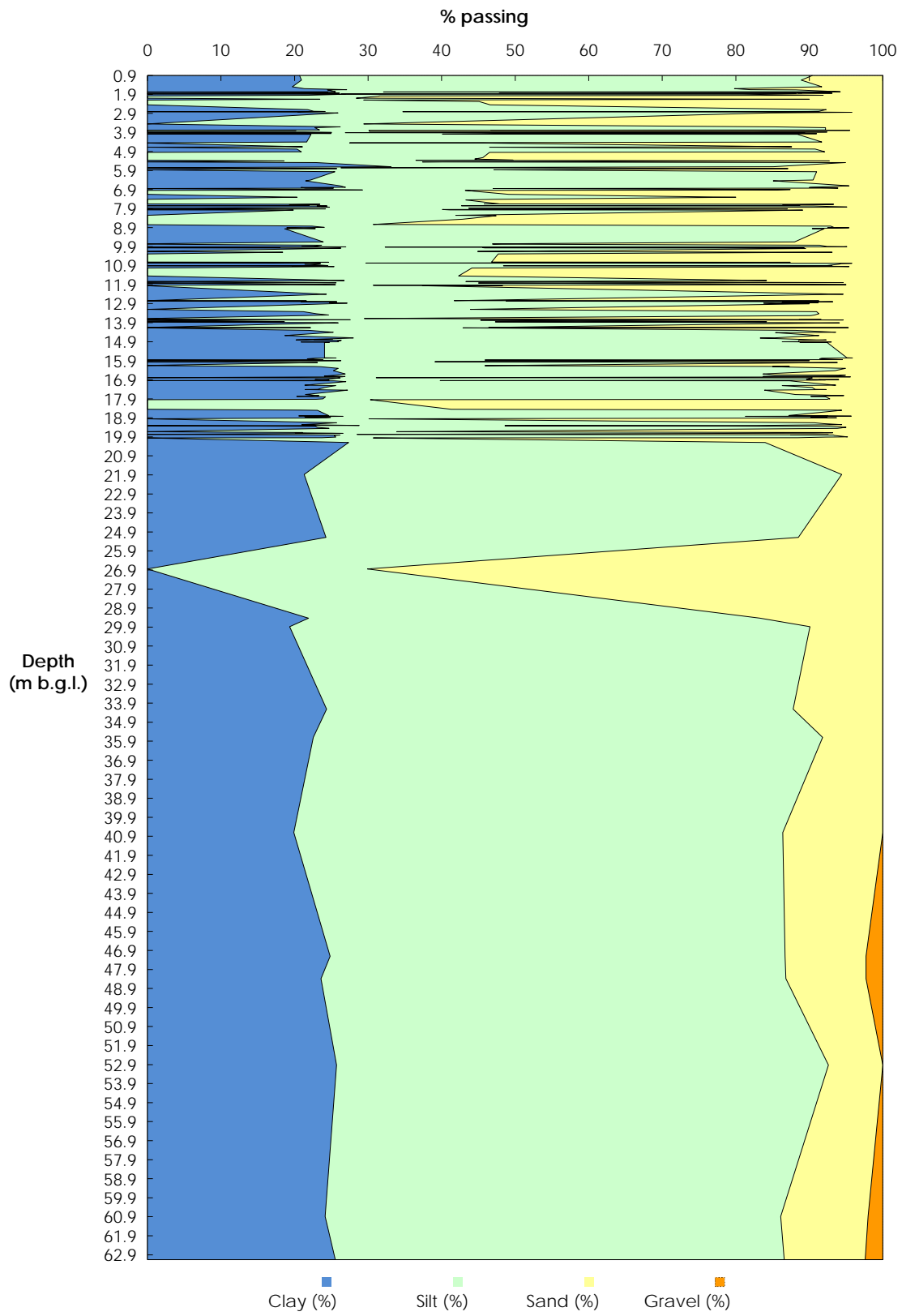
Figure B.2: Particle distribution with depth
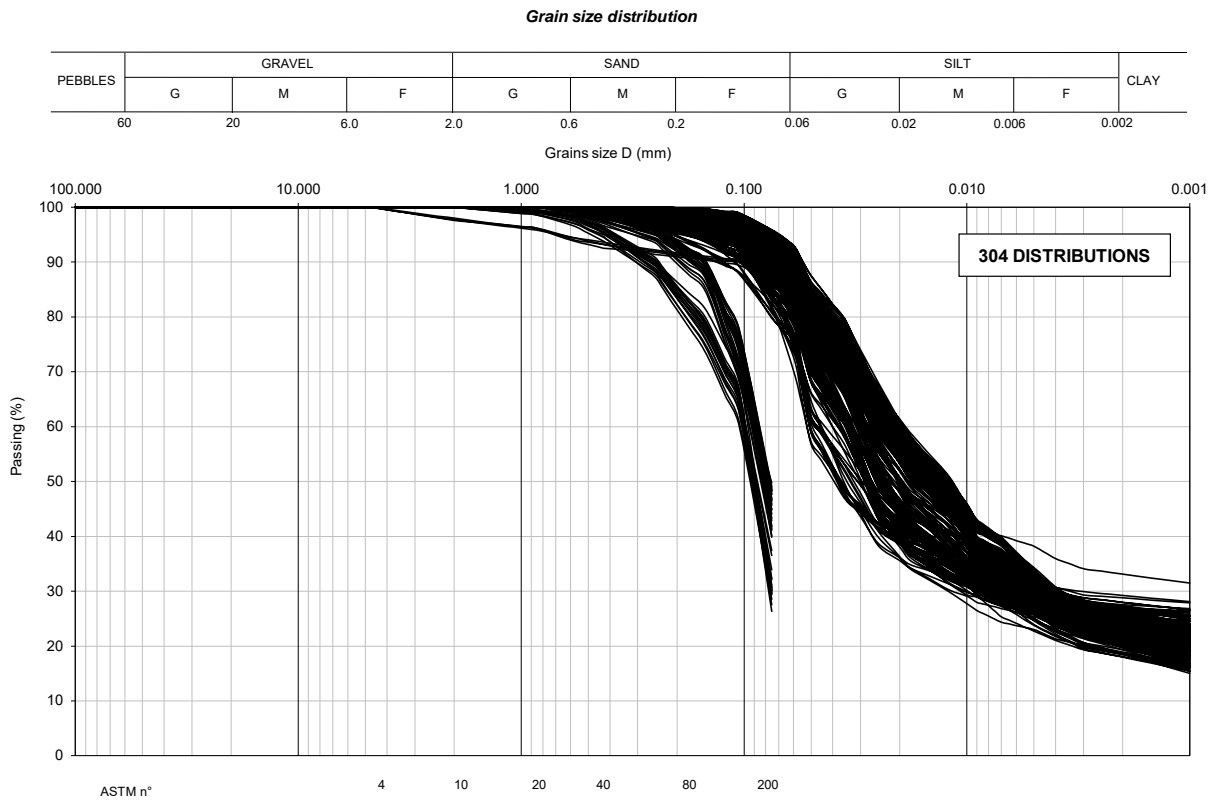
Figure B.3: Grain size distribution curves

CPTU test

CPTU tests hae been interpreted according to widely known technical literature, in terms of following parameters (fig. B.4, fig. B.9):

- q_c = cone tip resistance;

- f_s = sleeve friction.

The measured induced pore water pressure u_w is assumed to be unreliable as in absence of constant water table the measurements are likely to be corrupted.

<u>Soil classification</u>

Soil classification has been carried out, further than analysis of grain size distribution according to ASTM D422 standard, by interpretation of CPTU tests, through the approach proposed by (Robertson, 2010), which takes into account (fig. B.5, fig. B.10):

- Normalized cone resistance, Q_t, defined as $Q_t = (q_t - \sigma_{v0})/\sigma'_{v0}$;

- Friction ratio, FR, defined as $FR = f_s/q_t$.

being $q_t = q_c + (1-a) \cdot u_2$ = corrected cone resistance. q_c = cone resistance;

a = net area ratio; u_2 = pore pressure measured just behind the cone.

Undrained shear strength for fine grained materials

The undrained shear strength of cohesive formations has been determined according to CPTU interpretation using the bearing capacity approach according to (Lunne et al., 1997) (fig. B.6, fig. B.11):

$$s_u = \frac{q_t - \sigma_{v0}}{N_k} \tag{B.1}$$

As discussed in details by various authors, because of the anisotropy of the undrained shear strength, the value of N_k depends largely on the type of the problems that is dealt with. For foundation design, it is considered that the average undrained shear coming from direct sample shear ($s_{u,DSS}$) should be used, and consequently a cone factor $N_k = 14$ has been selected.

Small strain shear modulus

For a coarse-grained material small strain shear modulus has been determined according to the method proposed by (Rix and Stokoe, 1991), as:

$$G_0 = 1634 \cdot (q_c)^{0.250} \cdot (\sigma'_V)^{0.375} \tag{B.2}$$

For fine-grained material small strain shear modulus has been determined according to the method proposed by (Mayne et al., 1993):

$$G_0 = 99.5 \cdot (P_a)^{0.305} \cdot \frac{(q_t)^{0.695}}{(e_0)^{1.13}} \tag{B.3}$$

being

p_a = atmospheric reference pressure;

e_0 = initial void ratio (deduced from laboratory tests).

Results are represented in the fig. B.8 and fig. B.13.

Constrained modulus

For fine-grained material constrained modulus M is determined from the relationship proposed by (Sanglerat, 1982):

$$M = \alpha \cdot (q_t - \sigma_{v0}) \tag{B.4}$$

Where

$$\alpha = \begin{cases} 5 - 15 \ for \ OC \ clays \\ 4 - 8 \ for \ NC \ clays \end{cases}$$

For coarse-grained material constrained modulus M is determined from the relationship:

$$M_0 = \begin{cases} 4 \cdot q_c & q_c < 10 \ MPa \\ 2 \cdot q_c + 20 & q_c = 10 - 50 \ MPa \\ 120 & q_c > 50 \ MPa \end{cases} \tag{B.5}$$

Operative Young's modulus

The operative Young's modulus is determined from the relationship (**??**, fig. B.12):

$$E_{op} = \frac{)1 + \nu) \cdot (1 - 2 \cdot \nu)}{(1 - \nu)} \cdot M \tag{B.6}$$

Relative density

The relative density was estimated only for coarse-grained materials by the following relationship proposed by (Lancellotta, 1983):

$$D_r = 68 \cdot log \left[\frac{q_c}{(p_a \cdot \sigma'_{v0})^{0.5}} - 1 \right] \tag{B.7}$$

Peak friction angle

The peak friction angle was estimated on the base of the following relationship proposed by (Bolton, 1986):

$$\varphi' = \varphi'_{cv} + m \cdot [D_r \cdot (Q - ln(p')) - R] \tag{B.8}$$

Where

$Q = 10$;

$R = 1$;

$m = 3$ - for axi-symmetric conditions;

$p' = 381$ kPa.
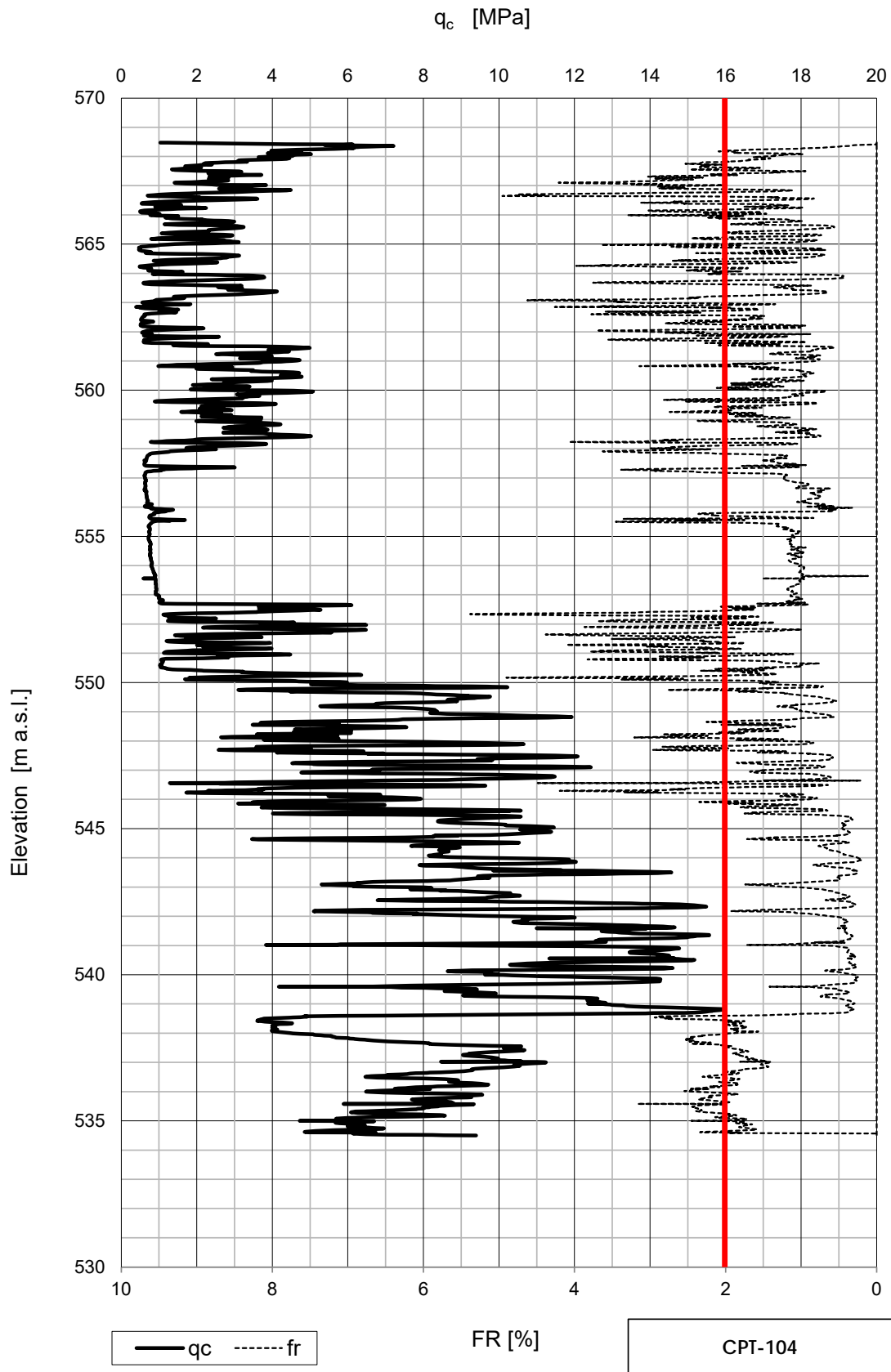
Figure B.4: Cone tip resistance and friction ratio (CPT-104)
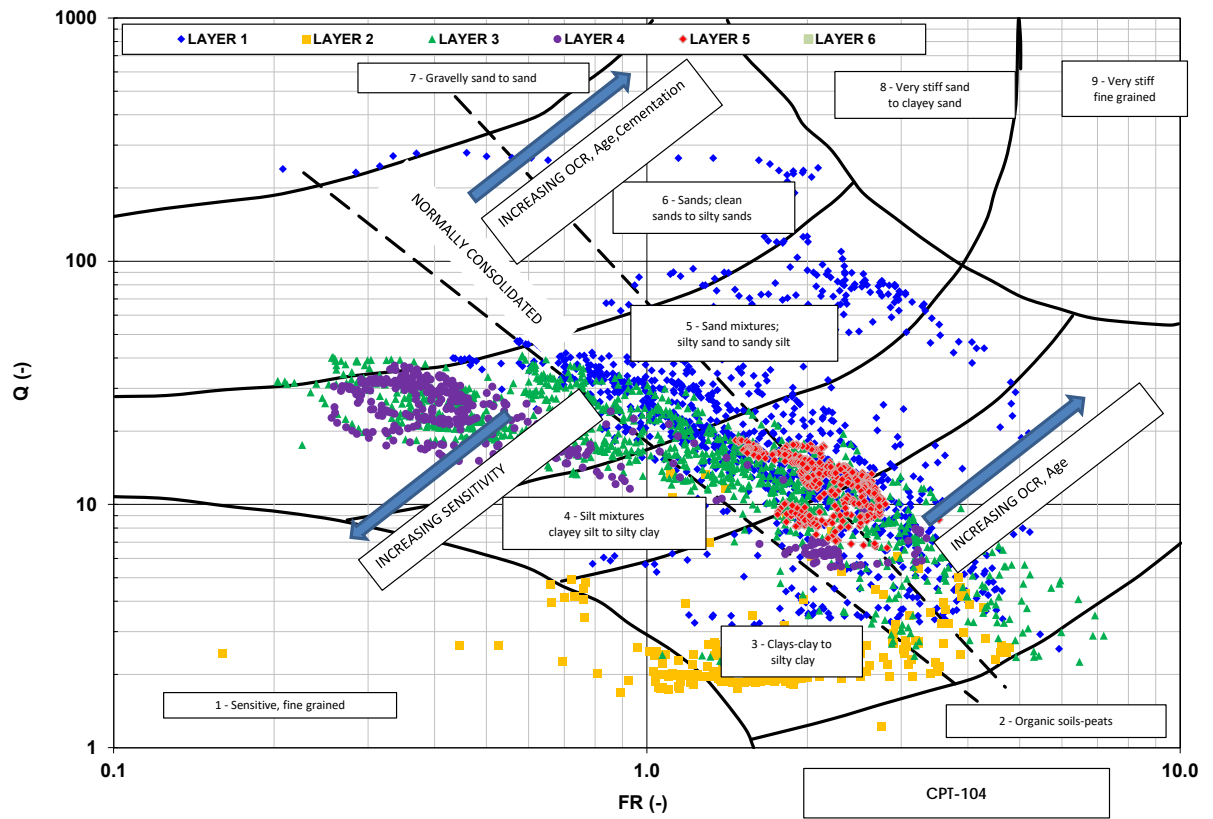
Figure B.5: Soil type classification (CPT-104)
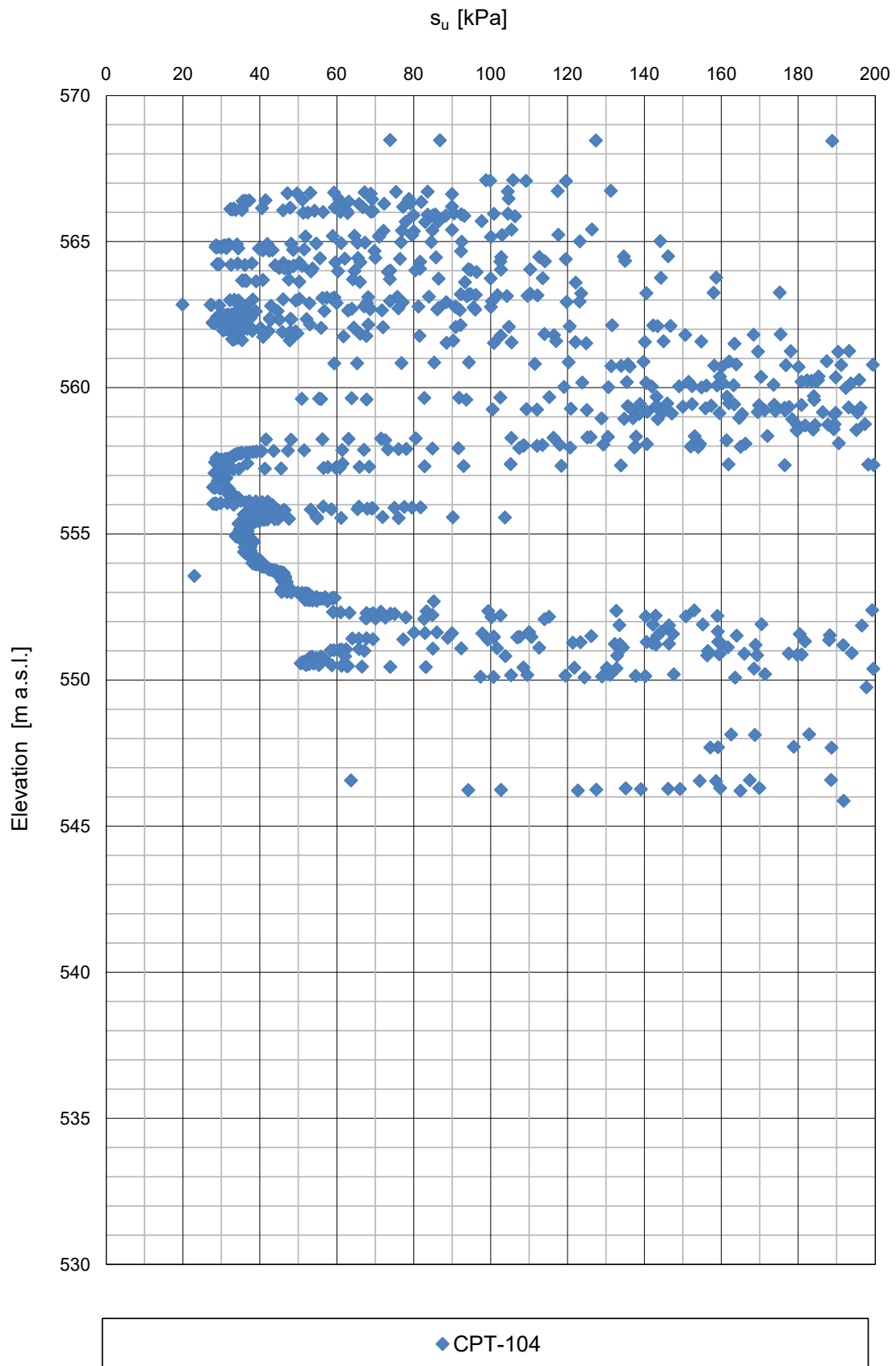
Figure B.6: Undrained shear strength (CPT-104)
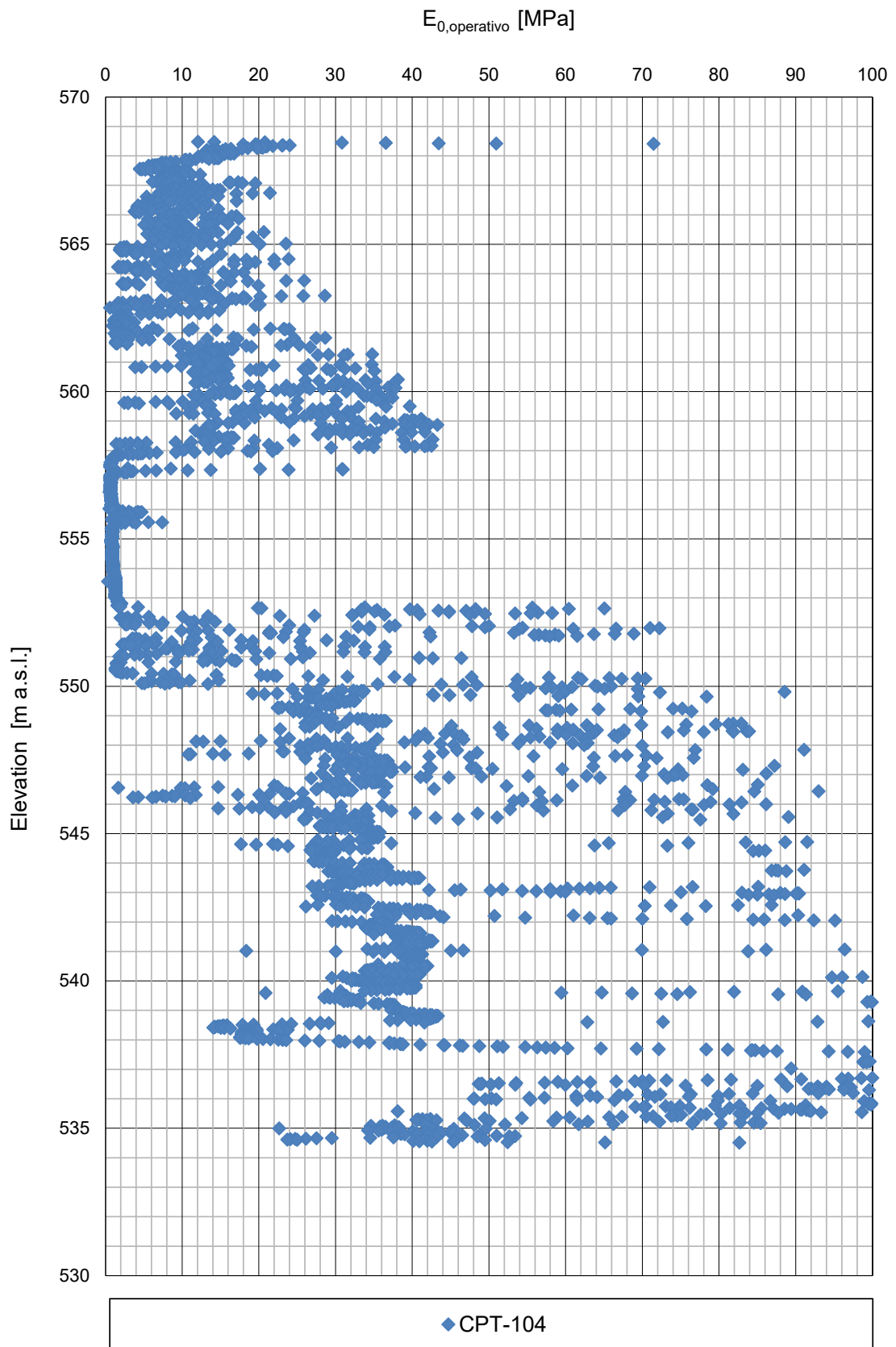
Figure B.7: Operational Young's modulus (CPT-104)
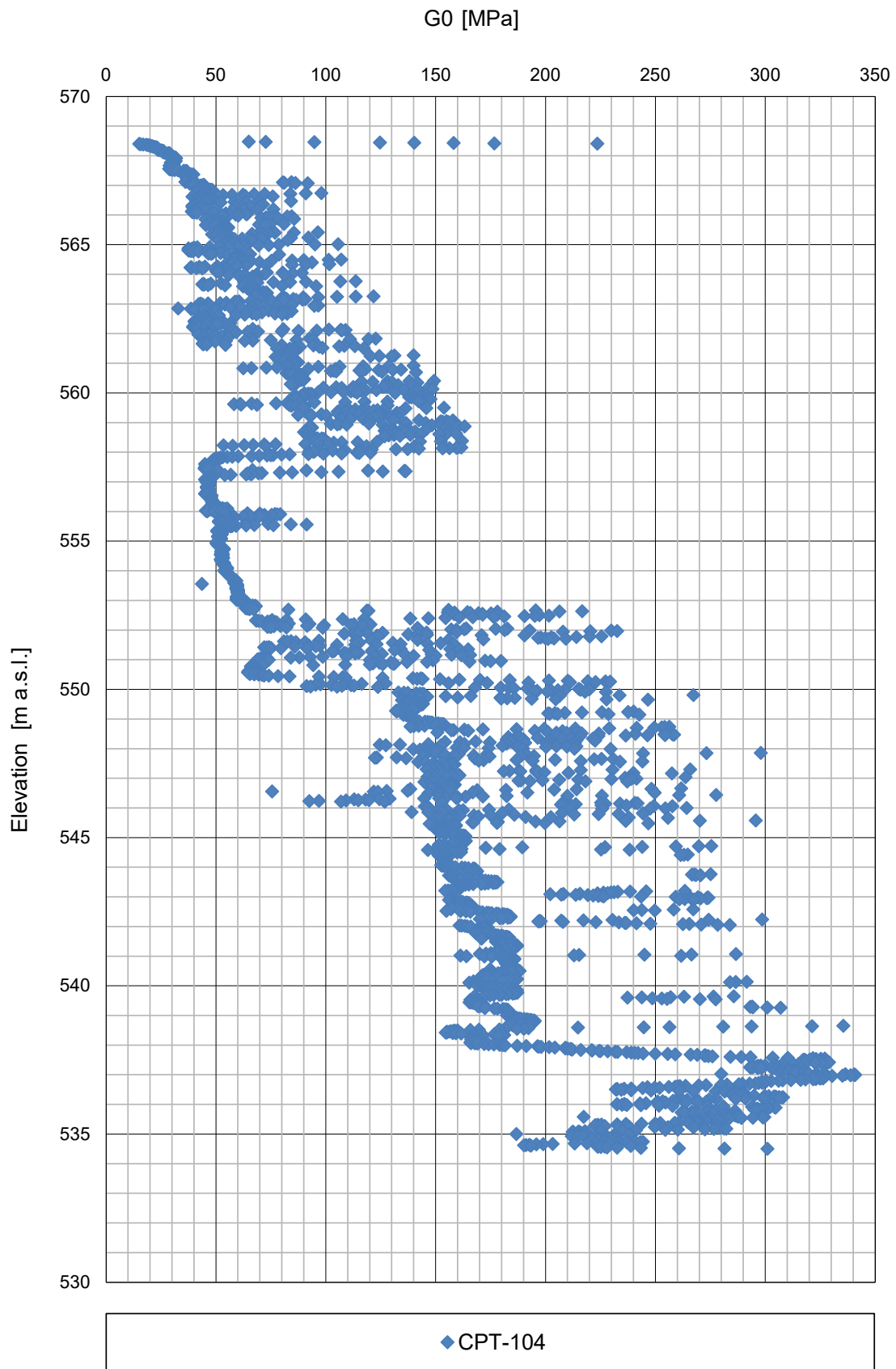
Figure B.8: Small strain shear modulus (CPT-104)
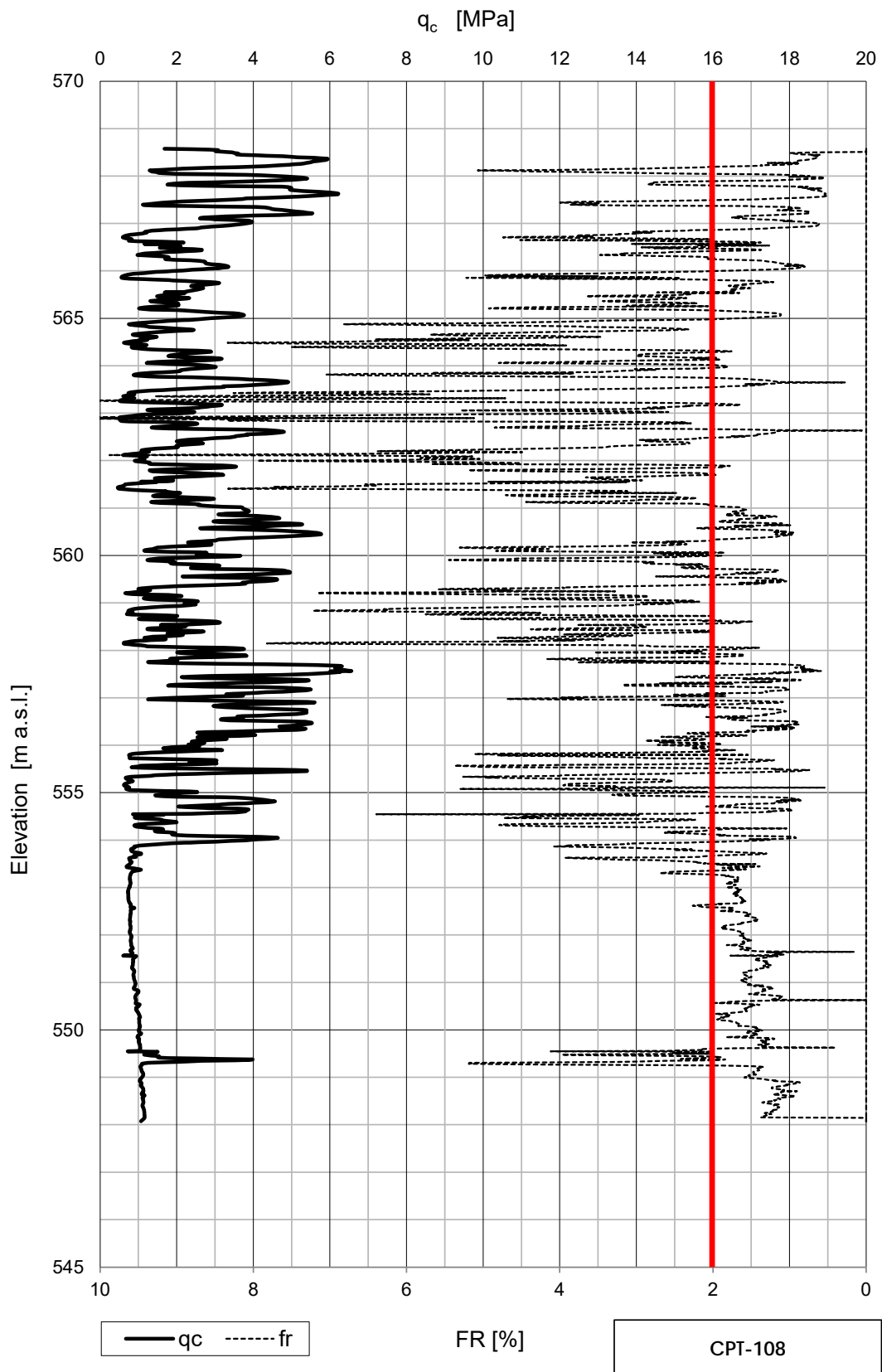
Figure B.9: Cone tip resistance and friction ratio (CPT-108)
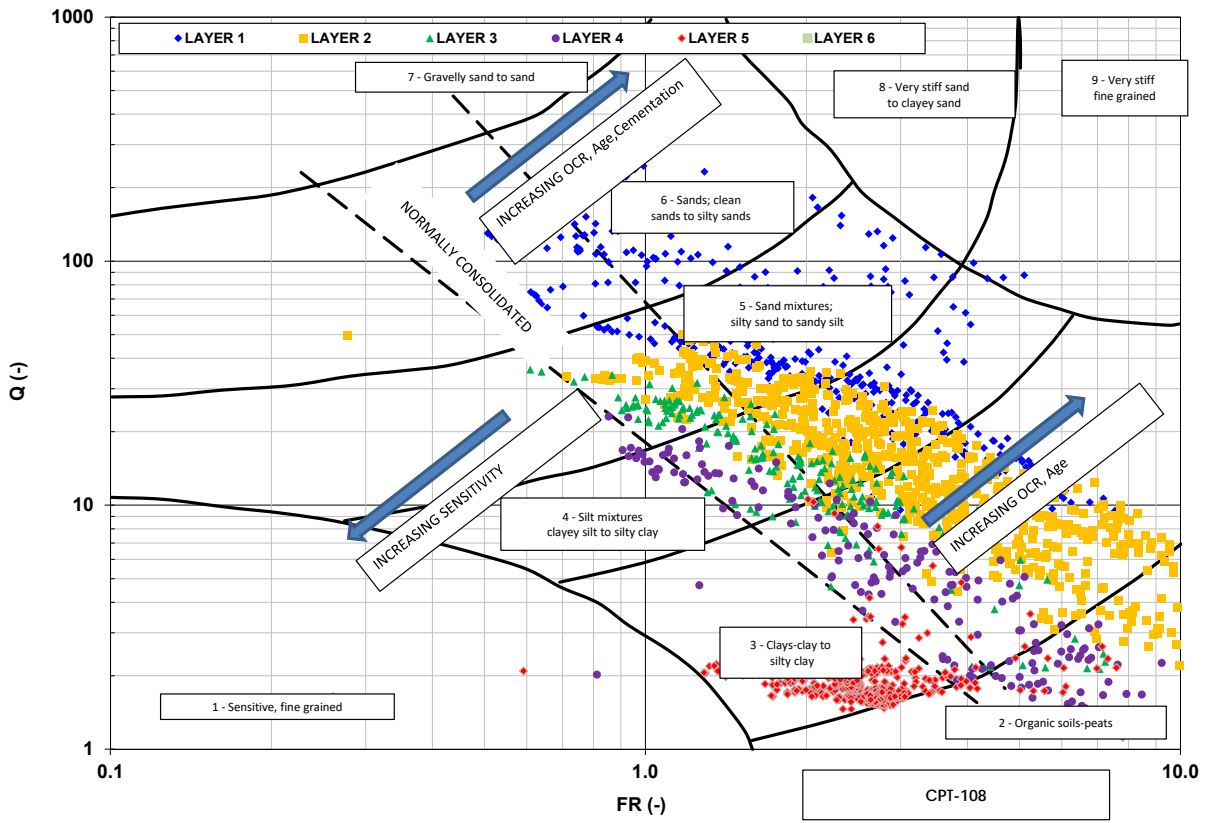
Figure B.10: Soil type classification (CPT-108)
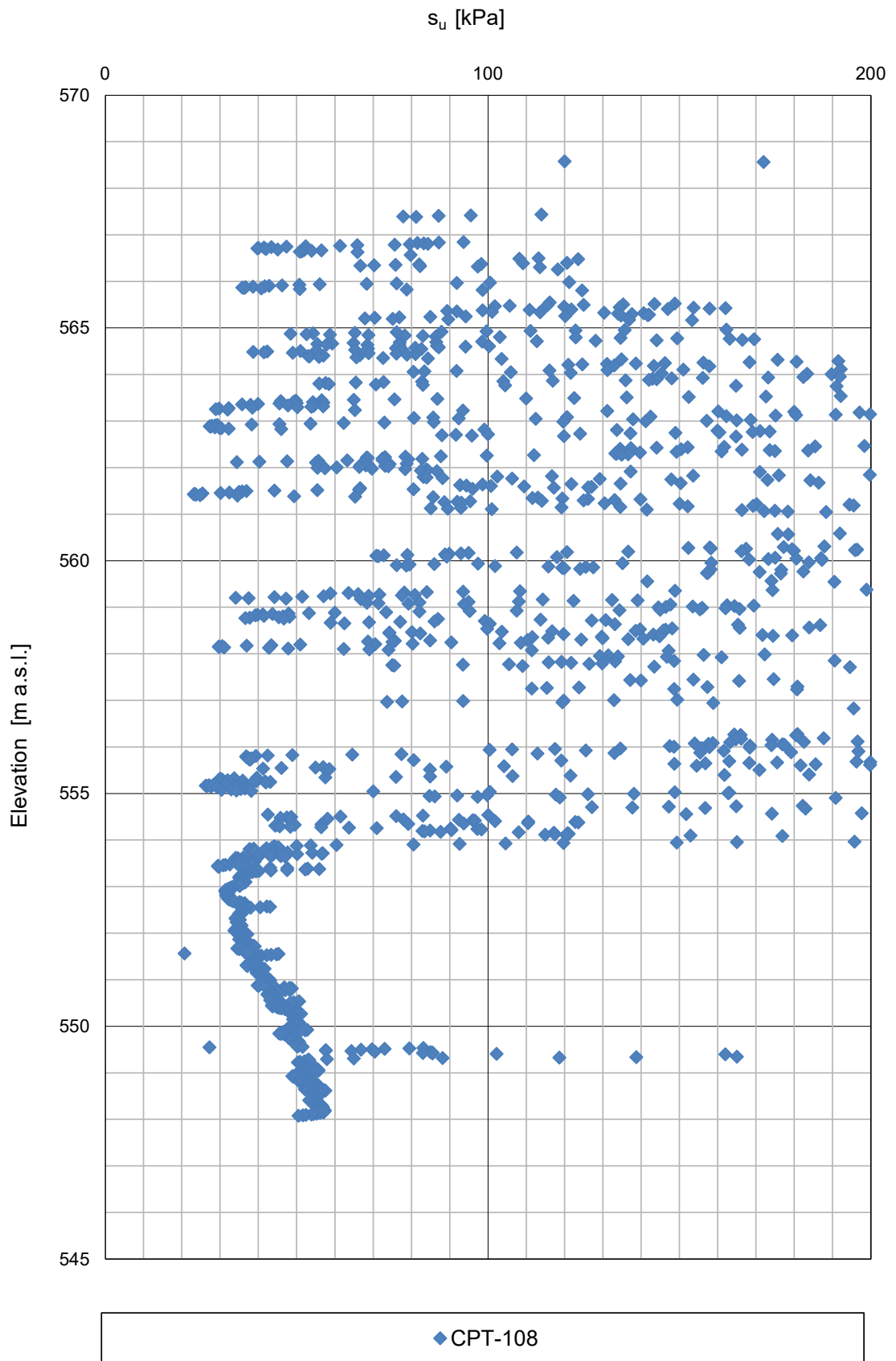
Figure B.11: Undrained shear strength (CPT-108)
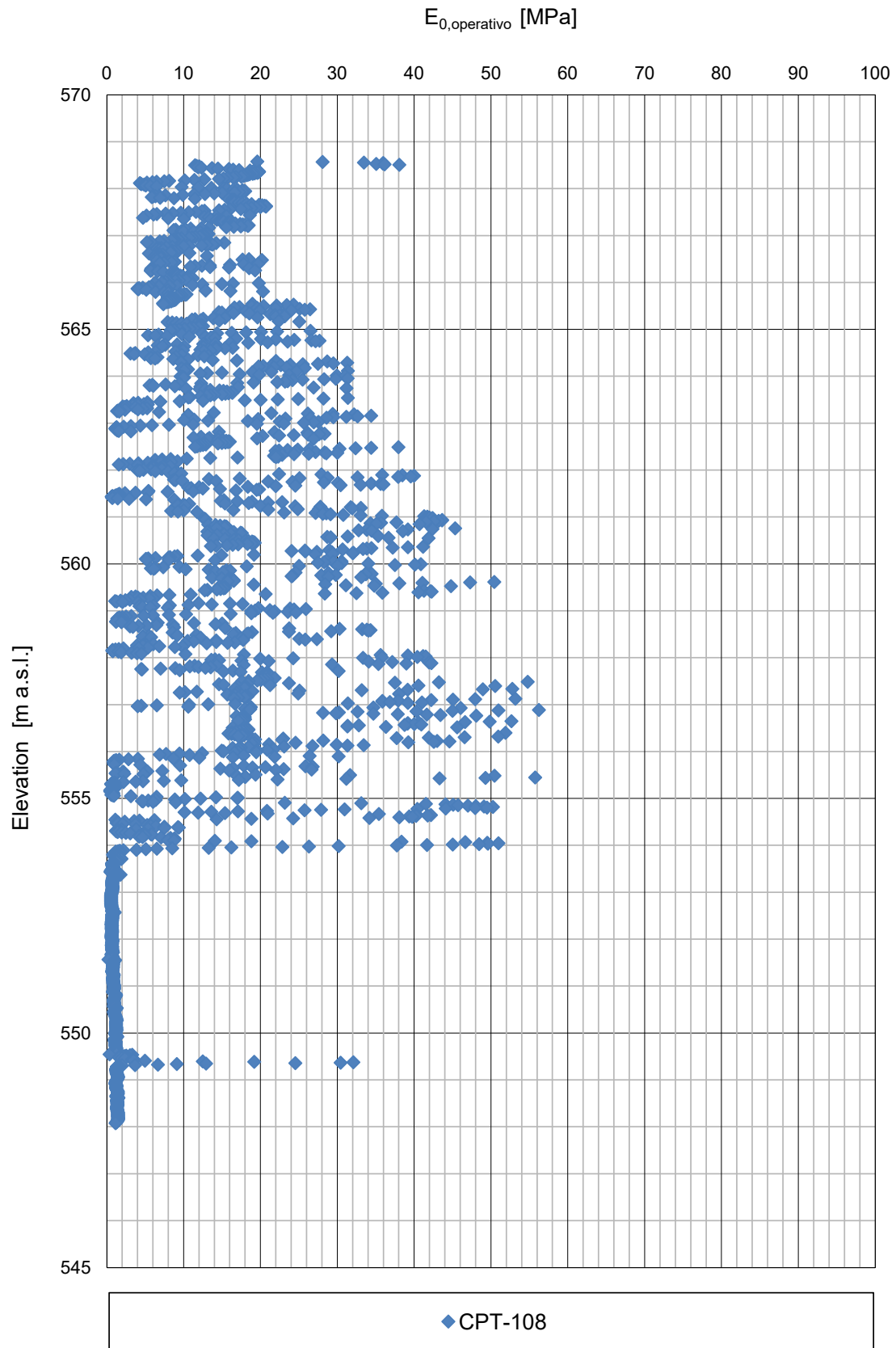
Figure B.12: Operational Young's modulus (CPT-108)
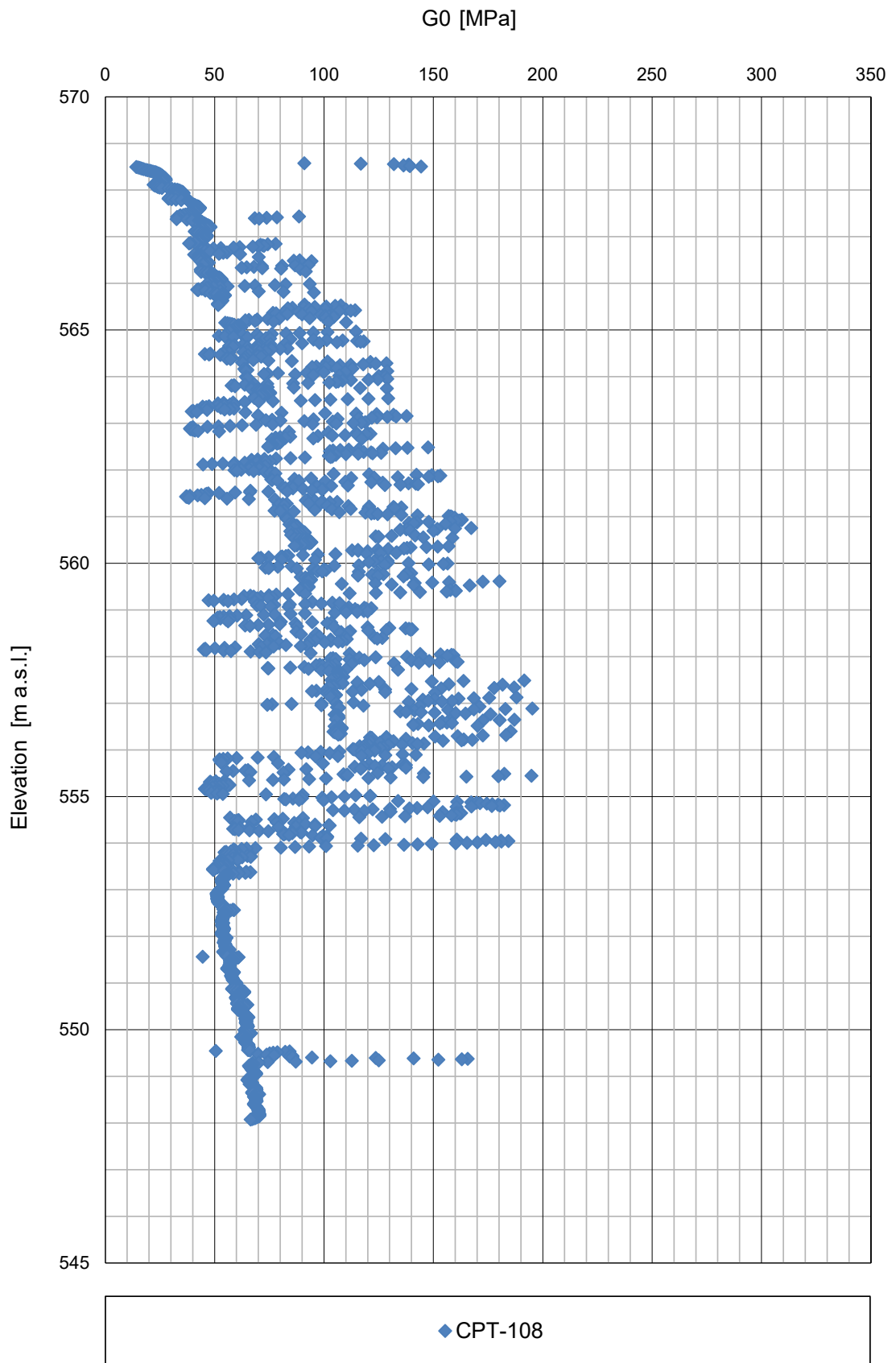
Figure B.13: Small strain shear modulus (CPT-108)

SPT test

The N_{SPT} values are plotted in fig. B.14. N_{SPT} values vary from 5 to 35 for different layers showing the strong heterogeneity of soils in the area. Typically, soft soil layer is found from the top with corresponding N_{SPT} values from 5 to 10.

The following paragraphs summarize the methods assumed for SPT interpretation, and the outcome of their application, determining the following parameters:

  - Undrained shear strength for cohesive material;

  - Relative density and peak friction angle for coarse-grained soils;

  - Small-strain shear modulus for all materials;

  - Operational Young's modulus for all materials.

Undrained shear strength

The undrained shear strength has been estimated according to (Stroud, 1975):

$$s_u \approx (4 \div 6) \cdot N_{60} \ (kPa) \tag{B.9}$$

However, due to due to groundwater conditions of the area, undrained shear strength is likely to play a secondary role in design.

s_u values are divided according to the geological units are summarized in the fig. B.15.

Peak friction angle

The angle of shear resistance (φ') of coarse-grained soil encountered at the site have been determined according to the method suggested by (Bolton, 1986):

$$\varphi' = \varphi'_{cv} + m \cdot Dl; \tag{B.10}$$

$$Dl = D_r \cdot [Q - ln(p'_f)] - 1. \tag{B.11}$$

Where
φ'_{cv} = angle of shear resistance at critical state, [°];
$Q = 10$, [-];
$p'_f \approx 1.4 \cdot (\sigma'_1 - \sigma'_3)$, [kPa];
m = empirical coefficient depending on the mode of shearing failure (see table B.1), [°];
D_r = relative density, [-];
σ'_1 = maximum principal effective stress, [kPa];
σ'_2 = intermediate principal effective stress, [kPa];
σ'_3 = minimum effective stress, [kPa].
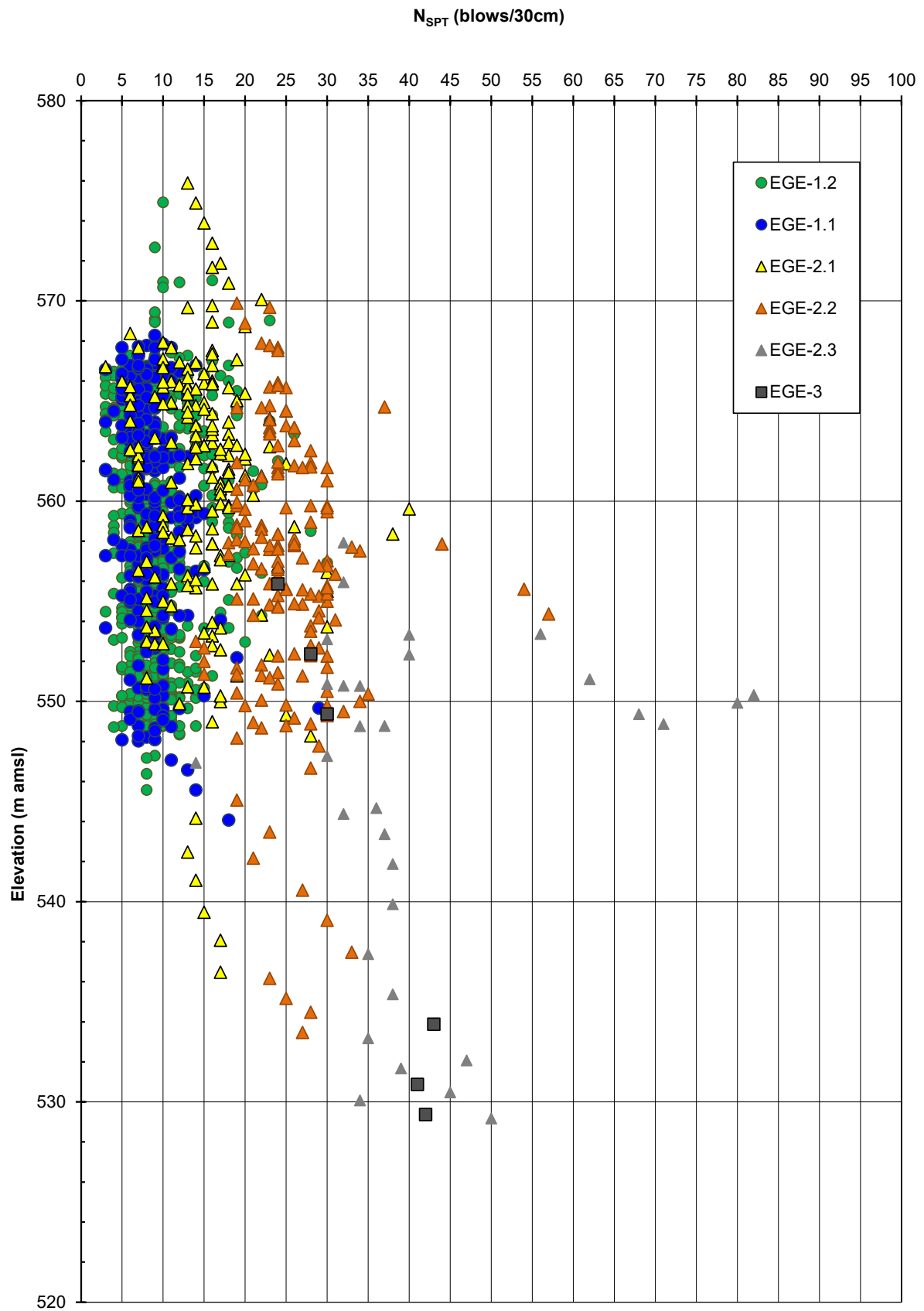
Figure B.14: N_{SPT} distribution with the elevation
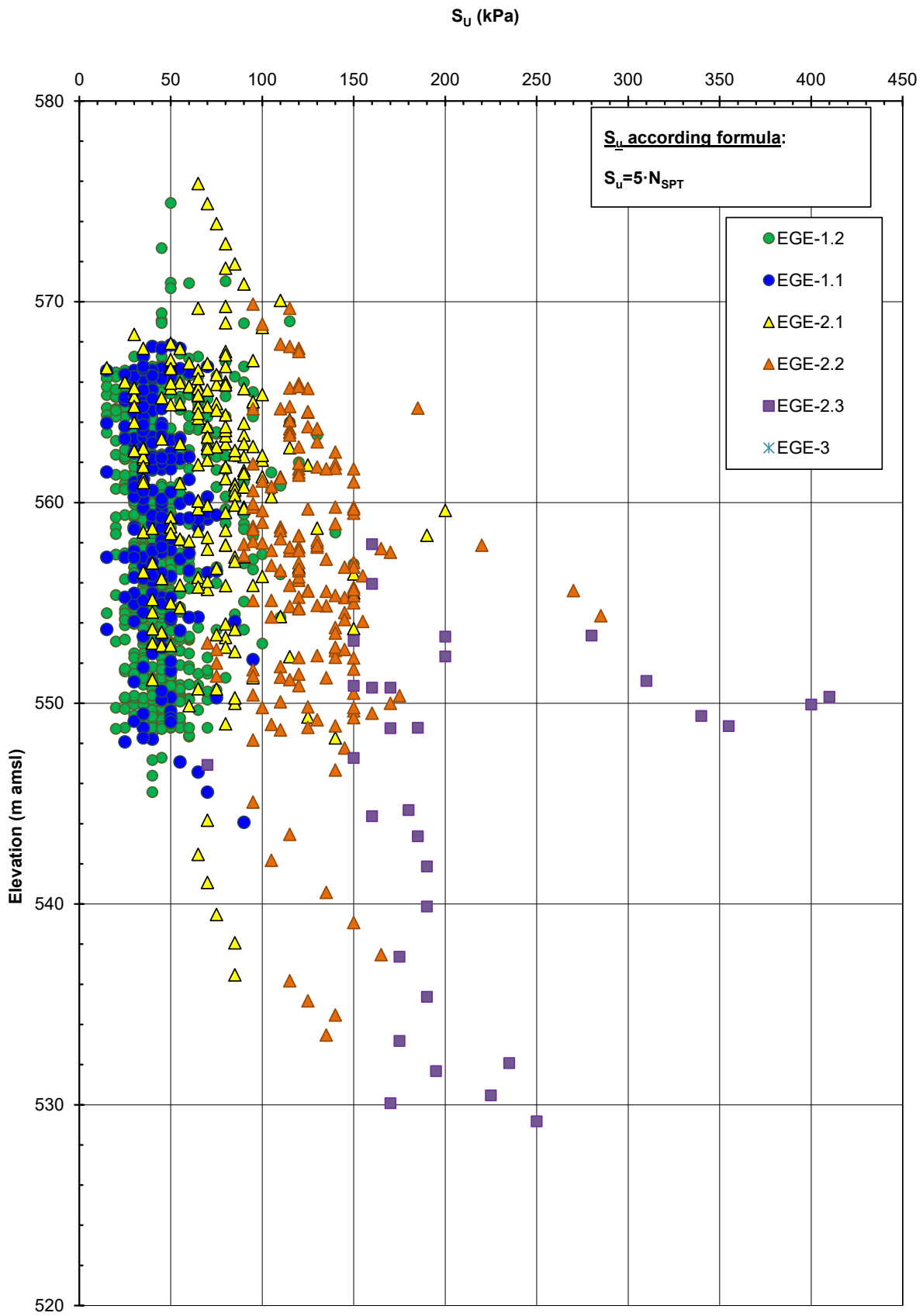
Figure B.15: Undrained shear strength (SPT)

Table B.1: Empirical coefficient m according to (Bolton, 1986)

Mode of shearing failure	m [°]
Triaxial test in compression ($\sigma'_2 = \sigma'_3$)	3
Triaxial test in extension or plane strain conditions ($\sigma'_2 \neq \sigma'_3$)	5

On the safe side, the parameters m and φ'_{cv} have been selected equal to 3 and 30°, respectively. The fig. B.16 represents the results.

Relative density

The values of relative density D_r for sandy soils are determined from N_{SPT} based on the method of interpretation proposed by (Skempton, 1986):

$$D_r = \left(\frac{1}{A + B \cdot (\sigma'_{v0}/100)} \cdot N_{60} \right)^{0.5} \tag{B.12}$$

Where:

A, B = empirical constants as per table B.2. For this case, the interpretation has been carried out considering, on safe side, the values for normally consolidated coarse sands;

σ'_{v0} = in situ vertical effective stress at the depth of SPT test, [kPa];

N_{60} = results of SPT corrected to a transmitted energy equal to 60 %, [blows/30cm];

$k_{0,NC} = 0.5$ = coefficient of earth pressure at rest for normally consolidated soils, [-];

$k_{0,OC} = 0.5 \cdot (OCR)^{0.5}$ = coefficient of earth pressure at rest for overconsolidated soils, [-];

OCR = overconsolidation ratio, [-];

D_r = relative density, [-].

Table B.2: Empirical constants A and B according to (Skempton, 1986)

Soil type	A	B
Normally consolidated fine sands	27.5	27.5
Normally consolidated coarse sands	43.3	21.7
Overconsolidated sands	27.5÷43.3	$(21.7 \div 27.5) \cdot \dfrac{1 + 2 \cdot k_{0,OC}}{1 + 2 \cdot k_{0,NC}}$

Stiffness at small strain

Small strain stiffness was derived based on the shear wave velocities V_s, which were estimated from N_{SPT} data, by means of the relationship proposed by (Ohta and Goto, 1978):

$$V_s = C \cdot N_{60}^{0.171} \cdot z^{0.199} \cdot f_A \cdot f_G \ (m/s) \tag{B.13}$$

Where:

C = empirical constant = 67.3;

z = depth in meters below ground level, [m];

$f_A = 1.3$ = accounting for site geological age, i.e. Neoproterozoic age as stated in the chapter 1, [-];

f_G = according to the table B.3, [-].

Table B.3: Empirical constants A and B according to (Skempton, 1986)

f_G	Gravel	Gravelly sand	Coarse sand	Medium sand	Fine sand	Silt & Clay
	1.45	1.15	1.14	1.07	1.09	1.00

The shear modulus at small strains G_0 is determined as:

$$G_0 = \rho \cdot V_s^2 \tag{B.14}$$

Where ρ is the bulk density of the soil.

The Young's modulus at small strains E_0 is determined as:

$$E_0 = 2 \cdot (1 + \nu) \cdot G_0 \tag{B.15}$$

Where ν can be assumed equal to 0.25.

The operational Young's modulus E_{op} is determined as:

$$E_{op} = E_0/10 \tag{B.16}$$

V_s, G_0 and E_op values are provided for each geological unit in fig. B.17, fig. B.18 and fig. B.19.
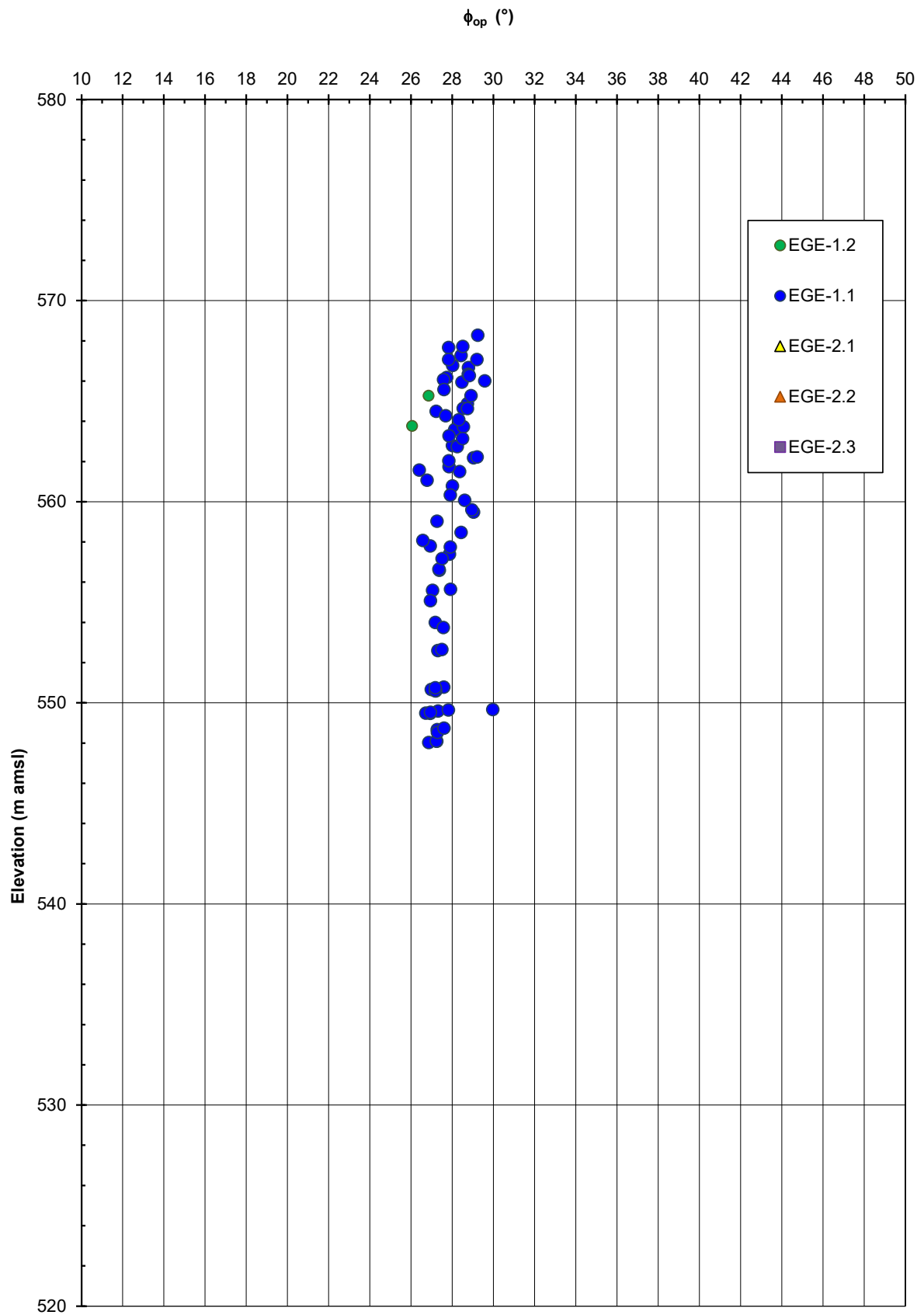
Figure B.16: Friction angle of coarse-grained materials (SPT)
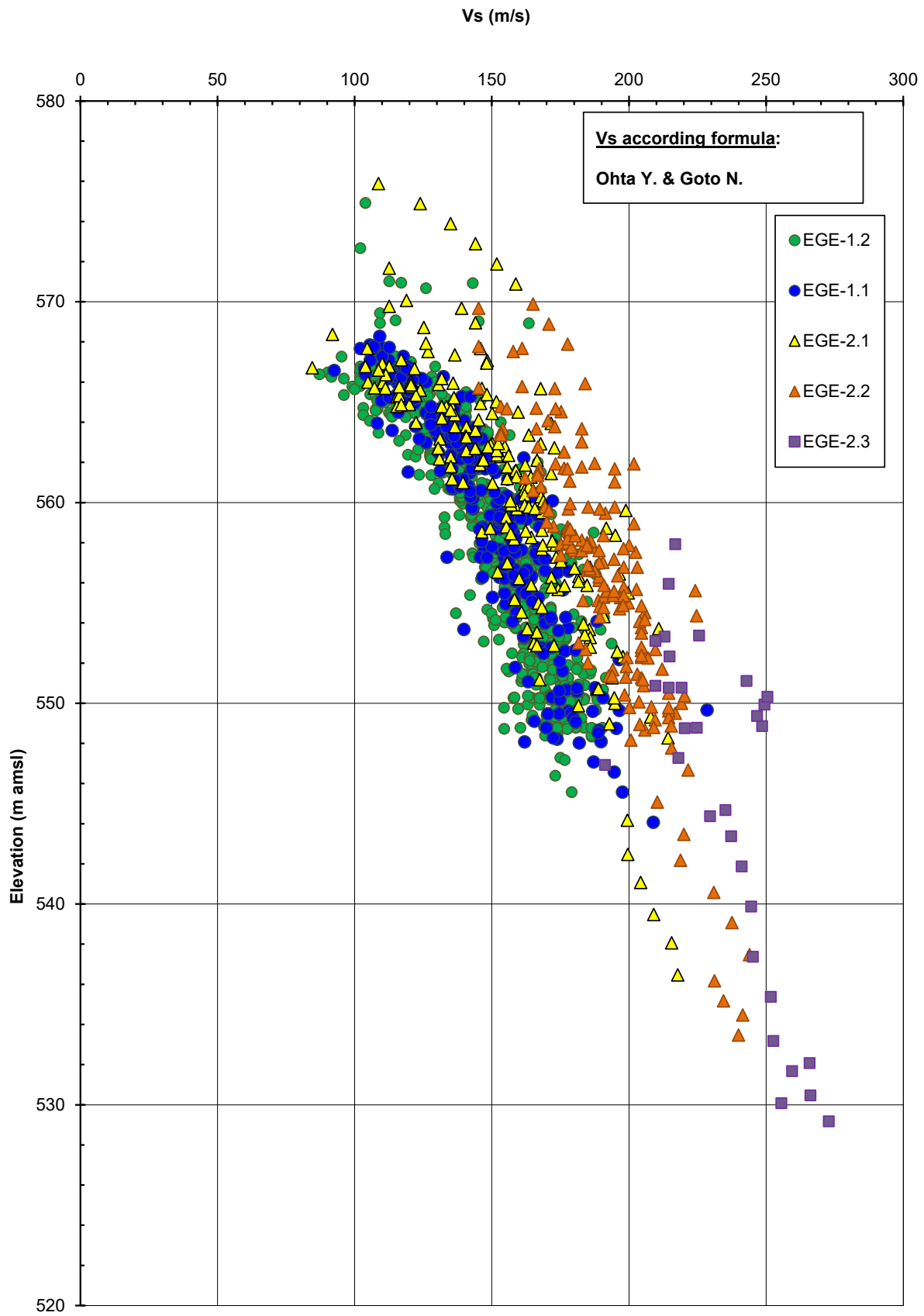
Figure B.17: Shear wave velocity (SPT)
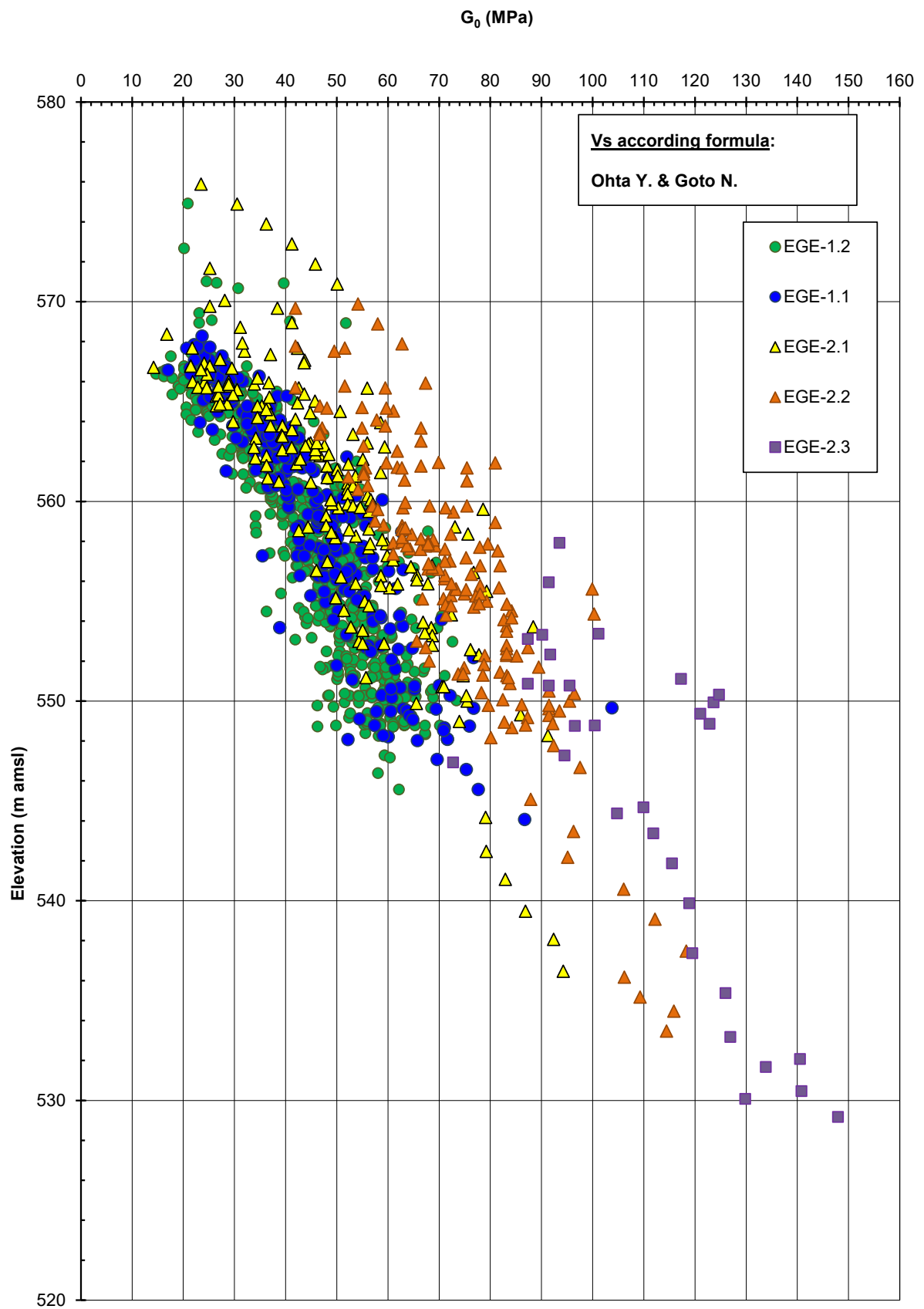
Figure B.18: Small strain shear modulus (SPT)
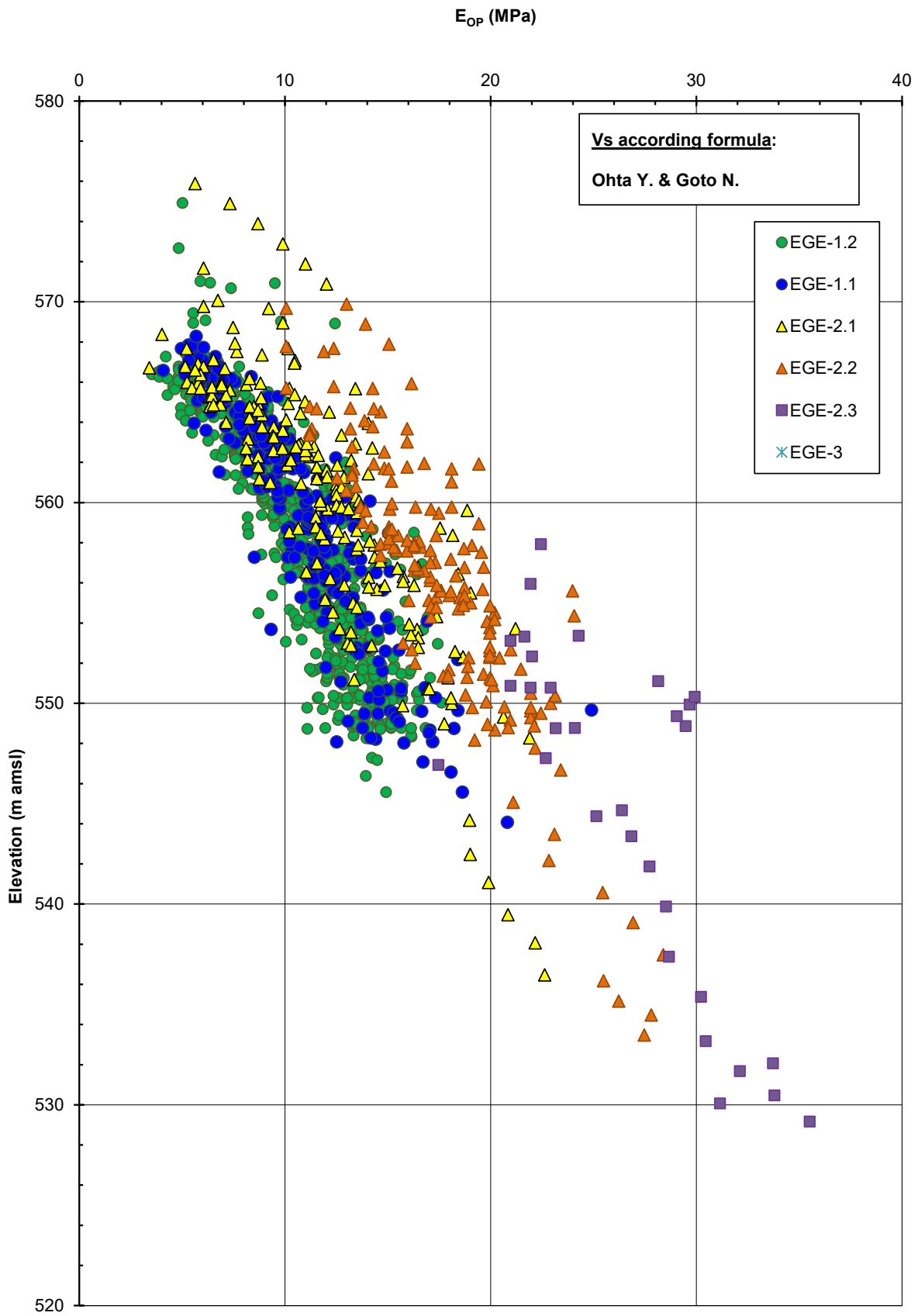
Figure B.19: Operational Young's modulus (SPT)

B.1.1. Soil model parameters calibration

For the hardening soil model the parameters of triaxial reference stiffness and power m were calibrated according to the procedure described in the section 3.2.2. The data for the tests used for calibration is reported here.

The derivation of the reference stiffness from the triaxial test for several samples is represented in the fig. B.20, fig. B.21 and fig. B.22.
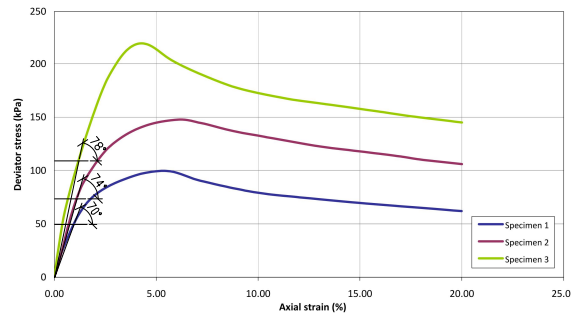
Figure B.20: Estimation of E_{50} for the EGE-1.1 from BH-165
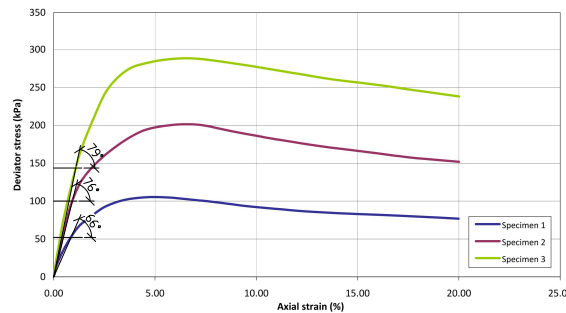
Figure B.21: Estimation of E_{50} for the EGE-1.2 from BH-167
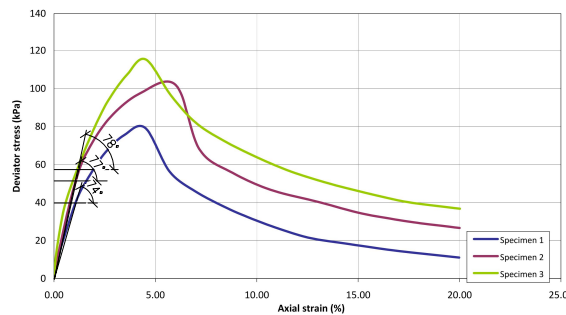
Figure B.22: Estimation of E_{50} for the EGE-1.1 from BH-189

For the same samples mentioned above the derivation of the power m is represented in

the fig. B.23, fig. B.24 and fig. B.25. Corresponding values are $m = 0.5$, $m = 0.76$ and $m = 0.43$.
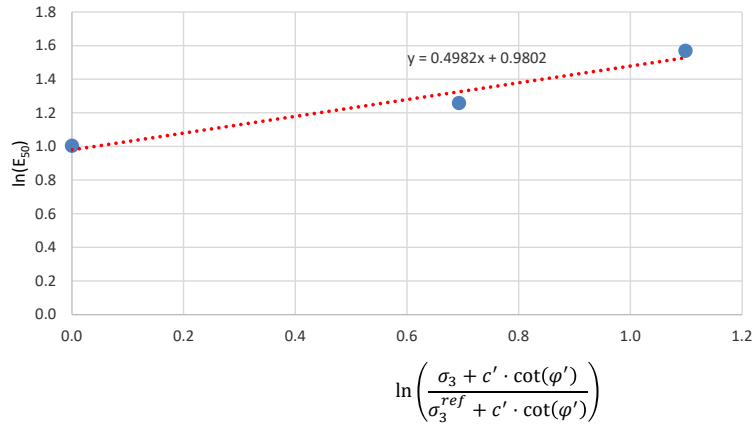
Figure B.23: Estimation of the power m for the EGE-1.1 from BH-165
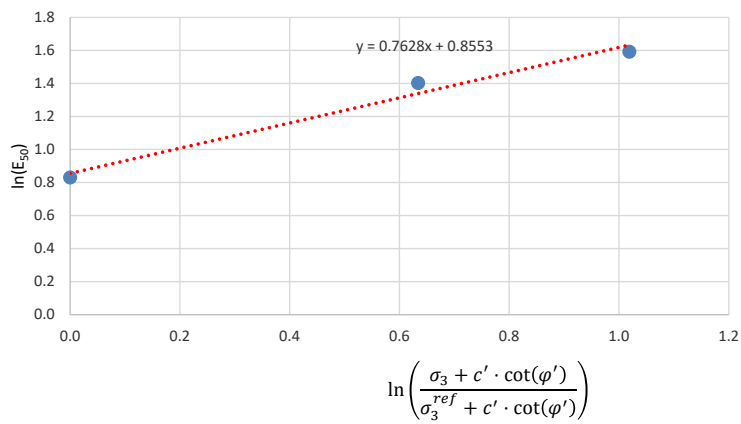
Figure B.24: Estimation of the power m for the EGE-1.2 from BH-167
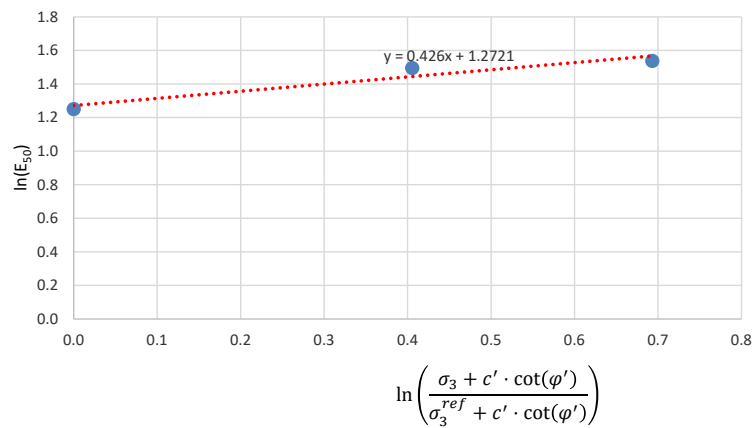
Figure B.25: Estimation of the power m for the EGE-1.1 from BH-189

B.1.2.   Embedded beam model parameter calibration

Derivation of the pile bearing capacity according to the CPT tests performed is based on the method proposed by the (Bustamante and Gianeselli, 1982).

The method is based on the determination of pile bearing capacity as sum of the point and shaft bearing capacities as following:

$$Q_L = Q_L^P + Q_L^F \tag{B.17}$$

Where

$$Q_L^P = q_{ca} \cdot k_c \cdot \frac{\pi D^2}{4} \tag{B.18}$$

$$Q_L^F = \sum_1^i Q_{Li}^F = \sum_1^i q_{si} \cdot \pi D l_i \tag{B.19}$$

Where successively: q_{ca} is the equivalent cone resistance at the level of the pile point (in kN/m^2); k_c is the penetrometer bearing capacity factor; D is the diameter of the foundation (m); q_{si} is the limit unit skin friction at the level of the layer i (kN/m^2) and l_i is the thickness of the layer i (m).

The equivalent cone resistance is found by averaging measured cone resistance over an interval of $+a$ over the cone and $-a$ below the pile point as shown in the fig. B.26.
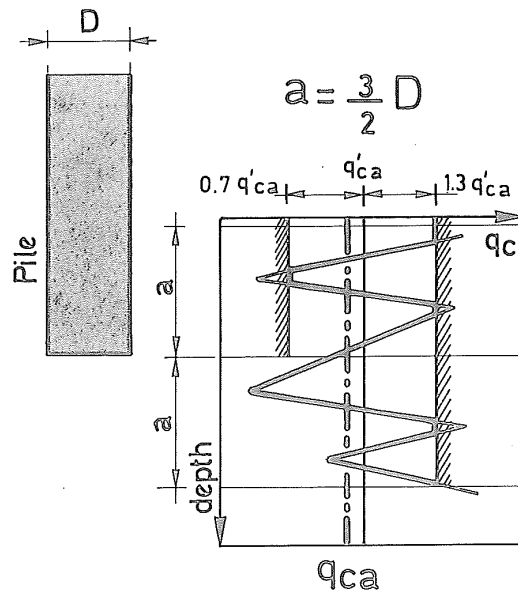
Figure B.26: Equivalent cone resistance q_{ca} according to (Bustamante and Gianeselli, 1982)

The penetrometer bearing capacity factor k_c derived by authors from the full scale pile load tests and it depends on the nature of the soil and pile construction procedure.

The limit unit skin friction q_{si} is calculated as following:

$$q_s = \frac{q_c}{\alpha} \tag{B.20}$$

Where α is the coefficient which depends on the nature of the soil and the pile construction technique.

C | Numerical investigation results

C.1. End-bearing piles

General view of the system is represented in the fig. C.1.
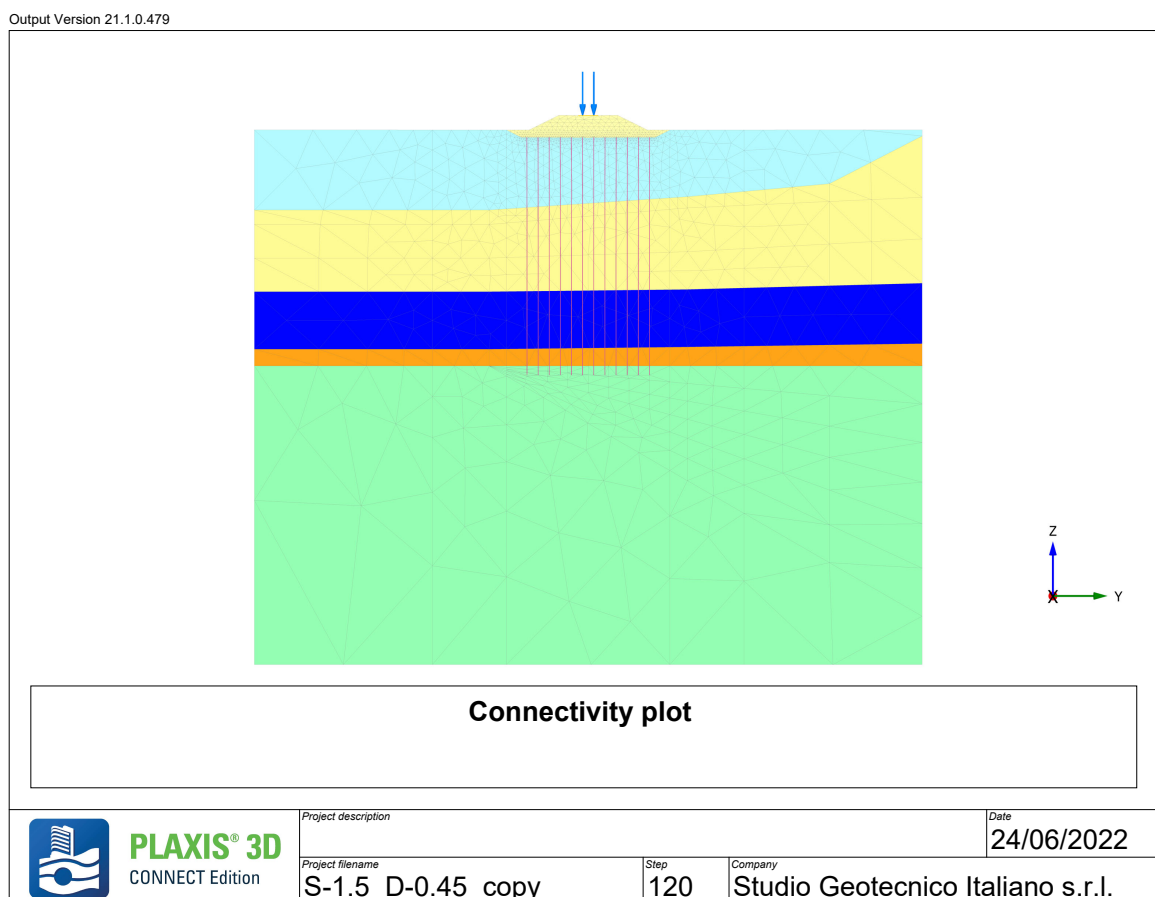
Figure C.1: Model view for the case of the clamped piles

Displacement within the embankment body is shown in the fig. C.2. Maximum settlement

developed along the centreline is 0.060 m.
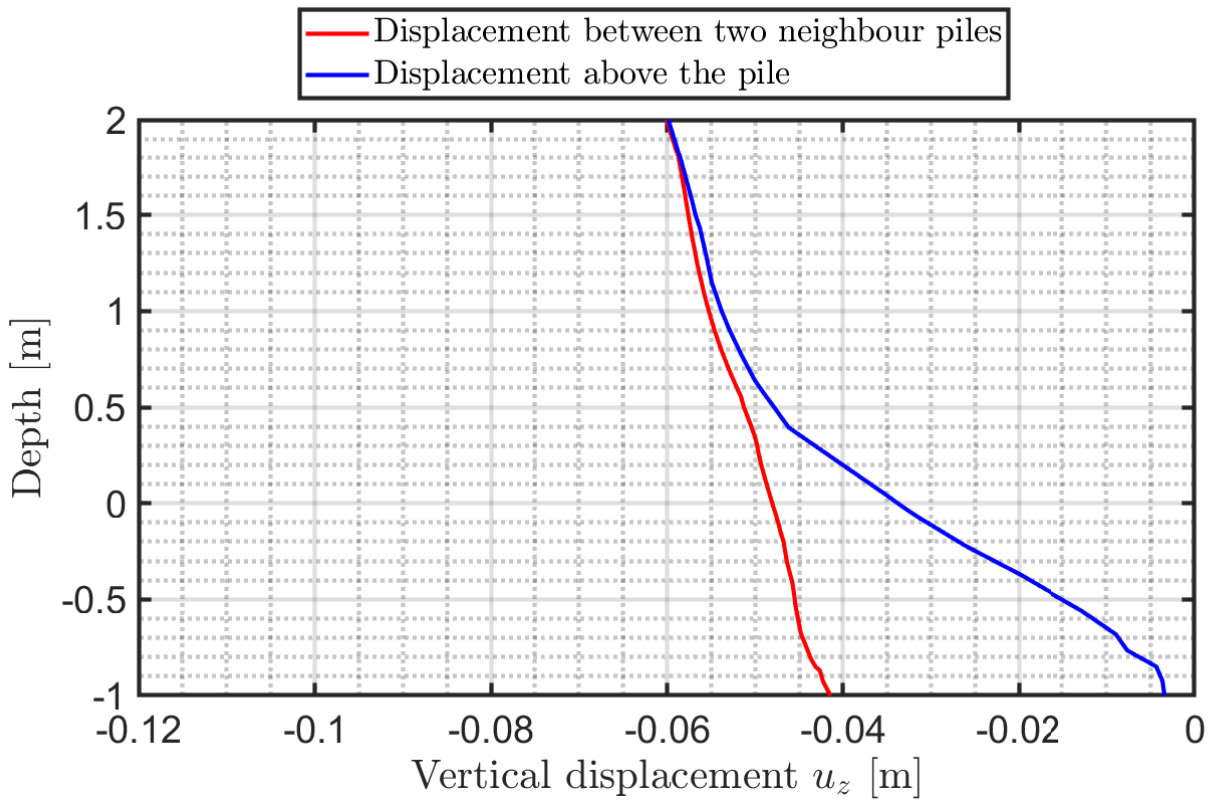
Figure C.2: Vertical settlement of the embankment body

The piles response is reported in the fig. C.3.
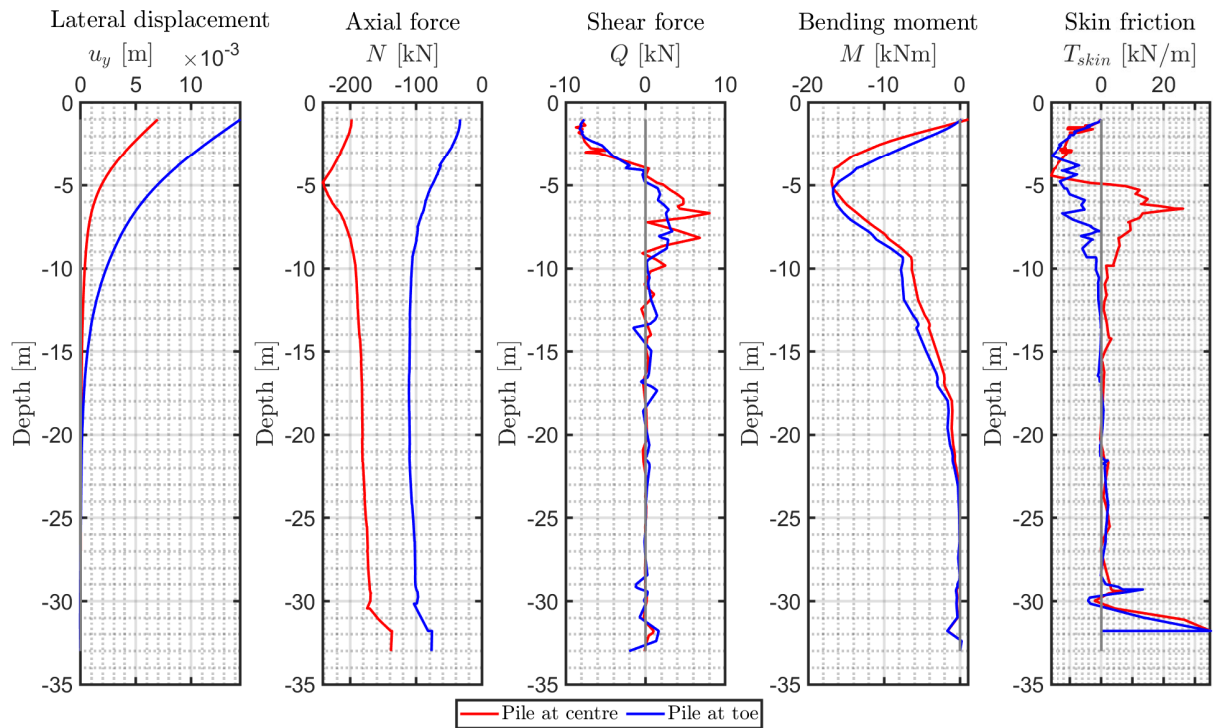
Figure C.3: Piles behaviour in the case of end-bearing piles

Settlement of the geogrid is reported in the fig. C.4.

Figure C.4: Vertical displacement within the geogrid along the cross-section including piles

Tensile force developed in the geogrid is shown in the fig. C.5.
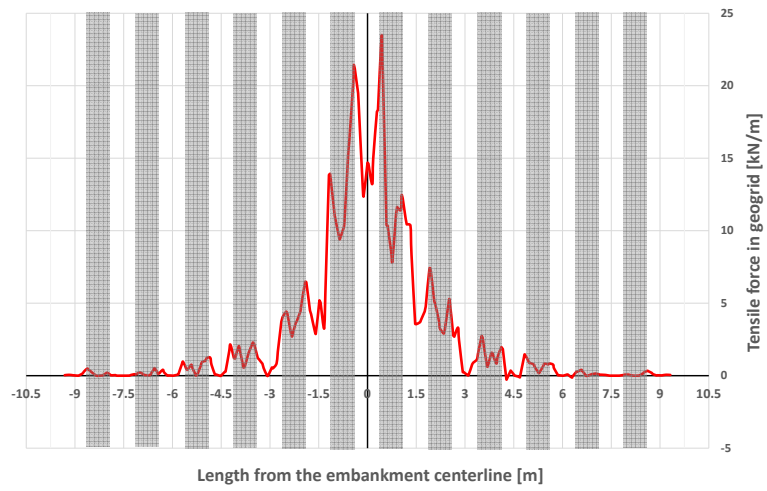
Figure C.5: Tensile force distribution within the geogrid along the cross-section including piles

C.2. Floating piles

General view of the system is represented in the fig. C.6.
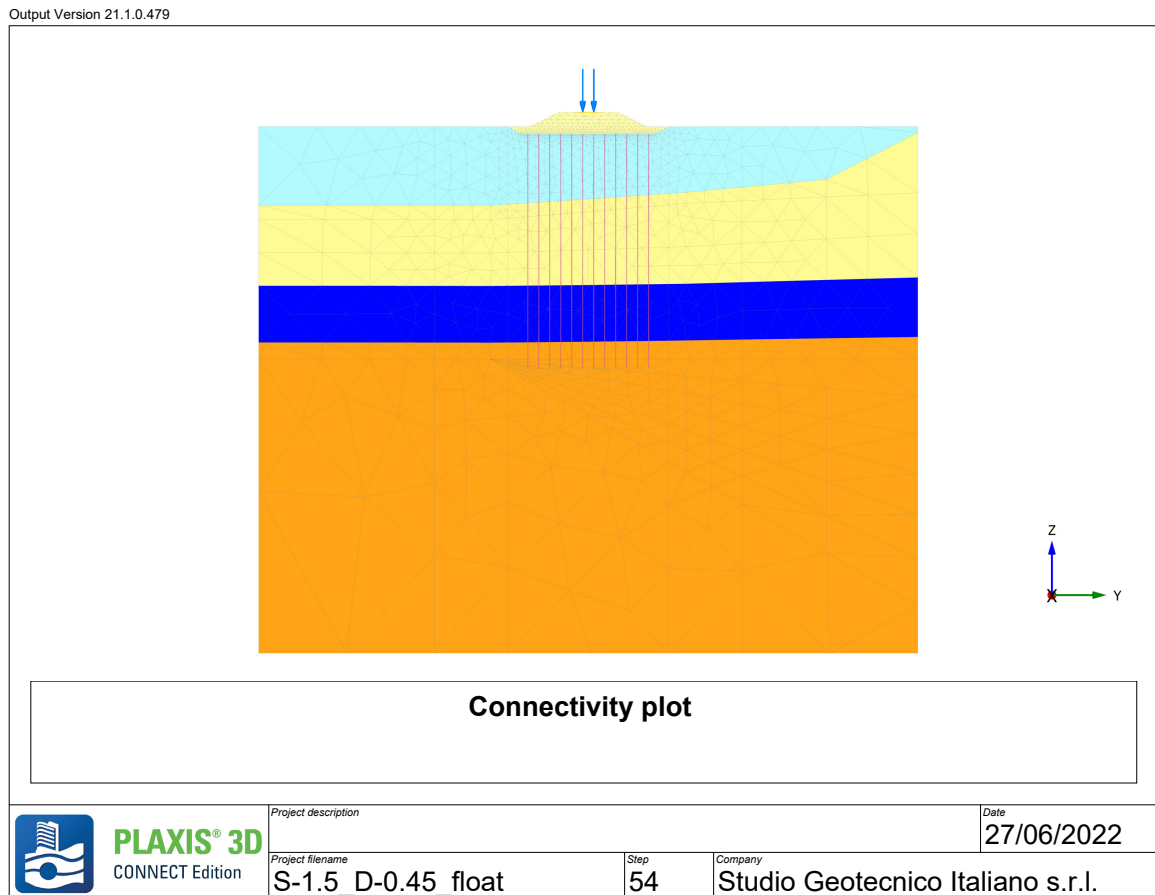
Figure C.6: Model view for the case of floating piles

Displacement within the embankment body is shown in the fig. C.7. Maximum settlement developed along the centreline is 0.102 m.
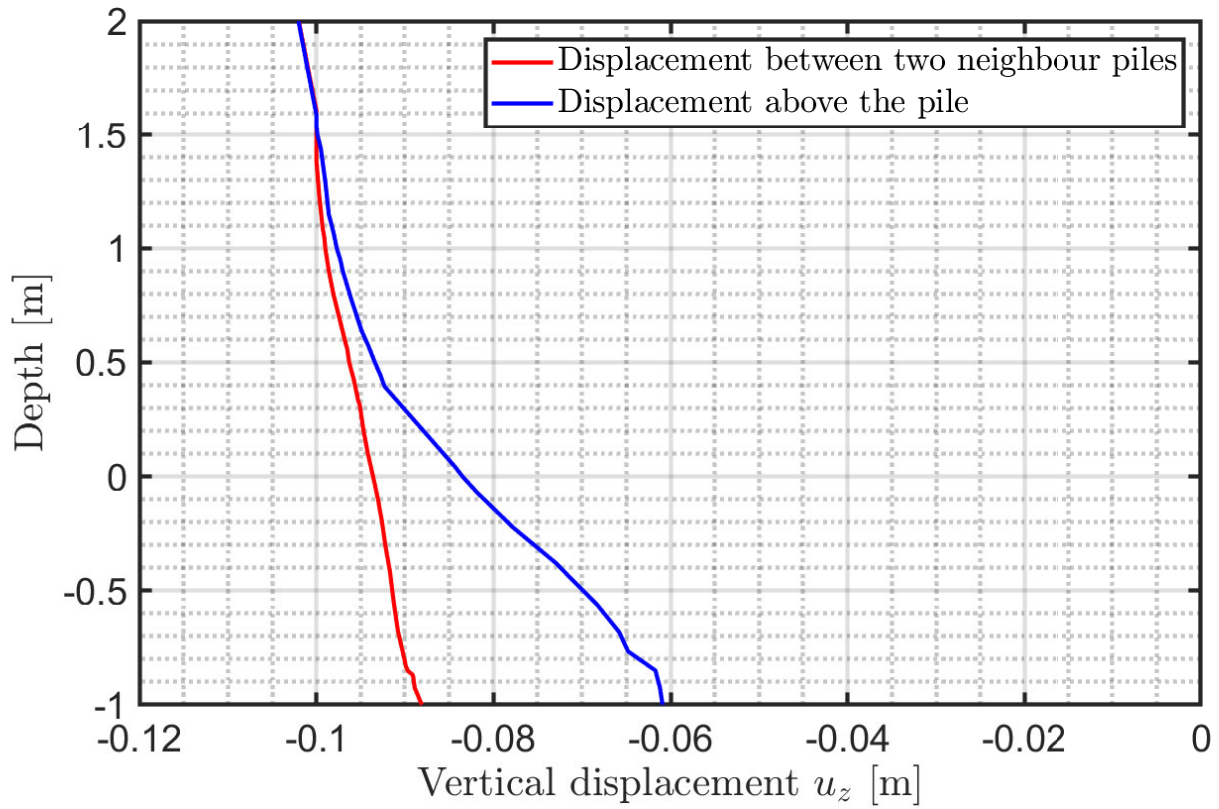
Figure C.7: Vertical settlement of the embankment body

The piles response is reported in the fig. C.8.
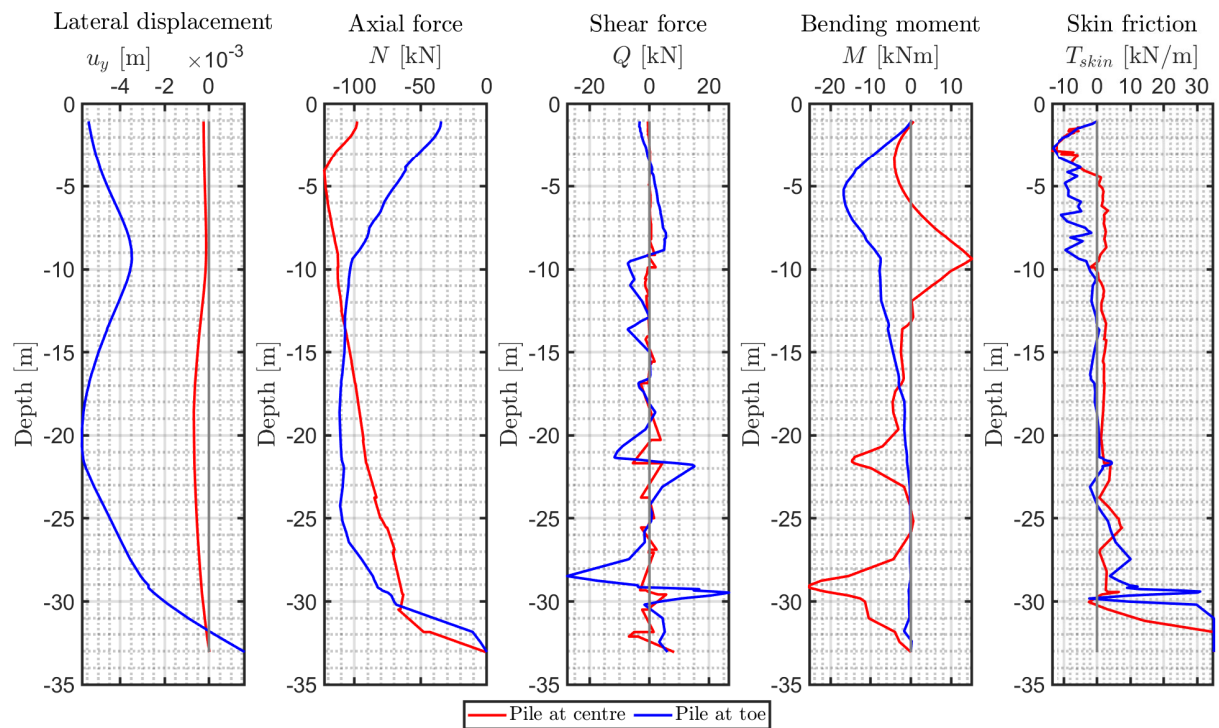
Figure C.8: Piles behaviour in the case of floating piles

Settlement of the geogrid is reported in the fig. C.9.
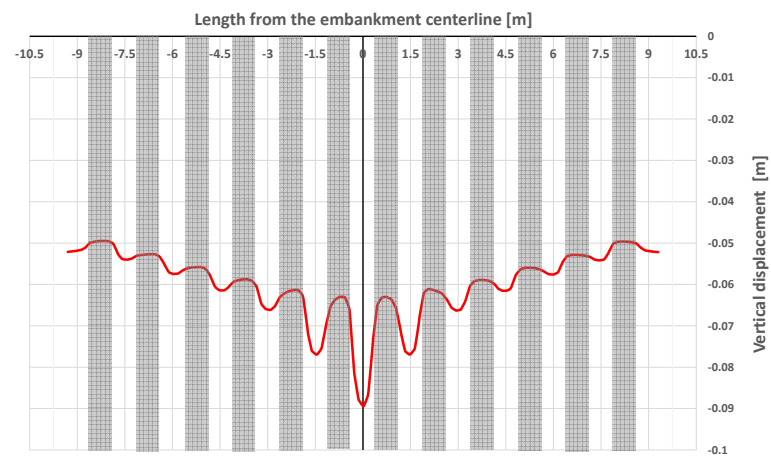
Figure C.9: Vertical displacement within the geogrid along the cross-section including piles

Tensile force developed in the geogrid is shown in the fig. C.10.
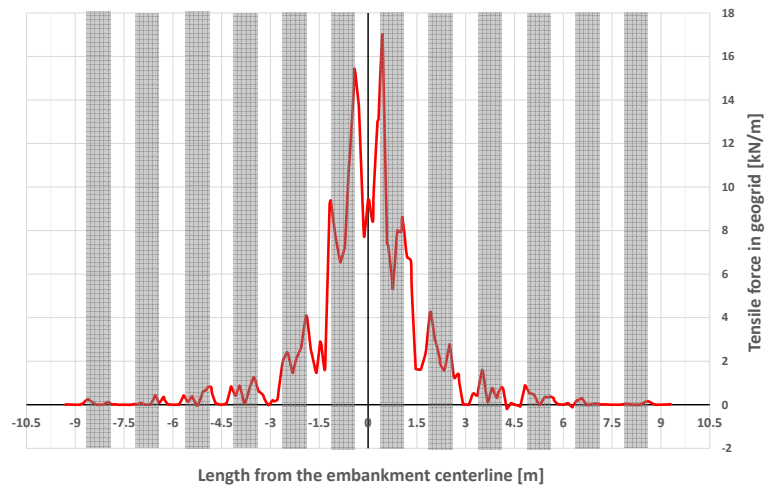
Figure C.10: Tensile force distribution within the geogrid along the cross-section including piles

C.3. Inclination of $5°$

General view of the system is represented in the fig. C.11.
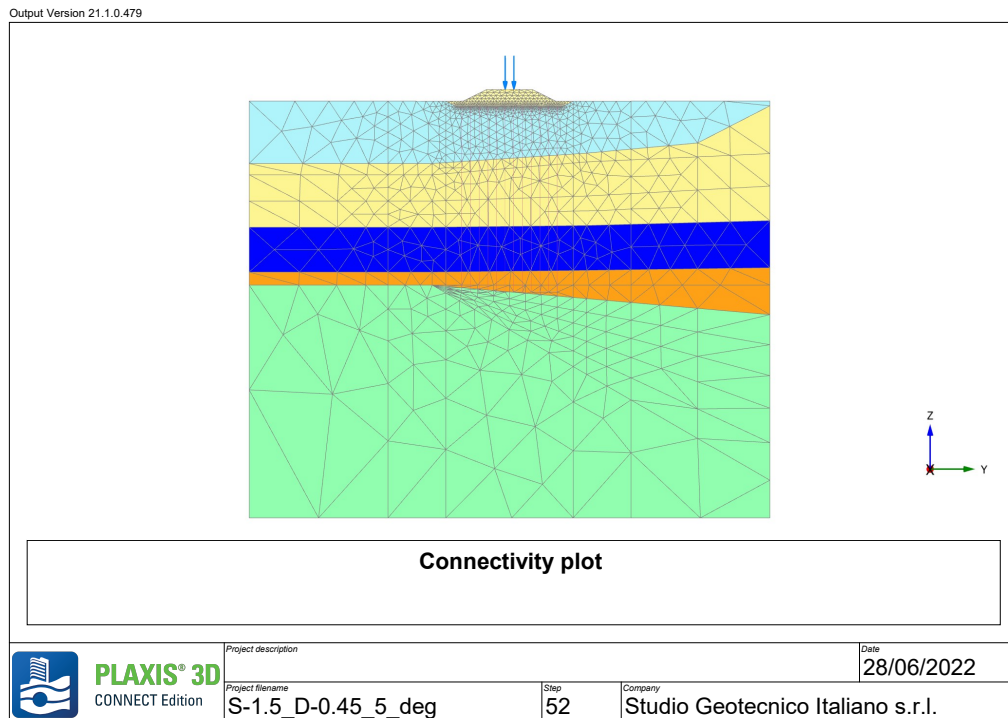
Figure C.11: Model view for the case of $5°$ bearing layer inclination

Displacement within the embankment body is shown in the fig. C.12. Maximum settlement developed along the centreline is 0.062 m.
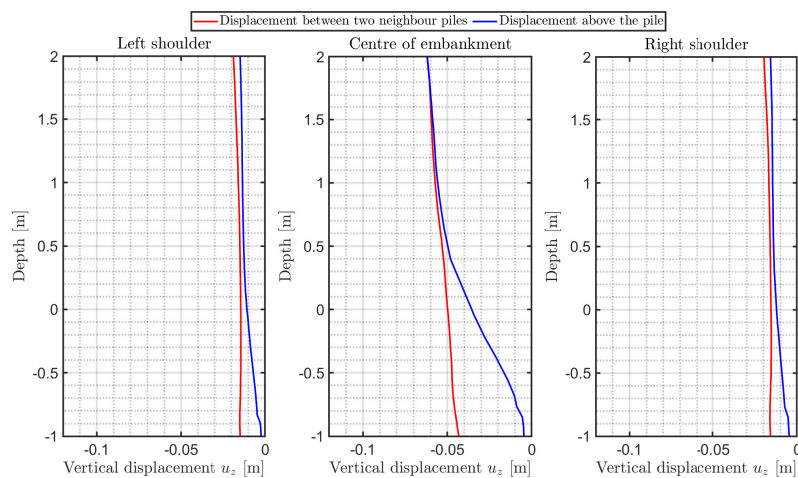
Figure C.12: Vertical displacement developed in the embankment in case of $5°$ bearing layer inclination

The piles response is reported in the fig. C.13.
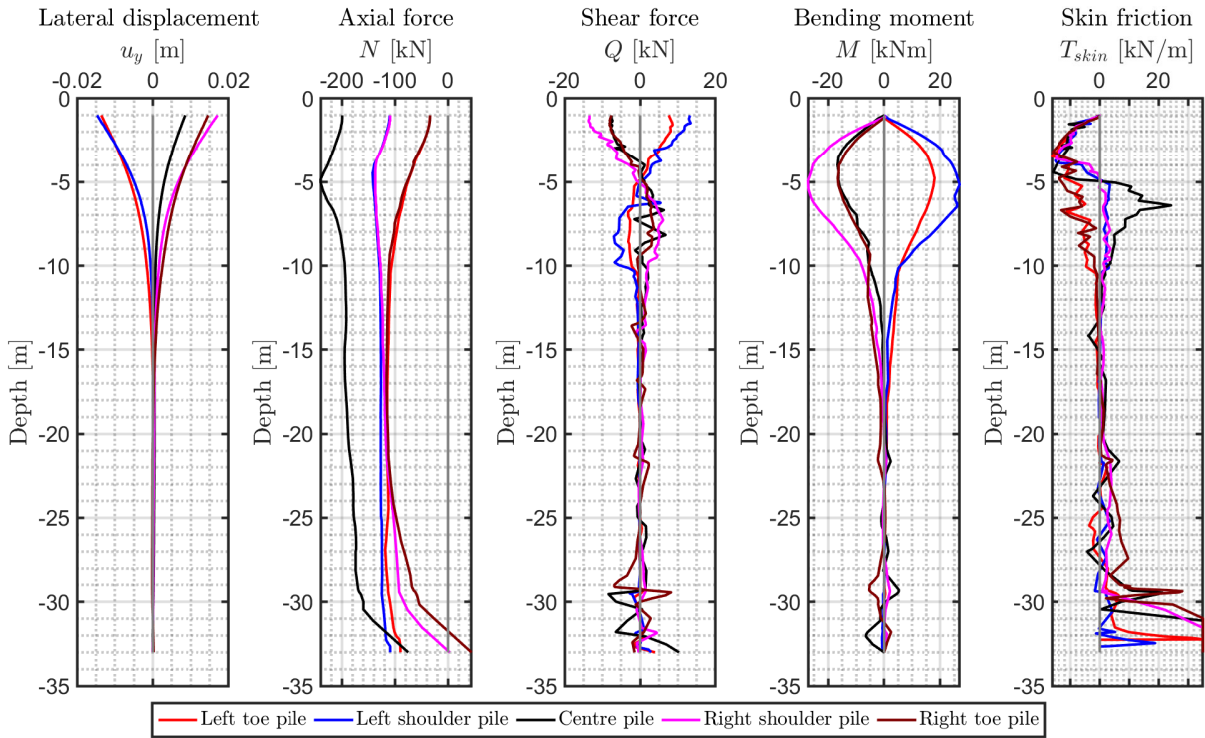
Figure C.13: Piles behaviour in case of 5° bearing layer inclination

Tensile force developed in the geogrid is shown in the fig. C.14.
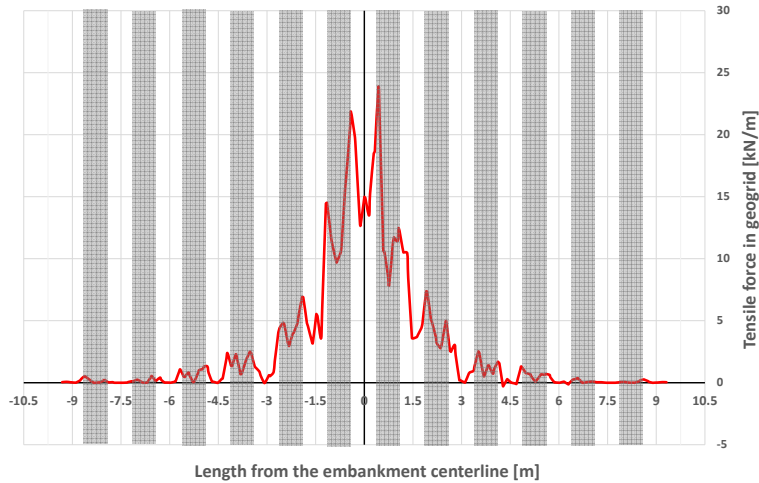
Figure C.14: Forces developed within the geogrid in case of 5° bearing layer inclination

Settlement of the geogrid is reported in the fig. C.15.
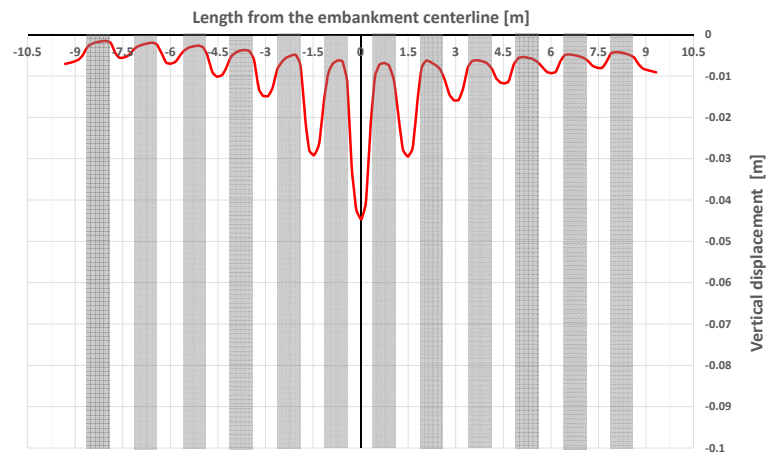
Figure C.15: Vertical displacement of the geogrid in case of 5° bearing layer inclination

Iso-lines of settlement is reported in the fig. C.16.
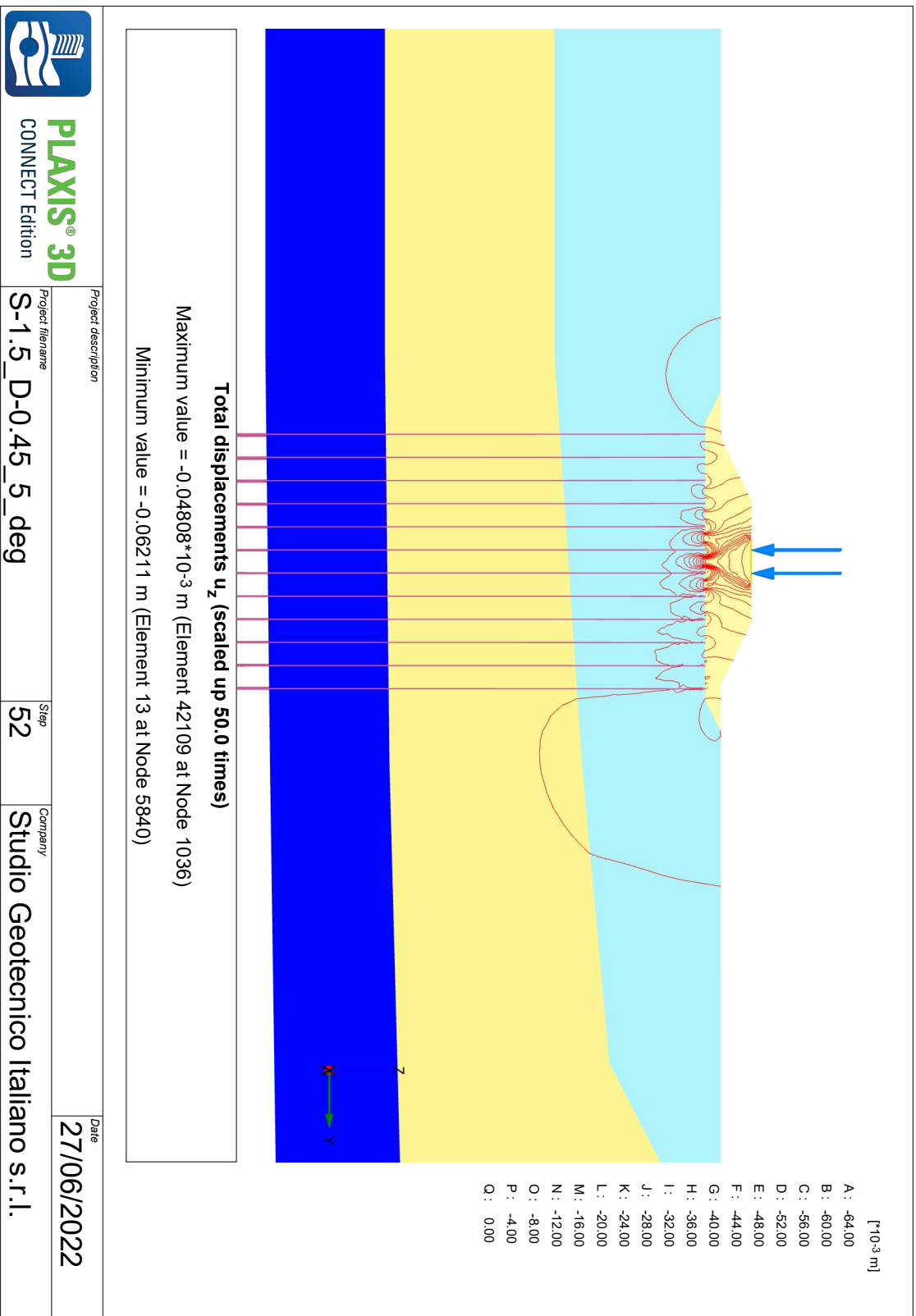
Figure C.16: Iso-lines of developed displacement within the system, 5° bearing layer inclination

C.4. Inclination of $10°$

General view of the system is represented in the fig. C.17.
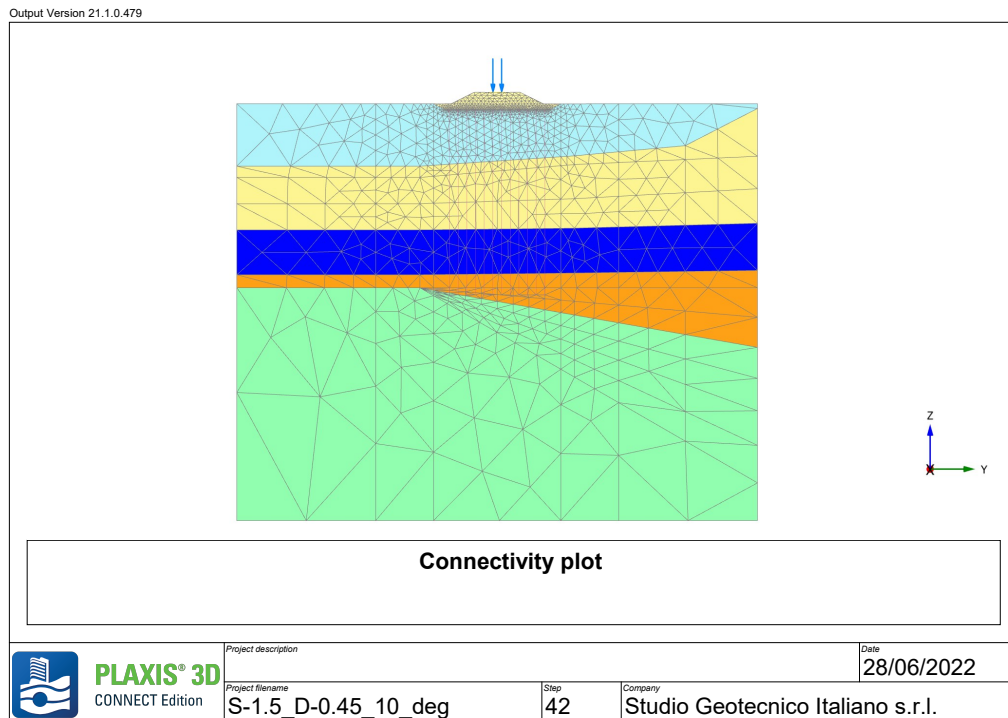
Figure C.17: Model view for the case of 10° bearing layer inclination

Displacement within the embankment body is shown in the fig. C.18. Maximum settlement developed along the centreline is 0.066 m.
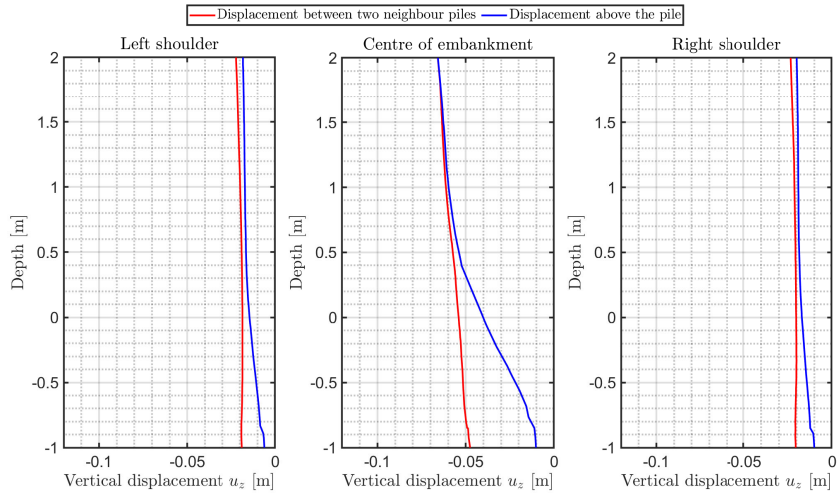
Figure C.18: Vertical displacement developed in the embankment in case of 10° bearing layer inclination

The piles response is reported in the fig. C.19.
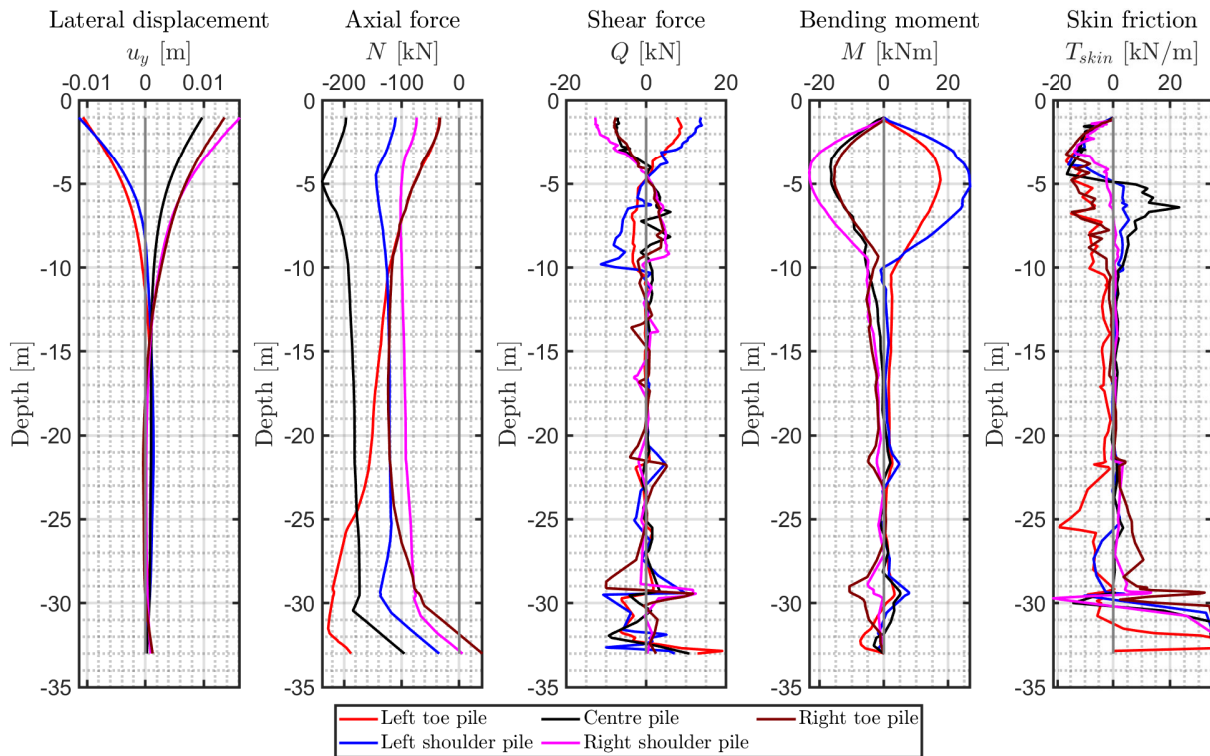
Figure C.19: Piles behaviour in case of 10° bearing layer inclination

Tensile force developed in the geogrid is shown in the fig. C.20.
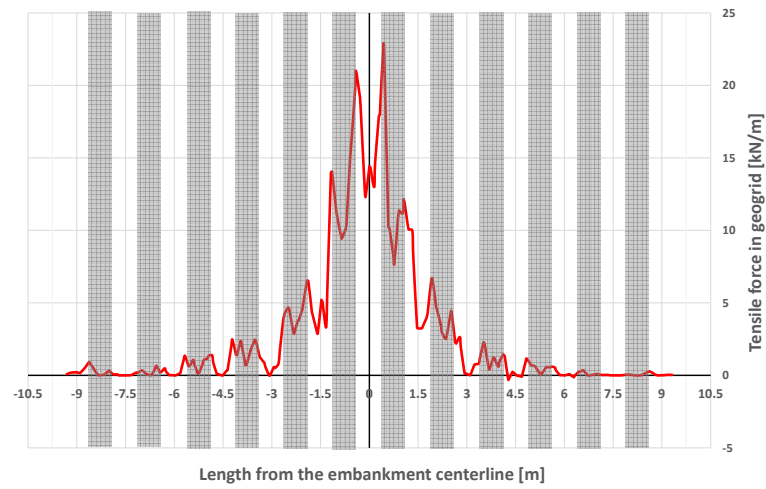
Figure C.20: Forces developed within the geogrid in case of 10° bearing layer inclination

Settlement of the geogrid is reported in the fig. C.21.
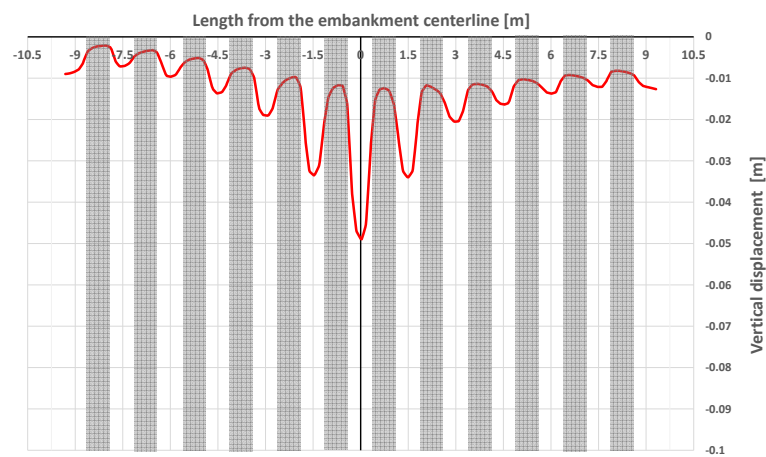
Figure C.21: Vertical displacement of the geogrid in case of 10° bearing layer inclination

Iso-lines of settlement is reported in the fig. C.22.
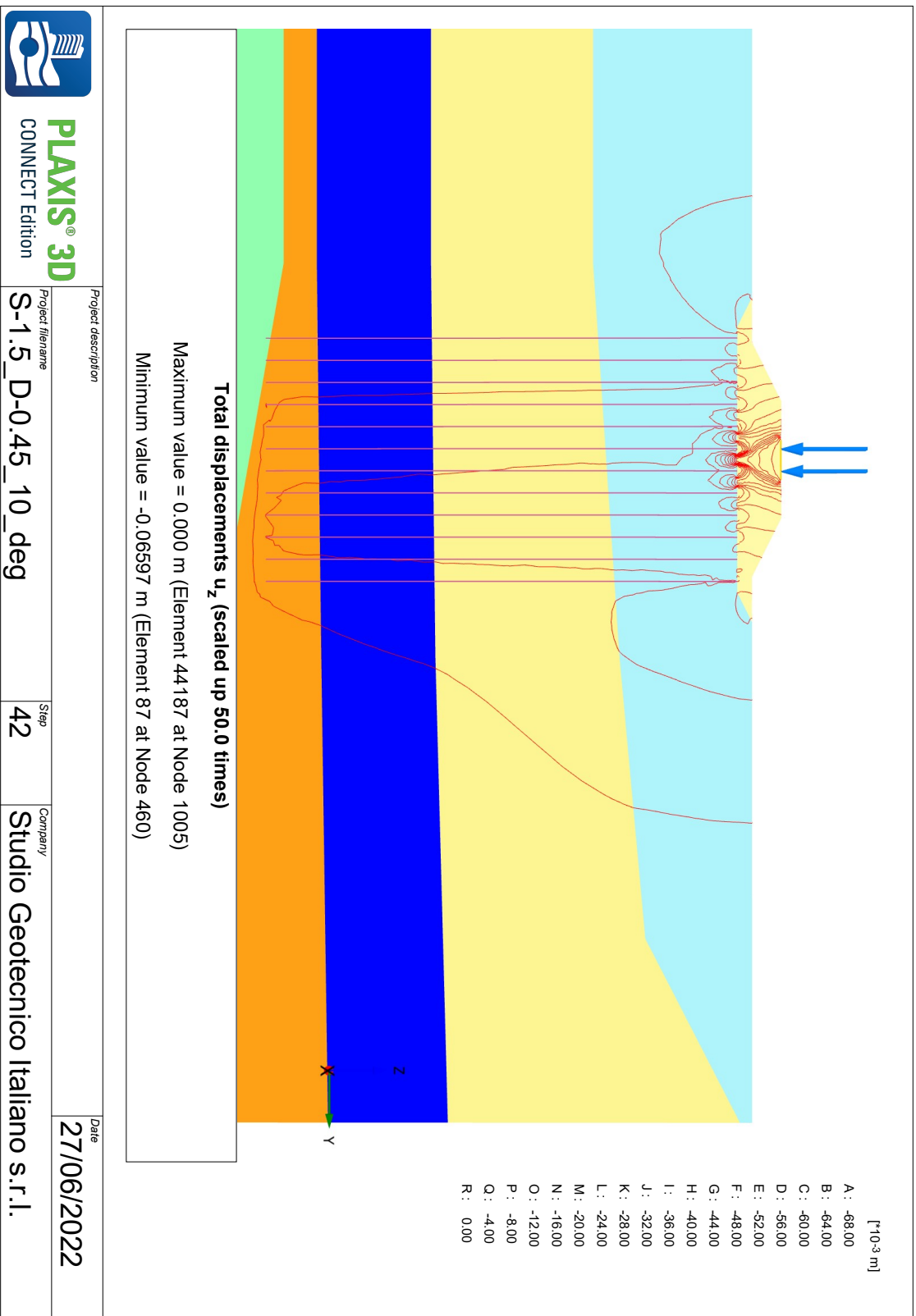
Figure C.22: Iso–lines of developed displacement within the system, 10° bearing layer inclination

C.5.   Inclination of $15°$

General view of the system is represented in the fig. C.23.
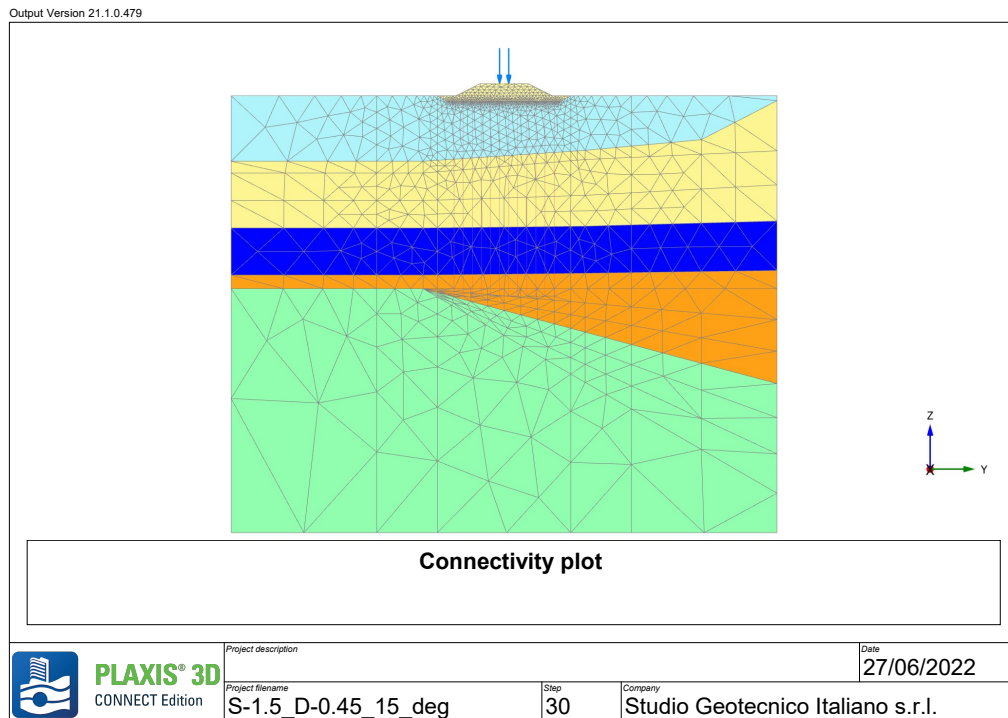
Figure C.23: Model view for the case of 15° bearing layer inclination

Displacement within the embankment body is shown in the fig. C.24. Maximum settlement developed along the centreline is 0.068 m.
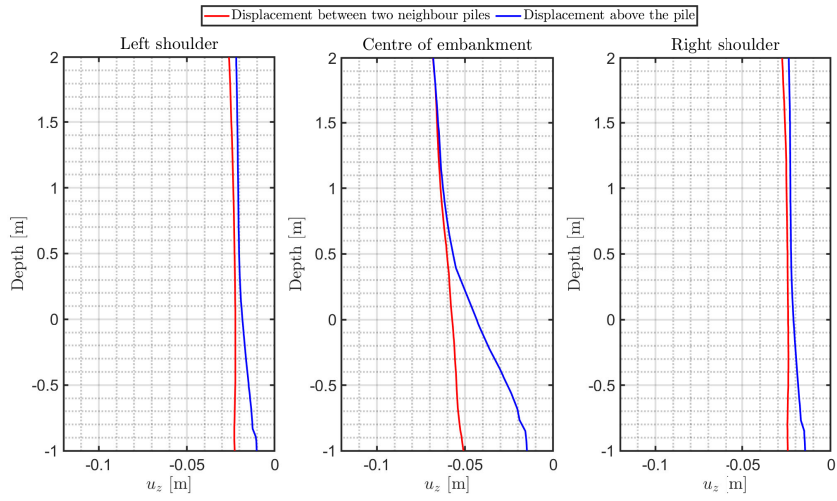
Figure C.24: Vertical displacement developed in the embankment in case of 15° bearing layer inclination

The piles response is reported in the fig. C.25.
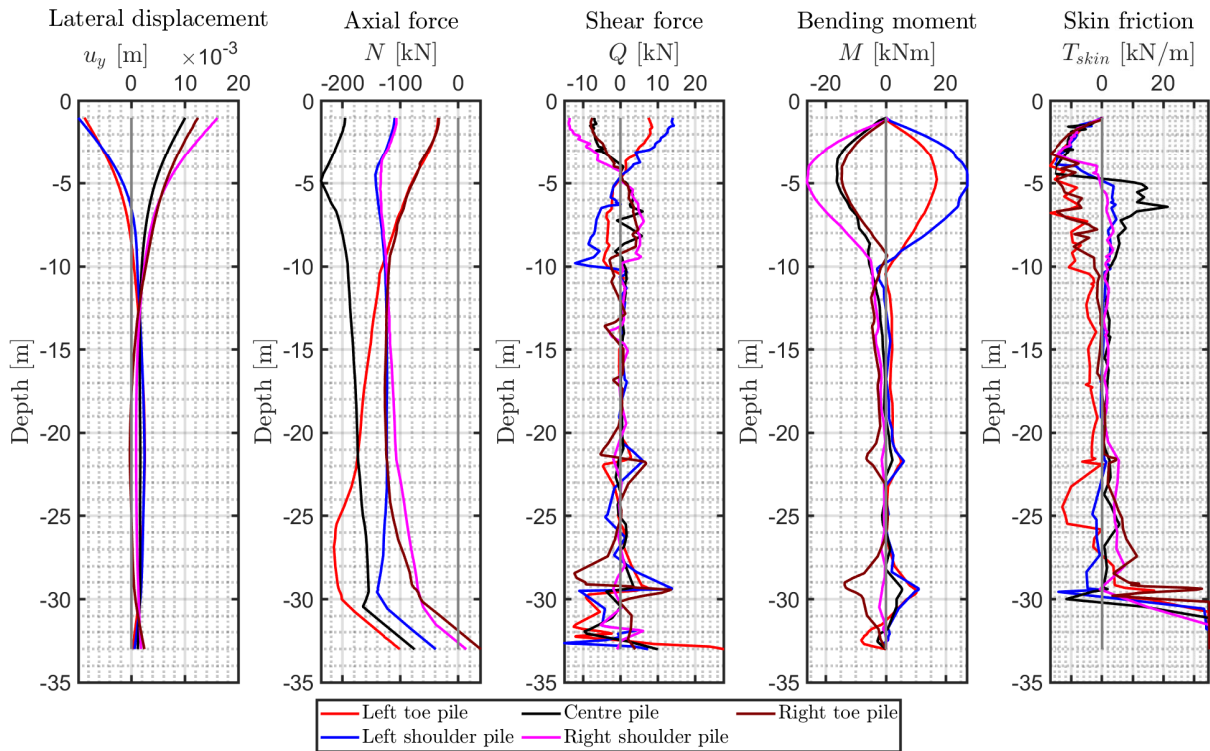
Figure C.25: Piles behaviour in case of 15° bearing layer inclination

Tensile force developed in the geogrid is shown in the fig. C.26.
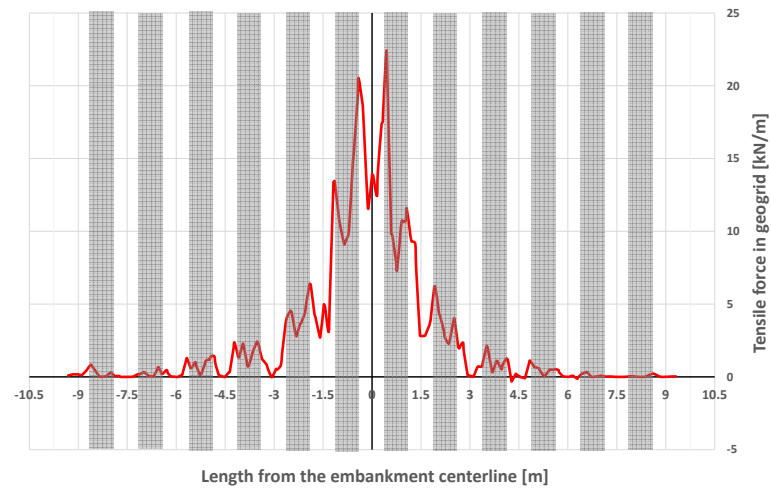
Figure C.26: Forces developed within the geogrid in case of 15° bearing layer inclination

Settlement of the geogrid is reported in the fig. C.27.
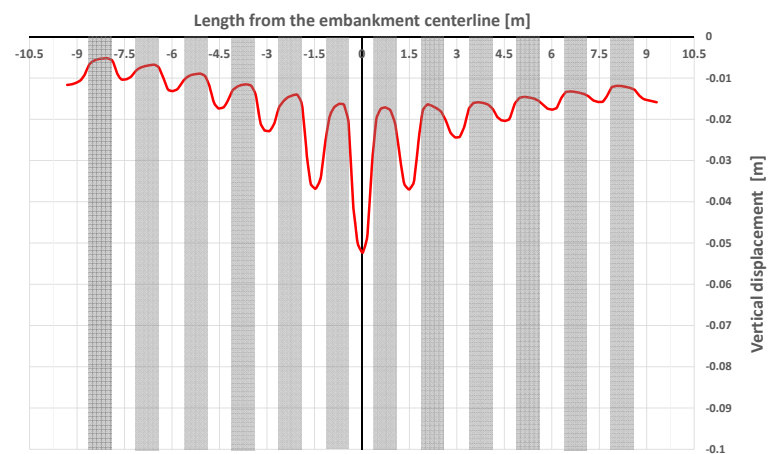
Figure C.27: Vertical displacement of the geogrid in case of 15° bearing layer inclination

Iso-lines of settlement is reported in the fig. C.28.
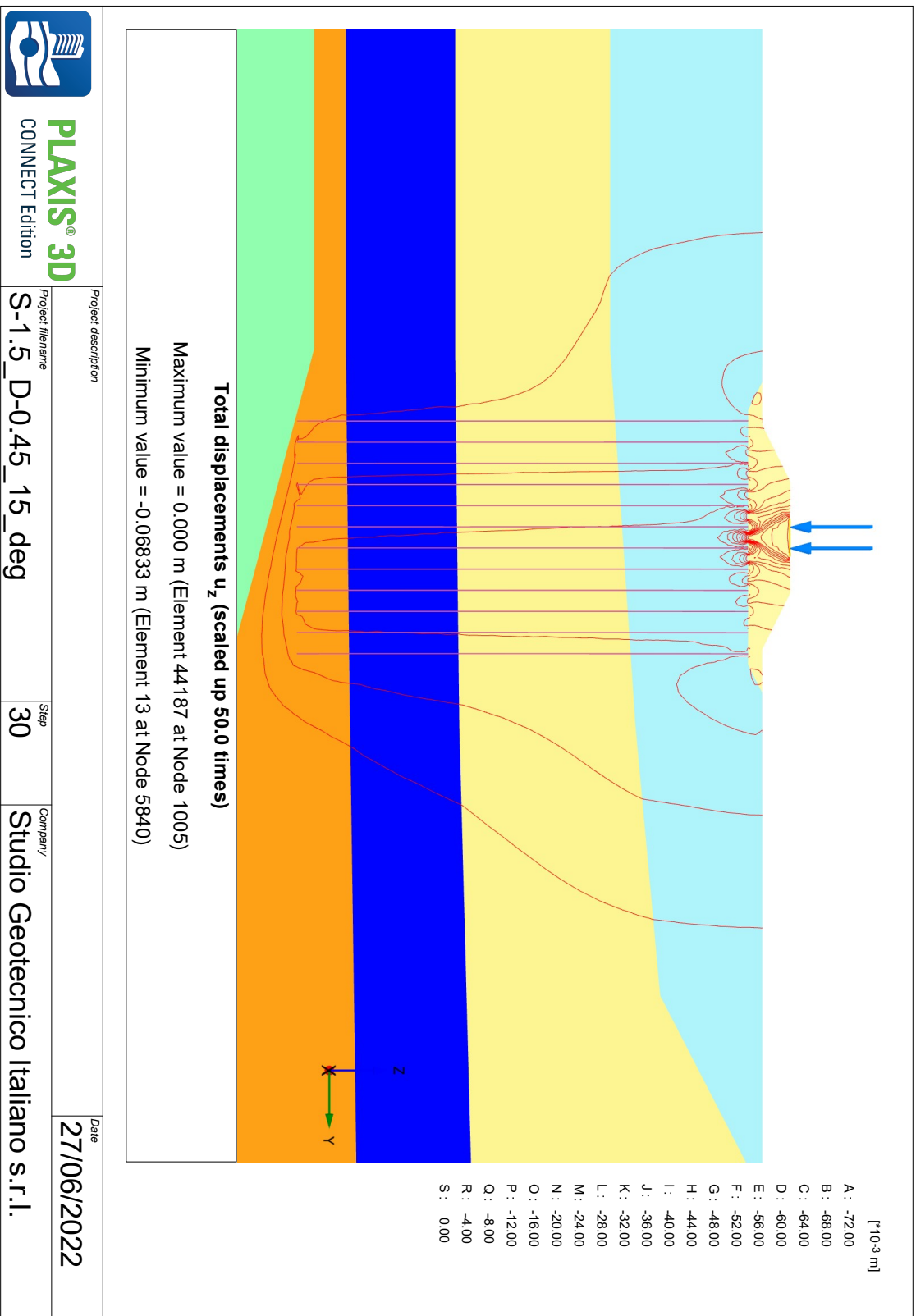
Figure C.28: Iso-lines of developed displacement within the system, 15° bearing layer inclination

C.6. Inclination of $20°$

General view of the system is represented in the fig. C.29.
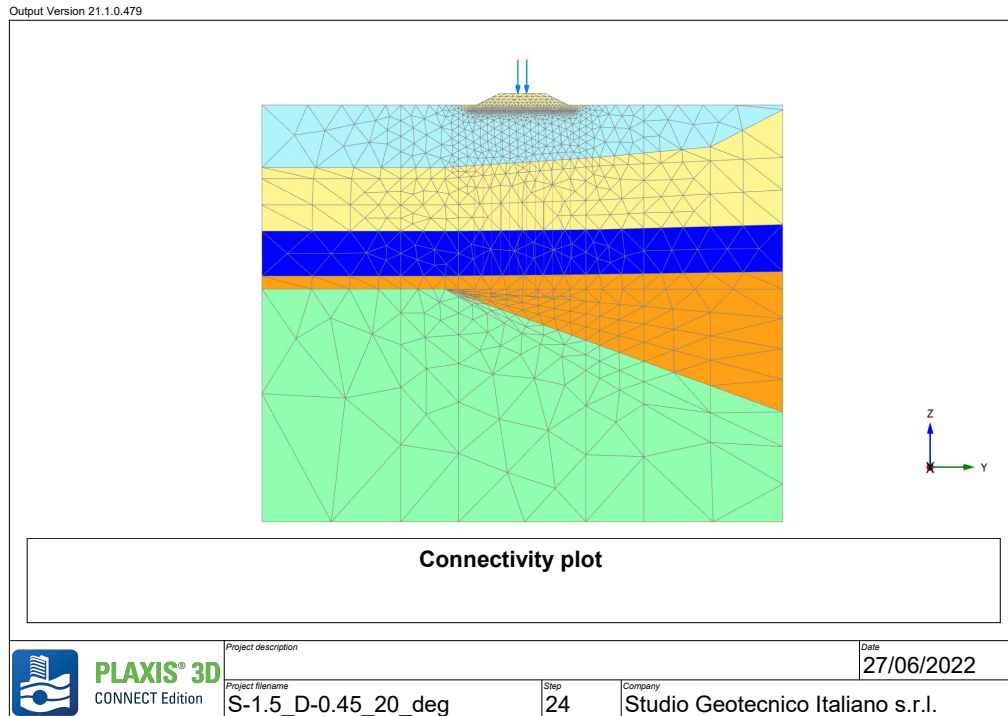
Figure C.29: Model view for the case of 20° bearing layer inclination

Displacement within the embankment body is shown in the fig. C.30. Maximum settlement developed along the centreline is 0.071 m.
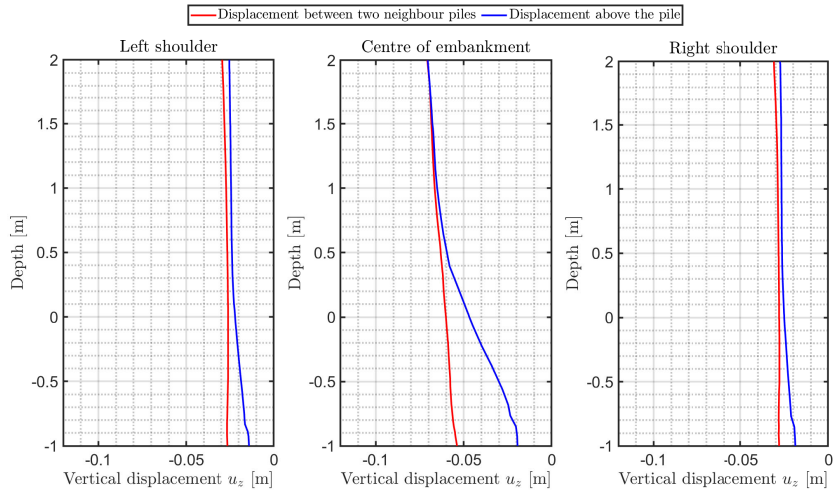
Figure C.30: Vertical displacement developed in the embankment in case of 20° bearing layer inclination

The piles response is reported in the fig. C.31.
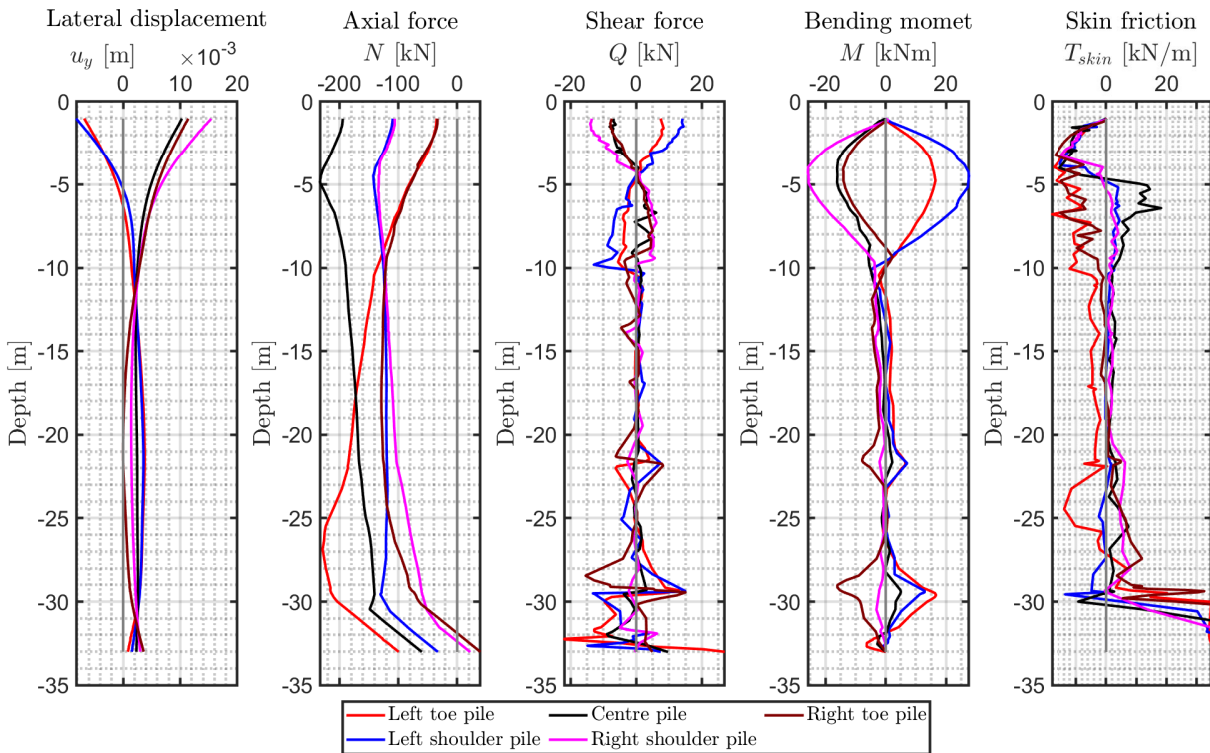
Figure C.31: Piles behaviour in case of 20° bearing layer inclination

Tensile force developed in the geogrid is shown in the fig. C.32.
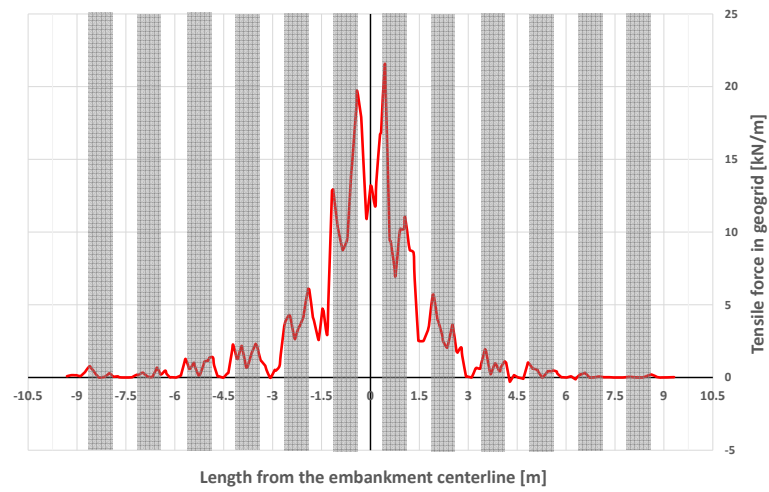
Figure C.32: Forces developed within the geogrid in case of 20° bearing layer inclination

Settlement of the geogrid is reported in the fig. C.33.
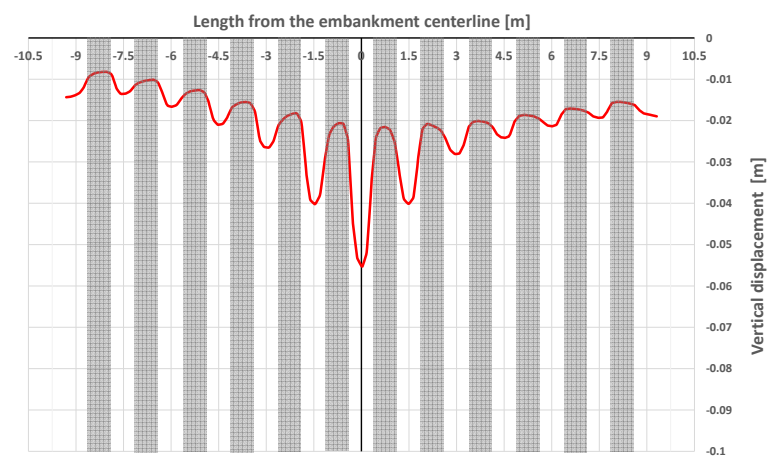
Figure C.33: Vertical displacement of the geogrid in case of 20° bearing layer inclination

Iso-lines of settlement is reported in the fig. C.34.
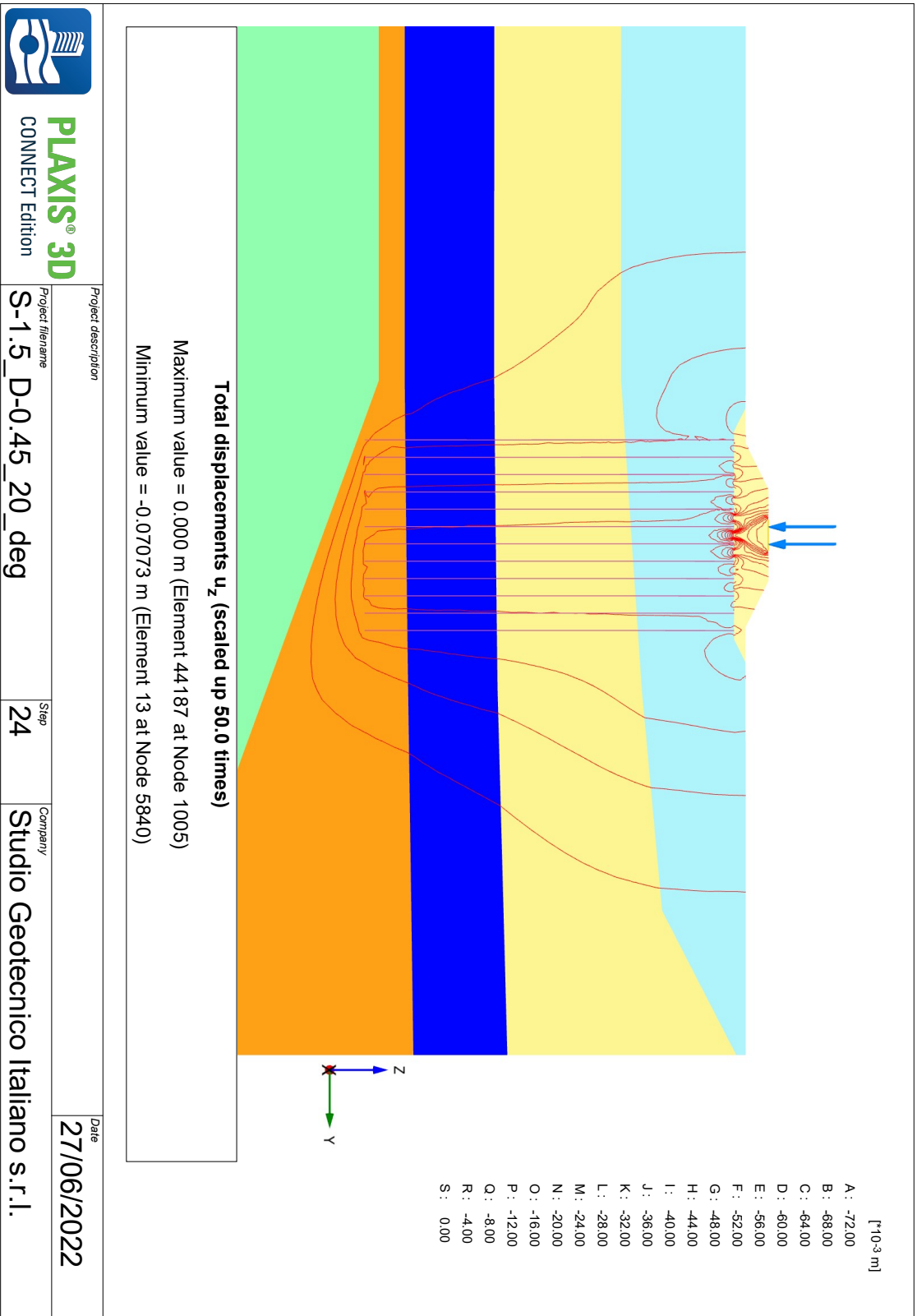
Figure C.34: Iso-lines of developed displacement within the system, 20° bearing layer inclination

C.7.   Inclination of $25°$

General view of the system is represented in the fig. C.35.
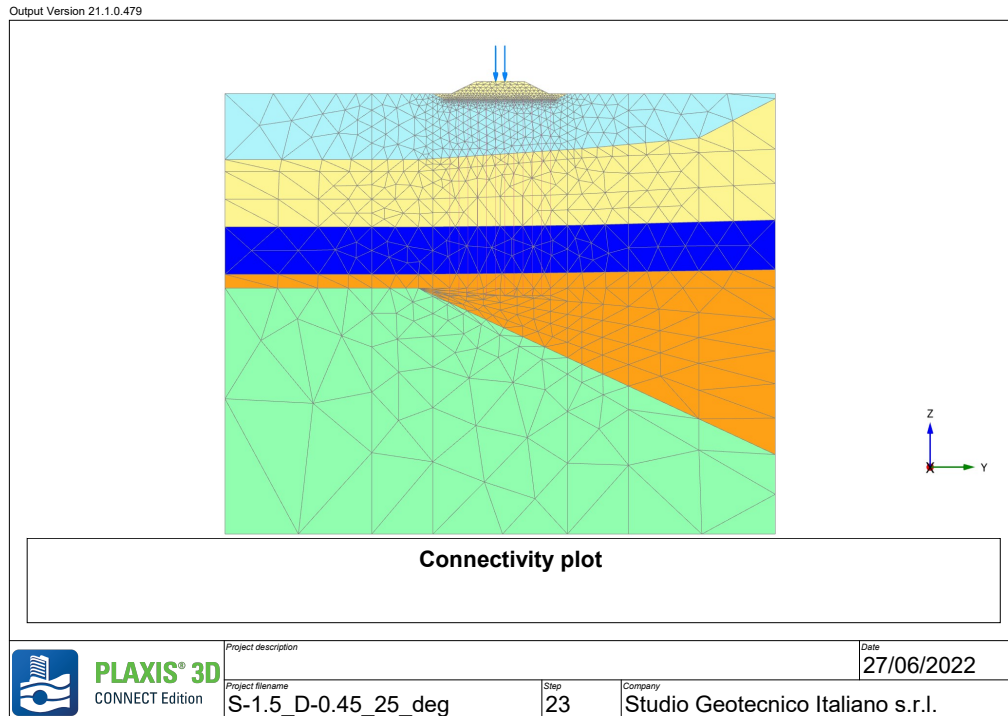
Figure C.35: Model view for the case of 25° bearing layer inclination

Displacement within the embankment body is shown in the fig. C.36. Maximum settlement developed along the centreline is 0.073 m.
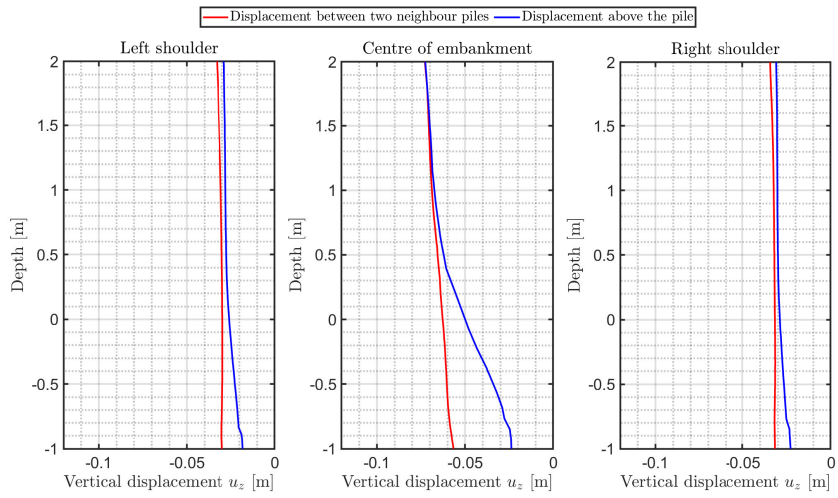
Figure C.36: Vertical displacement developed in the embankment in case of 25° bearing layer inclination

The piles response is reported in the fig. C.37.
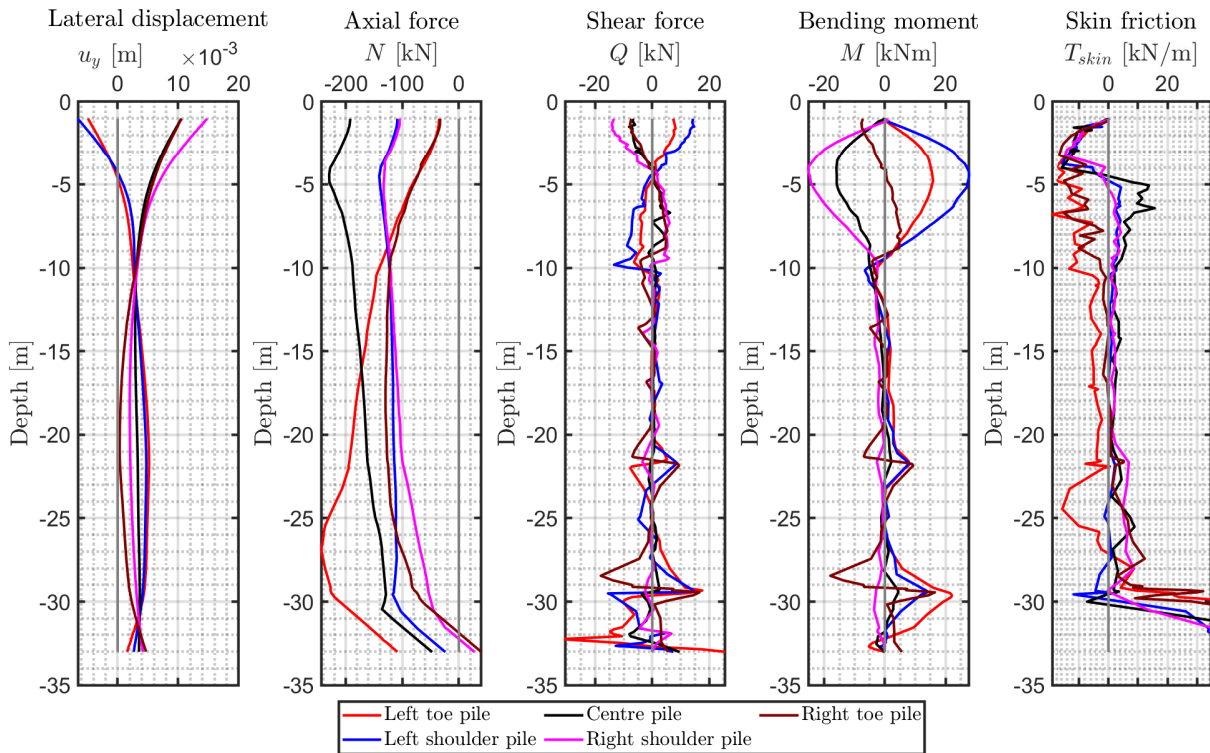
Figure C.37: Piles behaviour in case of 25° bearing layer inclination

Tensile force developed in the geogrid is shown in the fig. C.38.
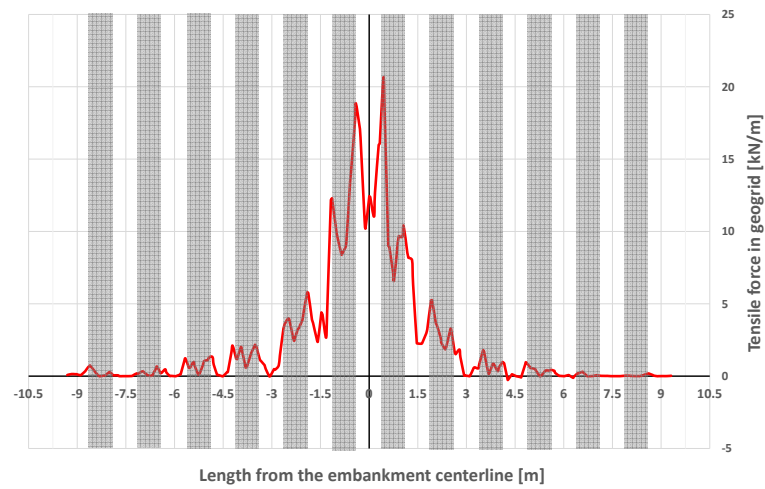
Figure C.38: Forces developed within the geogrid in case of 25° bearing layer inclination

Settlement of the geogrid is reported in the fig. C.39.
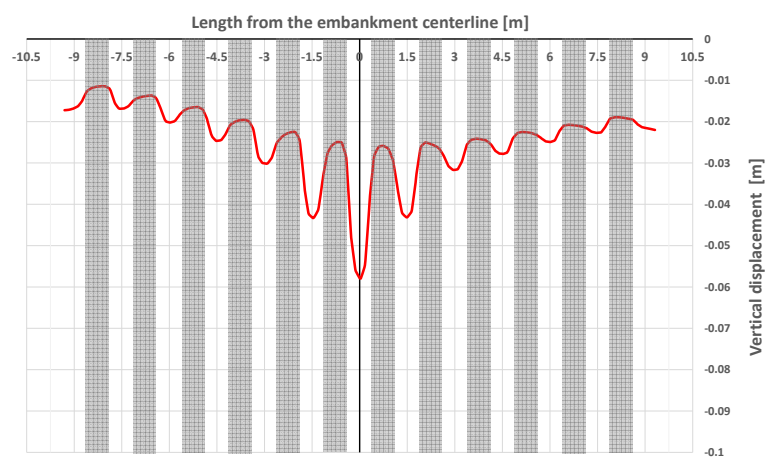
Figure C.39: Vertical displacement of the geogrid in case of 25° bearing layer inclination

Iso-lines of settlement is reported in the fig. C.40.
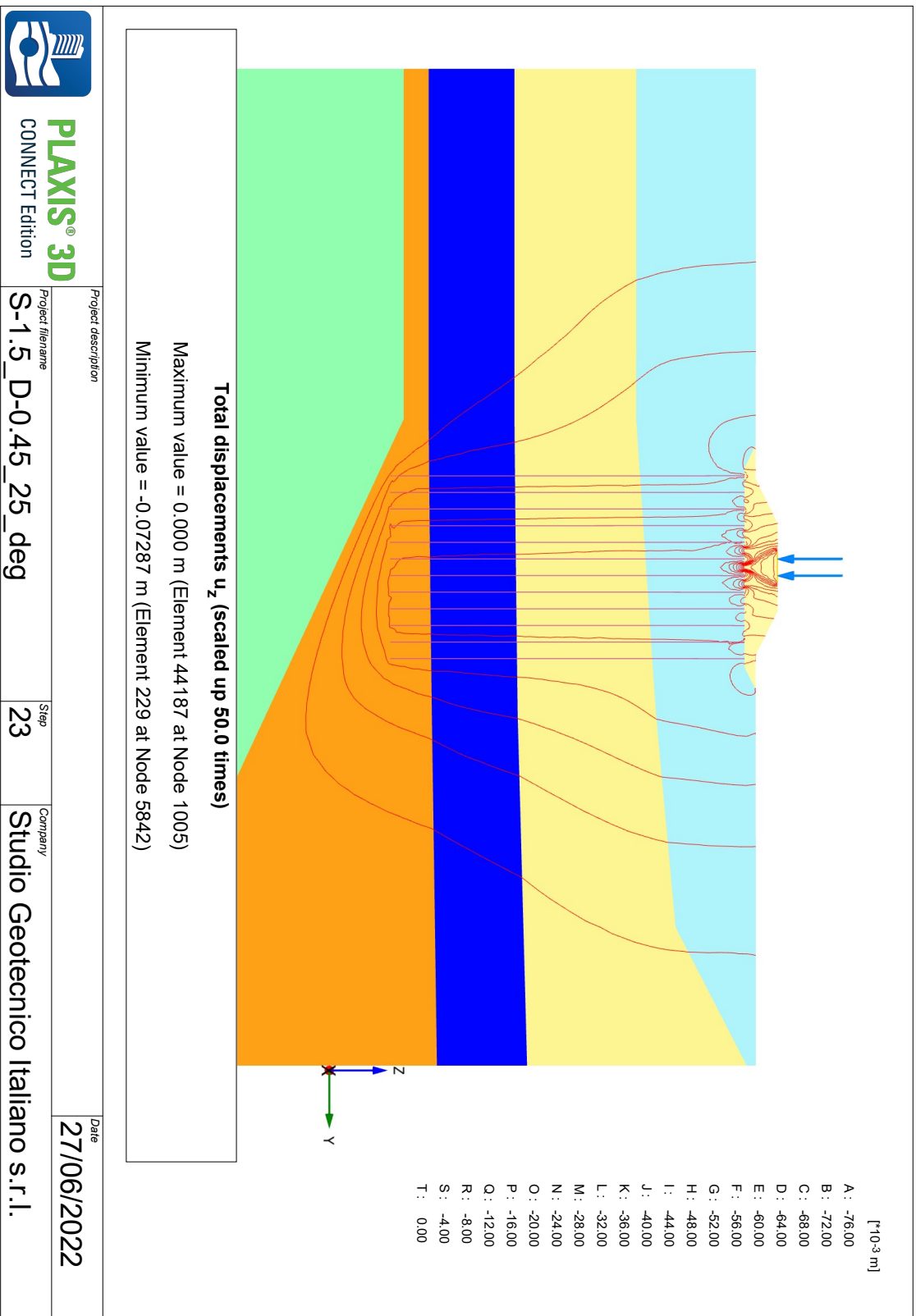
Figure C.40: Iso-lines of developed displacement within the system, 25° bearing layer inclination

C.8.   Inclination of $30°$

General view of the system is represented in the fig. C.41 and 3D model view is given in fig. C.42.
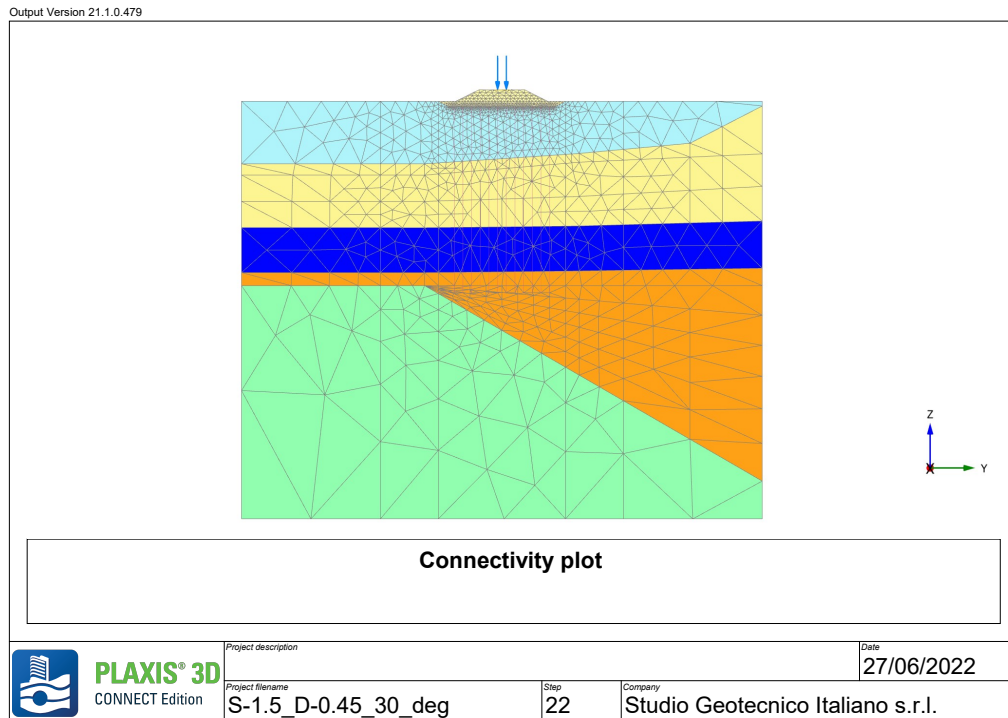
Figure C.41: Model view for the case of 30° bearing layer inclination
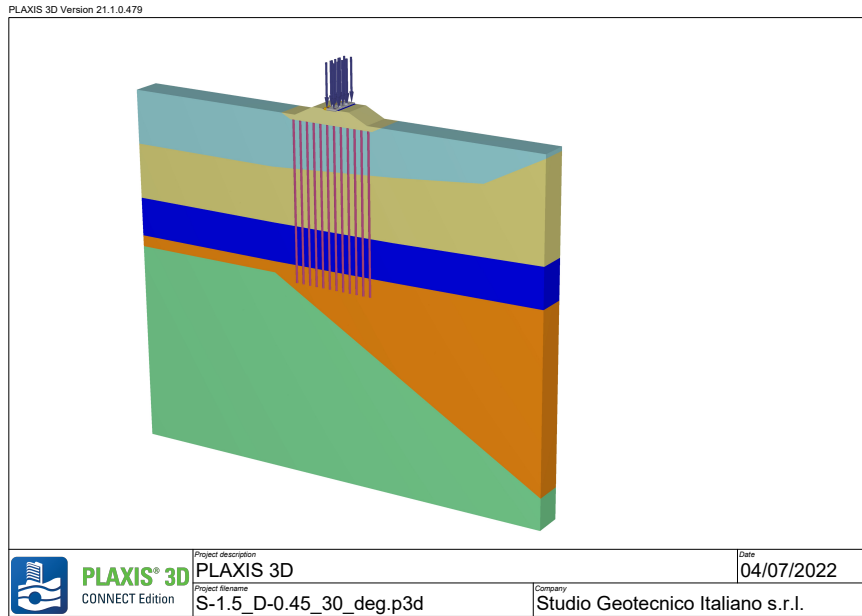
Figure C.42: 3D model view for the case of 30° bearing layer inclination

Displacement within the embankment body is shown in fig. C.43 and 3D view of the settlement is shown in fig. C.44. Maximum settlement developed along the centreline is 0.075 m.
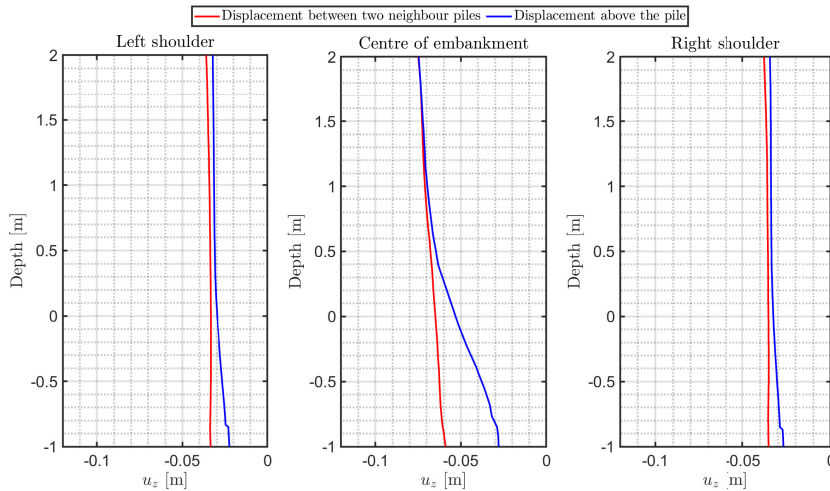
Figure C.43: Vertical displacement developed in the embankment in case of 30° bearing layer inclination
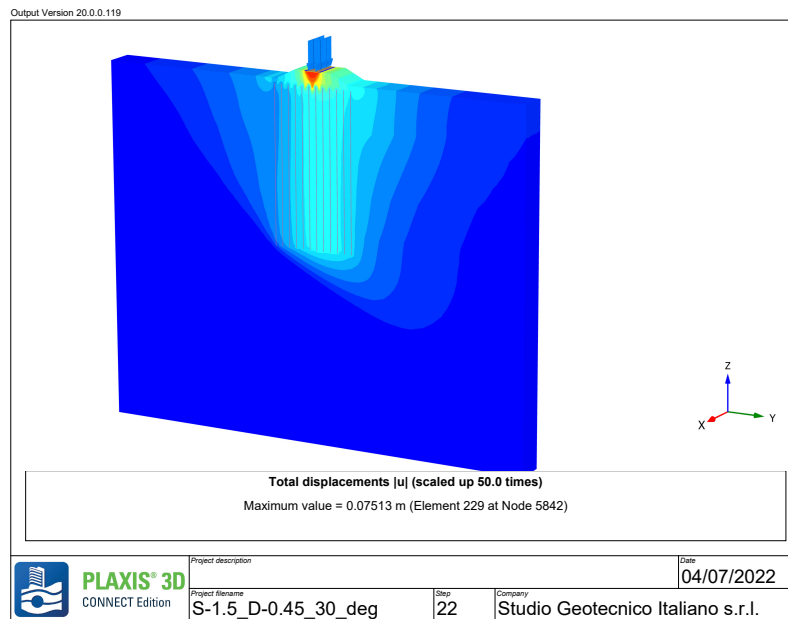
Figure C.44: 3D model view of system's settlement for the case of 30° bearing layer inclination

The piles response is reported in the fig. C.45.
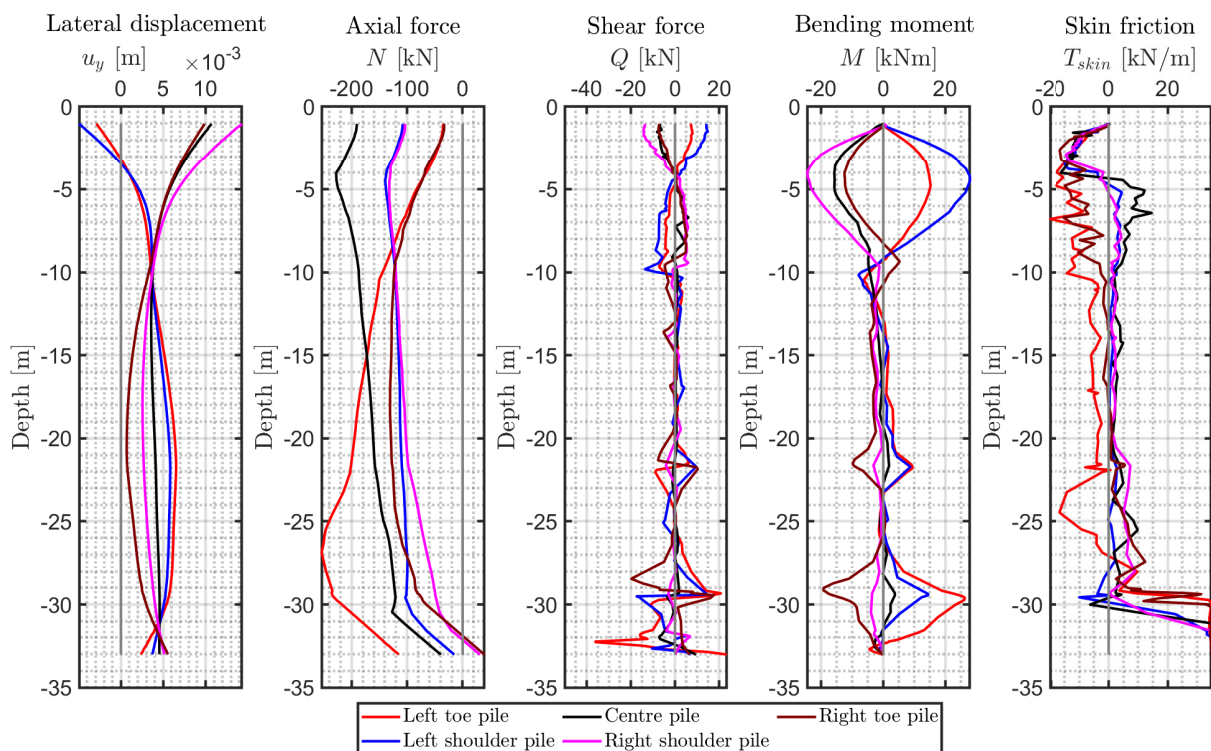
Figure C.45: Piles behaviour in case of 30° bearing layer inclination

Tensile force developed in the geogrid is shown in the fig. C.46.
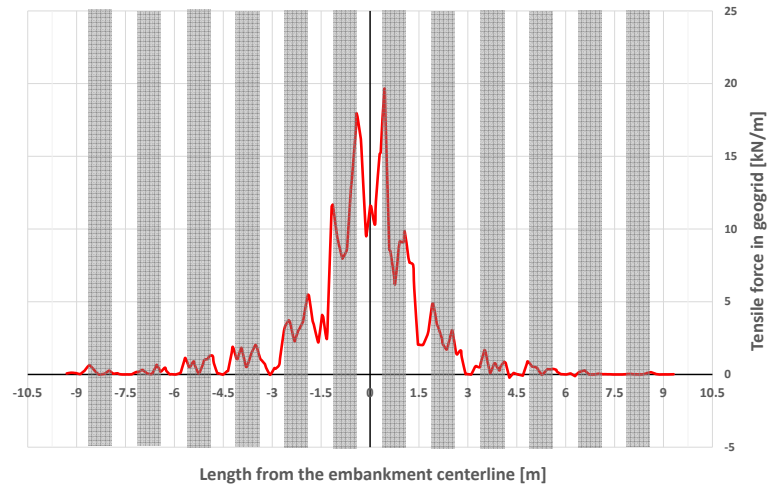
Figure C.46: Forces developed within the geogrid in case of 30° bearing layer inclination

Settlement of the geogrid is reported in the fig. C.47.
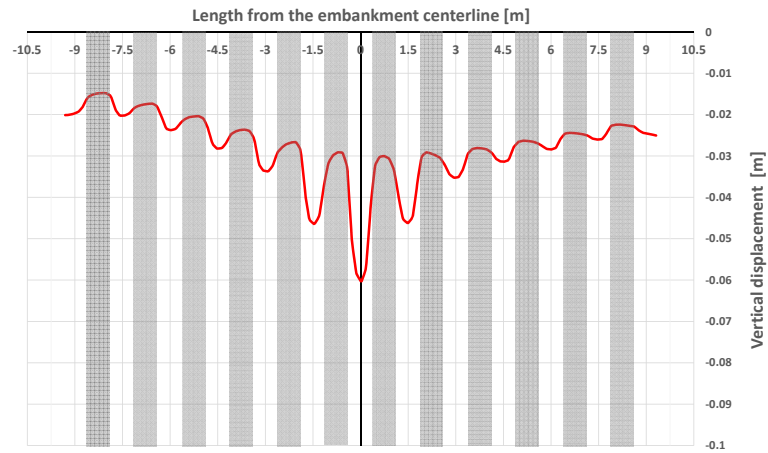
Figure C.47: Vertical displacement of the geogrid in case of 30° bearing layer inclination

Iso-lines of settlement is reported in the fig. C.48.
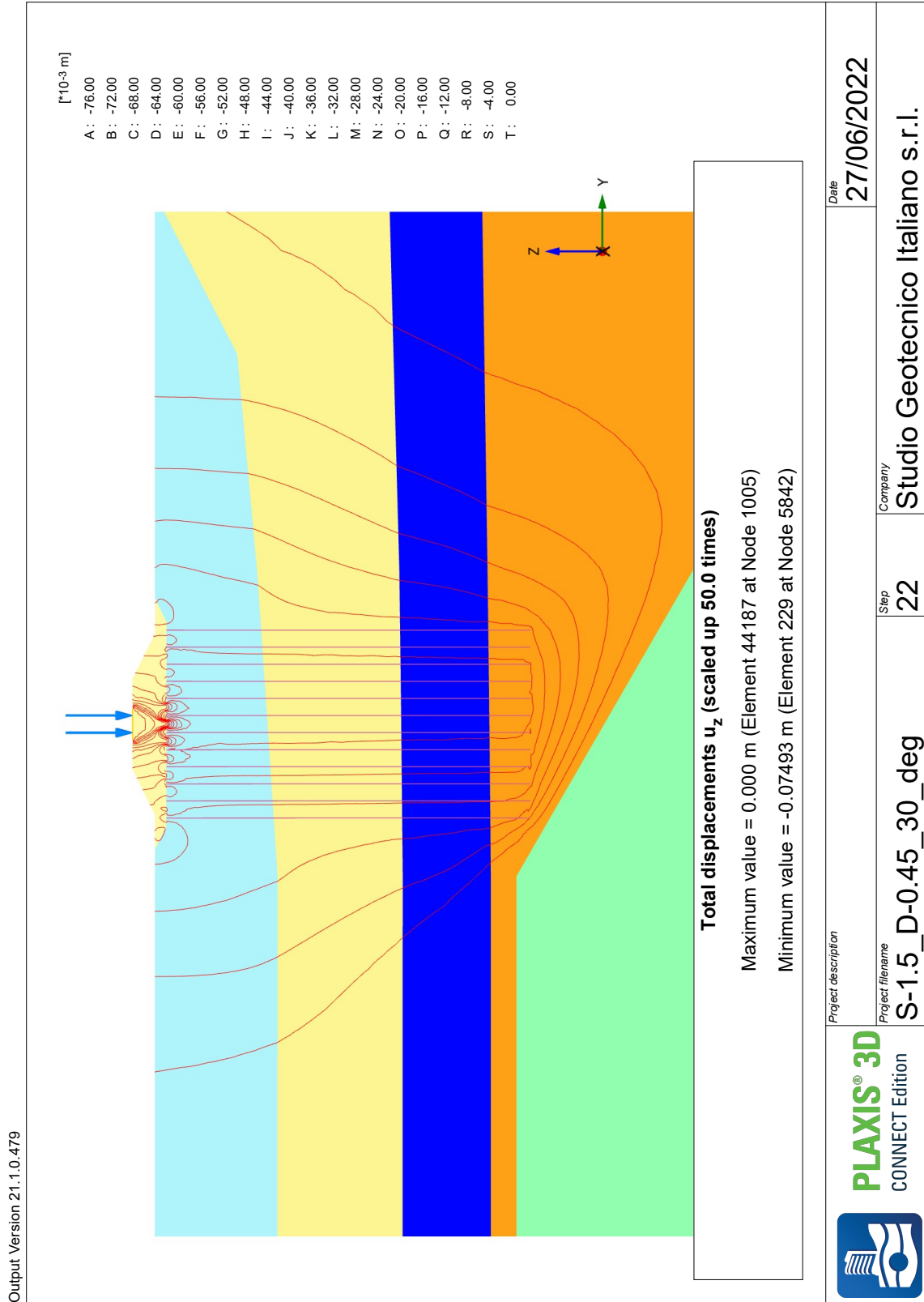
Figure C.48: Iso-lines of developed displacement within the system, 30° bearing layer inclination

C.9.   Implementation of solution

General view of the system is represented in the fig. C.49.
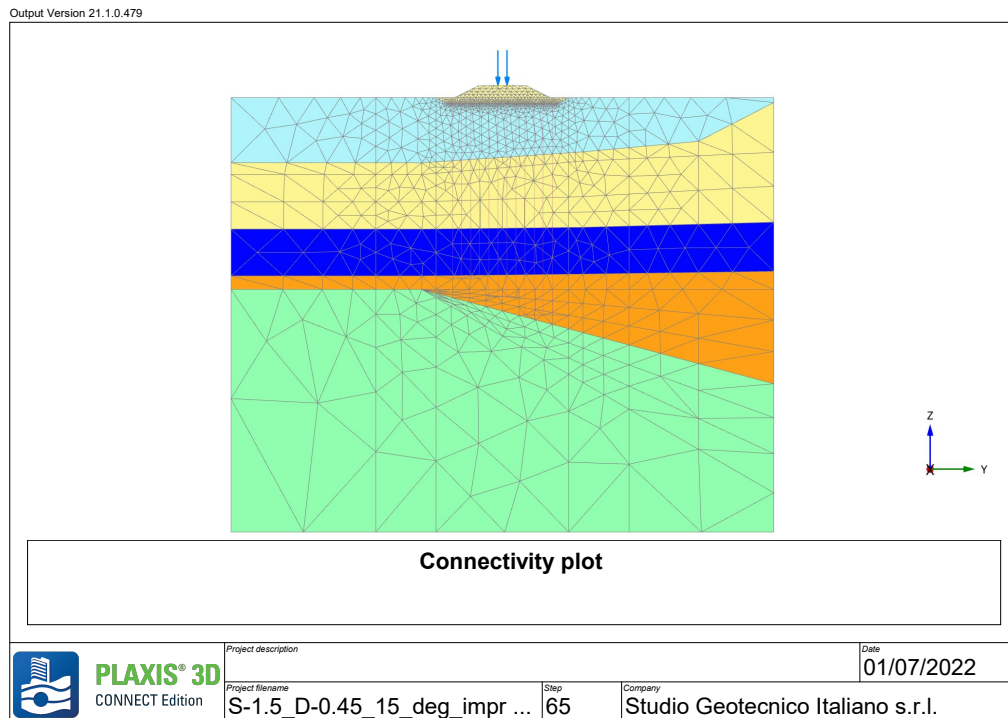
Figure C.49: Model view for the case of 15° bearing layer inclination with stepwise pile groups

Displacement within the embankment body is shown in the fig. C.50. Maximum settlement developed along the centreline is 0.046 m.
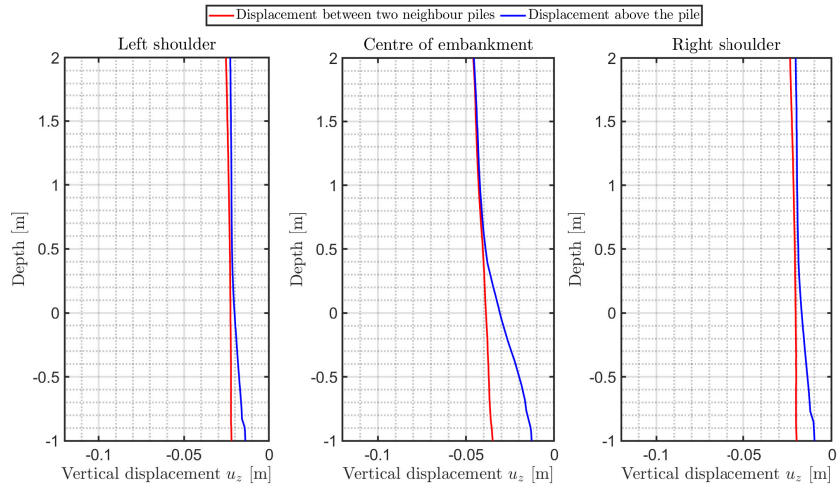
Figure C.50: Vertical displacement developed in the embankment in case of 15° bearing layer inclination with stepwise pile groups

The piles response is reported in the fig. C.51.
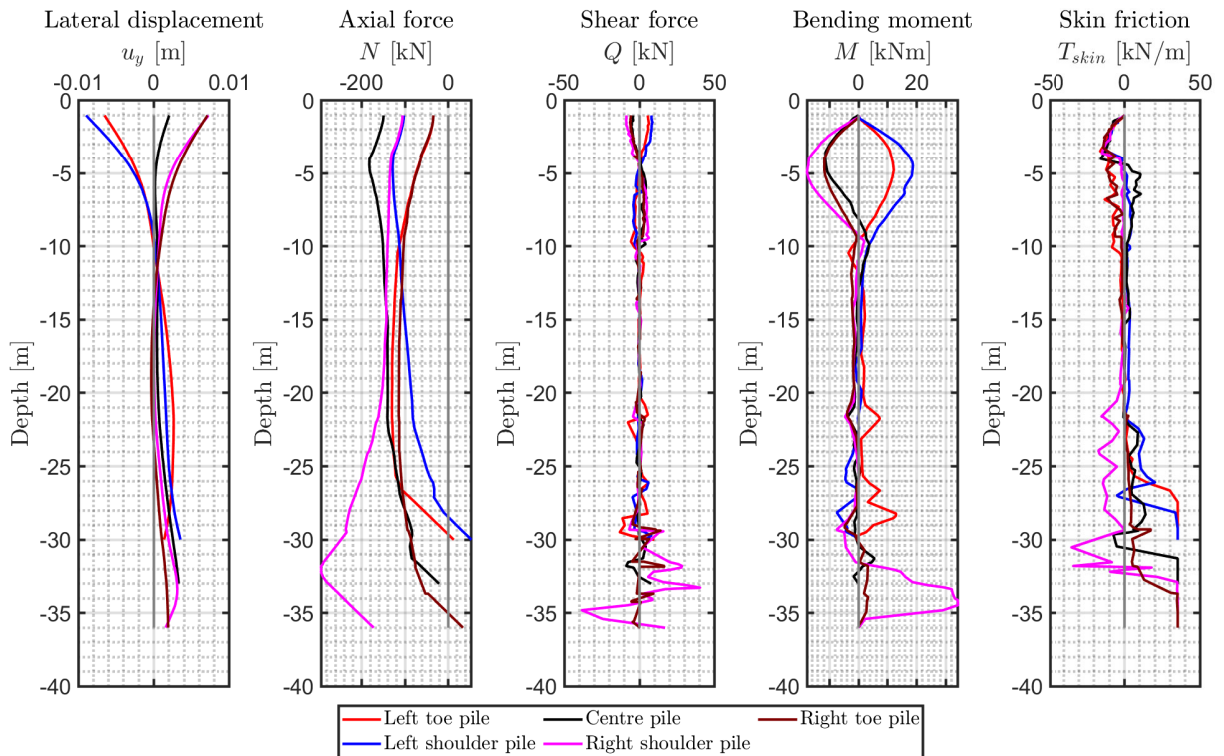
Figure C.51: Piles behaviour in case of 15° bearing layer inclination with stepwise pile groups

Tensile force developed in the geogrid is shown in the fig. C.52.
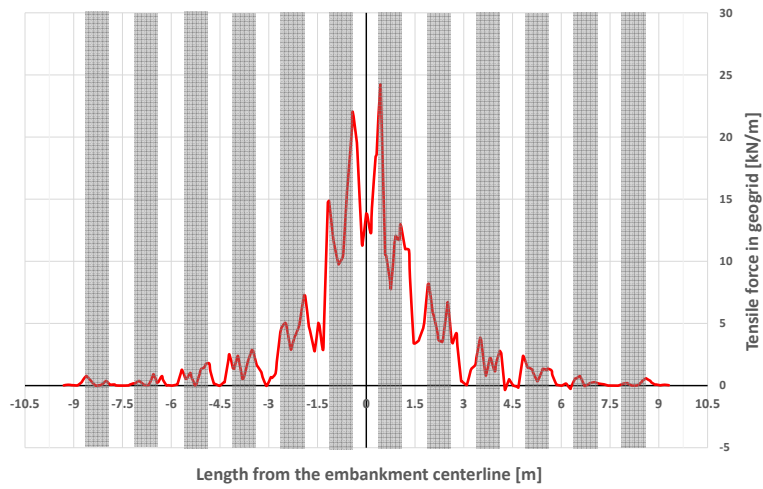
Figure C.52: Forces developed within the geogrid in case of 15° bearing layer inclination with stepwise pile groups

Settlement of the geogrid is reported in the fig. C.53.
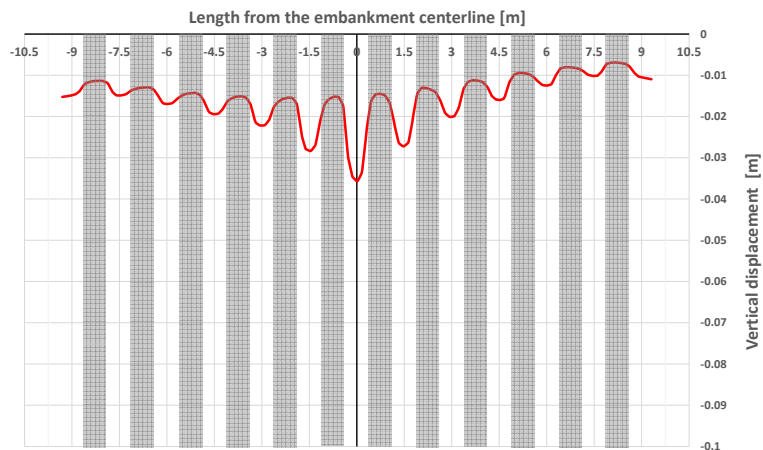
Figure C.53: Vertical displacement of the geogrid in case of 15° bearing layer inclination with stepwise pile groups

Iso-lines of settlement is reported in the fig. C.54.
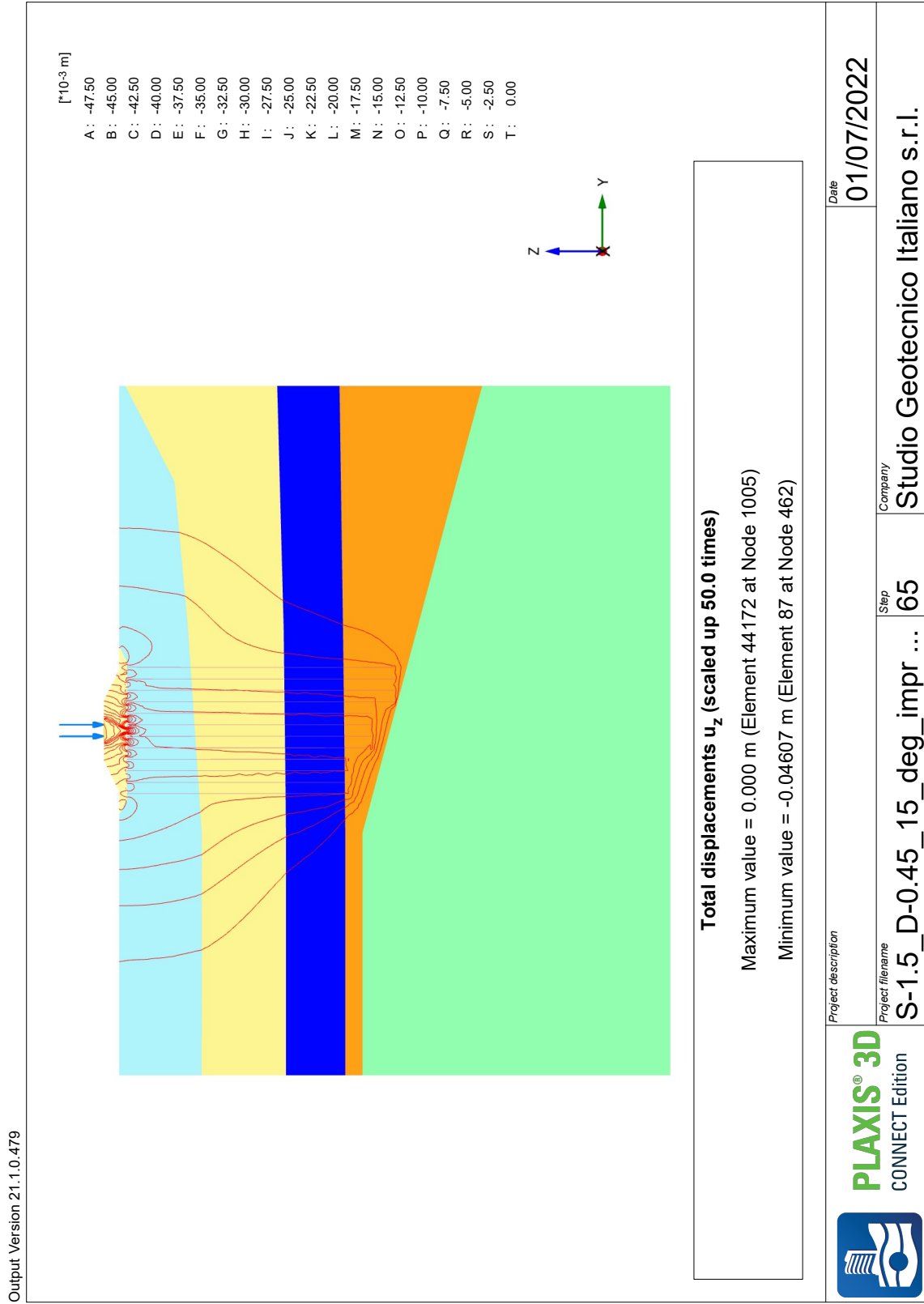
Figure C.54: Iso-lines of developed displacement within the system, case of 15° bearing layer inclination with stepwise pile groups

D | Graphical part

In this appendix the graphical part is contained.
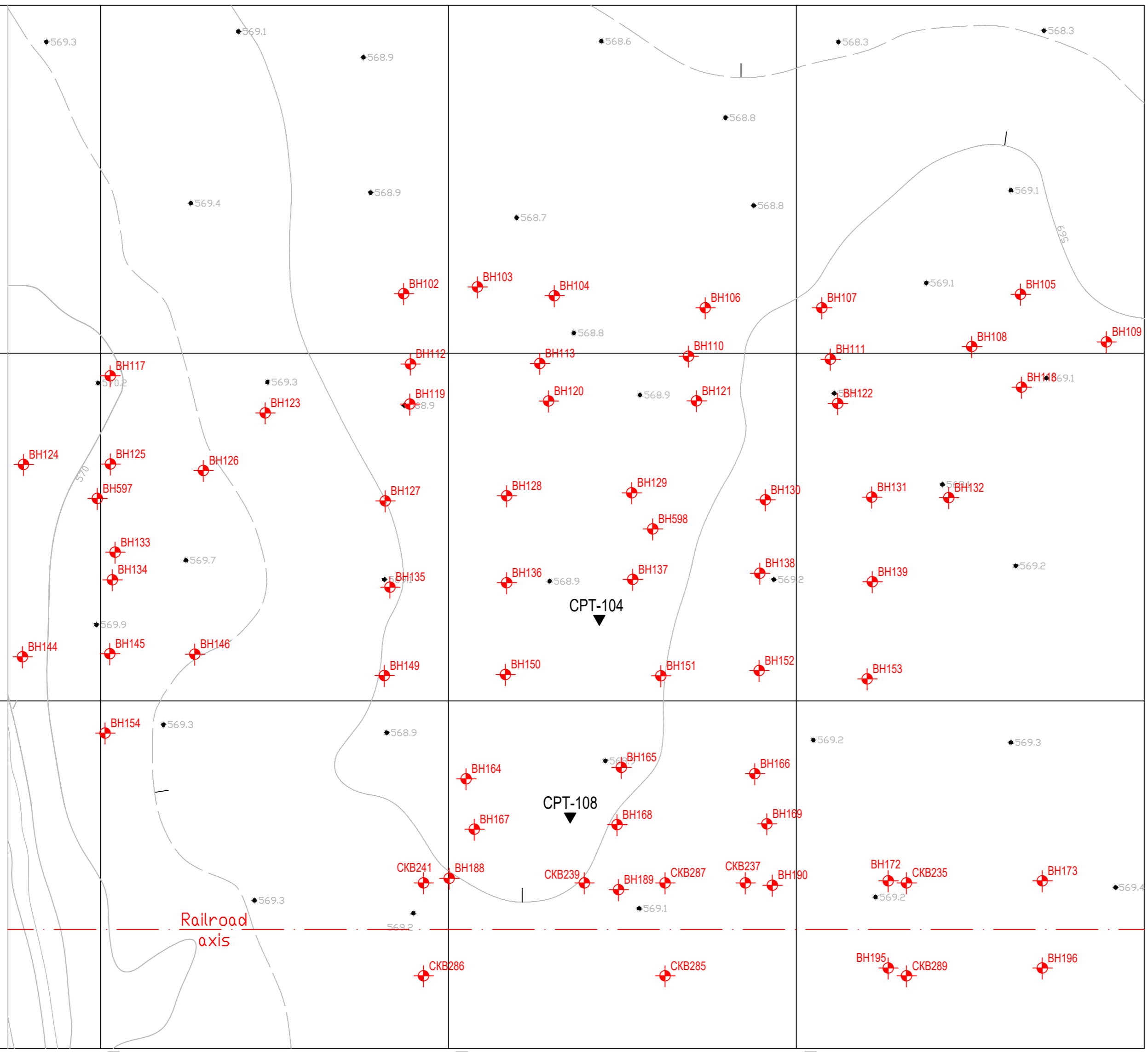
Legend

⊕ – Borehole

▼ – Cone Penetration Test (CPT)

• – Surface elevation point

— – Elevation line

Railroad axis

CPT-104

CPT-108

Page
1-1

SECTION 1

Boreholes	BH135	BH136	BH137 BH598	BH138
CPT, CH, DH			CPT104	

Elevation (m a.s.l.)

570
565
560
555
550
545
540
535
530
525
520
515
510
505
500

Nspt
30 20 10

Nspt
30 20 10

qc [MPa]
20 15 10 5

Nspt
10 20 30 40 50

Nspt
10 20 30

S1
S2
S3
S4
S5

S3
S5
S8
S11

S1
S1
S2
S3
S3
S4
S5
S6
S7
S8
S11

S1
S2
S3
S5

Scale:
V 1:200
H 1:1000

Ground level, m a.s.l.	152.30 568.8	185.78 568.5	212.45 568.5 222.05 568.5 227.78 568.5	258.56 568.5
Progressive distance, m				

Legend

- EGE-1.2	- EGE-2.2	- EGE-4
- EGE-1.1	- EGE-2.3	S7 - Sample
- EGE-2.1	- EGE-3	

Page
2-2

SECTION 2

Boreholes		BH149	BH150	BH151	BH152
CPT, CH, DH					

Elevation (m a.s.l.)
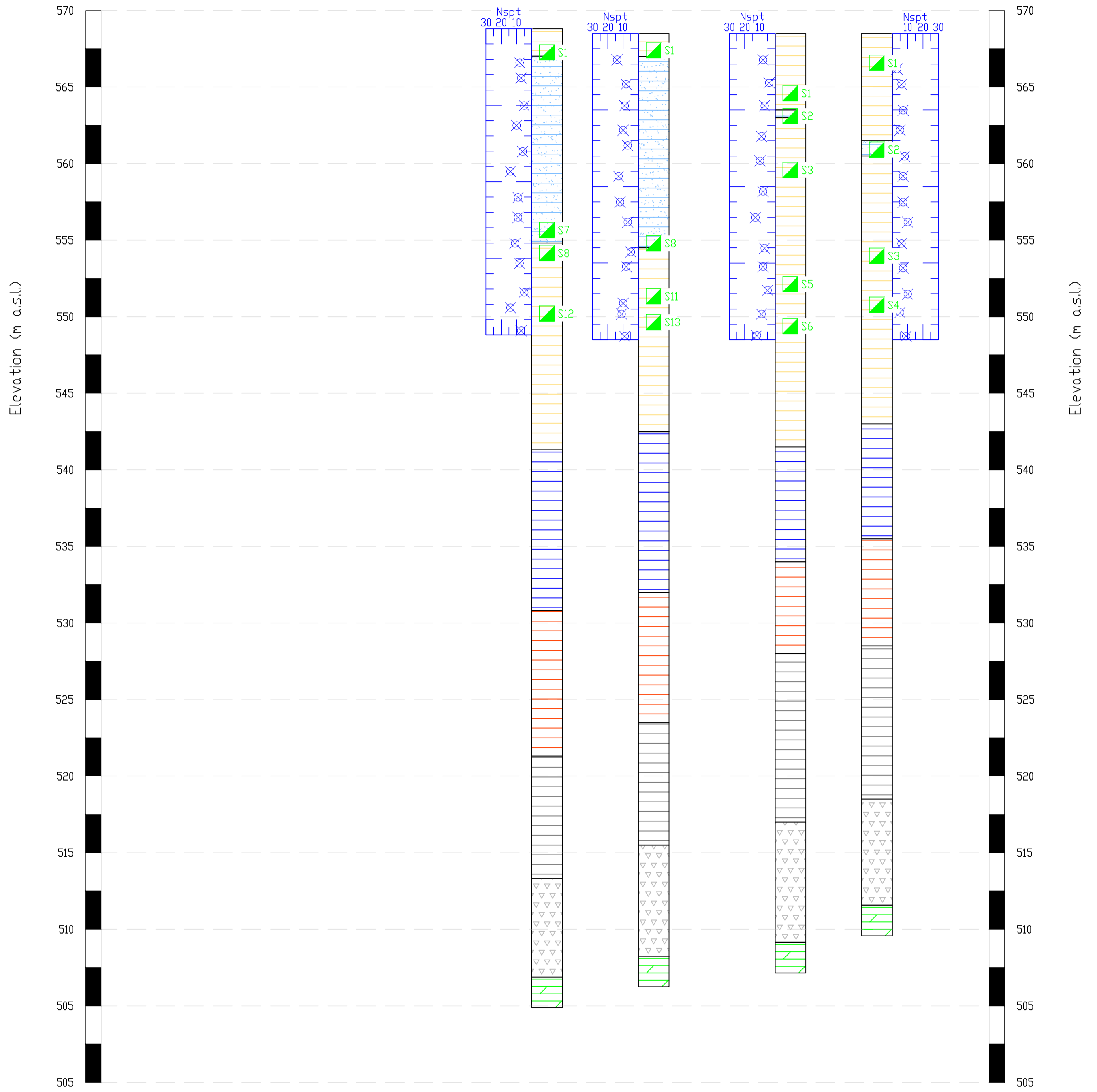
Scale:
V 1:200
H 1:1000

Ground level, m a.s.l.		568.8	568.5	568.5	568.5
Progressive distance, m		150.66	185.47	230.14	258.39

Legend

	– EGE-1.2		– EGE-2.2		– EGE-4
	– EGE-1.1		– EGE-2.3	S7	– Sample
	– EGE-2.1		– EGE-3		

SECTION 3

Boreholes		BH164	BH165	BH166
CPT, CH, DH				

Elevation (m a.s.l.)

Nspt
30 20 10

Scale:
V 1:200
H 1:1000

Ground level, m a.s.l.		568.6	568.5	568.6
Progressive distance, m		174.17	218.76	257.11

Legend

- EGE-1.2
- EGE-1.1
- EGE-2.1
- EGE-2.2
- EGE-2.3
- EGE-3
- EGE-4
- S7 – Sample

SECTION 4

Boreholes		BH167	BH168	BH169
CPT, CH, DH		CPT108		
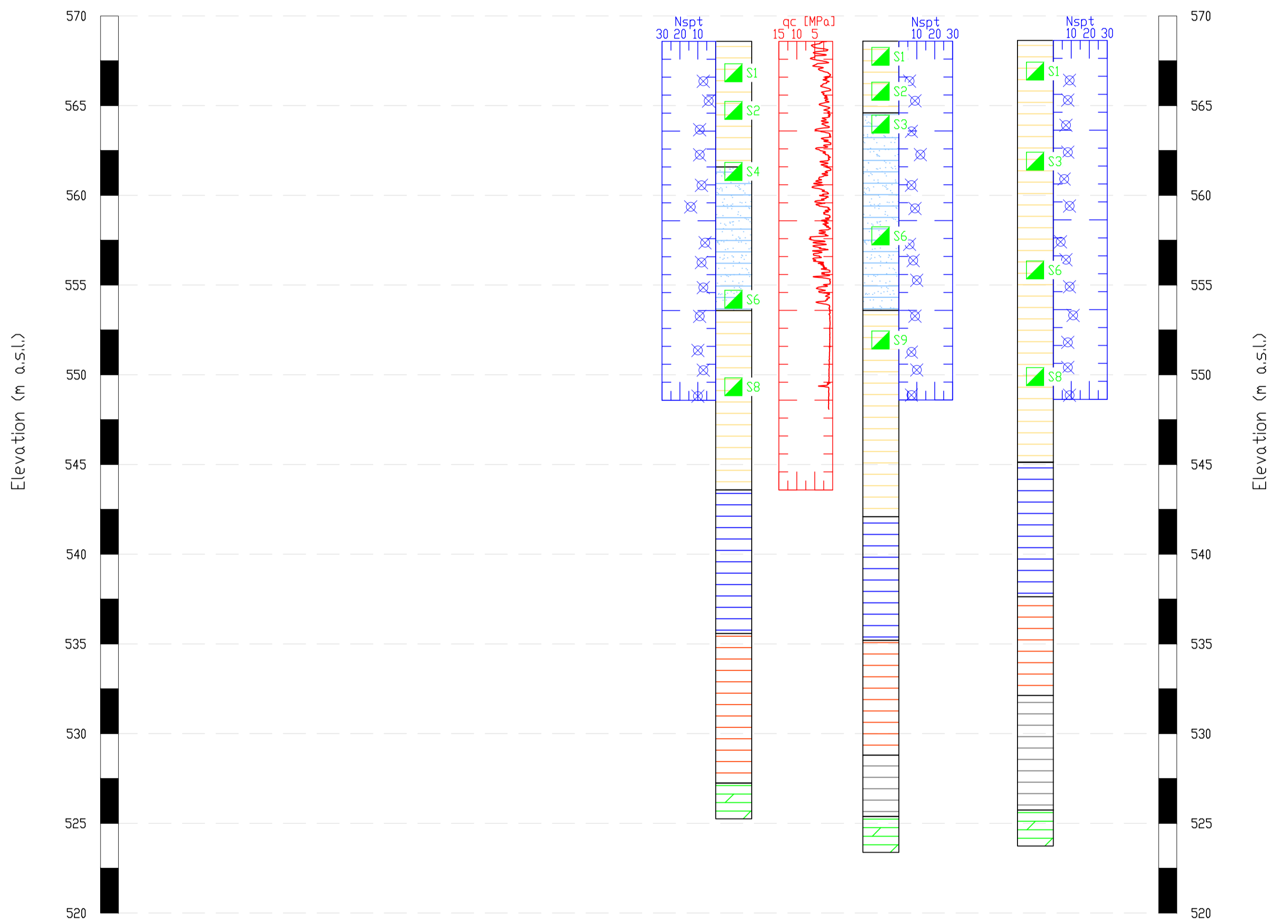
Scale:
V 1:200
H 1:1000

Ground level, m a.s.l.		568.6	568.6	568.6	568.6
Progressive distance, m		176.52	204.09	217.53	260.62

Legend

- EGE-1.2   - EGE-2.2   - EGE-4

- EGE-1.1   - EGE-2.3   S7 - Sample

- EGE-2.1   - EGE-3

SECTION 5

Boreholes		CKB241	BH188		CKB239	BH189	CKB287		CKB237	BH190
CPT, CH, DH										

Scale:
V 1:200
H 1:1000

Ground level, m a.s.l.		569.3	568.7		568.8	568.7	568.5		568.6	568.7
Progressive distance, m		161.91	169.31		208.14	217.96	254.44		231.33	262.18

Legend

- EGE-1.2   - EGE-2.2   - EGE-4
- EGE-1.1   - EGE-2.3   S7 - Sample
- EGE-2.1   - EGE-3

Page
2-6

SECTION 6

Boreholes	CKB286	CKB285
CPT, CH, DH		

Elevation (m a.s.l.)

570	570
565	565
560	560
555	555
550	550
545	545
540	540
535	535
530	530
525	525

Elevation (m a.s.l.)
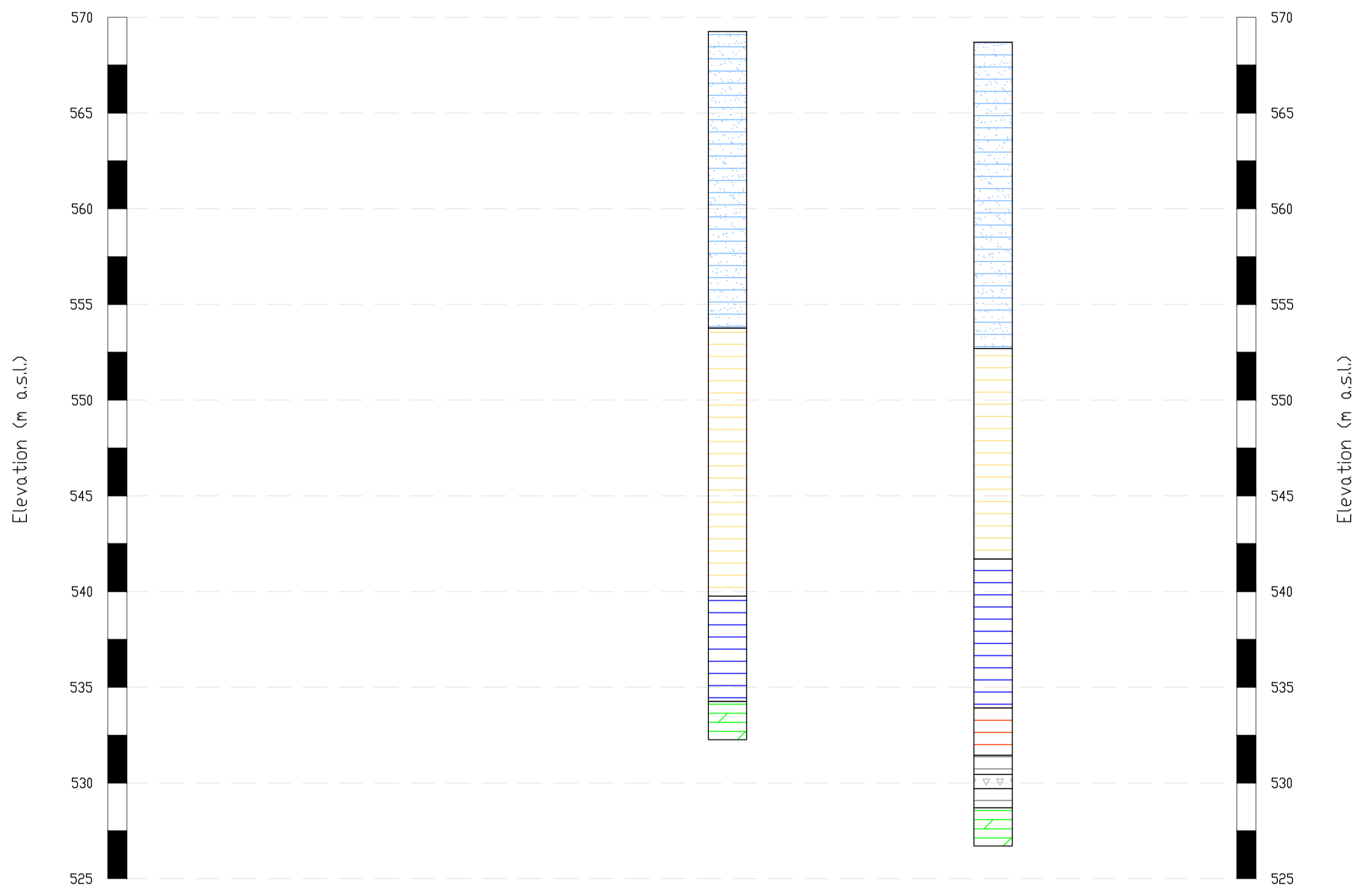
Scale:
V 1:200
H 1:1000

Ground level, m a.s.l.	569.3	568.7
Progressive distance, m	161.91	231.33

Legend

- EGE-1.2   - EGE-2.2   - EGE-4

- EGE-1.1   - EGE-2.3   S7 - Sample

- EGE-2.1   - EGE-3

SECTION A

Boreholes	BH598	BH37		BH151	BH165	BH168	CKB287 BH189	CKB285
CPT, CH, DH			CPT104			CPT108		
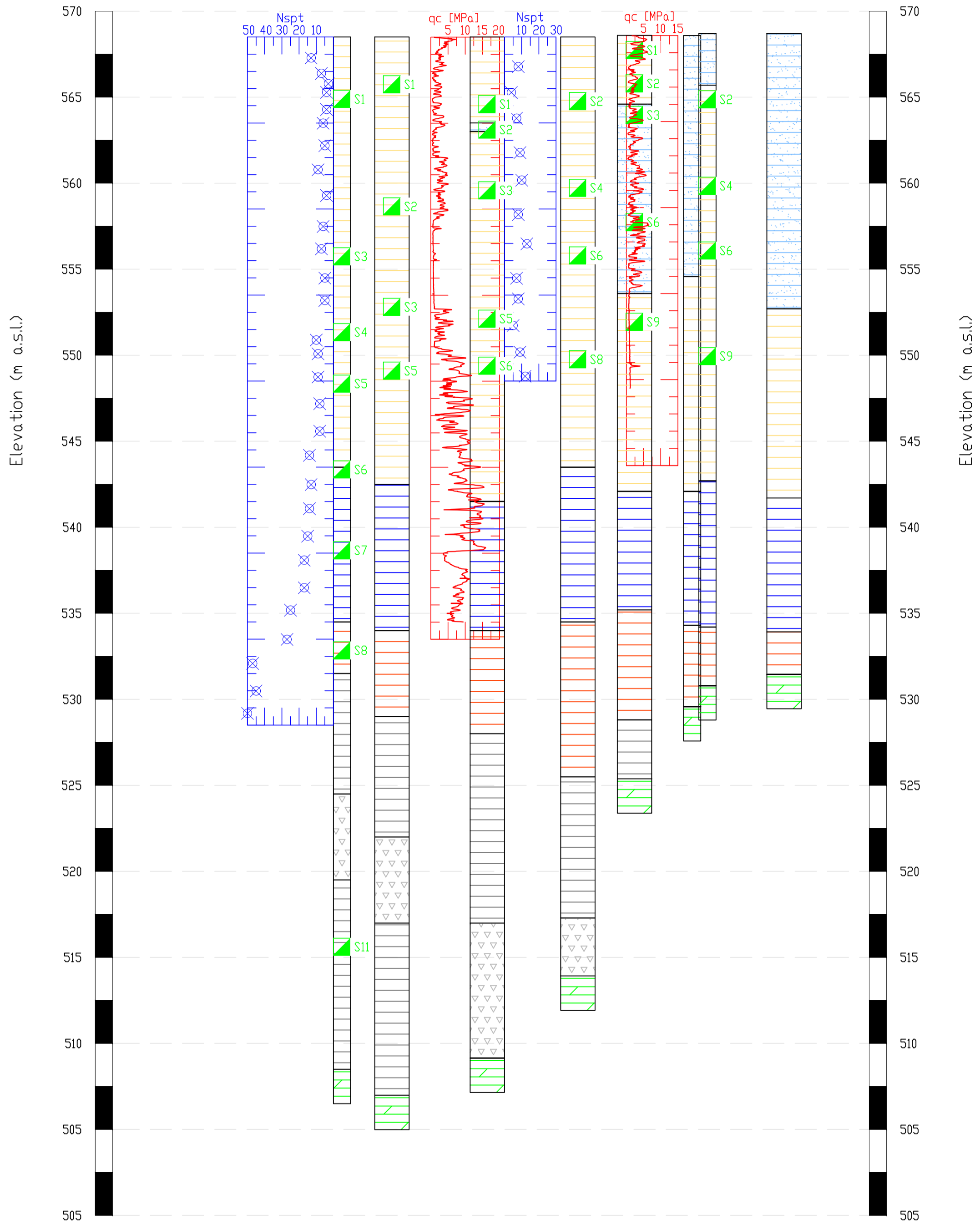
Scale:
V 1:200
H 1:1000

Ground level, m a.s.l.		568.5	568.5	568.5	568.5	568.5	568.6 568.6	568.5 568.7	568.7
Progressive distance, m		227.78	222.05	212.45	230.14	218.76	204.09 217.53	254.44 217.96	231.33

Legend

- EGE-1.2	- EGE-2.2	- EGE-4
- EGE-1.1	- EGE-2.3	S7 - Sample
- EGE-2.1	- EGE-3	

List of Figures

List of Tables

Acknowledgements

With this thesis work, my university career ends and, consequently, an important phase of my life. It has not always been an easy path, studded with anxiety and pain, Sunday evenings spent in the university and missed parties, but at the same time, also full of joy and satisfaction, personal growth and new acquaintances.

It is therefore difficult to thank in a few lines all those who, in one way or another, have been the architects of this achievement of mine.

First of all, I sincerely thank my family for being close to me, always supporting my choices and never making me feel alone even if we are apart.

My gratitude then goes to the professors, in particular my supervisor, Prof. Cristina Jommi for believing in me and entrusting me with this project, for her extreme helpfulness and for turning out to be great teacher, both from a professional and a human point of view.

I would like to thank the people at Studio Geotecnico Italiano srl, in particular Eng. Andrea Masella and Dr. Paolo Mazzoni for their patience and support during these months.

I would also like to thank the Politecnico di Milano for having welcomed me into its stimulating, multicultural environment full of opportunities and prospects for the future.

Lastly, thank you to my friends, those in Milan for becoming my new family, and those in Munich and Saint-Petersburg for always being a point of reference in my life and for wringing a laugh out of me on the phone even in the most difficult moments.

Thank you. Grazie. Спасибо.